An Experimental Study of Oil / Water Flow in Horizontal Pipes

by

Geir Elseth

Department of Technology (HiT-TF)
Telemark University College
Kjølnes Ring, N-3914 Porsgrunn
Norway

Thesis submitted to
The Norwegian University of Science and Technology (NTNU),
for the degree of Dr. Ing

Porsgrunn, June 2001

URN:NBN:no-1301

AKNOWLEDGLEMENTS

The work presented in this thesis is not a product of my effort alone. Several people have offered their help during the course of this work.

First of all, I will like to thank my supervisor Professor Morten C. Melaaen at Telemark University College (Høgskolen i Telemark, HiT, in Norwegian) for excellent guidance during the four years that I have spent working here. His knowledge within multiphase flow together with his encouragement has helped me a lot. In particular I would like to mention his contributions regarding the modelling part of this work. Finally, I am very satisfied with his quick response whenever I experienced problems and for good organisation of the study.

Secondly, I am grateful to senior research scientist Harald-Knut Kvandal at Norsk Hydro. With his experience related to multiphase flow his contributions have been invaluable. A significant part of the work presented in this thesis (Chapter 9 in particular) is a partitive work between Harald and myself.

When something has gone wrong on the flow facilities technicians from Norsk Hydro have straightened things out each time. In particular I would like to thank Stein Solum and Pål Midtbøen for their help with the instruments.

By surface chemistry, Robert Orr, senior research scientist at Norsk Hydro, improved the tracer particles needed for the LDA experiments so that they could be used both in water and oil. This increased the data rate, hence reduced the time required for each LDA experiment significantly. I would like to thank Robert.

In the finishing months I also worked together with the research scientists Ingunn Granstrøm and Sampath Munaweera at Norsk Hydro and Håvard T. Nordborg, a diploma student at HiT. They took some of the pictures and conducted some of the hold up measurements presented in the thesis. I thank them all.

In the years I have been working on this thesis I have spent many hours side by side with the laser equipment. Without the help from Werner Martinsen at Mestec, PhD Martin Fischer at the University of Erlangen and Britt Halvorsen at HiT I would have had to spend a lot more time.

Finally, I will like to take the opportunity to thank Telemark University College and all my colleagues, in particular, Aage I. Jøsang, Martin Siljan, Rune Engeskaug and Qianpu Wang for making the years enjoyable, and my present employer Norsk Hydro for their support.

ABSTRACT

The purpose of this thesis is to study the behaviour of the simultaneous flow of oil and water in horizontal pipes. In this connection, two test facilities are used. Both facilities have horizontal test sections with inner pipe diameters equal to 2 inches.

The largest facility, called the *model oil facility*, has reservoirs of 1 m^3 of each medium enabling flow rates as high as 30 m^3/h, which corresponds to mixture velocities as high as 3.35 m/s. The flow rates of oil and water can be varied individually producing different flow patterns according to variations in mixture velocity and input water cut. Two main classes of flows are seen, *stratified* and *dispersed*. In this facility, the main focus has been on stratified flows.

Pressure drops and local phase fractions are measured for a large number of flow conditions. Among the instruments used are differential pressure transmitters and a traversing gamma densitometer, respectively. The flow patterns that appear are classified in flow pattern maps as functions of either mixture velocity and water cut or superficial velocities. From these experiments a smaller number of stratified flows are selected for studies of velocity and turbulence. A laser Doppler anemometer (LDA) is applied for these measurements in a transparent part of the test section. To be able to produce accurate measurements a partial refractive index matching procedure is used.

The other facility, called the *matched refractive index facility*, has a 0.2 m^3 reservoir enabling mainly dispersed flows. Mixture velocities range from 0.75 m/s to 3 m/s. The fluids in this facility are carefully selected to match the refractive index of the transparent part of the test section. A full refractive index matching procedure is carried out producing excellent optical conditions for velocity and turbulence studies by LDA. In addition, pressure drops and local phase fractions are measured.

CONTENTS

1. INTRODUCTION

Background

Offshore production of oil and gas on the Norwegian continental shelf has been going on for more than 30 years and the production of crude oil has been around 3 million barrels per day since 1996. Still, according to the Norwegian Oil and Energy Department (2001), great reserves are unexploited or not yet discovered.

The oil and gas reserves are located in reservoirs, some more than 2 km below the bottom of the sea. In the early years of production the wells were mainly vertical, but in the last decade technology has enabled horizontal or near horizontal wells to be drilled. These horizontal wells can be more than 7 km long. A typical inner pipe diameter is 4 inches. When it comes to transport pipes for oil they can be over 200 km long with an inner diameter of 29 inches (Source: Norwegian Oil and Energy Department, 2001).

A gas/oil/water reservoir consists of a gas zone on top, an oil zone in the middle and a water zone at the bottom due to the differences in density. When oil is produced from a reservoir a well is drilled through the ground, vertically at first, then following a slope before it enters the reservoir horizontally, into the oil phase. The well will produce single-phase oil in the first period of its ”lifetime”. As time goes by, water will cone into the well from inside the reservoir and the well will produce water in addition to crude oil. If the position of the well is close to the gas/oil interface eventually gas might be produced as well. As the well ages water production increases. The well might be economical to operate even for water cuts as high as 90%.

The presence of water in the pipe will affect the transport of oil from the reservoir to the processing unit in the sense that when two immiscible liquids flow together in a pipe, the mixture will behave different from single-phase flow. Depending on the mixture velocity and the water cut several flow configurations, known *as flow patterns*, or *flow regimes* will be formed. Transport of mixtures with different flow patterns might influence the input power required to pump the mixture.

A phenomenon that occurs when two immiscible liquids flow together in a pipe is *phase inversion*. Phase inversion will occur provided the mixture velocity is high enough for dispersions to be formed for the various ranges of water cuts. Phase inversion is defined as a change in continuity from one phase to another (e.g. from oil continuous to water continuous). At low water cuts water will be dispersed as droplets in the continuous oil phase, but as the amount of water is increased, the system changes to a dispersion of oil droplets in a continuous water phase. The water cut that inverts the system is a function of several parameters like the physical properties of the crude oil. The viscosity at the inversion water cut can be several magnitudes higher than the viscosity of the individual liquids. This often results in increased pressure drops, something that is highly undesirable when the mixture is to be transported over long distances. Thus, it is important to understand and to be able to predict when phase inversion will occur.

Both temperature and pressure are high in the reservoir but fall as the mixture is transported to the processing unit provided it is located at sea level or somewhere on shore. Some of the problems in crude oil/water pipe transport that is associated with the presence of water and the temperature and pressure conditions in the pipe are:

- Saline deposits known as *scale*. Although scale insulates the pipe it reduces the cross section and has to be removed.
- Formation of crystalline *hydrates* by combination of water molecules and natural gas under high pressure.
- Deposition of high molecular constituents of crude oil, known as *asphaltenes*, as a consequence of reduced solubility when the temperature is reduced. Formation of asphaltenes is irreversible and once they are deposited on the pipe wall they can only be removed mechanically.
- Formation of *wax*, which is a high molecular deposit that is formed if the temperature becomes too low. The formation of wax is reversible in the sense that the wax may be removed by increasing the temperature.

- Production of *sand*. In addition to production of water and oil, sand particles will enter the well from the reservoir.

In general the formation of deposits will reduce the pipe cross-section and therefore has direct influence on the production and pressure drop.

The model system

The work presented in this thesis has focused on the transport of oil and water in a horizontal pipe. In contrast to the transport of crude oil and seawater with the possibility of deposits, experiments are conducted on a pure model oil/tap water system and a system of a mixture of two diesel oils combined with a solvent. The model fluids are transparent, which enables laser Doppler anemometry, and has physical properties that are comparable to a crude oil/sea water system. Tap water is used to avoid problems that can be caused by the saline environment in seawater. The inner diameter of the test pipe that simulates the pipes is 2 inches.

The goals

The goal is to measure the velocity and turbulence distributions or profiles in two-phase oil/water horizontal pipe flow and compare them to single-phase flow distributions. Identification of velocity and turbulence distributions are important for instance in the development of computer models. By using laser Doppler anemometry (LDA) such distributions can be measured accurately in transparent model systems as described above.

Prior to these measurements studies of local phase fraction (i.e. holdup) and the pressure drop in the pipe need to be conducted in order to classify the flow patterns and provide a basis of comparison for the LDA measurements. E.g. information of the position and the width of the interface between oil and water in stratified flow are needed to fully understand the velocity and turbulence distribution across the pipe. A traversable gamma densitometer provides this kind of information. Likewise, measurements of pressure drop by dp-transmitters can be compared to the pressure drops derived from Reynolds stress distributions calculated from LDA measurements.

The framework of the thesis

The thesis is divided into ten chapters, which fall into two main parts. The first five chapters, including this introduction, describe the goals of the thesis, the theory and a literature review on key topics, the model flow systems and the instruments. The last five chapters, including the conclusions, present and discuss results from experiments.

Thus, Chapter 2 presents a review of liquid-liquid flow in horizontal pipes. The list of contributors to the subject is large, and only the work of a few is mentioned here. Chapter 3 describes the two flow facilities that are constructed to model horizontal transport of oil/water from a reservoir. Chapter 4 contains both a literature review on Laser Doppler Anemometry and a description of the basic theory on the topic as well as a presentation of the laser system and the measurements procedures that will be used in the experiments. Chapter 5, which completes the first main part, gives an examination of the principles of gamma densitometry and a description of the equipment and the measurement procedures that will be used.

Measurements of flow patterns and local phase fractions for mixture velocities ranging from 0.4-3 m/s with variations in water cut from 0-100% are presented in Chapter 6. Chapter 7 presents pressure drop measurements for the same mixture velocities and water cuts and compares them to the *two-fluid model* for stratified flows and the *homogeneous model* for dispersed flows. LDA measurements of velocity and turbulence distributions in stratified flow are presented in Chapter 8. This study is conducted for mixture velocities ranging from 0.4-2 m/s and water cuts varying from 0-100% provided that the flow is stratified. Chapter 9 contains LDA measurements of velocity and turbulence together with measurements of local phase fraction and pressure drops in dispersed flows. The measurements presented in this chapter are conducted on a different flow facility and the chapter itself is an extract of a published paper. The final chapter contains conclusions and proposes further work.

2. LIQUID-LIQUID FLOW – LITERATURE REVIEW AND BASIC MODELS

In 1949, Clark and Shapiro patented a process for the injection of demulsifying agents with water into crude oil pipelines. The agents were added to prevent destruction of the water film in the pipe. The formation of a water film on the inside of the pipe after injection of water into oil was observed a year earlier. The added water seemed to have a lubricating effect on the oil flow. Charles and Redberger (1962) reported on the reduction of pressure gradients in oil pipelines with water addition. They measured a maximum reduction between 12 and 31% for different oils. The pressure gradient reductions occurred at water contents ranging from 12 to 93%, respectively. Pressure drops in liquid-liquid two-phase flow can be quite different from those in single-phase flows. These observations are among the first important studies of oil-water flow in pipes.

Studies of liquid-liquid flow in a pipe often include observation of flow patterns, that is, the shape and spatial distribution of the two-phase flow within the pipe. But even more important is the investigation of pressure drop. Today, measurements of the pressure gradient in the different flow patterns, as well as the development of models is subjected to a lot of research.

Through the years several investigators have contributed to the understanding of liquid-liquid flow in general and oil-water flow in particular. The inclination angle of the two-phase flow is one parameter that affects the flow pattern. Pure horizontal flow and pure vertical flow are often idealized cases. Some researchers, represented by Sööt and Knudsen (1973) and Rashid Hasan and Shah Kabir (1990) studied vertical flows while others studied horizontal flows with or without a small inclination angle. In reality, (gas)/oil/water flow in transport-pipes and wells often have an inclination angle different from 0 or 90 degrees. However, this review is limited to describing some of the most important work done on oil-water flows in horizontal pipes.

2.1 FLOW PATTERNS OF OIL/WATER FLOW IN HORIZONTAL PIPES

Formation of different flow patterns will appear when two immiscible liquids flow together in a horizontal pipe. Input phase ratio, mixture flow rate, density ratio, viscosity ratio, wetting properties, surface tension and pipe geometry are decisive parameters for the formation of each flow pattern. Identification of the different flow patterns can be done in several ways:

- Visually through transparent pipes. Equipment like cameras and video camera recorders are helpful tools. Early studies by Russel et al. (1959) and Charles et al. (1961) together with the more recent work of Arirachakaran et al. (1989) make use of this technique. The weakness of visual observations is that they always are subjective and even have the disadvantage of being exposed to light refractions.

- The use of conductivity probes as in Trallero et al. (1997) and Nädler and Mewes (1995) as well as the use of high frequency impedance probes as in Vigneaux et al. (1988) and Angeli and Hewitt (2000) gives perhaps a more precise and objective discrimination of flow regimes.

- Gamma ray densitometry used by for instance Soleimani (1999), Elseth et al. (2000) and Kvandal et al. (2000) represents another useful method.

Flow pattern studies presented later in this work are done with a digital video camera in combination with a traversing gamma densitometer.

Before the rest of the review is presented, some of the basic terms of liquid-liquid flow are defined. Consider oil and water flowing simultaneously in a horizontal pipe with cross section area A. The input volumetric flow rates of oil and water are Q_o and Q_w, respectively. The input volumetric oil and water fractions are then given by:

$$C_o = \frac{Q_o}{Q_o + Q_w} \qquad C_w = \frac{Q_w}{Q_o + Q_w} \tag{2.1}$$

Superficial velocities of oil and water are based on the input flow rates and the cross sectional area of the pipe and are defined by:

$$U_{so} = \frac{Q_o}{A} \qquad U_{sw} = \frac{Q_w}{A} \tag{2.2}$$

Combining Equations 2.1 and 2.2 gives the relationship between superficial velocities and input fractions:

$$\frac{U_{so}}{U_{sw}} = \frac{C_o}{C_w} \tag{2.3}$$

It is assumed that each phase in separated two-phase flow occupies different parts of the cross section. The actual velocity of each phase, the in-situ velocity, becomes different from the superficial velocity because the velocity is calculated from the volumetric flow rate passing a smaller area than the cross sectional area. If the cross section areas occupied by oil and water are respectively A_o and A_w, the actual velocities are given by:

$$U_o = \frac{Q_o}{A_o} \qquad U_w = \frac{Q_w}{A_w} \tag{2.4}$$

From Equations 2.2 and 2.4 it follows that the actual velocity always exceeds the superficial velocity for each phase. The actual or the in-situ area fraction of oil and water is simply defined by:

$$\varepsilon_o = \frac{A_o}{A} \qquad \varepsilon_w = \frac{A_w}{A} \tag{2.5}$$

The actual and the superficial velocity of each phase is related by the in-situ area fraction:

$$U_o = \frac{U_{so}}{\varepsilon_o} \qquad U_w = \frac{U_{sw}}{\varepsilon_w} \tag{2.6}$$

Finally, the mixture velocity is defined by dividing the total volumetric flow by the cross sectional area of the pipe:

$$U_m = \frac{(Q_o + Q_w)}{A} \tag{2.7}$$

which also is equal to the summation of the superficial velocities ($U_m = U_{so} + U_{sw}$).

2.1.1 Classification of flow patterns and flow pattern maps

Through the years from the late 1950's and to the present time the investigation of flow patterns has developed both in observation techniques and presentations. Here, the pioneer contributions of Russel et al. (1959) and Charles et al. (1961) are presented along with the work of Arirachakaran (1989) and the recent studies of Trallero et al. (1997) and Nädler and Mewes (1997).

Russel et al. (1959) describe three flow patterns in oil-water flow in a horizontal circular pipe. These are mixed flow (M), stratified flow (S) and bubble flow (B). They varied the oil-water volume ratio, R_v, from 0.1 to 10.0, and the superficial water velocity from 0.0354 to 1.082 m/s. Table 2.1 includes the experimental data. The purpose was to study the effect of input ratios on the flow patterns. Figure 2.1 shows the flow patterns at the highest superficial water flow rate with varying input ratio. The figure contains drawings prepared from photographs as they were presented in their publication.

Table 2.1 Experimental data – Russel et al. (1959).

Fluids: water and transparent mineral oil (paraffinic)		
Flow temperature: 42 ^{o}C	Oil viscosity: 18 mPas	Pipe diameter: 24.5 mm
Water viscosity: 0.894 mPas	Oil density: 834 kg/m^3	Test section length: 8.6 m

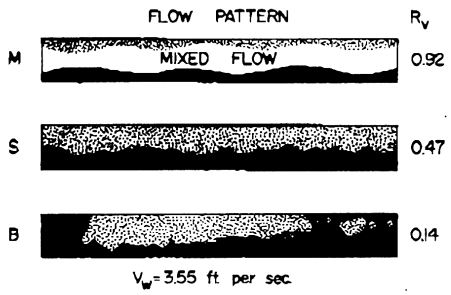

Figure 2.1 Flow patterns of mixed flow (M), stratified flow (S) and bubble flow (B) for a fixed water flow rate. Drawings from photographs [Russel et al. (1959)].

The three flow regimes were found to appear in both laminar and turbulent flows. At the lowest input ratio the oil phase appears as large stretched out bubbles. With increasing input ratio the flow approaches the stratified pattern. By further increase of input ratio the flow becomes mixed or dispersed.

Charles et al. (1961) did a similar study of three different oils, each mixed with water in a horizontal pipe. They varied the superficial oil velocity from 0.015 m/s to 0.91 m/s and the superficial water velocity from 0.03 m/s to 1.07 m/s. The input oil-water ratios ranged from 0.1 to 10.0. Table 2.2 adds up the experimental data.

Table 2.2 Experimental data – Charles et al. (1961).

Fluids: Water and three commercial oils; [1]Marcol GX (clear), [2]Wyrol J (clear), [3]Teresso 85 (dark green-brown)		
Flow temperature: 25 °C	Oil viscosities [mPas]: 6.29 [1], 16.8 [2], 65 [3]	Pipe diameter: 26.4 mm
	Oil densities: 998 kg/m^3	Test section length: 7.3 m

Charles et al. (1961) observed a series of flow patterns for a decrease of the oil flow rate at constant water flow rate. Figures 2.2 to 2.4 represent drawings from photographs of the different flow regimes.

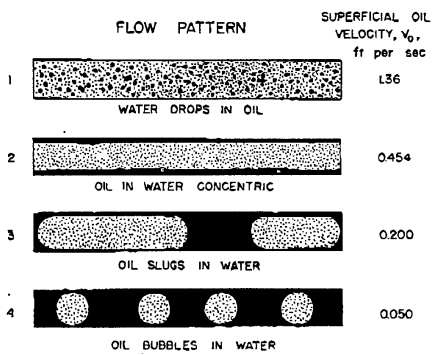

Figure 2.2 Water and the 16.8 mPas viscosity oil at varying oil velocities for a low fixed water velocity of 0.03 m/s [Charles et al. 1961].

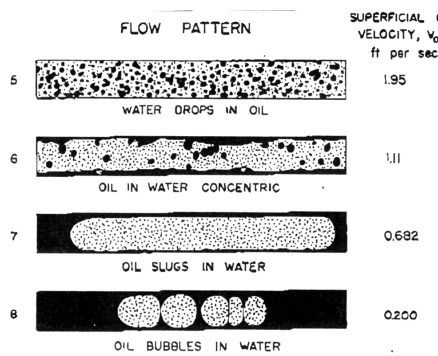

Figure 2.3 Water and the 16.8 mPas viscosity oil at varying oil velocities for a fixed water velocity of 0.21 m/s [Charles et al. 1961].

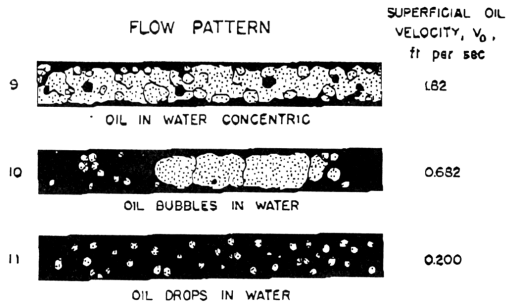

Figure 2.4 Water and the 16.8 mPas viscosity oil at varying oil velocities for a high fixed water velocity of 0.62 m/s [Charles et al. 1961].

The flow patterns varied from water drops in oil through concentric (annular) oil flow in water to oil drops in water. Each of the flow patterns was observed not only for the 16.8 mPas oil but for the other two as well. Figures 2.2 and 2.3 show the effect of reducing the oil velocity at a relatively low water velocity. At high oil velocity oil is the continuous phase, and water exists as drops dispersed over the entire cross section. By reduction of the oil velocity both phases becomes continuous and the flow is concentric or annular. Further reduction of oil velocity leads to water being the continuous phase and oil being present as slugs and finally as drops. At higher water velocities as in Figure 2.4 the same transitions were observed but the flow patterns were more disturbed. Based on the variations of superficial velocities of oil and water the different flow regimes are summarized for the 6.29 and the 16.8 mPas viscosity oils in Figure 2.5.

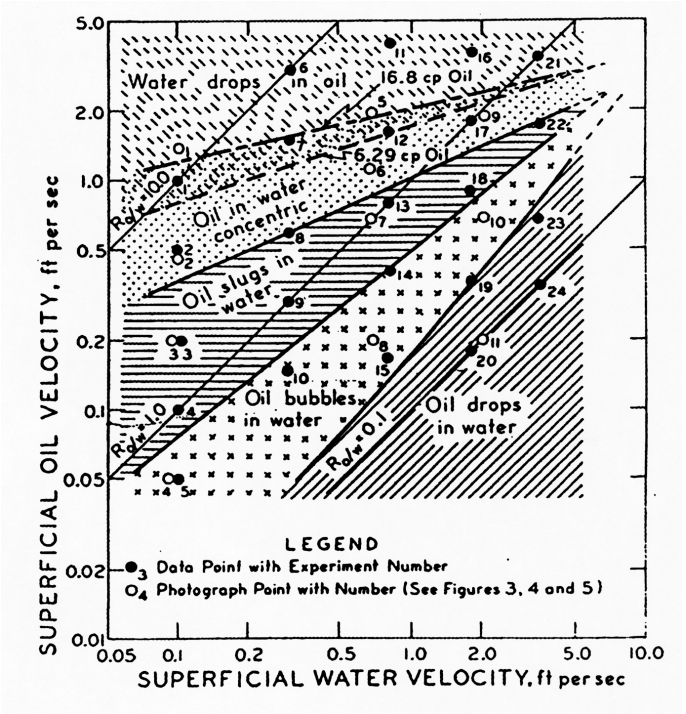

Figure 2.5 Flow regimes for oils of viscosity 6.29 and 16.8 mPas and density 998 kg/m^3, flowing in the presence of water with the same density [Charles et al. 1961].

The lines that separate each flow pattern represent gradual transitions since it was difficult to define the exact change from one regime to another. The flow regimes in Figure 2.5 are almost the same for both oils with the exception of the boundary between water drops in oil and the concentric flow pattern. The boundary lies at higher oil velocities for the 16.8 mPas oil than the 6.29 mPas oil. Figure 2.6 presents the flow regimes for the 65 mPas oil flowing together with water. The patterns are similar to the two-phase systems with the less viscous oils except at low water velocities. At such low water velocities a series of oil continuous flow patterns were identified and an inversion line (P-Q) was drawn. For given oil velocities, mixtures with lower water velocity than indicated at the inversion line gave oil continuous flow. Mixtures with higher water velocity than indicated at the inversion line gave water continuous flow.

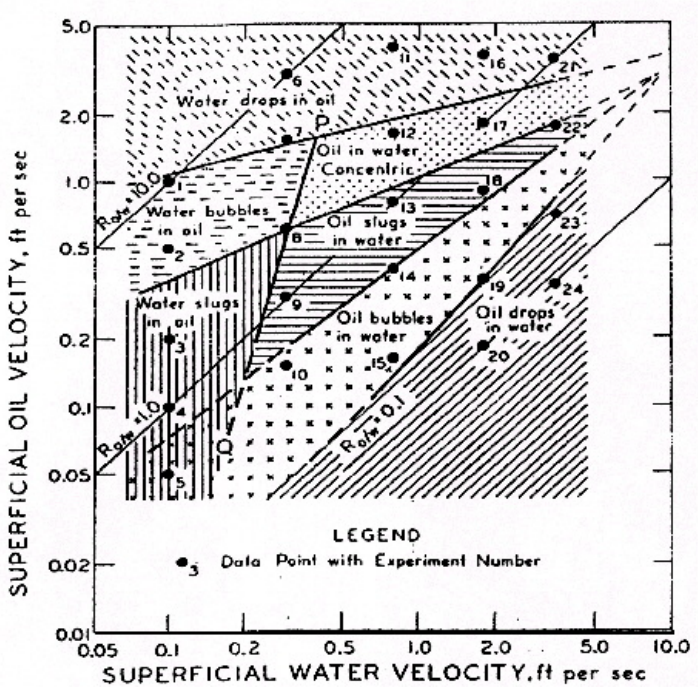

Figure 2.6 Flow regimes for oil of viscosity 65 mPas and density 998 kg/m^3, flowing in the presence of water with the same density [Charles et al. 1961].

Arirachakaran et al. (1989) acquired experimental data for oil/water flow in horizontal pipes for a selection of viscosities in order to determine any viscosity effect on the flow patterns. They used two flow facilities with different geometries of the test sections and with different oils. Table 2.3 lists the experimental data. Among their studies were flow patterns and the flow pattern transition at the phase inversion point. Figure 2.7 is a sketch of the observed flow patterns and Figure 2.8 displays the flow pattern map. Stratified flow (S) with or without mixing at the interface and fully dispersed flow, either an oil-in-water dispersion or a water-in-oil dispersion (DO, DW) were the extremes. The mixed flow (MO, MW), and mixed in the sense that the flow consists of both a dispersed and a "free" phase, could appear with either water or oil as the "free" phase. Annular flow (AO, AW) had a core of one phase within the other. The core could be both oil and water. Finally, intermittent flow (IO, IW) was described as a flow pattern that was alternating between a "free" phase flow and a fully dispersed flow.

When water was the continuous phase they could observe no effect of oil viscosity on the flow pattern and the same sequence of flow patterns was identified at the same mixture velocity to the right of the inversion line in the flow pattern map. When oil was the continuous phase they were not able to draw any general conclusions apart from the fact that the oil annulus in the annular flow pattern seemed to be reduced as the oil viscosity was decreased. For low-viscosity oils the annular flow pattern was not even present.

Table 2.3 Experimental data – Arirachakaran et al. (1989).

Fluids: tap water and diesel fuel oil[1] tap water and two refined oils[2]		
Flow temperature:	Oil viscosity:	Pipe diameter:
28-54 °C	4.7- 2116 mPas	26.6 [2] and 41 [1] mm
Interfacial tension:	Oil density:	Test section length:
σ =29-32.2 $\cdot 10^{-5}$ N/cm	868-898 kg/m^3	6.1[2] and 12.8[1] m

[1]Data for flow facility 1 and [2]data for flow facility 2.

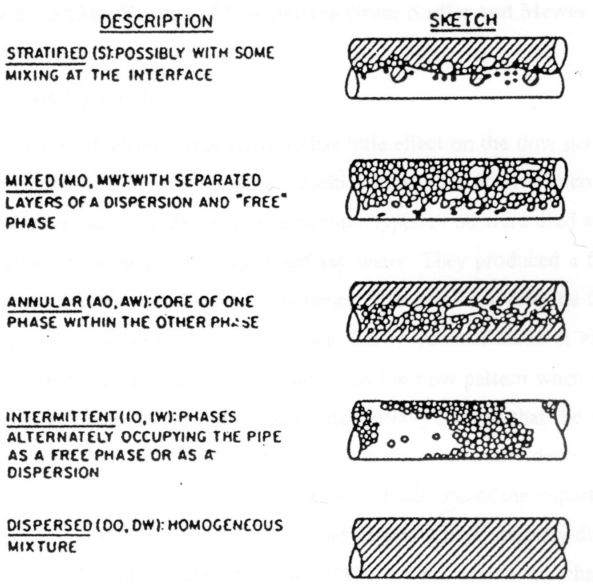

Figure 2.7 Flow patterns - Arirachakaran et al. (1989).

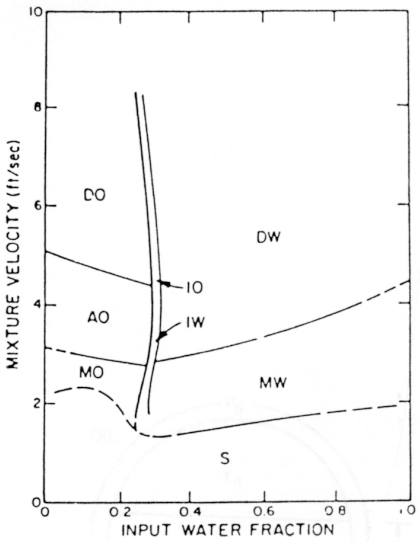

Figure 2.8 Flow pattern map – Arirachakaran et al. (1989).

The experimental data by Trallero et al. (1997) are listed in Table 2.4. They report six different flow patterns as shown in Figure 2.9. They classified them into two main categories. Segregated flow is represented by stratified flow (ST) and stratified flow with mixing at the interface (ST & MI). The other category, dispersed flow, is either water dominated or oil dominated. Dispersion of oil in water over a water layer (DO/W & W) and the oil in water emulsion (O/W) are water continuous flows. A dual dispersion of water droplets in oil and oil droplets in water (DW/O & DO/W) and the water in oil emulsion (W/O) were classified as oil dominated flows.

Table 2.4 Experimental data – Trallero et al. (1997).

Fluids: tap water and mineral oil		
Flow temperature: 25.6 ^{o}C	Viscosity ratio: $\mu_o/\mu_w = 29.6$	Pipe diameter: 50.13 mm
Interfacial tension: $\sigma = 36 \cdot 10^{-5}$ N/cm	Density ratio: $\rho_o/\rho_w = 0.85$	Test section length: 15.54 m

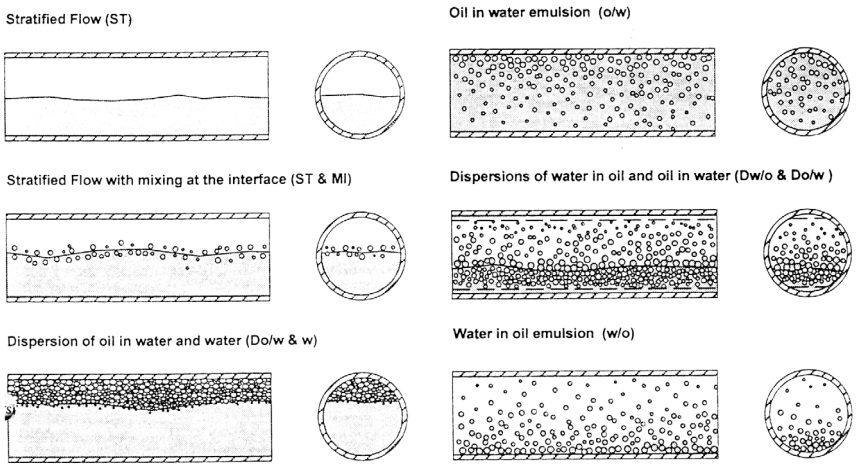

Figure 2.9 Horizontal oil-water flow patterns [Trallero et al. (1997)].

From the same experiments they constructed corresponding flow pattern maps. Figure 2.10 shows the flow patterns at different superficial velocities. Figure 2.11 displays the same patterns as functions of mixture velocity and water fraction.

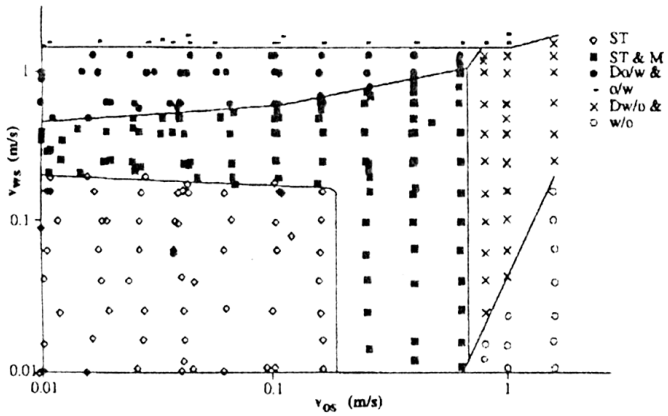

Figure 2.10 Experimental flow pattern map – superficial velocities [Trallero et al. (1997)].

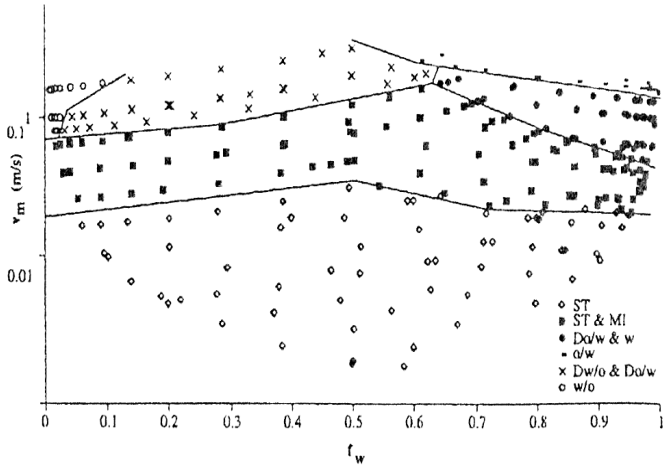

Figure 2.11 Experimental flow pattern map – mixture velocity and input water cut [Trallero et al. (1997)].

Nädler and Mewes (1997) measured flow regimes and pressure drops in oil-water flows. By varying the flow temperature between 18 and 30 ^{o}C the oil-water viscosity ratio varied from approximately 35 to 28. The experimental data are presented in Table 2.5. The observed flow regimes are schematically presented in Figure 2.12 and compared in the flow pattern maps in Figure 2.13.

Table 2.5 Experimental data – Nädler and Mewes (1997).

Fluids: water and mineral white oil (Shell Ondina 17)		
Flow temperature: 18-30 ^{o}C	Viscosity ratio: $\mu_o/\mu_w \approx 35 - 28$	Pipe diameter: 59 mm (pipe material: perspex)
	Density ratio: $\rho_o/\rho_w \approx 0.85$	Test section length: 48 m

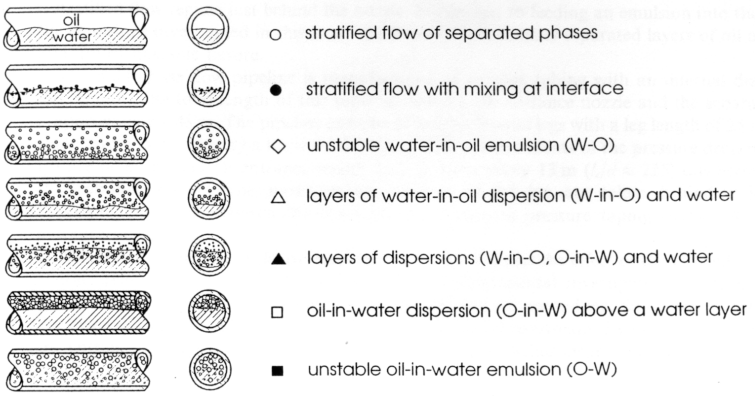

Figure 2.12 Horizontal oil-water flow patterns [Nädler and Mewes (1997)].

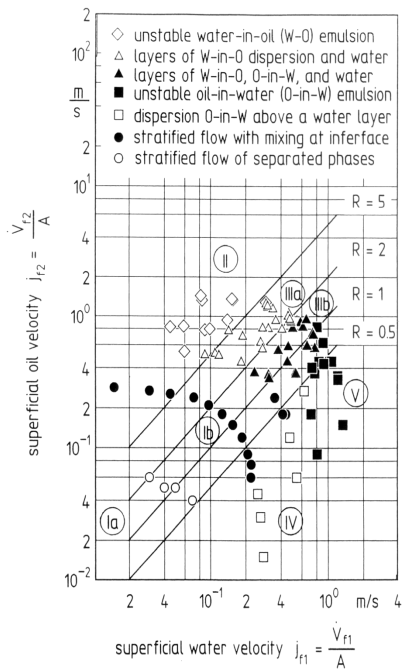

Figure 2.13a Experimental flow pattern map – superficial velocities [Nädler and Mewes (1997)].

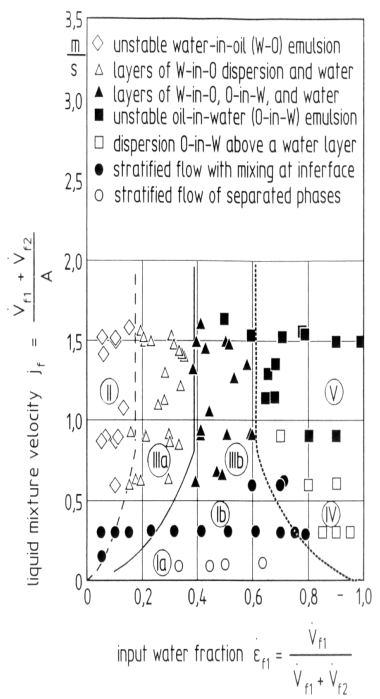

Figure 2.13b Experimental flow pattern map – mixture velocity and input water fraction [Nädler and Mewes (1997)].

Nädler and Mewes (1997) classifies the flow patterns into stratified and stratified with mixing at the interface as seen as the top two patterns in Figure 2.12. Further, they use the terms unstable water-in-oil (W-O) and oil-in-water (O-W) emulsions for fully dispersed flows. The other three flow patterns they observed were partial dispersions as shown in Figure 2.12.

The classifications of flow patterns presented in these works are subjective. Different investigators use different terms or names for each identified flow regime. All investigators, however, generally report separated or stratified flow and fully or partially dispersed flow. When the different flow patterns are identified, the flow pattern map can be constructed. Usually, the axes are the two superficial velocities or the mixture velocity and the input water fraction. Apart from the obvious dependence on superficial velocities, mixture velocity and input water fraction, several other parameters have influence on the flow regimes.

2.1.2 Parameters with impact on the flow patterns

Mixture velocity and input water cut:

The effect of mixture velocity and water cut was investigated early by Russell et al. (1959). In general low mixture velocities allows the flow to be separated or stratified, while high mixture velocity disperses the flow. However, dispersed flows may appear at low velocities provided the water cut is very low or very high.

Viscosity, density and surface tension: The viscosity effect, studied by Russell et al. (1959), Charles et al. (1961) and Arirachakaran et al. (1989), seems to have little or no effect on the observed flow patterns for oil/water flows. The sequence or the number of observed flow patterns is the same, but transitions from one flow regime to another may appear at different superficial velocities when oils of different viscosities are used. This means that the size of the various flow regime areas on the map can vary slightly. Reports on the isolated effect of density and surface tension are limited. In two-phase flows with high density difference between the phases, stratified flow will generally appear for a larger range of mixture velocities and water fractions than for the case of low density difference two-phase flows.

Flow geometry and wetting properties:

The flow geometry such as pipe diameter, inlet design, studied by for instance Soleimani et al. (1997), and the inclination angle of the pipe are other parameters that can be decisive for which flow pattern that appears. Inlets (i.e. the oil/water mixing unit) can be shaped in a way that it tends to keep the flow stratified (see the mixing unit described in Chapter 3.1). Alternatively, inlets can be shaped to disperse the flow.

The wetting properties can also influence the flow patterns as investigated by Clark (1949), Angeli (1996) and Angeli and Hewitt (2000). In general materials that prefer wetting by oil favour oil continuous dispersions and materials that prefer wetting by water favour water continuous dispersions.

Temperature and pressure:

Temperature and pressure have influence on the flow patterns in the sense that they influence the physical properties like viscosity, density etc.

2.1.3 Flow pattern transitions

Oil-water flows are gravity dominated and flows separately when the flow rates of each phase are low, that is, when superficial velocities are low. The interface between the phases is smooth without waves. At higher flow rates waves start to appear at the interface. The wavelength is about twice the pipe diameter as stated by Trallero et al. (1997). Small water droplets exist in the oil layer while small oil droplets appear in the water layer. Both the oil droplets and the water droplets flow close to the interface. Different forces act on the droplets but gravity forces overcome dynamic forces and the droplets are kept close to the interface. Guzhov et al. (1973) reports that the relative movement of the phases results in vortex motion at the interface. Vortices formed in the oil layer penetrate the water layer and vice versa. This turbulence at the interface eventually disperses the flow. Transition from separated to dispersed flow can be illuminated by a stability analysis. The instability occurs because there exist either a difference in tangential velocity or a significant jump in viscosity across the interface. Dispersions can be formed at both low water fractions and low oil fractions. Either way, the low fraction phase loses its continuity and becomes dispersed in the high fraction phase.

Several investigators have studied the stability of two-phase flows. For gas / liquid flow this is done by for instance Barnea and Taitel (1993) while for liquid-liquid flow the two contributions from Brauner and Moalem Maron (1992[1] and 1992[2]) are central. The latter of Brauner and Moalem Marons work deals with oil-water flow in particular. The details of their stability analysis are not presented here, but Figure 2.14 represents the basic propositions from the oil-water study. Continuity and momentum equations of an oil-water system are analyzed and a stability analysis is conducted. Criteria for transition from smooth stratified to other flow regimes are then given. They proposed two transition lines. Both the zero neutral stability (ZNS) line and the zero real characteristics (ZRC) line are shown in Figure 2.14. The two lines define three zones in the figure. Below the ZNS boundary the flow is smooth stratified.

The "buffer zone" positioned in between the two boundaries includes stratified flows with the existence of interfacial waves. Beyond the ZRC boundary other flow regimes than stratified wavy exist. Thus, the ZNS boundary represents the transition from stable smooth stratified flow to stratified wavy flow and the ZRC boundary represents the transition from stratified wavy flow to other flow regimes. Also presented in Figure 2.14 is the effect of density and viscosity ratios on the boundaries. Brauner and Moalem Maron (1992[2]) found that as the oil-water density ratio was decreased, the area of stable smooth stratified flow also decreased (Figure 2.14 a and b). A similar effect appeared when the oil-water viscosity ratio was reduced (Figure 2.14 b and c).

2.1.4 Phase inversion

One special phenomenon that occurs in dispersed liquid-liquid flows under certain conditions is called phase inversion. According to Angeli (1997), the phase inversion of a dispersion of two immiscible liquids can be defined as the transition of a phase from being dispersed to being continuous. The result is that the dispersed and the continuous phases in the system are changed. Arirachakaran et al. (1989) presented a sketch of the inversion process for an oil-water system as shown in Figure 2.15.

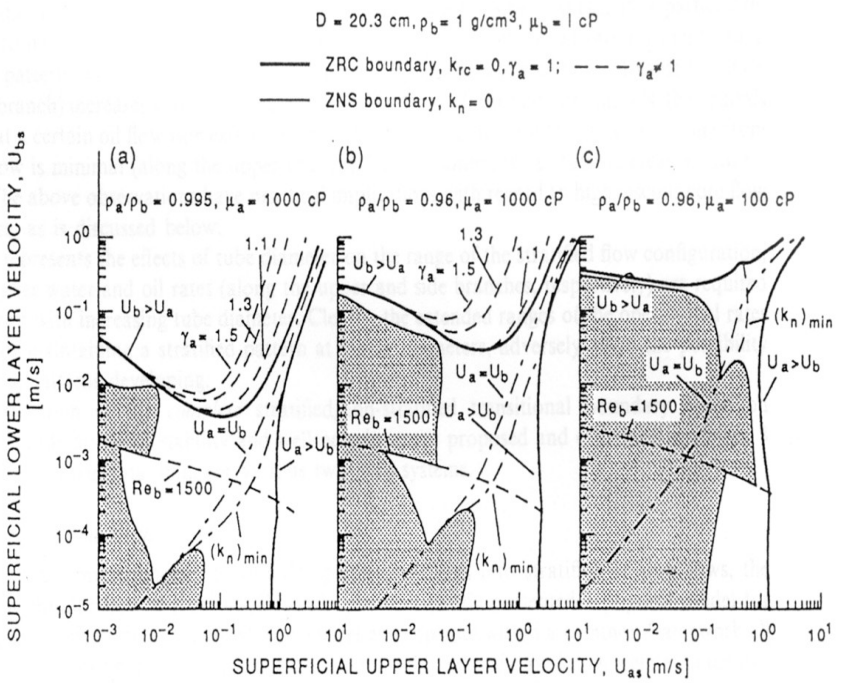

Figure 2.14 The effect of density and viscosity ratios on the location of ZNS and ZRC boundaries [Brauner and Maron (1992[2])]

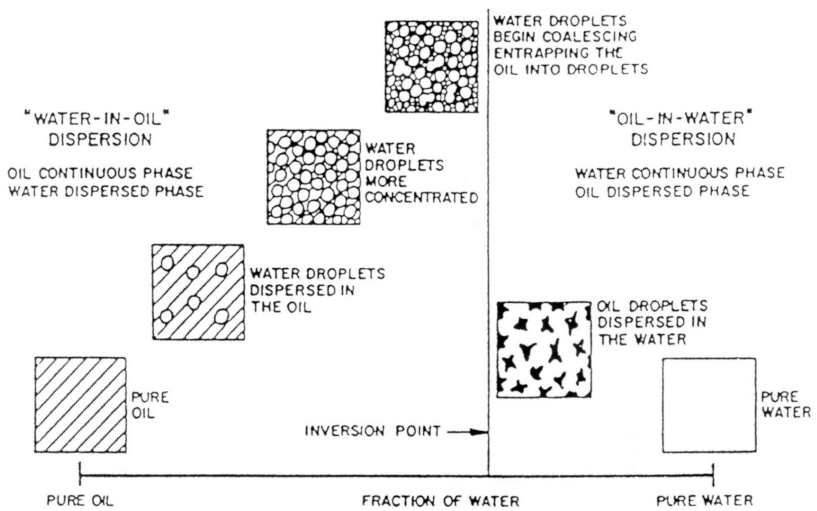

Figure 2.15 The phase inversion process presented by Arirachakaran et al. (1989).

Consider a flow of single-phase oil in a horizontal pipe at sufficiently high velocity for dispersions to exist. Then, a small amount of water is added. At low water fractions water droplets will be dispersed in the oil phase. Water is the dispersed phase and oil is the continuous phase. By increasing the water fraction and keeping the mixture velocity constant, the concentration of water droplets in oil also increases. At one point, the concentration of water droplets is so high that the droplets start to coalesce and entrap oil in small pockets. At this point, the water phase is transformed from being dispersed to being continuous. The entrapped oil droplets are now dispersed in the water phase.

One of the reasons to why phase inversion is important is that it has a significant influence on the pressure drop in the pipe. Several investigators, for instance Guzhov (1973), Valle and Utvik (1997) and Soleimani (1999), have shown measurements of a significant increase in the pressure gradient near the inversion point when approaching from low water fractions, that is, from the left side in Figure 2.15. The pressure gradient reaches its maximum value somewhere near the inversion point and falls rapidly just after the inversion.

Pal (1993) did experiments in laminar oil/ water flow and found similar trends for the relative or mixture viscosity of dispersions. Pal (1993) also examined what he called unstable emulsions of water-in-oil (W/O) and oil-in-water (O/W). Figure 2.16 shows the variation of mixture viscosity with water fraction for unstable emulsions. One of the findings was that the mixture viscosity had a peak at the inversion between W/O and O/W emulsions. The mixture viscosity was calculated from laminar data using the Hagen-Poiseuille law [Hewitt et al. (1997)] given by Equation 2.7, which states that, the volumetric flow rate Q of a fluid of a viscosity μ through a pipe of radius R and length L is related to pressure drop by:

$$Q = \frac{\Delta p \pi R^4}{8 \mu L} \tag{2.7}$$

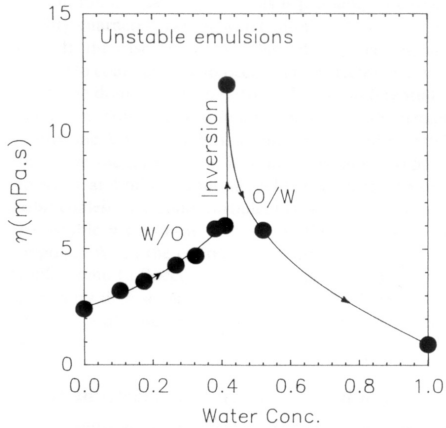

Figure 2.16 Mixture viscosity as a function of water concentration for unstable emulsions – laminar pipe flow [Pal 1993].

The viscosity was found to increase initially as the fraction of the dispersed phase (water) increased. At the inversion point a sudden increase was measured as indicated in Figure 2.16. Further increase in water fraction lead to a decrease in the viscosity.

Pacek and Nienow (1995) used a video technique to study the inversion process of an aqueous (A)/organic (O) liquid-liquid flow in a stirred vessel. They discovered oil droplets in drops of water from volume fractions of water greater than 20% and up to the inversion point. Just after the inversion from A/O to O/A the droplets in drops phenomenon was found to disappear. When approaching the phase inversion point from the other side, that is from O/A to A/O, the investigators expected to observe water droplets in drops of oil. This phenomenon was not seen. They concluded that the inversion process had a lack of symmetry. They also found that inversion occurred at a higher concentration of the dispersed phase, φ_d, when going from O/A to A/O than in the opposite direction. This led to the conclusion that O/A dispersions are more stable than A/O dispersions.

The mechanism of the inversion process is not completely understood, but there is agreement among investigators that it has to do with *break-up* and *coalescence* of droplets. A presentation of these phenomena will not be given here.

Prediction of under which operating conditions phase inversion might occur is important. Due to the large pressure gradients that might appear at phase inversion it is obvious that the transport of oil/water in pipes should take place far off the inversion point. The phase inversion mechanism in an oil / water dispersion is probably influenced by several parameters such as:

- input flow rates
- density ratios
- viscosity ratios
- interfacial tension
- temperature and pressure
- mixture velocity
- geometry of the pipe (diameter, inclination angle, mixing unit)
- construction material of the pipe

2.2 PRESSURE DROP IN LIQUID-LIQUID FLOW

Several models for prediction of pressure drop in liquid-liquid flow exist. Below, the *two-fluid model* for stratified flow and the *homogeneous model* for dispersed flow are presented. Among others, Brauner and Moalem Maron (1989) and Valle and Kvandal (1995) employed the two-fluid model for stratified flow on liquid-liquid systems. For dispersed liquid-liquid flow investigators like Mukherjee et al. (1981) and Valle and Utvik (1997) used the homogeneous model.

2.2.1 Stratified flow

For stratified steady state pipe flow the two-fluid model employs the momentum equations for each phase. The gravity forces together with wall and interfacial shear forces balance the pressure gradient.

$$A_o\left(\frac{dp}{dx}\right) - \tau_o S_o - \tau_{ow} S_{ow} - \rho_o A_o g \sin\theta = 0 \tag{2.8}$$

$$A_w\left(\frac{dp}{dx}\right) - \tau_w S_w + \tau_{ow} S_{ow} - \rho_w A_w g \sin\theta = 0 \tag{2.9}$$

Elimination of the pressure drop from the two equations above and inserting:

$$\varepsilon_w = \frac{A_w}{A} \tag{2.10}$$

gives for a horizontal flow:

$$\varepsilon_w \tau_o S_o + \varepsilon_w \tau_{ow} S_{ow} - (1-\varepsilon_w)\tau_w S_w + (1-\varepsilon_w)\tau_{ow} S_{ow} = 0 \tag{2.11}$$

This non-linear algebraic equation has to be solved iteratively with respect to the in-situ water fraction.

Perimeters

The oil-wetted perimeter, S_o, the water-wetted perimeter, S_w and the interfacial perimeter, S_{ow}, are calculated through the equations developed from Figure 2.17. Here the interface that separates oil and water in the pipe is imagined to form a straight line.

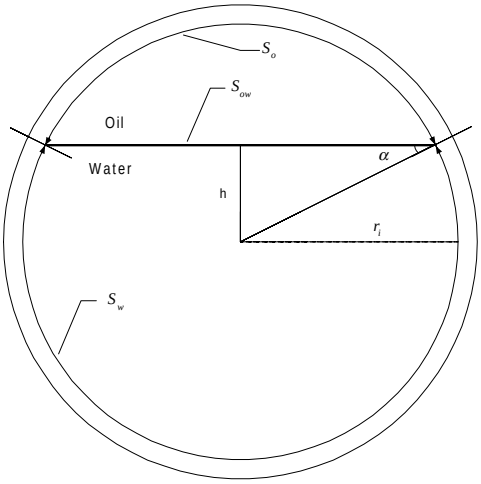

Figure 2.17 Cross-sectional view of stratified oil/water flow in a pipe.

The areas occupied by each phase are expressed by:

$$A_w = \frac{\pi r_i^2}{2} + 2\left[\frac{h r_i \cos(\alpha)}{2} + \frac{\alpha}{2\pi}\pi r_i^2\right] \qquad A_o = A - A_w \tag{2.12}$$

The perimeters are given by:

$$S_o = (\pi - 2\alpha) r_i \qquad S_w = (\pi + 2\alpha) r_i \qquad S_{ow} = 2 r_i \cos(\alpha) \tag{2.13}$$

Hydraulic diameters

By dividing the area with the perimeter for each of the phases a length parameter known as the hydraulic diameter appears:

$$D_{ho} = \frac{4A_o}{S_o} \qquad D_{hw} = \frac{4A_w}{S_w} \tag{2.14a}$$

According to Brauner and Moalem Maron (1989) the above equations should be used when the average velocities of each phase are approximately the same. Otherwise they proposed to calculate the hydraulic diameters by:

$$D_{ho} = \frac{4A_o}{S_o + S_{ow}} \qquad D_{hw} = \frac{4A_w}{S_w} \quad \text{for } U_o > U_w \tag{2.14b}$$

$$D_{ho} = \frac{4A_o}{S_o} \qquad D_{hw} = \frac{4A_w}{S_w + S_{ow}} \quad \text{for } U_o < U_w \tag{2.14c}$$

Reynolds numbers

For separated or stratified two-phase flow the Reynolds number is defined differently to that of a single-phase flow. Usually Reynolds numbers are defined for each phase according to Equation 2.15:

$$\mathrm{Re}_o = \frac{\rho_o U_o D_{ho}}{\mu_o} \qquad \mathrm{Re}_w = \frac{\rho_w U_w D_{hw}}{\mu_w} \tag{2.15}$$

Friction factors

The friction factors of both phases are calculated using the equation developed by Haaland (1983).

$$f_o = \left[-3.6 \log_{10} \left(\frac{6.9}{\mathrm{Re}_o} + \left(\frac{e}{3.7 D_{ho}} \right)^{1.1} \right) \right]^{-2} \tag{2.16a}$$

$$f_w = \left[-3.6 \log_{10} \left(\frac{6.9}{\mathrm{Re}_w} + \left(\frac{e}{3.7 D_{hw}} \right)^{1.1} \right) \right]^{-2} \tag{2.16b}$$

where e is the roughness parameter.

The interfacial friction coefficient is often set equal to the friction coefficient of the faster flowing phase:

$$f_{ow} = f_o \qquad \text{for } U_o > U_w \tag{2.17a}$$

$$f_{ow} = f_w \qquad \text{for } U_o < U_w \tag{2.17b}$$

For approximately equal velocities of the phases the interfacial friction coefficient is sometimes ignored. This is due to the interface being seen as a free surface with respect to each of the phases.

Shear stresses

Finally, the wall shear stresses produced by each phase together with the interfacial stress can the be expressed by:

$$\tau_o = 0.5 f_o \rho_o U_o^2 \tag{2.18a}$$

$$\tau_w = 0.5 f_w \rho_w U_w^2 \tag{2.18b}$$

$$\tau_{ow} = 0.5 f_{ow} \rho_o (U_o - U_w) |U_o - U_w| \tag{2.18c}$$

2.2.2 Dispersed flow

The homogeneous model for the pressure gradient in a liquid-liquid dispersion is often given as:

$$\frac{dp}{dx} = -\frac{f_m \rho_m U_m^2}{2 d_i} - \rho_m g \sin(\theta) \tag{2.19}$$

For horizontal pipes the last term in Equation 2.19 is obviously dropped. By further expressing the mixture velocity as:

$$U_m = U_{so} + U_{sw} \tag{2.20}$$

The phase fractions assuming no slip are given by:

$$\varepsilon_w = \frac{U_{sw}}{U_m} \qquad \varepsilon_o = 1 - \varepsilon_w \tag{2.21}$$

The density of the mixture is then:

$$\rho_m = \varepsilon_w \rho_w + \varepsilon_o \rho_o \tag{2.22}$$

Several models for predicting the viscosity of liquid-liquid dispersions can be found in the literature. Pal and Rhodes (1989) presented an empirical model based on the ratio between the dispersed phase concentration, φ, and the concentration giving a relative viscosity equal to 100. The details in the development of the model are not presented here. The relative viscosity, μ_r is the ratio of the dispersion mixture viscosity, μ_d, to the continuous phase viscosity, μ_c ($\mu_r = \mu_d / \mu_c$). The relative viscosity as they suggested is:

$$\mu_r = \mu_r\left(\frac{\varphi}{\varphi_{\mu=100}}\right) = \left[1 + \frac{0.8415\dfrac{\varphi}{\varphi_{\mu=100}}}{1 - 0.8415\dfrac{\varphi}{\varphi_{\mu=100}}}\right]^{2.5} \tag{2.23}$$

From this relationship the mixture viscosity for oil continuous dispersions is:

$$\mu_m = \mu_o \ \mu_r \tag{2.24}$$

For water continuous dispersions the mixture viscosity is expressed by:

$$\mu_m = \mu_w \ \mu_r \tag{2.25}$$

Søntvedt and Valle (1994) suggested $\varphi_{\mu=100}$=0.765.

According to Hewitt et al. (1997), the mixture viscosity is estimated by the classical Einstein equation for flows of small bubbles (diameter less than 1mm) suspended in a liquid:

$$\mu_m = \mu_c \ (1+2.5\,\varphi) \tag{2.26}$$

In this equation subscript c denotes the continuous phase and φ the dispersed phase fraction. Guth and Simha (1936) extended this model to:

$$\mu_m = \mu_c \ (1+2.5\,\varphi+14.1\,\varphi^2) \tag{2.27}$$

All of these viscosity relations used on liquid-liquid systems are based upon knowledge of the inversion concentration. In other words, it must be known when the dispersion is oil continuous and when it is water continuous. If this is not the case the mixture viscosity can be estimated in a similar manner as mixture density:

$$\mu_m = \varepsilon_w \mu_w + \varepsilon_o \mu_o \tag{2.28}$$

The Reynolds number of a dispersed mixture can be calculated using a single-phase analogy if the dispersion is homogeneous (or close to):

$$\mathrm{Re}_m = \frac{\rho_m U_m d_i}{\mu_m} \tag{2.29}$$

Similarly the friction coefficient can be determined by inserting the mixture Reynolds number into for instance the Blasius equation:

$$f_m = 0.312\mathrm{Re}_m^{-0.25} \tag{2.30}$$

CHAPTER 3:
FLOW FACILITIES

In this chapter, two flow facilities called the model oil facility (MOF) and the matched refractive index facility (MRIF) are outlined. The MRIF system is discussed only in brief since the majority of the experiments in this thesis are carried out in the MOF system.

3.1 THE MODEL OIL FACILITY

3.1.1 Simplified flow sheet

The model oil flow facility is a test loop designed to handle petroleum distillates, seawater and inert gas environment. A schematic layout of the facility is shown in Figure 3.1.

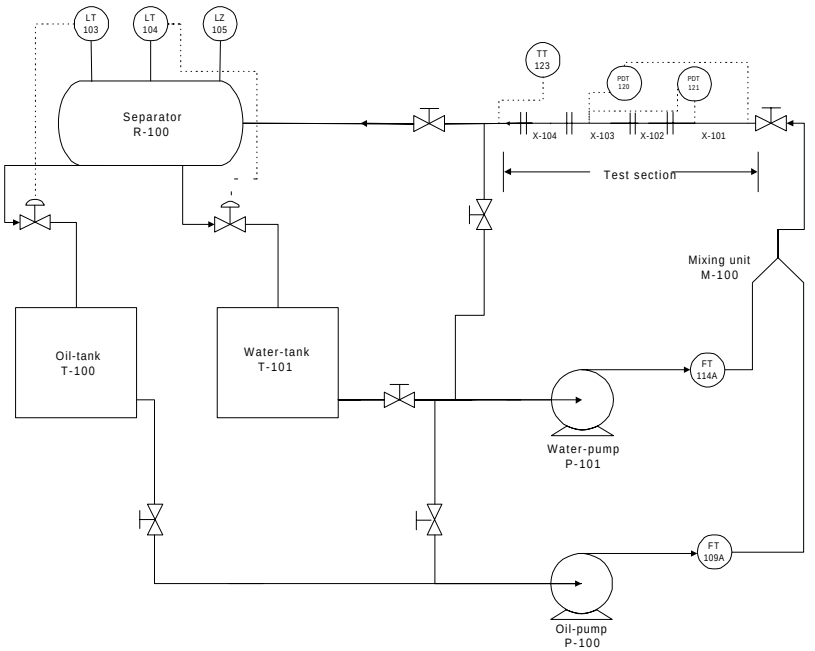

Figure 3.1 A simplified flow sheet of the separated flow facility (full flow sheet in Appendix A1).

The main components are:

- Oil-water separator (R-100)
- Intermediate storage tanks (T-100, T-101)
- Individual pumps for oil and water (P-100, P-101)
- Oil-water mixing unit (M-100)
- Horizontal test section (X-101, X-102, X-103, X-104)
- Control and safety instrumentation

3.1.2 Oil/water separator and storage tanks

The oil/water separator is shown in Figure 3.2. The separator has an inner diameter of 0.8 m and a length of 2 m, which gives a total volume of the separator of approximately 1.0 m^3. However, the level control instrumentation limits the volume for use to about 0.9 m^3. It is made out of glass fibre and has a view section of transparent acryl. The right end is flanged, which allows it to be removed for installation of different internal flow configurations. It also enables easy cleaning. At the present time the separator includes a flow straightening section, which is a bundle of small tubes covering almost the full cross section in a length of about 0.8 m. This improves the separator. In between the two outlets there is mounted a partition wall. Level controllers for both the water-phase (LT-104) and the oil-phase (LT103) are installed. The first one prevents the water level from rising above the partition wall while the second one makes sure the oil level does not reach the top of the separator, during normal operation. In addition there exists a level switch (LZ-105), which shuts down of the pumps if the separator is overfilled.

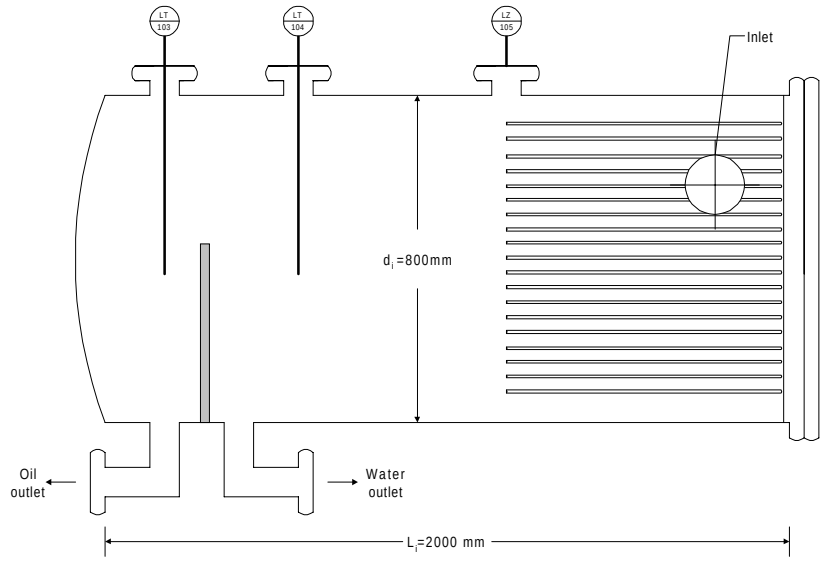

Figure 3.2 The oil/water separator.

The two identical vessels, one for each fluid phase, have approximate dimensions of 1x1x1 meter, which gives a total volume of about 1 m^3. They are made from polypropylene and are covered with a steel shielding connected to a truck transportation rack. The inlet pipes to the vessels are located at the top of the vessels and bent the opposite direction of the outlet section. The outlet pipes are connected to ball valves. In that way, it is easy to close the vessels for transportation, filling, emptying and otherwise when operation requires it. Both vessels are closed, but vented through a thin slit around the inlet pipe. Between the vessels about 30 cm from the top there is a 2" tube connecting them to prevent flooding. A rubber float indicates the liquid level in each vessel.

3.1.3 Pumps

Two high capacity pumps, one for each phase, are installed. Both are selected based on following criteria:

- *Low shear*. This is to prevent any further mixing if the oil or water phase contains dispersed droplets from the vessels.
- *Small pressure pulses*. Since the measured pressure drops downstream of the pumps can be as low as a few mbar, it is desirable to avoid fluctuations in these values caused by the pumps.
- *Low noise level*. Since the experimental facility is installed in a laboratory frequently used by a lot of people the noise level must be low.

The oil pump is a positive displacement pump. The principle is to capture a volume at the inlet and transport it 180° around to the outlet. The pump is also a constant volume pump and delivers a volume of 0.946 litres per revolution independent of the pressure difference between the inlet and outlet. The maximum capacity is 30 m^3 /h and the maximum differential pressure is 6 bar from inlet to outlet. The pump medium is used as lubricant.

The water pump is a mono eccentric screw pump with a stainless steel screw eccentrically rotating in a rubber stator. This pump is also a constant volume pump and delivers a total volume of 1.285 litres per revolution. It has a maximum capacity of 30 m^3 /h.

Both pumps are connected to a shutdown circuit that cuts the power to their drives if there is blockage in the pipe (high pressure) or overflow in the separator. The electric motors are cooled using air fans directly connected to the main shaft and would therefore need a minimum of revolutions to maintain sufficient cooling. This results in finite minimum capacity on both pumps, which is about 5 m^3/h. To overcome this restriction, the piping arrangements around both pumps include a by-pass loop to lower the minimum flow rate to the test section to practically zero m^3/h.

To regulate the volumetric flow through the pumps frequency control modules are installed, and these can either be operated manually or by the PC control program.

3.1.4 Transport pipes and mixing unit

The piping from the pumps to the mixing unit is made of polypropylene with an outer diameter of 63 mm and a wall thickness of 6 mm. It is designed to stand pressures up to 10 bar and temperatures up to 90 °C. The total length of the piping is approximately 2x25 m.

The unit where oil and water is mixed before entering the test section is designed to initiate a separated flow pattern and is shown in Figure 3.3.

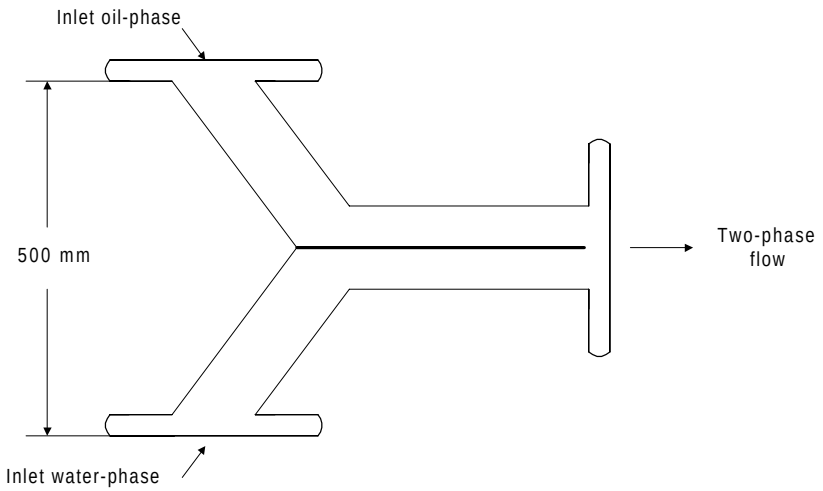

Figure 3.3 The mixing unit.

The oil is introduced at the top and water at the bottom. A plate separates both phases until the entrance to the test section. The piping and flange arrangements around the mixing unit are designed in a way that makes changing to different mixing configurations easy. The mixing unit material is stainless steel. Downstream of the test section a 3“ stainless steel pipe is installed to pre-separate the fluids before entering the oil/water separator.

3.1.5 Test pipe and measurement sections

The test pipe, which is located 2 meters (L/D = 35) downstream of the mixing unit, is made of stainless steel, except for a 0.8 m transparent plexiglass pipe for LDA measurements. The pipe has an outer diameter of 60.3 mm and an inner diameter of 56.3 mm. The test pipe is divided into an entry section and two different test sections, one for LDA measurements and one for measurements of local volume fractions by a gamma densitometer. The test pipe, including the measurement sections, is shown in Figure 3.4. The entry section is made long enough to make the flow fully developed before the measurement sections. Differential pressure is measured over two stretches as indicated in Figure 3.4. The LDA measurement section is described in detail in Chapter 4, and the gamma densitometer section is described in Chapter 5.

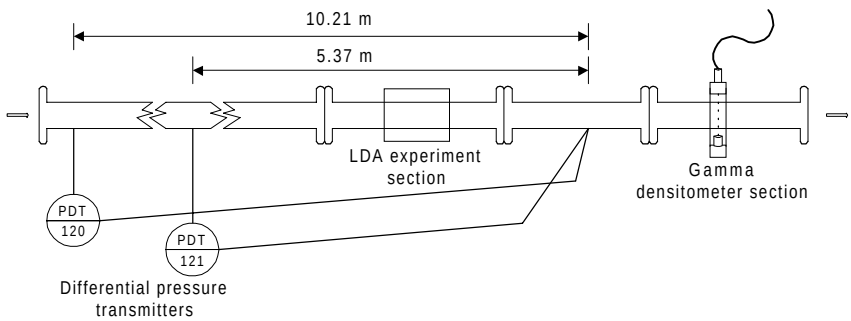

Figure 3.4 Test section.

3.1.6 Control and safety instrumentation

Temperature

The temperature is detected by a thermocouple instrument located in the 3 " stainless steel-pipe downstream of the test pipe. There exist no possibilities for regulation of temperature and hence when operating the pumps at high speed, the temperature rises by a few degrees in the flow. The temperature is logged on a computer.

Pressure drop

The static pressure in the system is measured in both oil and water pipes and is not allowed to rise above 3.5 bar because of the transparent plexiglass pipe. As a consequence of this restriction, both pumps are regulated to shut down if this limit is exceeded. In the test section, two equal differential pressure transmitters are mounted in connection to the test pipe. The first one (PDT-120) measures the differential pressure over a length of 10.21 m while the other (PDT-121) measures over 5.37 m. Both transmitters are calibrated and scaled for their measurement range and delivers the pressure drop in mbar/meter. The accuracy is +/- 0.075% of the measurement range. The long-range transmitter (PDT-120) is mounted to detect eventual effects of inlet conditions. However, experiments with the mixing unit presented in Figure 3.3 assure a fairly short entry length. Though only minor differences in the measured pressure drop from the two transmitters were detected, the short-range transmitter (PDT-121) is the one that is used in all experiments that are presented later. The pressure drops are logged and displayed on the computer.

Pump speed

Frequency transformers regulate the speed of each pump, and the values are logged on the computer.

Flow rate

Four different turbine meters measure the liquid flow rates downstream of the pumps. Each phase has two flow meters placed in parallel, one for the low flow rates (0.68-6.8 m^3/h) and one for the high flow rates (3.2-32 m^3/h). Only the flow meters for detection of high flow rates (FT-109A and FT-114A) are indicated on the flow chart in Figure 3.1. All four flow meters are from the same manufacturer: Euromatic Machine & Oil Co. Ltd. The small meters have an accuracy of +/- 0.5 % of the output signal while the larger ones have an accuracy of +/- 0.3%.

The principle of turbine meters is that the flowing fluid in the pipe will make the turbine rotate and its rotary speed depends on the flow rate of the liquid. The speed of the turbine can be measured simply by counting the rate at which the turbine blades pass a given point using a magnetic proximity pickup to produce voltage pulses. By

feeding these pulses to an electronic pulse-rate meter one can measure the flow rate. The total flow is obtained by accumulation of the total number of pulses during a given time interval.

3.1.7 Instrumental accuracy

All instruments have a specified accuracy, and this accuracy leads to a certain deviation even when the instruments are operated within the calibrated range. Table 3.1 indicates the accuracy for the most important instruments with the exception of the laser Doppler anemometer and the gamma densitometer, which is treated separately.

Table 3.1 Total instrumental deviations.

Parameter	Instrument tag number	Range	Specific Instrument accuracy*
Large vol. flow	FT-109A FT-114A	53-533 litres/min.	+/- 0.3%
Small vol. flow	FT-109B FT-114B	11-113 litres/min.	+/- 0.5%
Long diff. pressure	PDT-120	0-100 mbar	+/- 0.1%
Short diff. pressure	PDT-121	0-50 mbar	+/- 0.1%

** The percentages are calculated of the span, which is equal to upper range value (URL) – lower range value (LRL).*

As an example, the expected deviation for flow meter, FT-109A, is +/- 0.3% of span = 480 litres/min., which equals +/- 1.44 litres/min. For the dP-cell, PDT-120, the accuracy is +/- 0.1% of span = 100 mbar, which equals +/-0.1 mbar. These deviations are well inside the accepted level for the measurements.

3.1.8 Verification experiments

As a part of the testing and verification of the flow facility three preliminary experiments were conducted.

- Verification of pump specifications - volumetric delivery as a function of pump speed.
- Verification of differential pressure transmitters - friction coefficient as a function of Reynolds number.
- Comparison of the volumetric flow from an integrated LDA velocity profile with flow meter readings.

The basic test pipe data and fluid properties needed for the experiments are presented in Table 3.2.

Table 3.2 Test pipe data and fluid properties.

Density Exxsol D-60:	790 kg/m^3(25^{o}C)
Viscosity Exxsol D-60:	0.00164 Pa s (25^{o}C)
Density water:	1000 kg/m^3 (20^{o}C)
Viscosity water:	0.00102 Pa s (20^{o}C)
Interfacial tension (o/w):	43 mN/m (25^{o}C)
Inner pipe diameter:	0.00563 m
Flow area:	0.0024895 m^2
Length PDT-120:	10.21 m
Length PDT-121:	5.37 m
Pipe roughness:	1.00x10^{-5} m

1. **Verification of the pump specifications - pump speed and volumetric flow**. The experiment is done to verify the pump specifications given by the suppliers. The delivery or the volume flow rate should be linear with respect to the pump speed. The speed is measured by conversion from the frequency transformers by Adam modules and the volume flow rates are measured with the turbine flow meters. A high degree of linearity in the operating range for the pumps would also serve as verification of the flow meters. The results from the experiments are presented in Figure 3.5

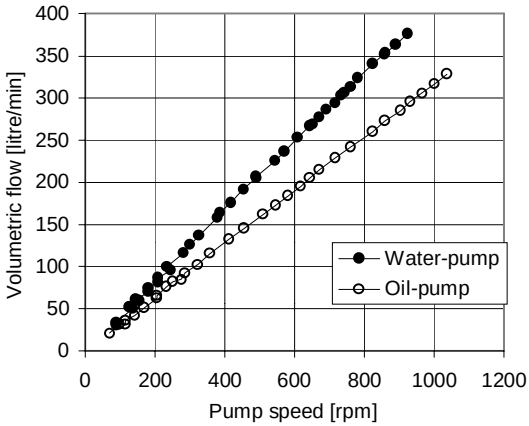

Figure 3.5 Volumetric flow versus pump speed.

The measurements of volume flow are done with the turbine flow meters FT-114A and FT-109A, which are indicated in the simplified flowchart in Figure 3.1. They have a range from 53-533 litres/min. From Figure 3.5 it can be seen that the experiments follow a linear path as expected for volumetric pumps. For high pump speeds the linearity is very clear, but for low speeds, especially below 200 rpm and thus below the flow meter range, the volume flow measurement starts to be more inaccurate. To prevent poor volume flow measurements in this area additional flow meters are installed, which operates only at low flow rates, see Table 3.1. These are indicated on the full flow sheet presented in Appendix A1. For most of the experiments presented in

this thesis though, it is sufficient to use only the flow meters for large flows. In general the results from the experiments presented above are in accordance with the given data from the suppliers.

2. Verification of pressure drop and volumetric flow instruments – friction coefficient and Reynolds number.

The second experiment is to see how well measured volume flow and the resulting measured pressure drop fits analytical data. The experimental friction factor or friction coefficient is calculated from Equation 3.1

$$f = \frac{d_i}{\frac{1}{2}\rho u_b^2}\frac{dp}{dx} \tag{3.1}$$

Here, u_b is the bulk velocity of the flow calculated from the volumetric flow and the flow area and dp/dx is the measured pressure drop per meter. The friction coefficient is plotted against the Reynolds number given by:

$$\mathrm{Re} = \frac{\rho\, u_b\, d_i}{\mu} \tag{3.2}$$

The data should fit analytical data quite well. Presented in Figure 3.6 and 3.7 are the experimental friction coefficient compared to three empirical friction coefficients or correlations for single-phase water and single-phase oil, respectively. The empirical correlations are given in Eqs. 3.3-3.5. The first is the friction factor correlation of Haaland (1983)

$$\frac{1}{\sqrt{f}} = -1.8\log\left(\frac{6.9}{\mathrm{Re}} + \left(\frac{e}{3.7d_i}\right)^{1.1}\right) \tag{3.3}$$

The coefficient of Haaland (1983) is valid for Re between 4000 and 10^8. The roughness parameter, e, which is used for the experiments, is $1.00\text{x}10^{-5}$ m.

The next correlation is the classical Blasius friction factor [Kays and Crawford (1993)] given by:

$$f = 0.312\,\mathrm{Re}^{-0.25} \tag{3.4}$$

This correlation is known to fit experimental data well for Re between 10000 and 50000.

The last is an empirical correlation that closely fits the Kármán-Nikuradse equation (i.e. it is a correlation that is much more convenient to use than the awkward Kármán-Nikuradse equation, which requires an iterative solution procedure) and is valid for Re between 30000 and 1000000 [Kays and Crawford (1993)]:

$$f = 0.184\,\mathrm{Re}^{-0.20} \tag{3.5}$$

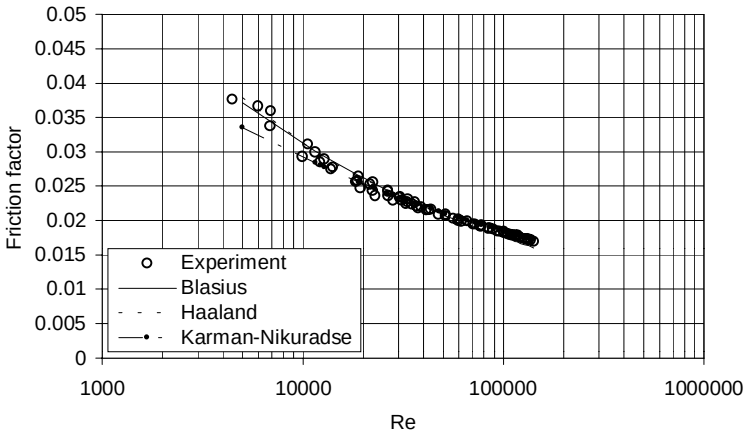

Figure 3.6 Single-phase flow of water.

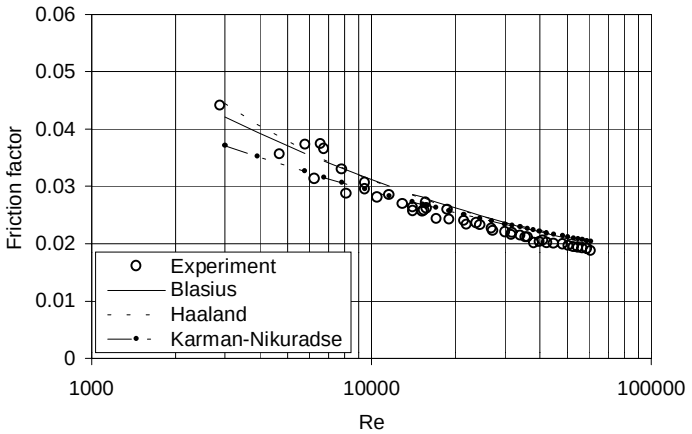

Figure 3.7 Single-phase flow of oil.

From Figure 3.6 it is evident that the experiments in single-phase water fit the analytical data well. For lower Re, the experiments seem to follow the curves from Haaland and Blasius better than the Kármán-Nikuradse fit off. Figure 3.7 displays the

single-phase oil measurements. Here, the experimental friction coefficient differs a little from the analytical friction correlations of Haaland and Blasius. The fit off of the Kármán-Nikuradse equation gives the best prediction of the friction coefficient compared to experimental data. The overall conclusion from the pressure drop measurements in single-phase flow is that the experiments show good agreement with analytical correlations. This means that the pressure drop measurements done by the dP-cells are satisfactory.

3. Comparison of the mean velocities from volume flow meters and LDA. Presented in Figure 3.8 is the LDA measurement of the axial velocity in flows of single-phase water and single-phase oil. The velocity profiles presented are from measurements in a volume flow of 150 litres/min corresponding to a bulk velocity of 1.0 m/s.

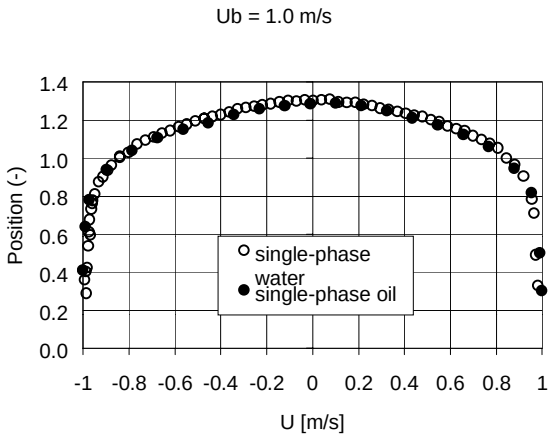

Figure 3.8 Axial velocity profiles for single-phase flows of water and oil at a bulk velocity of 1.0 m/s.

Both the velocity profile for single-phase water and single-phase oil are integrated over the entire cross-section of the pipe. The resulting volume flows are compared with the flow meter readings and presented in Table 3.3

Table 3.3 Comparison of flow meter reading and LDA measurement.

	Water flow rate [litres/min]	Oil flow rate [litres/min]
Flow meter reading:	150.1	150.1
Integrated velocity profile:	153.2	153.0
Deviation:	2.1%	1.9%

The differences seen in Table 3.3 are small and it shows that the LDA measurements are quite good for single-phase flow. The integrated velocity profile gives a volume flow that is about 2% higher than the flow meter reading. The reason for this deviation can perhaps be explained by optical or statistical errors in the LDA measurements. However, it is more likely that the flow meters cause the deviation since the LDA instrument in itself is a very accurate instrument. This is thoroughly discussed in the Chapter 4. The deviations of the flow meter readings have been previously discussed.

Summary

The three verification experiments show satisfactory results compared to the expectations and acts as basis for the experiments presented later in the thesis.

3.2 THE MATCHED REFRACTIVE INDEX FACILITY

The name of this flow facility, *the matched refractive index flow facility*, originates from the later to be discussed refraction index matching method (in Chapter 4) for optical improvement in laser Doppler anemometry. Since our matched refractive index system includes a hazardous and expensive solvent, a small-volume test facility was built in order to handle that particular liquid. The overall layout of the facility is displayed in Figure 3.9. The test rig consists of an enclosed vessel with a volume of 200 litres, including a mixer/blender to homogenise the oil and water phases. The vessel is connected to a low shear pump, with a capacity of 35 m^3/h, which transports

the dispersion through a Coriolis mass flow meter, to monitor the total mass flow and the mixture density, and further into the test section.

The test section is an 8 m long horizontal stainless steel pipe with inner diameter of 56.3 mm, except for a 0.9 m long transparent glass section. This section provides optical access for LDA measurements and includes a rectangular box built around the cylindrical pipe. The test section also includes a differential pressure transmitter to monitor the pressure drop, a traversing gamma densitometer (described in Chapter 5) to measure local phase fractions and a temperature sensor. Downstream of the test section a heat exchanger provides stable temperature during the experiments.

To initiate the experimental conditions, the tank volume is homogenised by the mixer before circulation starts. The system is switched to tank bypass operation by opening valve V-3 when the phase ratio is close to desired water cut. Monitoring the density readings from the Coriolis mass flow meter makes the switch. The water cut is then adjusted by opening of valve V-1 or V2, which will either increase or decrease the water cut.

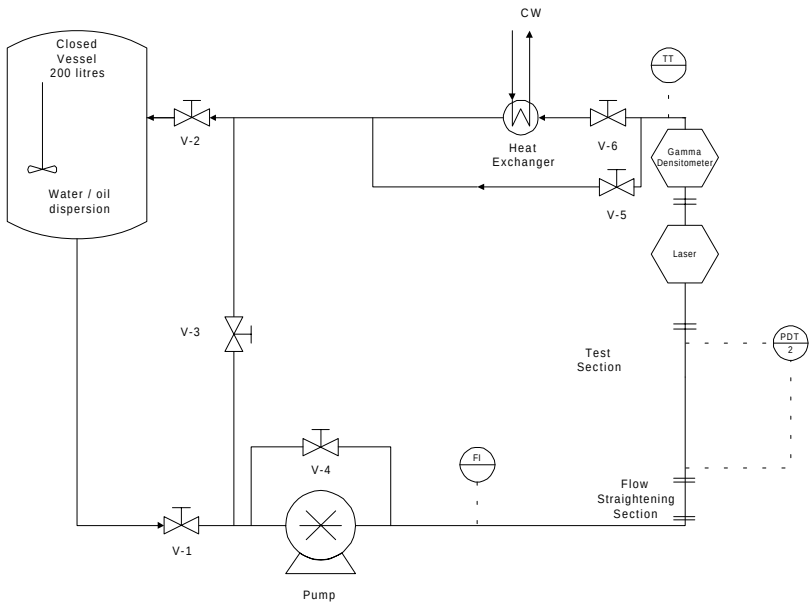

Figure 3.9 The experimental layout for the MRIF system.

CHAPTER 4:
LASER DOPPLER ANEMOMETRY – LITERATURE REVIEW AND BASIC THEORY

4.1 INTRODUCTION

Laser Doppler anemometry (LDA) is one of several optical measurement techniques. If we travel a few decades back in time Durst et al. (1981) divided the optical techniques into two classes. Image formation and interference pattern formation. Image formation techniques treat information of the spatial intensity distribution of the image of an object. This is exemplified by for instance ordinary photography. The interference pattern technique makes use of both the intensity distribution and the phase distribution of the light. Laser Doppler anemometry is an example of such a technique and phase Doppler anemometry (PDA) is another. The formation of an interference pattern makes it possible to determine the velocity of a particle by measuring its transit time across a given number of interference fringes. Figure 4.1 displays a general laser Doppler anemometer layout.

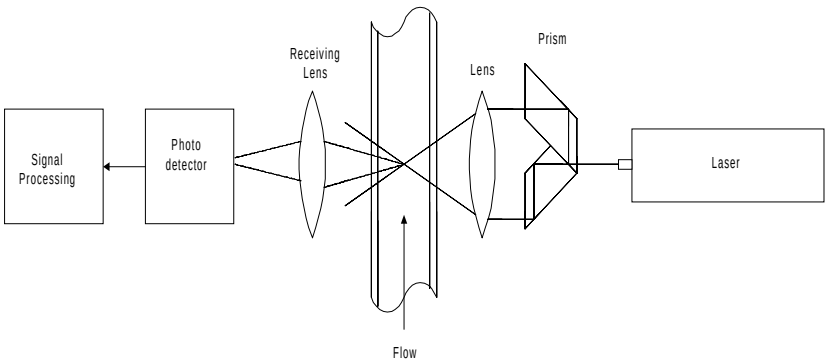

Figure 4.1 Schematic representation of a laser Doppler anemometer [Durst et al. (1981)].

The laser source in Figure 4.1 produces coherent light as opposed to pulsating lasers. The beam is split into two parts in a prism and focused by a lens to cross somewhere

inside the flow in which velocity is to be measured. An interference pattern occurs in the crossing volume of the two laser beams. Scattered light from particles passing this crossing volume is observed by the receiving part of the system consisting of the receiving lens and a photo detector. The photo detector converts the scattered light into an electronic signal that is processed by a signal processing system.

4.1.1 Three measurement modes

At least three different measurement principles or modes exist. These are the *reference beam mode*, the *dual beam mode* and the *two-scattered beam mode*. Different optical arrangements are possible in each of those modes. Several of these arrangements are outlined in detail in Durst et al. (1981). The reference beam arrangements and the dual beam arrangements are the ones most used. When applying the reference mode the laser beam is split into one intense scattering beam and one less intense reference beam. The reference beam is directed to the detector where it is compared with the scattered light from particles passing the stronger beam. Since the frequency of the scattered light is altered due to the Doppler effect it has a frequency difference compared to the frequency of the reference beam that is proportional to the particle velocity. In the early years of LDA, several investigators used optical set-ups using the reference beam mode. Yeh and Cummins (1964) who were the first to demonstrate the LDA technique in practice used an optical arrangement classified as a *reference beam mode*. They measured the laminar flow of a mono dispersion of polystyrene spheres in water in a circular tube. Their optical setup is the one presented in Figure 4.2. It is also worth to notice that they used a Bragg cell to add a frequency shift to the reference beam. Bragg cells in general will be discussed later.

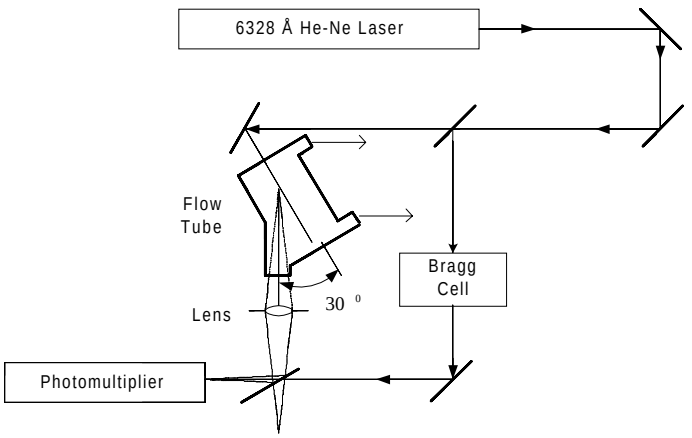

Figure 4.2 Optical setup of Yeh and Cummins (1964) using the reference beam mode.

The *dual beam mode* implies two intersecting laser beams of equal intensity. In the intersection they produce an interference pattern with fringes. This will be discussed in detail in Section 4.2.3. When a particle passes the fringes, the intensity of the scattered light that hits the photo-detector varies. The variation is proportional to the particle velocity. Brayton, Kalb and Crosswy (1973) used an optical setup that falls in the category of the dual beam mode. They measured two velocity components simultaneously in a wind tunnel. Figure 4.3 shows this optical setup using the dual beam mode.

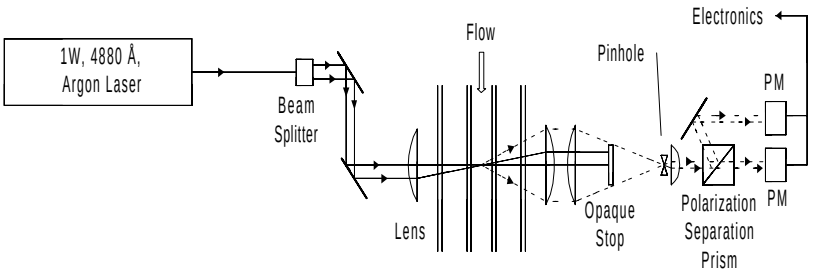

Figure 4.3 Optical setup of Brayton, Kalb and Crosswy (1973) using the dual beam mode.

Finally, the *two-scattered beam mode*, involves a single focused laser beam. When a particle in the flow is exposed to the laser beam, light can be scattered in all space. The scattered light in two of the directions is captured symmetrically about the system axis. The captured beams are then combined and their relative difference in wave front phase indicates the distance of the particle from each detector. In that way, when a particle crosses the laser beam the scattered light beams interfere in a manner that makes the light intensity at the detector fluctuate at the Doppler frequency. The simultaneous measurement of two velocity components that are perpendicular to each other is the main advantage. Mazumder and Wankum (1970) were among the first to use the two-scattered beam mode. They also extended the method to use two incident laser beams instead of one. They concluded that this extension improved the optical alignment procedures. Their optical setup is presented in Figure 4.4.

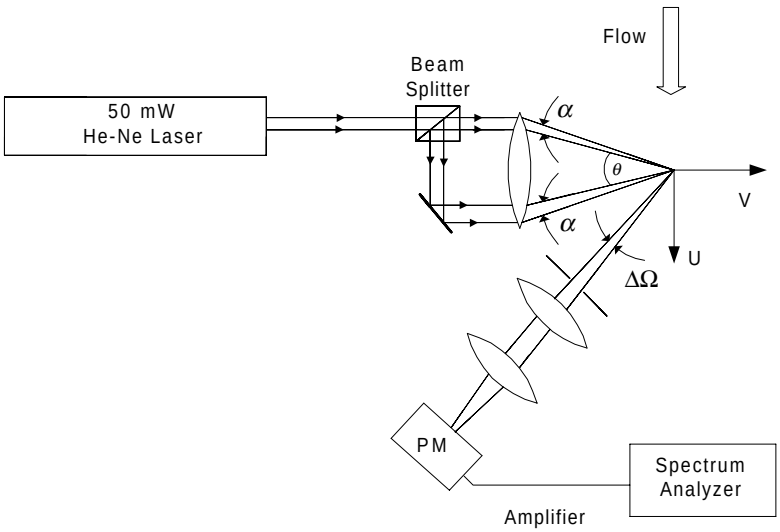

Figure 4.4 Optical setup of Mazumder and Wankum (1970) using the two-scattered beam mode.

Although the differences between the last two modes may appear small they still are classified as two modes by several investigators. It is also important to remember that the three mentioned modes are results from the early development in LDA

technology. Today's LDA principles take advantage of more than 35 years of research but the set-up used in this thesis are similar to the basic dual-beam mode.

During the sixties and seventies the optical setups for laser Doppler anemometers developed rapidly. In the beginning laser Doppler anemometers were difficult to operate in the sense that the alignment procedures were tedious. The development in the technique as well as the invention and use of new parts made them easier to operate. While the first laser Doppler anemometers could only measure one velocity component at a time, it is now common that they have the ability to measure three velocity components simultaneously. And while the first investigators used the laser Doppler anemometer to measure mean velocities, the method soon developed into measurements of turbulence. George and Lumley (1973) were among the first to successfully employ LDA to measure the turbulence in the form of spectrum analysis in a closed circuit water tunnel using homogenized milk as tracers. Today laser Doppler anemometers are easy to operate and extensively used in research and development. Areas like the aerospace industry and the petroleum industry are among them.

4.1.2 From LDA to PDA

Durst and Zarè (1975) showed that large particles, that is, even larger than the size of the measurement volume could produce Doppler signals. The Doppler shifts for the two special cases of a reflecting spherical particle and a refracting spherical particle were found. They proposed that if two laser beams are used, reflection, refraction and scattering from a particle contributes to the total distribution of light in space. They also proposed that a fringe pattern existed in space, and that the location of this fringe pattern depends on the arrangement of the incident beams and the shape and location of the reflecting surface. This discovery meant that the particle size could be obtained as well as particle velocities. A decade later Saffmann, Buchhave and Tanger (1984) extended the techniques of Durst and Zarè when publishing a paper on phase Doppler anemometry (PDA) for determining simultaneous measurements of velocity and size of particles. Today, PDA is a common measurement technique, and many laser systems can be operated both as an LDA system and as a PDA system. However,

LDA is the focus of this work and thus the principles of the PDA technique are not outlined out here.

4.1.3 LDA in multiphase flow

Several publications in the early days of LDA include measurements in two-phase flows. For example, Davis and Unger (1973) did velocity measurements of gas bubbles in water in a circular tube. They were able to discriminate between scattering signals derived from bubbles and the ones from water. They also used a refractive index matched viewing cell to reduce displacement errors due to the travel of laser beams through media with different refractive indices. The effects of the refractive index matching viewing cell and such a system in particular will be discussed in Section 4.4. Durst and Zarè (1975) showed that LDA could be employed to measure velocities in two-phase flows of gas bubbles in liquid and liquid drops carried by a gas. Sullivan and Theofanous (1979) used LDA for measurements of nitrogen bubbles carried by water in a glass pipe. Through the years, LDA became a useful tool in the study of multiphase flow. Special techniques were developed to discriminate between Doppler signals from tracer particles and larger particles or bubbles. Zisselmar and Molerus (1979) took advantage of the method of refractive index matching in LDA measurements in a solid-liquid (optical glass-methyl benzoate) system. The principle in this method is to choose phases with equal refractive indices. For instance when studying liquid-bubble flow, the tracer particles and the continuous liquid phase should have the same refractive index. The laser beams will not "see" the tracers, and the Doppler signals from a third component, like a larger particle or bubble, can be detected. Shao (1996) used this technique when carrying out measurements in both two- and three-phase systems. One of the experiments was measurement of velocity distributions of bubbles in water. Considering measurements in liquid-liquid two-phase systems there have been very few experiments conducted using LDA.

In this thesis focus is set on oil/water systems. The petroleum industry is one that often involves simultaneous flow of gas, oil and water. When laser Doppler anemometry is applied to flows with more than one phase, measurements are often restricted by the lack of optical visibility in the flow. For instance, when studying oil/water flow in a horizontal pipe, the mixture of oil and water must be transparent

for LDA to be used. When two flows of transparent liquids are mixed, the resulting mixture might be transparent or non-transparent depending on the mixture velocity and water cut. A stratified or separated flow will be transparent, while a fully dispersed flow will contain droplets that make the mixture much less transparent. To overcome some of the problems, refractive index matching techniques can be used.

4.1.4 Advantages and disadvantages using LDA

Compared to other techniques for measuring velocity components like for instance, constant temperature anemometry (CTA) using a hot wire and pitot-tubes, the LDA technique offers several advantages:

- *Non-intrusive*. The technique does not affect the flow field in any way, except for the fact that it needs a certain concentration of suspended particles to obtain light scattering. The effect of such particles will be discussed later. Both hot-film and pitot-tubes are intrusive techniques.

- *High spatial resolution*. The technique offers the possibility to make local measurements since the measuring control volume usually is in the range of 100-200 micrometers. Neither CTA nor pitot-tube techniques can offer such a small measuring volume. For CTA the resolution is about 1 mm.

- *Fast dynamic response*. The fast signal processing electronics, in combination with on line monitoring with a computer, displays the velocity components virtually as the tracer particles pass the control volume.

- *Well-defined velocity component*. Once the LDA system is properly installed and adjusted the detected velocity, which is the projection of the velocity vector on the measuring direction determined by the optical system, has a well-defined direction in space.

- *Wide measuring range*. Velocities down to a few centimeters/second and up to several meters/second can be detected with the same LDA system.

- *No need for calibration.* The measurements are based on the stability of electromagnetic waves, which are practically unaffected by physical parameters such as temperature and pressure.

The major disadvantages of the LDA technique are:

- *Velocity measurements of suspended particles (tracers) and not the fluid itself.* The actual velocity information comes from the scattered light of the suspended particles as they penetrate the measuring control volume. A fluid without tracers will not produce any information for the LDA technique. Highly dynamic flows with very strong acceleration or deceleration can cause severe problems for accurate LDA measurements. In such a flow, the particles can no longer be expected to follow the streamlines of the flow.

- *Optical properties of the experimental setup*. The nature of the technique is to have full optical access to the desired measuring location. This means that velocity measurements in a pipe flow require both the pipe material and the fluid to be optically transparent. The refracting properties of all materials involved are also important since this can distort the path of the laser beams and effectively destroy the measuring control volume. For instance dispersed droplets with a refractive index different from the continuous phase can cause severe problems with respect to keeping a well-defined shape and location of the control volume.

- *Expensive equipment.* A modern LDA system can be very expensive. The laser system used in this work needs regular maintenance.

- *Immobility*. Small portable LDA systems exist, but often the laser with all the supplementary equipment requires a couple of square meters. Once a LDA system is placed in a laboratory it is not rare to bring the flow facility to the laser instead of the laser to the flow facility.

4.2 BASIC PRINCIPLES

In this chapter the basic concepts in LDA measurements are discussed. Among these are the classical interpretations of the Doppler shift, the fringe model and the control volume.

4.2.1 The laser beam

A laser beam from a gas laser is coherent in space. The intensity of the beam has a Gaussian distribution at all cross sections along the beam as shown in Figure 4.5.

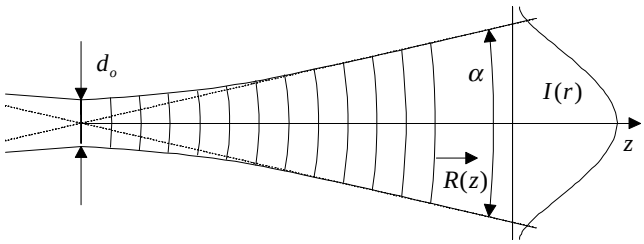

Figure 4.5 Laser beam with Gaussian intensity distribution [Dantec reference guide (2000)].

By defining z as zero in the beam waist it is possible to express the divergence and the diameter of the laser beam as well as the radius of the wave front in terms of wavelength, beam diameter at beam waist and z. The divergence, α, together with the beam diameter, d, and the wave front radius, R(z), are given by Eqs. 4.1-4.3:

$$\alpha = \frac{4\lambda}{\pi d_0} \tag{4.1}$$

$$d(z) = d_0\sqrt{1+\left(\frac{4\lambda\, z}{\pi d_0^2}\right)^2} \quad , \qquad \lim_{z\to\infty} d(z) = \alpha z \tag{4.2}$$

$$R(z) = z\left[1 + \left(\frac{\pi d_0^2}{4\lambda z}\right)^2\right] \quad , \quad \lim_{z\to 0} R(z) = \infty \quad , \quad \lim_{z\to\infty} R(z) = z \tag{4.3}$$

It is common to define the width of the beam by the edge intensity equal to $1/e^2$ of the core intensity. Here, e is a mathematical constant equal to 2.71828. This corresponds to about 13.5% of the core intensity. The cross section of the laser beam is narrowest at the beam waist. The beam waist diameter is a unique property of a laser beam. Visually it is difficult to observe the beam waist. The laser beam appears to be straight and to have constant thickness. The reason why the beam waist is so important is that this is the part of the laser beam where the measurements of particles should be done. The wave front is plane in the beam waist and curved elsewhere. Another way of saying this is that the radius of the wave front approaches infinity as z approaches zero. Thus the theory of plane waves can be employed in the beam waist area of the laser beam [Dantec reference guide (2000)].

4.2.2 The Doppler shift

The basic concept of LDA is the detection of the Doppler shift (or Doppler effect) of scattered light from suspended particles in the flow. This phenomenon is caused by a frequency change of a wave motion due to the relative movement between the wave source and the wave receiver. This can either be obtained with a moving source and a stationary receiver or vice versa.

Doppler effect caused by a moving source

Consider the illustration of a moving source and a stationary receiver in Figure 4.6. If the propagation speed of the wave is c, then for a stationary source the emitted wave has traveled a distance of ct during the time t. If the wavelength of the waves from the stationary source is λ, then the frequency recorded by the receiver is:

$$f = \frac{c}{\lambda} \tag{4.4}$$

The wave source is now moving at a velocity $\vec{V}$. If the unit vector along the axis from the source to the receiver is $\vec{e}$, the source has traveled a distance $(\vec{V} \cdot \vec{e})$ t in the direction from the source to the stationary detector or receiver.

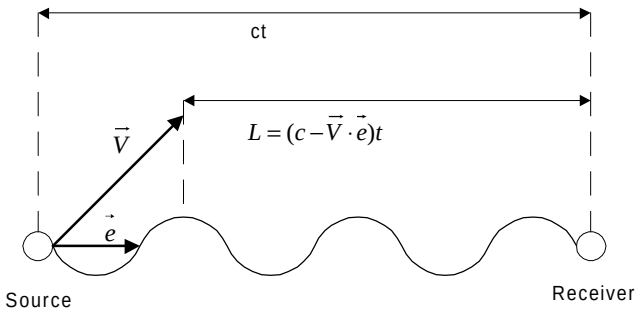

Figure 4.6 Doppler effect in a system with a moving source and a stationary receiver [Shao (1996)].

When the source is moving, the emitted wave is squeezed into a space given by the length L:

$$L = (c - \vec{V} \cdot \vec{e})t \tag{4.5}$$

The stationary receiver will then receive a wavelength from the *m*oving source (ms) equal to:

$$\lambda_{ms} = \frac{c - \vec{V} \cdot \vec{e}}{f} \tag{4.6}$$

The receiver will record the corresponding frequency of the emitted waves from a moving source:

$$f_{ms} = \frac{c}{\lambda_{ms}} = \frac{f}{1 - \frac{\vec{V} \cdot \vec{e}}{c}} \tag{4.7}$$

The frequency difference between the wave emitted from a stationary source and a moving source is:

$$\Delta f_s = f_{ms} - f = \frac{\vec{V} \cdot \vec{e}}{\lambda \left(1 - \frac{\vec{V} \cdot \vec{e}}{c}\right)} \tag{4.8}$$

If the velocity of the moving source is much smaller than the velocity of propagation of the emitted wave, the frequency difference is reduced to:

$$\Delta f_s = \frac{\vec{V} \cdot \vec{e}}{\lambda} \tag{4.9}$$

Doppler effect caused by a moving receiver

If the receiver is moving at a velocity $\vec{V}$ and the wave source is stationary, the Doppler effect again results in a frequency difference recorded by the moving receiver. The Doppler effect caused by a moving receiver is shown in Figure 4.7.

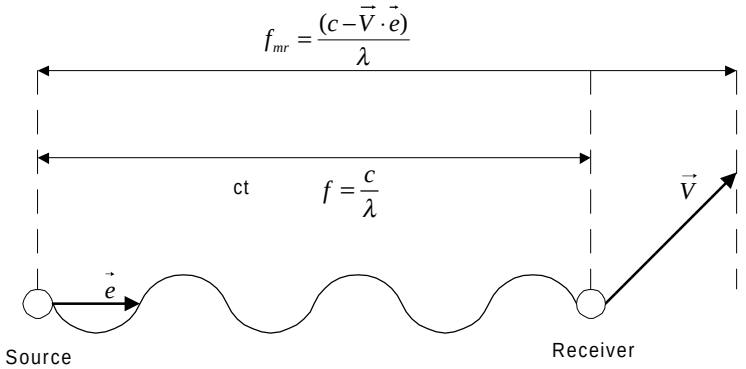

Figure 4.7 Doppler effect in a system with a moving receiver and a stationary source [Durst et. al. (1981)].

At an instant of time, t, the receiver is at a certain distance from the stationary source. In unit time the receiver has moved a distance of $\vec{V} \cdot \vec{e}$ from the source where the wave was emitted towards the receiver. Compared to the number of wave fronts the source transmits, the receiver will, because it is moving, record more or fewer wave fronts, depending on the direction of movement. The wave frequency from the stationary source recorded by the moving receiver is then given by:

$$f_{mr} = \frac{c - \vec{V} \cdot \vec{e}}{\lambda} = f\,(1 - \frac{\vec{V} \cdot \vec{e}}{c}) \tag{4.10}$$

The frequency difference recorded by a stationary receiver compared to a moving receiver becomes:

$$\Delta f_r = f - f_{mr} = \frac{\vec{V} \cdot \vec{e}}{\lambda} \tag{4.11}$$

Doppler effect caused by a scattering particle

In LDA velocity measurements the laser is a light source. Small particles suspended in a flow will scatter the light when passing through the laser beam. In this system illustrated in Figure 4.8, a scattering particle acts as a moving receiver with respect to the stationary laser source and as a moving source with respect to the stationary light detector.

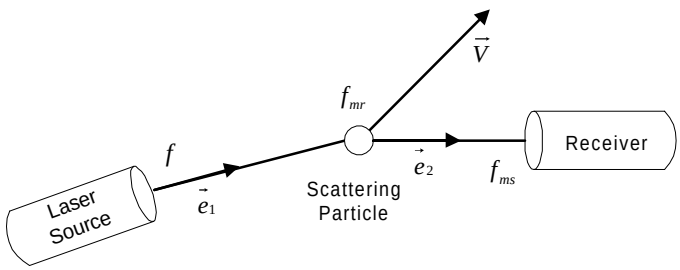

Figure 4.8 Doppler effect caused by a moving scattering particle [Shao (1996)].

The frequency of the waves recorded by the moving scattering particle acting as a moving receiver is:

$$f_{mr} = f\,(1-\frac{\vec{V}\cdot\vec{e_1}}{c}) \tag{4.12}$$

The frequency of the wave recorded by the light detector from light scattered by the particle acting as a moving source is given by:

$$f_{ms} = f_{mr}\left(\frac{1}{1-\frac{\vec{V}\cdot\vec{e_2}}{c}}\right) = f\,\frac{\left(1-\frac{\vec{V}\cdot\vec{e_1}}{c}\right)}{\left(1-\frac{\vec{V}\cdot\vec{e_2}}{c}\right)} \tag{4.13}$$

where $\vec{e}_1$ is the unit vector in the direction from the light source to the scattering particle and $\vec{e}_2$ is the unit vector in the direction from the scattering particle to the light detector.
For this system the total frequency shift is given by:

$$\Delta f_D = f_{ms} - f = f\left(\frac{\frac{\vec{V}\cdot(\vec{e_2}-\vec{e_1})}{c}}{1-\frac{\vec{V}\cdot\vec{e_2}}{c}}\right) \tag{4.14}$$

The absolute value of $\vec{V}$ is much smaller than c, thus the denominator in Equation 4.14 can be neglected. The simplified equation then becomes:

$$\Delta f_D = \frac{\vec{V}\cdot(\vec{e}_2-\vec{e}_1)}{\lambda} \tag{4.15}$$

Doppler shift for the differential (dual beam) mode LDA

As described in Section 4.1 the dual beam mode is when two laser beams of equal light intensity intersects at the point of investigation. Two incident beams with a crossing angle α illuminate the scattering volume simultaneously. The scattered light is observed from a third direction by a light detector. Figure 4.9 shows in principle, a sketch of a moving particle at the intersection of two incident laser beams.

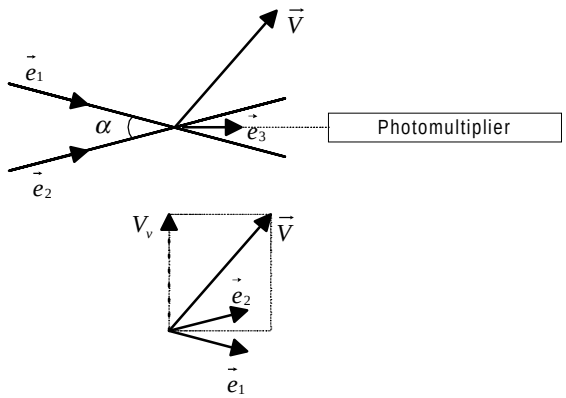

Figure 4.9 Principal sketches of the vectors in dual beam LDA [Shao (1996)].

Since the light scattered by the particle originates from two independent light beams the scattered light will also have two distinctive angles. The beams reach the detector at the same time. A so-called beat is obtained with a frequency equal to the difference in Doppler shift, corresponding to the two angles of scattering. The Doppler shift from dual beam scattering are given by Equation 4.15, and rewritten they become:

$$\Delta f_{D1} = \frac{\vec{V} \cdot (\vec{e_3} - \vec{e_1})}{\lambda} \tag{4.16}$$

$$\Delta f_{D2} = \frac{\vec{V} \cdot (\vec{e_3} - \vec{e_2})}{\lambda} \tag{4.17}$$

thus, the beat frequency received by the detector is:

$$f_D = \Delta f_{D2} - \Delta f_{D1} = \frac{\vec{V} \cdot (\vec{e_1} - \vec{e_2})}{\lambda} \tag{4.18}$$

If we decompose the vectors in the perpendicular direction to the bisections of the two incident laser beams and denote $\vec{n}$ as the difference between $\vec{e_1}$ and $\vec{e_2}$, Eq. 4.18 becomes:

$$f_D = \frac{\vec{V} \cdot \vec{n}}{\lambda} = \left(\frac{2\sin(\alpha/2)}{\lambda} \right) (\vec{V} \cdot \vec{n_0}) = \frac{2V_v \sin(\alpha/2)}{\lambda} \tag{4.19}$$

where $\vec{n}_0$ is the unit vector in the given direction and V_v is the velocity projection in the same direction. The calculation of velocity is given by:

$$V_v = \frac{\lambda}{2\sin(\alpha/2)} f_D \tag{4.20}$$

From Equation 4.19 it can be seen that the value of the frequency of the Doppler signals is independent of the receiving direction. This means that the scattered light can be collected over a wide aperture. It also means that all the scattered light will contribute to the signal. For LDA operated in the reference beam mode this will not be the case [Shao (1996)].

4.2.3 The fringe model

An alternative way to describe the dual beam system is to consider the interference of two laser beams in their intersection or measuring control volume. Rudd (1969) proposed a theoretical model for the interpretation of LDA signals based on the interference or fringe pattern. This model was later called the fringe model, and it considers two laser beams (with Gaussian intensity distribution) intersecting at their waist regions. Here, the wave front can be treated as plane, and a pattern of plane

interference fringes will be generated in the intersection region. Figure 4.10a illustrates this fringe pattern, which will be parallel to the bisector of the two beams. In the figure, velocity is measured in the x-direction. Figure 4.10b is a similar sketch that is useful in the calculation of the fringe spacing.

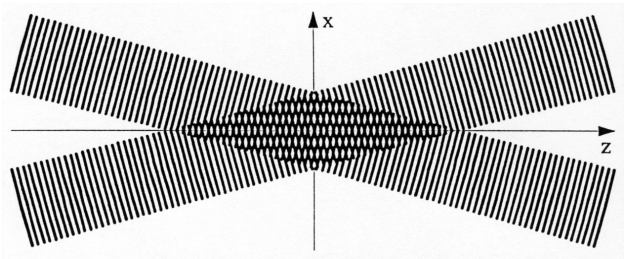

Figure 4.10a Fringe pattern arising from two laser beams [Dantec reference guide (2000)].

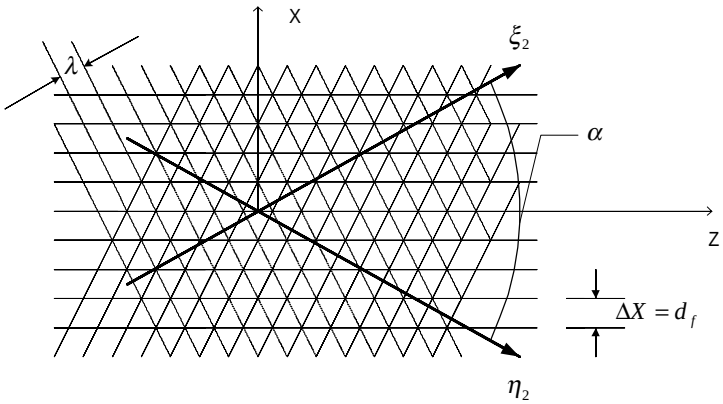

Figure 4.10b Determination of the fringe spacing.

By elementary geometry the spacing between the fringes, d_f, is proportional to the wavelength and inversely proportional to the sine of half the intersecting angle α:

$$d_f = \frac{\lambda}{2\sin(\alpha/2)} \tag{4.21}$$

The light intensity varies inside the interference area, and thus the scattered light from a particle moving through this area will vary accordingly to this intensity. A photo detector can detect the intensity variation of the scattered light. The frequency of this variation in scattered light intensity can be expressed as:

$$f_D = \frac{\vec{V} \cdot \vec{n}_0}{d_f} = \frac{2V_v \sin(\alpha/2)}{\lambda} \tag{4.22}$$

This result is equal to the one of Equation 4.19. The above relation between the Doppler frequency shift and the velocity of the particle indicates that the perpendicular velocity component can be found when the Doppler frequency shift is known.

Above it is stated that the two laser beams intersect at the beam waist. If this is not the case, the wave fronts can no longer be regarded as plane in the volume of intersection. Further the fringe spacing is no longer constant, but varies within the intersection volume. The measured Doppler frequency will as a consequence also vary, depending on the position of the particle within the intersection volume. The Doppler frequency is no longer proportional to the particle velocity when the wave fronts are curved. The final result is measurement errors [Dantec reference guide (2000)].

Fringe distortion

Investigation of fringe distortion is reported by for instance Ruck (1991) and Zhang and Eisele (1998). When tracer particles pass the laser beams shortly before the control volume, a distorted fringe pattern may occur. This is examined in the experimental work reported in Ruck (1991). Here, the fringe pattern variations were studied by use of video imaging techniques. When a particle is passes the centre of the control volume at the same time as a particle is passing one of the beams outside the control volume, a disturbed signal will be produced. The period length of the signal will vary according to the distortion of fringe spacing. Particles that pass the beams several millimetres away from the control volume can, according to Ruck (1991), affect the measurements. Ruck (1991) also observed that not only particles passing the laser beams shortly outside the control volume, but particles inside as well could disturb the fringe pattern.

The latter is often the case when two or more particles are located inside the control volume at the same time.

Consider two particles passing the fringes at, for instance, the centre of the control volume. Then the first "disturbing particle" might leave behind a distorted fringe pattern for the second signal-producing particle. The result of fringe distortion is often a broadening of the velocity probability distribution, which again means a higher measured turbulence level. The size and concentration of tracer particles should therefore be selected with care. As a consequence of the results reported by Ruck (1991) it is natural to assume that not only tracer particles but also bubbles and droplets will have the same effect. In the experiments reported in this thesis, water droplets in oil and oil droplets in water might occur. These droplets might be located in the flow and pass the laser beams at positions close to the control volume. Droplets that are attached to the pipe wall and "fall" down to cross one or more beams can also appear.

Zhang and Eisele (1998) classified the fringe distortion into three groups. These are fringe distortion due to improper optical layout, fringe distortion due to astigmatism because of beam refractions (in other words errors from lenses), and local fringe distortion due to local laser light diffraction through particles in the transmission paths of the laser beams. The latter is the same as reported by Ruck (1991). As opposed to the qualitative experiments conducted by Ruck (1991), Zhang and Eisele (1998) developed a quantitative understanding of fringe distortion. For the case of fringe distortion due to improper optical layout, they developed a fringe distortion number and related it to overestimation of turbulence. Their conclusion was that overestimation of turbulence and mean velocity normally was negligible, except for flows with very low turbulence.

4.2.4 The measuring control volume

The fringe model provides an easily visualized picture of the generation of the Doppler signals and renders a basis for explaining a number of features related to the Doppler signal. If we combine this model with a Gaussian light intensity distribution we get a

complete picture of the interference or fringe region formed in the intersection of the two beams. Figure 4.11 displays the measuring control volume.

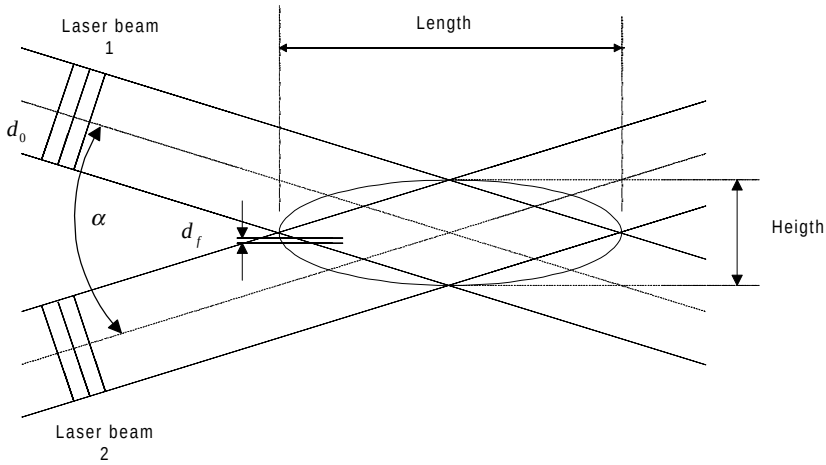

Figure 4.11 Measuring control volume [Dantec reference guide (2000)].

The intersection of the two beams forms the measuring control volume. The control volume forms an ellipsoid with the following dimensions:

$$Height = \frac{d_0}{\cos(\alpha/2)}, \qquad Width = d_0, \qquad Length = \frac{d_0}{\sin(\alpha/2)} \tag{4.23}$$

As mentioned earlier, the control volume is defined as the contour where the light intensity is $1/e^2$ or 13.5 % of the peak light intensity of the beam. The width of the control volume is d_0. Thus the measuring control volume can be visualized as an ellipsoid whose volume is filled with parallel fringe planes in the crossing volume. The number of fringes is calculated from the fringe spacing, d_f, and the height of the control volume:

$$N_f = \frac{height}{d_f} = \frac{\frac{d_0}{\cos(\alpha/2)}}{\frac{\lambda}{2\sin(\alpha/2)}} = \frac{2d_0}{\lambda}\tan(\alpha/2) \tag{4.24}$$

The number of fringes is related to a particle passing along the vertical axis through the centre of the control volume. If a particle is passing through the control volume closer to the edge, it will pass fewer fringes. A particle should pass a sufficiently high number of fringes to produce high quality measurements. The number should typically be between 10 and 100 fringes [Dantec reference guide (2000)]. It is possible to set the signal processor to validate only signals from particles passing an acceptable number of fringes. The frequency shift will make fringes rolling through the control volume. As a result of this fringe movement the effective number of fringes passed by a particle will either increase, if the fringe movement is toward the particle movement, or decrease if the fringes move in the same direction as the particle [Dantec reference guide (2000)].

It is important that the beams overlap as much as possible, but also that the beams intersect at their waists, i.e. where the wave front can be regarded as planar. It can have a severe effect on the LDA measurements if the intersection is outside the beam waist. Then spherical, rather than planar wave fronts, interfere and the fringe surfaces generated are no longer parallel, as is the case for beams with planar wave fronts. Under these conditions two particles penetrating the control volume at different locations but with equal velocity will generate different Doppler signals and hence different velocities.

4.2.5 Frequency shift

From Equation 4.19 it is evident that negative velocities will produce negative frequencies. However, the receiver will not be able to distinguish between positive and negative frequencies, and a directional ambiguity occurs. This ambiguity without the use of frequency shift is shown in Figure 4.12.

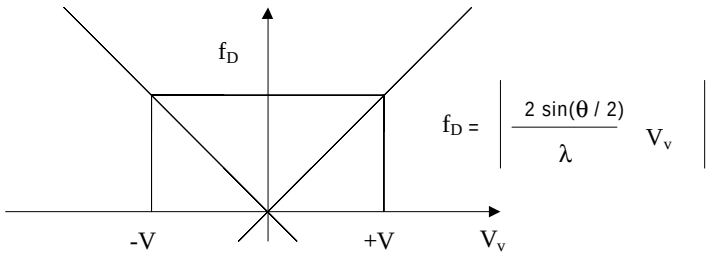

Figure 4.12 Directional ambiguity without frequency shift [Dantec reference guide (2000)].

To overcome this problem one of the laser beams is passed through a Bragg cell. The Bragg cell, whose principle is shown in Figure 4.13, consists of an oscillating slab of glass.

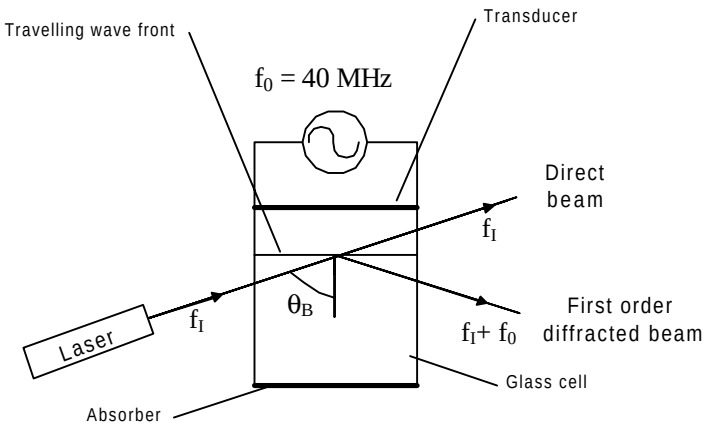

Figure 4.13. Bragg cell [Dantec reference guide (2000)].

At the upper side there is an oscillator driven electro-mechanical transducer. The transducer creates an acoustic wave that propagates through the slab generating a periodic moving pattern of high and low density. The lower side of the slab is shaped to minimize reflection of the acoustic wave and is attached to an acoustic absorbing material. The incident laser beam with frequency, f_I, hits the travelling wave front,

which acts as a diffraction grating. The interference of the scattered light by each acoustic wave front will cause emission of intensity maximum in several directions. By adjusting the tilt angle of the Bragg cell, θ_B, it is possible to adjust the intensity balance between the direct beam and the first-order diffracted beam. The Bragg cell ads a fixed frequency shift, f_0, to the diffracted beam:

$$f_D = f_0 + \frac{2V_v \sin(\alpha/2)}{\lambda} \tag{4.25}$$

As long as negative particle velocity does not produce a larger negative last term in Equation 4.25 than the shift-frequency, f_0, the measured Doppler frequency will be positive. A typical value is f_0 = 40 MHz. Resolving of the directional ambiguity is shown in Figure 4.14 for velocity component U.

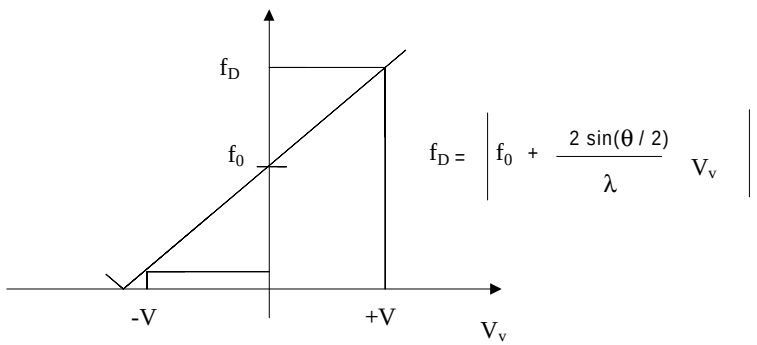

Figure 4.14. Resolving directional ambiguity with the use of frequency shift [Dantec reference guide (2000)].

The introduction of a frequency shift will tilt the fringes slightly. But since the frequency shift of 40 MHz is so much smaller than the frequency of the laser light, meaning that the difference in wavelength between the shifted and the unshifted beam is much smaller than the wavelength of the laser beam itself, the phenomenon can normally be ignored [Dantec reference guide (2000)].

4.2.6 Backscatter and forward scatter

When a particle passes through the control volume the majority of the laser light is scattered in directions away from the transmitting optics. In Figure 4.15 an incident laser beam hits a spherical particle. The three most important modes of scattering are the reflected light, the 1st order refracted light and the 2nd order refracted light. There are other higher orders of refraction, all with successively lower light intensity. Depending on the type of particle, droplet or bubble exposed to the laser light there may exist one scattering mode that is dominant with respect to the others.

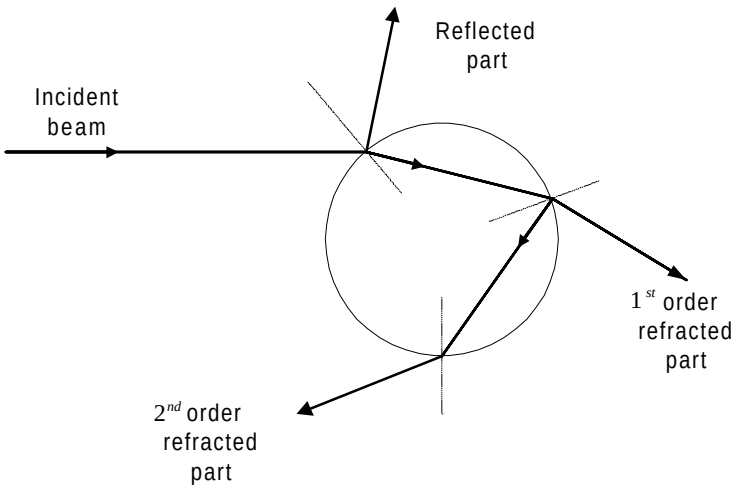

Figure 4.15 Light scattering by a particle [Dantec reference guide (2000)].

The term forward-scatter generally refers to the detection of the 1st order refracted light while backscatter refers to detection of 2nd order refracted light and reflected light. The conception of side scatter is sometimes used about detection of the reflected light. Instead of these definitions of forward scatter, backscatter and side scatter referring to which part of the scattered light detected, there exists a more practical definition. When both the transmitting optics and the receiving optics are placed in a common housing one can use the term backscatter. When the transmitting optics and the receiving optics

are placed in separate housings the term forward scatter can be employed. It is also sometimes referred to as side scatter or off axis scatter when the receiver has an angle relative to the transmitting optics. Figure 4.16 shows the difference between the LDA principles of forward scatter and backscatter.

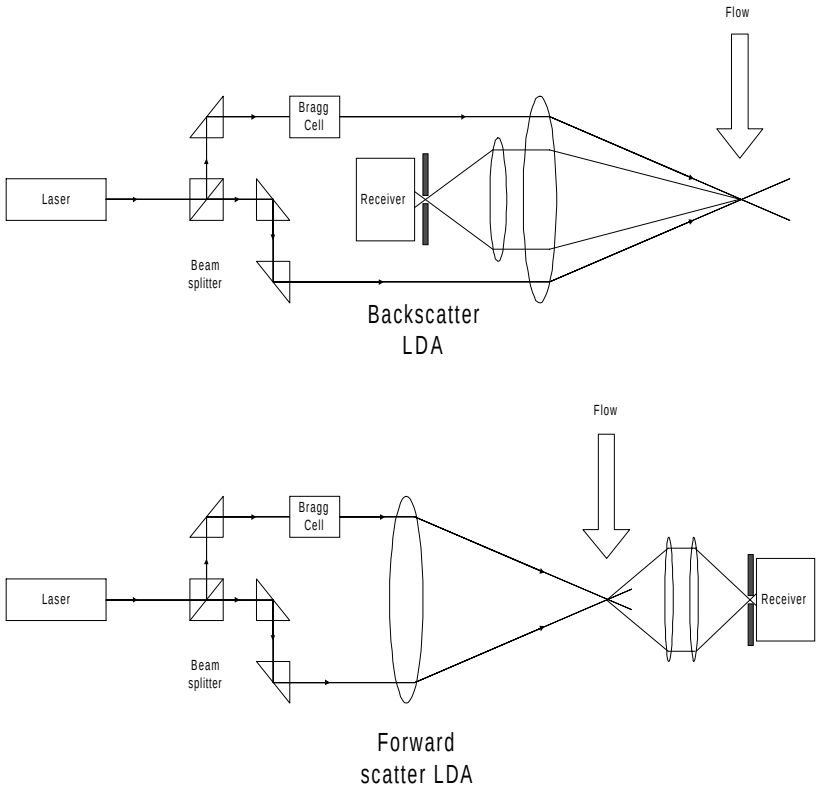

Figure 4.16 Backscatter setup and forward scatter setup [Dantec reference guide (2000)].

In the early days of LDA, forward scattering was most common and the receiving optics was positioned opposite to the transmitting laser probe, like the setup by Brayton, Kalb and Crosswy (1973) shown in Figure 4.3. The reason was that the amount of light scattered back to the receiver was much smaller. However, the

development in laser technology has made it possible to obtain good measurements even when the intensity of the scattered light is low. Thus, today the backscatter technique is most usual. In some cases though, forward scatter may be the only way to obtain measurements. One of the advantages of backscatter is the escape of the time-consuming alignment procedure using two separate units. In the LDA measurements presented in this thesis the backscatter setup is used [Dantec reference guide (2000)].

4.2.7 Signals

A current pulse from the photo detector contains information from the LDA measurement. The information is frequency related to the measured velocity. In addition to the frequency information the photo current also contains noise. By proper selection of the laser power, the type and size of seeding particles and other optical system settings the noise can be reduced. According to several investigators, like for instance Ruck (1991), the number of seeding particles present in the control volume simultaneously affects the signal quality. If on average much less than one particle is present in the control volume, it is called a burst type Doppler signal. Figures 4.17a and 4.17b show the non-filtered and the filtered Doppler burst, respectively. The filtered signal appears after a high-pass filter removes the DC-part and this signal also serves as the input to the signal processor.

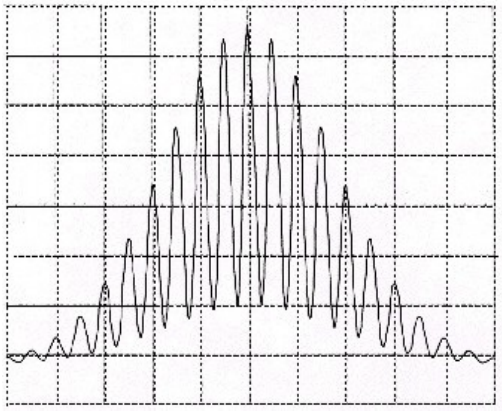

Figure 4.17a. Non-filtered Doppler burst [Dantec reference guide (2000)].

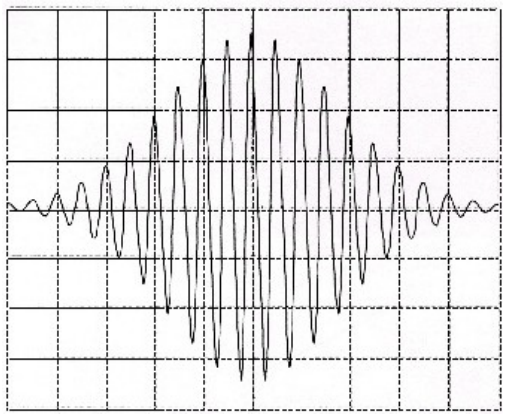

Figure 4.17b. Filtered Doppler burst [Dantec reference guide (2000)].

If more particles are present in the control volume simultaneously it is called a multi-particle signal. According to Dantec, most modern LDA-processors are designed to handle only single-particle bursts. When a multi-particle burst occurs the processor will normally estimate the velocity as a weighted average of the particles present in the control volume. Multi-particle scattering may create noise, which can be difficult to remove.

4.2.8 Seeding particles

It is important to choose the right seeding particles or tracers. It is the velocity of the particles suspended in the flow and not the flow itself that is measured. The particles must be small enough to follow the streamlines of the flow and at the same time large enough to scatter sufficient light. To make accurate velocity measurements of a certain flow, the seeding particles should according to Durst, Melling and Whitelaw (1981) possess the following properties:

- *Ability to easily follow the flow.* This is of course required since it is the velocity distribution of the flow itself we are trying to measure.

- *Scatter sufficient light.* Tracer particles must scatter light according to what is required for the detector system. Usually this is not a problem.

- *Easy to produce.* Tracer particles are often exchanged and to keep costs down they should be easy to produce.

- *Cheap.* For the same reason they should be cheap.

- *Non-toxic, non-corrosive and non-abrasive.* These requirements are necessary to prevent damage to pipes, pumps etc. They are also easier to dispose.

- *Chemically inert.* Tracer particles must be chosen with care so that they do not react with the fluid they are suspended in.

- *Clean*. Sometimes, tracer particles can pollute the system and introduce poorer optical conditions.

Seeding particles in the experiments

In the LDA experiments presented in this thesis different types of particles were tried but the final choice was polyamid particles manufactured by Dantec. Table 4.1 lists the properties of polyamid particles.

Table 4.1 Properties of polyamid.

Product	Mean diameter	Density	Toxic/inert	Cost
polyamid	5 μm	1.03 g/cm^3	no/yes	50 USD / 100g

Polyamid particles are dispersed in Exxsol D-60 so that the Doppler shift effect can be used to determine velocity. When water is also in the pipe it was found that the polyamid particles prefer to go in to the aqueous phase. Also a clustering effect on the interface is observed. This means that the velocity profile of the oil phase cannot be studied properly. One solution to the problem was to find surfactants, which could stabilise the particles in the oil phase, but not cause the formation of emulsions. Several surfactants were tested; most of these were Pluronics, i.e. copolymers of polyethylene oxide and polypropylene oxide. The particles were added to a surfactant solution of Exxsol D-60 and water added. The tendency to form emulsions and whether the particles were in the oil or the aqueous phase was monitored. It was found that the best surfactant was BASF PE 6100. This stabilises the particles well in the oil phase and at low enough concentration the formation of emulsions is not a problem. The only uncertainty is the concentration that should be used. It is estimated that it should be significantly less than 0.1% by weight. Hence, we used concentrations less than this in all experiments.

Information about other types of tracer particles and areas of use can be found in Durst et al. (1981).

4.3 THE LASER SYSTEM IN USE

Laser Doppler anemometry (LDA) is used to measure local velocities and velocity fluctuations in the transparent part of the test section. The LDA setup is a two-colour backscatter system that enables simultaneous measurement of axial (horizontal) and vertical velocity components. The system available at Telemark University College also enables PDA. However, since only LDA is used in this work, description of the PDA equipment is left out in this section. The LDA setup is displayed in Figure 4.18.

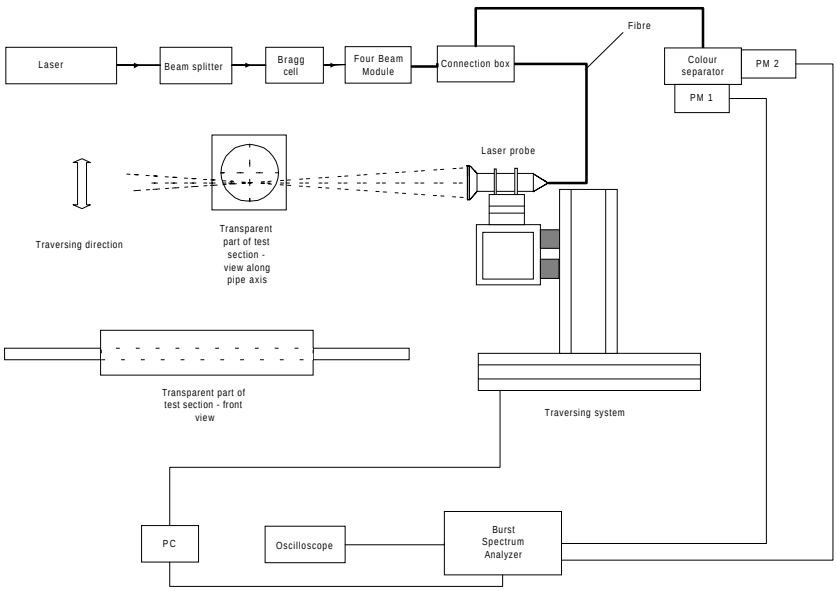

Figure 4.18. The LDA setup used on both flow facilities.

Laser and optics

The light source is a water-cooled 3 W *Lexel 80* argon-ion laser. It produces a coherent beam, which is directed into a housing that contains several units including prisms and mirrors. First, the beam enters the beam splitter. Here, the single laser beam is split into two parts by two prisms. The beams are then lead onto the Bragg cell where one of the beams is frequency shifted. The Bragg cell was discussed in Section 4.2.5. The laser system was originally bought as a one-dimensional LDA, but was later extended to two-dimensional LDA. The extension unit is called the Four Beam Module and it is mounted after the Bragg cell. The Four Beam Module is basically a colour beam splitter. Both the shifted and the non-shifted beam enter the module where they are split into two green and two blue beams. Each beam pair has separate wavelengths, 514.5 nm for green and 488 nm for blue, and contains one shifted beam and one non-shifted beam. After the Four Beam Module the four laser beams are directed into transmitting fibre optical cords, which are connected to the transmitting probe. Each

individual beam has the same power when the system is aligned properly. A digital optical power meter was used to measure the intensity of the beams and the maximum power was 180mW for each beam out of the probe. The front lens of the transmitting probe focuses the four beams at a focal point. The same unit that transmits the light also receives the scattered light from the tracer particles in the flow that passes the intersection volume. This is a consequence of the LDA being operated in the backscatter mode. Special lenses focus the backscattered light into receiving optical fibres, which transports the light to a colour separator. Here, the two components (the green and the blue) are separated and re-collimated before they are directed into each detector. The detector is a *p*hoto *m*ultiplier tube (PM), which converts the light into electrical signals that are fed to the signal processor.

Signal treatment and the display of velocity data

The signal processor is a Burst Spectrum Analyser (BSA) and is connected to an oscilloscope and a PC. The BSA converts the electrical signals, which are processed by the oscilloscope, into velocity data, which again are monitored online by a PC. Special software designed by Dantec, processes the raw-data into statistical values like mean velocities, RMS values and turbulent quantities.

Choice of transmitting front lens

The choice of a front lens for the transmitter was for the case of LDA in the Model Oil Facility a trade-off between resolution and sampling rate. The final choice was a front lens with focal length 400 mm. For the case of measurements in the Matched Refractive Index Facility, a front lens with focal length of 160 mm was chosen. The geometrical information of the lenses available is listed in Table 4.2. This includes the dimensions of the control volume as a function of focal length.

Traversing system

The laser probe that transmits the light is connected to a traversing system with a resolution of 0.0125 mm. The traversing unit is a Dantec lightweight system, which is operated from the computer. It enables three-dimensional movement.

Table 4.2 Geometrical data for different front lenses [Dantec reference guide (2000)].

Beam pair	Focal length of front lens [mm]	Number of fringes	Fringe spacing [μm]	Beam half-angle [deg]	Height [mm]	Width [mm]	Length [mm]
Green λ=514.5 nm	120	48	1.645	8.997	0.080	0.079	0.50
	160		2.182	6.772	0.106	0.105	0.89
	310		4.203	3.507	0.203	0.203	3.32
	400		5.422	2.720	0.262	0.262	5.52
	600		8.128	1.814	0.393	0.393	12.41
	1200		16.249	0.907	0.786	0.786	49.66
Blue λ=488.0 nm	120		1.560	8.997	0.075	0.075	0.48
	160		2.069	6.772	0.100	0.099	0.84
	310		3.989	3.507	0.193	0.193	3.15
	400		5.143	2.720	0.249	0.249	5.24
	600		7.709	1.814	0.373	0.373	11.78
	1200		15.412	0.907	0.746	0.746	47.10

Measurements are done without beam expander. The beam spacing is 38 mm from the front lens and the beam diameter is 1 mm.

4.4 REFRACTION OF LASER BEAMS

The goal of the LDA measurements is to measure velocities and turbulence along the vertical diameter through the pipe centre. To accomplish this, one must overcome problems involving refraction of the laser beams. In the following sections these problems are discussed, and some suggestions for improvements are made.

4.4.1 Snell's law of refraction

Refraction of laser beams is present in the majority of all LDA applications. The refractive index of a substance is defined according to:

$$n = \frac{c}{v} \tag{4.26}$$

where c is the speed of light in vacuum, equal to $2.998 \cdot 10^8$ m/s, and v is the speed of light in the substance. In every media except vacuum, light travels with a speed that is less than c. This means that n is equal to unity in vacuum and greater that unity in all other media. Refractive indices for substances related to the experiments are listed in Table 4.3.

Table 4.3 Refractive indices and physical constants for different substances at 20°C [Fischer and Jovanović (1998)].

Substance	Refractive index	Density ratio ρ / ρ_{H_2O}	Viscosity ratio ν / ν_{H_2O}
Vacuum	1.000	-	-
Air	1.00045	0.001	0.018
Sea water	> 1.333	1.02	1
Water	1.333	1.00	1
Crude oil	1.5?	0.8-1.0?	2-50?
Exxsol D-60	1.434	0.787	1.5
DMSO	1.4783	1.10	3.2
Diesel oil 1	≈1.46	0.84	3.6
Diesel oil 2	≈1.48	0.84	3.6
Plexiglass	1.51	-	-
Duran 50 glass	1.473	-	-

When one substance has a higher refractive index than another, it has a higher optical density. When light travelling in one substance hits the boundary of another substance, some of the light will be reflected, and assuming the substance is transparent, some of the light will enter the substance and travel through it. Very often the direction of the light changes when it travels from one substance to another, and that is referred to as refraction. Figure 4.19 shows the refraction of a beam of light in the boundary between two different substances.

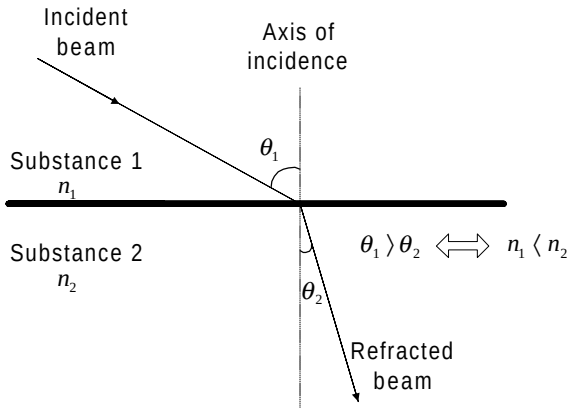

Figure 4.19 Refraction of a light beam in the boundary between two plane surfaces.

The angle of incidence, θ_1, is the angle between the incident beam and the axis of incidence. The angle of refraction, θ_2, is the angle between the refracted beam and the extension of the axis of incidence. For the refraction of a light beam travelling from a substance of refraction index n_1 to another substance of refractive index n_2, Snell's law of refraction is valid. The law states that the incident beam, the axis of incidence and the refracted beam all lie in the same plane, and that the relationship between the angle of incidence and the angle of refraction is given by:

$$n_1 \sin(\theta_1) = n_2 \sin(\theta_2) \tag{4.27}$$

When a light beam travels from a substance with one optical density to another substance with less optical density, the beam is refracted away from the axis of incidence. If the beam travels from a substance with a lower optical density to substance with higher optical density, it is refracted towards the axis of incidence.

4.4.2 Tracking of the laser beams

The location of the intersection point of the laser beams is of great importance since this is the point where the control volume is formed and velocity is calculated. When

the transmitting probe is moved, either manually or by a traversing unit, the point of intersection also moves. If the laser beams travel in open air all the time, the intersection point will follow the same path as the transmitting probe. However, this is not the case when measurements are done in a circular pipe. The challenge is to be able to control the movement of the intersection point as well as the movement of the transmitting probe.

The transmitted beam pairs from the probe are found in planes that are perpendicular to each other. When the objective is to measure the axial (horizontal) and the vertical velocities in a horizontal pipe, the transmitting probe is carefully aligned in such a way that the green beam pair is positioned in the horizontal plane and the blue beam pair is positioned in the vertical plane. When a beam pair hits a curved surface like the transparent pipe wall, each of the beams will be refracted according to Snell's law. And if two laser beams enters the pipe wall at the same angle of incidence, they are refracted equally. This is always the case for the green beam pair assuming proper alignment of the transmitting probe. The blue beams will only have the same angle of incidence when they intersect in the pipe centre, that is, when measurements of the centre velocities are conducted. Otherwise, the two blue beams will enter the pipe wall at different angles of incidence.

To track all four beams from the transmitting probe to the points of intersection, a specially designed MATLAB programme developed by Professor Melaaen is used. The beam tracking procedure itself can be used as a method not only to understand the movement of the laser beams, but also to compensate for refractive index variations, later discussed in Section 4.4.7. The input data are the vertical movement of the transmitter and the output is the path of each of the intersection points. From simulations using this programme it became clear that the two intersection points followed different paths when the transmitter was moved in a direction parallel to the vertical diameter of the pipe. Figure 4.20 displays the beam tracking in the centre of the pipe.

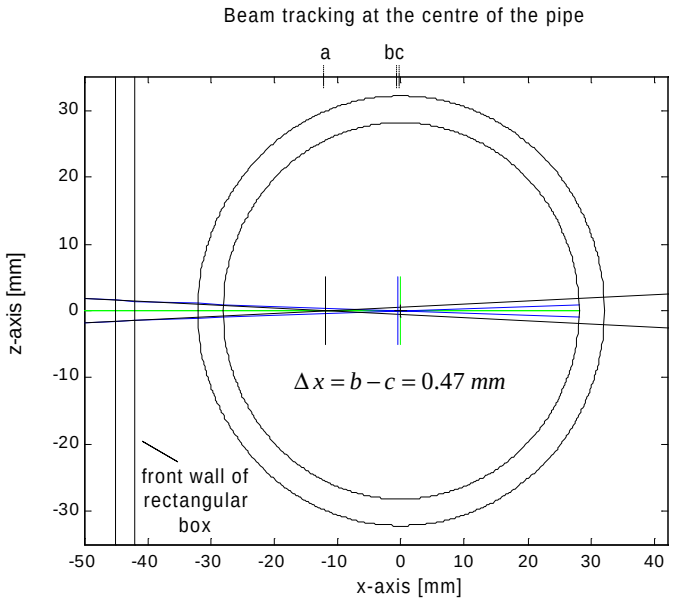

Figure 4.20 Beam tracking in the centre of the pipe. Control volume centres separated horizontally by 0.47 mm.

If the four laser beams travelled without any refraction they would cross at point a. Point b and c represents the position of the individual control volumes (b=blue and c=green) when the beams are subjected to refraction. In the pipe centre the separation of the centre of each control volume is 0.47 mm. The green beams intersect in the pipe centre while the blue ones intersect slightly off-centre. This position is accessible to LDA measurements. The mentioned number is dependent on the fluid used in both pipe and box. Here, water is used. The tracking of the beams near the pipe wall is illustrated in standard and increased scale in Figure 4.21a and b, respectively. Refraction of the beams is more evident in this position, which is about 1 mm from the wall.

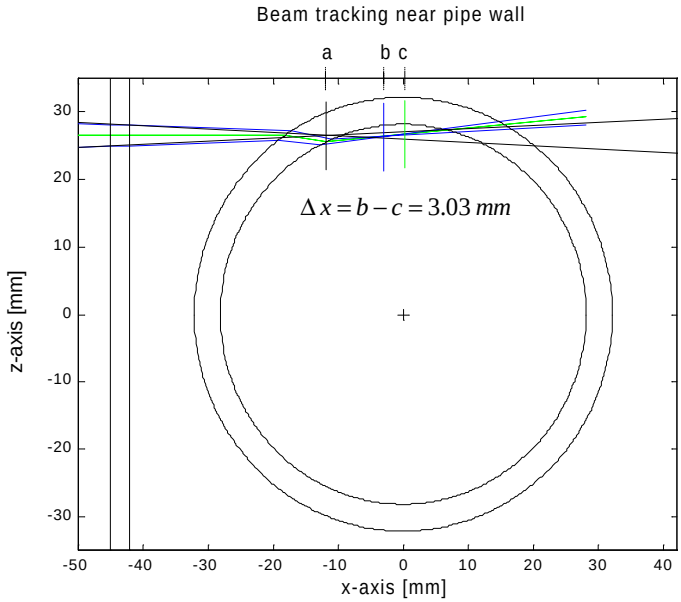

Figure 4.21a Beam tracking near the pipe wall – standard scale. Control volume centres separated horizontally by 3.03 mm.

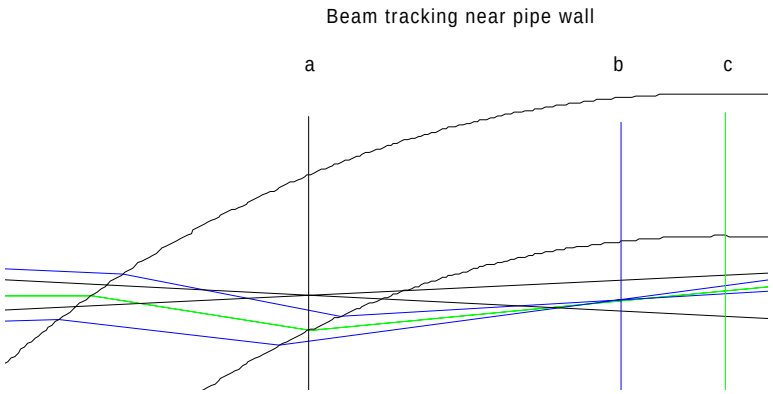

Figure 4.21b Beam tracking near the pipe wall – increased scale. Control volume centres separated horizontally by 3.03 mm.

The centre of the individual control volumes is now separated horizontally by 3.03 mm. Simulations of the paths for the individual control volumes are presented in

Figure 4.22. The path labelled a represents no refraction while b and c are the paths of the blue and green control volume, respectively. The green beams are less influenced by refraction and the green control volume can be seen to follow the centre line almost through the entire pipe diameter. On the other hand, the control volume created by the blue beams will follow a path that is parallel to the pipe diameter only in the centre region of the pipe. Further traversing towards the wall will make this control volume bend away from the vertical pipe diameter. When a front lens with focal length 400 mm is used, the lengths (along the x-axis) of each control volume are 5.52 and 5.24 mm, as listed Table 4.2. This means that there exists an overlap of the control volumes even if the centres are separated by as much as 2.5 mm. For the case presented in Figure 4.21, the control volumes are completely separated. This means that it is not possible to obtain simultaneous measurements of two velocity components in this position. For the most part of the pipe diameter though (from the centre to about z=27), it is possible to obtain 2-D measurements. However, the sampling rate falls drastically when approaching the wall compared to that in the pipe centre.

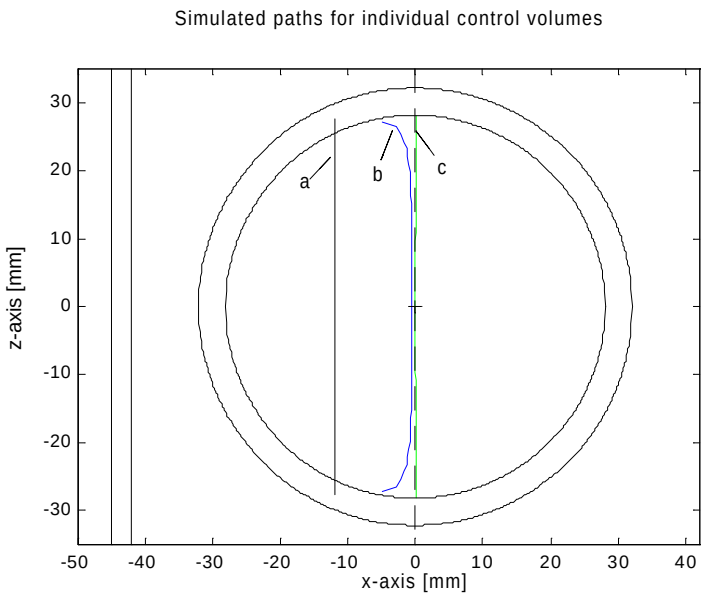

Figure 4.22 Simulated individual control volume paths.

4.4.3 Refractive Index Matching - RIM

LDA experiments in this thesis are conducted on the two different flow facilities described in Chapter 3. Both facilities have a test section that includes a transparent circular pipe where the measurements are done. The approach to improve the optical measurement conditions is slightly different in each of them. The goal for both facilities is to obtain optical measurement conditions that are as good as possible so that reliable 2-D measurements can be conducted. For both flow facilities, this implies Refractive Index Matching (RIM). RIM is a method that involves selection of fluids and substances, like the pipe material, so that they have equal or nearly equal refractive indices. A rectangular box is built around the circular pipe, and the box is filled with a fluid that has the same refractive index as the pipe material and the fluids flowing inside. Figure 4.23a displays the principle of the system and Figure 4.23b shows a picture of LDA measurements in oil/water flow in such a system.

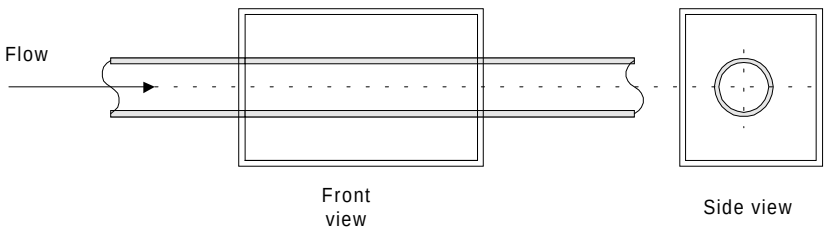

Figure 4.23a Rectangular box around pipe.

Figure 4.23b LDA measurements in oil-water flow in the Model Oil Facility.

When the RIM procedure is perfect, the laser beams will only be refracted when they travel from open air and further through the surface of the rectangular box. If this surface is parallel to the front lens on the transmitting probe, the refraction will be constant along the vertical diameter of the pipe. Then, the laser beams will travel non-refracted through the circular geometry of the pipe wall, as well as through the fluids flowing inside. In such a system, all positions in the flow geometry are optically accessible and the control volume of the green and the blue beams will coincide. Both control volumes will follow the vertical diameter of the pipe as opposed to the case presented in Figure 4.22

RIM is a well-established method used by several investigators. Durst, Jovanović and Sender (1995) describe a test section for LDA measurements consisting of a rectangular box built around a circular pipe. The section was made from Duran-50 glass. They intended to measure turbulent statistics in the near-wall region of the pipe. Two diesel oils, one with higher refractive index than Duran-50 and one with lower,

were used both inside the box and the pipe. By proper mixing of the two diesel oils they were able to get a mixture with the exact refractive index as the solid material. They also held the temperature in the system constant to prevent variations in the refractive index. Another procedure was suggested by den Toonder and Nieuwstadt (1997). They used a RIM procedure when they measured turbulent water flow in a pipe. To achieve good measurements also close to the pipe wall made from perspex (n=1.49) they partly replaced the pipe wall with a thin foil made from Teflon FEP (Fluorised Ethylene Propylene) with a refractive index of n=1.334.

Often RIM means that model fluids have to be used instead of the real ones. The model fluid should have physical fluid properties, such as density, viscosity and surface tension, which are as equal as possible to the real fluids. Model fluids can be difficult to find since they need to match the relatively high refractive index of plexiglass (or other transparent materials). Some solvents, like toluene and benzene have refractive indices that are high enough to match (or can be matched by adding water) plexiglass. However, they should not be used since they are highly toxic. Model fluids should therefore meet several expectations:

- *Refractive index*: The refractive index of the model fluids should match each other and the pipe material.

- *Physical fluid properties*: A model fluid should have similar density, viscosity and surface tension as the real fluid.

- *Non-toxic*: Preferably the model fluid should be non-toxic. If the model fluid is toxic it should flow in a closed loop and required precautions should be taken when handling it.

- *Non-corrosive and non-reactive*: No parts of the flow facility in contact with the fluids should be influenced. Especially, the pumps are vulnerable and often expensive units in a flow facility. Tracer particles must be available and non-influenced.

- *Cost*: Special solvents used as model fluids are often expensive. This leads to limitations in the amount that can be used and the size of the flow facility.

It can be difficult to find model fluids that meet all the expectations. Often one has to compromise in search for excellent optical conditions, and choose a model fluid that is less satisfactory than another. In some cases, like the LDA experiments in this work involving two-phase flow of oil and water in the Model Oil Facility, the fluids are already model fluids before the RIM technique is applied. The purpose of the study is to examine the flow of seawater and crude North Sea oil. However, the fluids have to be transparent, and thus transparent oil is selected. Also seawater is exchanged with tap water since it is less corrosive.

4.4.4 RIM procedure for LDA measurements of two-phase flow in the Matched Refractive Index Facility

The aim of the LDA measurements in this flow facility is to model the behaviour of a dispersed flow of crude oil and seawater. This flow facility is described in detail in Section 3.2. Both the rectangular box and the circular pipe are made from transparent Duran 50 glass. The model fluids are selected after the principles mentioned above. As a model fluid for the crude oil, a mixture of two transparent diesel oils is used. One of the diesel oils has higher refractive index, and the other a lower refractive index than Duran-50. By proper mixing, the mixture acquires the same refractive index as Duran-50. This procedure was conducted for the single-phase flow measurements described in Durst, Jovanović and Sender (1995). The solvent dimethylsulfoxid (DMSO) added to water is used as a model fluid for seawater. DMSO is transparent and has a refractive index that is slightly higher than Duran-50. By adding only small amounts of water, the refractive index is adjusted to match both the mixture of the diesel oils as well as the Duran-50. The refractive indices were measured by a refractometer. Either of the fluids can be used in the rectangular box. After this RIM procedure is conducted on the system, all positions inside the flow become optically accessible, and both forward scatter and backscatter techniques are possible.

4.4.5 RIM procedure for LDA measurements in oil-water flow in Model Oil Facility

This flow facility, which was described in Section 3.1, is designed to study stratified flows of oil and water. To obtain LDA-measurements, a very simplified RIM procedure is conducted. Both the rectangular box and the circular pipe are made from plexiglass with a refractive index of 1.51. The model fluids selected are Exxsol D-60 (n=1.434) and tap water (n=1.333). The difference in refractive index between the liquids and the solid creates limitations in the measurements. When stratified flow is introduced, the goal is to measure axial (horizontal) and radial (vertical) velocities through the vertical centre diameter of the pipe. By beam tracking, using the specially designed MATLAB programme, we were able to simulate paths of the individual control volumes during the traversing of the transmitting probe (Figures 4.20-4.22).

Separation of the individual control volumes is diminished if the same fluid is located inside the rectangular box as in the pipe. To achieve this, a calibration procedure is needed. The rectangular box is first filled with water and single-phase water is introduced in the pipe. The transmitting probe is aligned so that the intersection point of the laser beams lies in the pipe centre. Then the water in the box is exchanged with oil and single-phase oil is introduced in the pipe. Now the intersection point lies in an off-centre position (further away from the probe) but in the same horizontal plane. The probe is then traversed backward so that the intersection point again lies in the pipe centre. The traversed distance is a correction that is used in all vertical positions. The correction was 2.54 mm. For the horizontal beam pair (green) the use of a constant correction induces only small errors. For the vertical beam pair (blue) the errors become larger, but not more than was acceptable. In that way we use two different traversing matrixes, one for the water phase and one for the oil phase. The system is now ready for measurements in stratified flow. Measurements are first conducted in the water-phase with water inside the rectangular box. We start at the lower pipe wall and traverse upwards through the water phase and further a little bit into the oil phase. Then the water in the box is exchanged by oil, the horizontal position is corrected and measurements are conducted from the upper pipe wall, downward through the oil-phase and a little bit into the water-phase. The reason for the overlap by the two

traverse matrixes is to cover the waves at the interface. Figure 4.24 shows the two different systems.

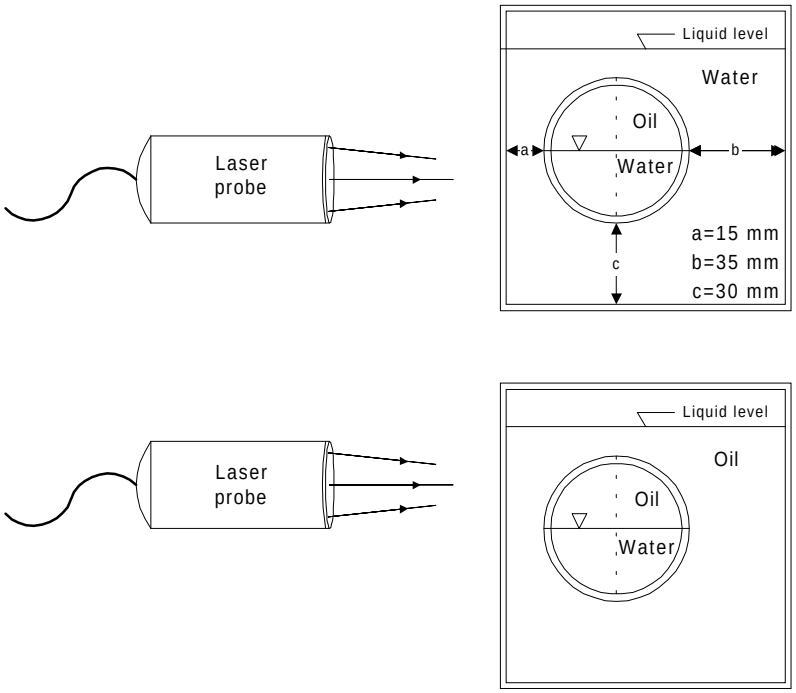

Figure 4.24 System for measurements in water-phase (above) and oil-phase (below).

Chervin, Petrie and Deutsch (1990) used a similar RIM method in a single-phase glycerine system. They used an acrylic transparent circular test section with a rectangular box around. Glycerine (n=1.47) and acrylic (n=1.49) have only small differences in refractive index, and when using glycerine in both the pipe and the box the curvature effects were small. In fact, they used ray-tracing techniques to estimate the control volume displacement and found it to be less than 1.2%.

4.4.6 Alternative methods to RIM

Sometimes it may be desirable to use the real fluids instead of model fluids. To improve measurement conditions without RIM two considerations involving the

standard LDA equipment are mentioned and discussed. Two alternative methods for refractive index compensation are outlined in brief in the following sections.

- *The correct choice of transmitting front lens*:

The curvature of the pipe wall can lead to partial or total distortion of the control volume. By choosing a longer focal length for the transmitting front lens, the size of the measurement volume increases. Consider measurements vertically through the centre diameter of a pipe. Then, the separation of the two control volumes, one for each beam pair, becomes a problem. To be able to obtain measurements of the two velocity components simultaneously, at least some parts of the individual control volumes have to coincide. Larger individual control volumes are more likely to overlap, and one may be able to obtain measurements over a greater part of the diameter. The dimensions of the control volume as a function of the focal length of the front lens are given in Table 4.2

- *The use of backscatter*:

A backscatter setup includes both the transmitting and the receiving optics in the same housing. Then, the light path from the transmitting optics to the tracer particle is nearly the same as the light path from the particle to the detector. Such a setup is highly desirable when optical conditions are poor. If forward scattering is used, the light path from the particle to the detector can be quite different from the path from the particle to the transmitter. Consider a system with separated liquid-liquid two-phase flow in a horizontal pipe. If measurements are conducted slightly above the interface, the incident laser beams may travel only in the less dense fluid, while the scattered beams, may travel also in the denser fluid. To obtain measurements using a forward scatter set-up it is necessary to adjust the angle between the detector and the transmitter at almost every measurement position. This can be avoided if a backscatter set-up is used.

4.4.7 Beam tracking or beam tracing

Beam tracking or beam tracing can be used as a method for compensating refractive index variations. Several have investigated problems with LDA measurements in

circular or curved geometries. Among them are Kehoe and Desai (1987). They were the first to develop a ray tracing technique for use in LDA experiments in circular geometries. The basic principle of their ray tracing method was to make sure the positioning or traversing of the LDA transmitting probe enabled measurements in all desired locations in the flow geometry. The technique required tracing of the laser beam paths from the source to the measurement point and back again. Snell's law was applied to each material interface in the beam paths. However, some positions inside the geometry, referred to as "blind spots", could not be measured. These “blind spots” occurred near the walls of the geometry where the refraction of the beams was most distinctive. It has to be pointed out that Kehoe and Desai studied only one velocity component at a time, but the results did compensate for the variations in refractive index.

4.4.8 Specially designed lenses

The use of specially designed lenses is another method for compensating refractive index variations. Contributions made by Els and Rouve (1985), Vikram and Billet (1986) outline procedures for design of special lenses for LDA measurements in cylindrical geometries.

The background for the work of Els and Rouve (1985) was to solve the problems with two-component LDA measurements in cylindrical pipes. A solution to the problem besides the one of index matching fluids was supplementary lenses. These lenses adjust the difference in the beam in such a way that separation of individual control volumes is prevented. One way was to glue a supplementary concave-convex lens to the circular pipe wall. The problem with such a lens was that it was difficult to produce and that it created extra alignment problems. The other solution was to use cheaper single curvature lenses that were easier to adjust. Procedures for calculation of curvature and position of the lenses were outlined. The drawback was that these lenses allowed only one-component LDA measurements. The main conclusion was that these methods could improve optical conditions in circular geometries, but never be an improvement on the RIM technique.

Vikram and Billet (1986) also used additional lenses to improve optical conditions in a circular geometry. The difference from the work of Els and Rouve (1985) is that Vikram and Billet (1986) also designed lenses to be used in combination with the conventional tank around the pipe.

4.5 DATA ANALYSIS

4.5.1 Measured data and calculated variables

The signal processor treats analog signals from the photo detectors. For each Doppler burst, a corresponding particle velocity is calculated. The calculated velocity is then sent to a computer for analysis. Figure 4.25 shows the steps in data analysis from raw data to moments, correlations and spectra. In the work presented in this thesis the spectral analysis is left out.

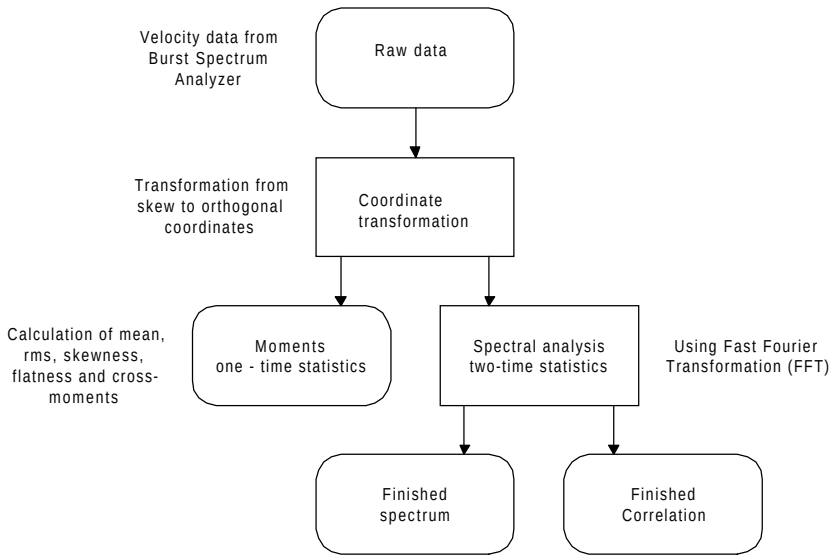

Figure 4.25 Calculation of moments, correlations and spectra using Fast Fourier Transformation techniques [Dantec reference guide (2000)].

From the calculated velocity data, which we call raw data, two main ways of treating the data exist. But first the raw data need to be transformed into orthogonal coordinates if they initially are skew. A 2-D LDA setup usually has orthogonal coordinates since the two beam pairs are fixed in planes that are perpendicular to each other. A 3-D setup involving two laser probes (a 2-D probe and a 1-D probe) might require transformation. The reason for this is that the "third" beam pair has an angle different from 90 degrees compared to the other two pairs. The simplest form of statistical analysis is calculation of moments while spectral analysis resulting in calculation of spectrum and correlation is more advanced and not used in the present work.

Two major types of statistical errors exist in the analysis of the measurements or the raw data. These are known as velocity bias and the lack of random arrival of seeding particles to the control volume. Velocity bias, which will be discussed in a later section, relates to the simple statistical analysis like in calculation of moments. The problem of random sampling depends on timing between events, and becomes an error source in calculation of spectrum and correlation. For calculation of mean velocities random sampling is usually not so important.

4.5.2 Moments

Moments are sometimes called one-time statistics since the samples are treated one at a time. The calculations are done on individual samples, and both relations between samples and the time between events are ignored. Moments include statistical quantities like mean, variance, root mean square (rms), turbulence intensity, skewness, flatness and cross-moments.

For our two-component LDA system the basis for the statistical analysis is the raw data of axial (u) and radial (v) velocities. These velocity components are orthogonal since the green (u) and the blue (v) beam pair is positioned in planes perpendicular to each other. Thus, there is no need for coordinate transformation. The calculated axial and radial mean velocities are given by:

$$\bar{u} = \sum_{i=1}^{N} \eta_i u_i \qquad \bar{v} = \sum_{i=1}^{N} \eta_i v_i \tag{4.28}$$

The rms velocities or the velocity fluctuations are given by:

$$u_{rms} = \sqrt{\sum_{i=1}^{N} \eta_i (u_i - \bar{u})^2} \qquad v_{rms} = \sqrt{\sum_{i=1}^{N} \eta_i (v_i - \bar{v})^2} \tag{4.29}$$

The turbulence intensity parameter is the ratio of the velocity fluctuation to the mean velocity and is given by:

$$T(u) = \frac{u_{rms}}{\bar{u}} \cdot 100\% \qquad T(v) = \frac{v_{rms}}{\bar{v}} \cdot 100\% \tag{4.30}$$

The statistical quantities of skewness and flatness are given by:

$$S(u) = \frac{1}{u_{rms}^3} \sum_{i=1}^{N} \eta_i (u_i - \bar{u})^3 \qquad S(v) = \frac{1}{v_{rms}^3} \sum_{i=1}^{N} \eta_i (v_i - \bar{v})^3 \tag{4.31}$$

$$F(u) = \frac{1}{u_{rms}^4} \sum_{i=1}^{N} \eta_i (u_i - \bar{u})^4 \qquad F(v) = \frac{1}{v_{rms}^4} \sum_{i=1}^{N} \eta_i (v_i - \bar{v})^4 \tag{4.32}$$

Finally, the cross-moments, which are proportional to the Reynolds stresses, are calculated by:

$$\overline{u'v'} = \overline{uv} - \bar{u}\bar{v} = \sum_{i=1}^{N} \eta_i (u_i - \bar{u})(v_i - \bar{v}) \tag{4.33}$$

4.5.3 Independent samples

In all the equations above the weighting factor η_i is used. If the samples are statistically independent the weighting factor is equal to the arithmetic mean:

$$\eta_i = \frac{1}{N} \tag{4.34}$$

Statistically independent samples can be obtained by using low concentrations of seeding particles in the flow. The time between bursts must at least exceed the integral time scale, τ_i, of the flow by a factor of two [Durst et al. (1981)]. The reason for this is that the integral time scale represents the time scale over which velocity fluctuations are correlated with themselves. Thus, velocity samples obtained within one integral time scale of one another will often not be statistically independent. One problem though, is to estimate the integral time scale. Often, it requires a high number of samples to obtain a good estimate of the integral time scale. To avoid a large total sampling time, measurements with high concentration of seeding particles should be employed. So basically, one needs high concentration to determine τ_i, but then the samples might not be statistically independent. One solution to this contradiction is to do preliminary measurements with a high seeding concentration in the flow you wish to study, to obtain τ_i, and then to remove the seeding particles from the flow, or to exchange the fluid with one having a low seeding concentration. Then, statistically independent sampling can be obtained on the flow with a known integral time scale.

Some processors, including our Burst Spectrum Analyzer, feature a **dead-time mode** (not employed in the present work) as an option of achieving statistically independent samples. Dead time is a specified time period after each burst during which the processor ignores further bursts. If the dead time is set to $2\tau_i$, the criteria for statistically independent sampling are satisfied [Dantec reference guide (2000)].

4.5.4 Number of samples required for obtaining statistically reliable measurements

The number of samples needed is associated with the above discussion of integral time scale. The integral time scale can be estimated by the way of length scales and velocity scales:

$$\tau_i = \frac{Length\ scale}{Velocity\ scale} \tag{4.35}$$

The sampling frequency is selected to be the inverse of the integral time scale:

$$Sampling\ \ frequency = \frac{1}{2\tau_i} \tag{4.36}$$

The number of samples needed to obtain measurements with a specified error within a desired confidence level can be decided. The maximum error of estimate of a large (N>30) random sample defined in Miller et al. (1990) is given by:

$$E = Z_{\alpha/2} \cdot \frac{\sigma}{\sqrt{N}} \tag{4.37}$$

In Equation 4.37, $Z_{\alpha/2}$ is the standardized mean associated with a specified probability or confidence 1-α and σ is the standard deviation. Miller et al. (1990) give the values of $Z_{\alpha/2}$ for different confidence intervals. For instance, if one can assert with 99% confidence that the error is at most equal to E, the corresponding standardized mean is $Z_{0.005} = 2.575$. Solving Equation 4.37 for N gives the number of samples:

$$N = \left(\frac{Z_{\alpha/2}}{E} \right)^2 \cdot \sigma^2 \tag{4.38}$$

Instead of using the standard deviation, it is equally common to use the variance σ^2. The disadvantage of this estimate is that the standard deviation or the variance of the sample has to be known. An estimate of the variance can be obtained by preliminary

LDA measurements. As an example, consider LDA measurements of a flow with a mean velocity of 1.5 m/s conducted in a pipe with inner diameter equal to 56 mm. The integral time scale of the system is estimated to τ_i = 0.056 / 1.5 = 0.037 s. The appropriate sample frequency then becomes 13 Hz. Assume that it is desirable to obtain measurements of mean values with a maximum error of 0.015 m/s (E=0.015) with a probability or confidence of 99%. If preliminary LDA experiments show that the turbulence intensity is 20 % of the mean, which according to Equation 4.38 corresponds to a variance of 0.09 m^2/s^2, the required sample size is:

$$N = \left(\frac{2.575}{0.015} \right)^2 \cdot 0.09 = 2652$$

With a sample frequency of 13 Hz the total averaging time becomes 204 seconds.

Another procedure for the determination of the number of samples required for reliable measurements is based on experience. The procedure is to measure the same flow conditions with an increasing number of samples until the desired variables are not altered anymore. In general from 1000 to a few thousand samples is often sufficient for calculating the mean velocity. When other quantities, like for instance cross-moments, are desired the number of samples required often exceeds 10000 and sometimes 100000 [Dantec reference guide (2000)]. Depending on the optical conditions in the flow it can be time consuming to achieve such a high number of samples. Both the time aspect and the fact that the laser tube itself has a specified lifetime, and is expensive to replace, suggest that the number of samples should not be higher than that which is absolutely necessary.

4.5.5 Velocity bias and bias correction

In many cases though, the use of Equation 4.34 will bias or displace the results. It may not be possible to achieve statistically independent samples for a number of reasons. According to McLaughlin and Tiederman (1973) velocity bias will occur in turbulent flows because a larger than average volume of fluid, and hence also a larger than average number of tracer particles, pass through the control volume during periods

when velocity is faster than the mean. The opposite is the case when the velocity is lower than the mean. This leads to the probability of measuring higher velocities than the mean exceeds the probability of measuring lower velocities than the mean. Thus, the use of arithmetic averaging will bias the results in favour of higher velocities. One way to compensate for this is to give fast particles less statistical weight than slow ones. This is often referred to as velocity bias-correction. Several investigators have contributed to the subject of bias correction, and among them are Durão, Laker and Whitelaw (1980) and Kusters et al. (1990). The most used method is called transit time weighting. The weighting parameter is expressed by:

$$\eta_i = \frac{t_i}{\sum_{j=0}^{N-1} t_i} \tag{4.39}$$

where t_i is the transit time of the particle crossing the control volume.

Durão, Laker and Whitelaw (1980) also reported of another type of bias. They called it photo multiplier bias, and found that it had the opposite effect of velocity bias. The basic explanation is that photo multipliers detect a proportionally larger number of lower-velocity signals. In several different flow measurements they found the two biases to be of the same order of magnitude, and hence cancelling each other out. The main conclusion from their work is that the removal of velocity bias will only lead to correct results if the photo multiplier bias is negligible. They also state that photo multiplier bias is reduced if the sampling rate is low.

Durão et al. (1982) compares velocity bias and amplitude bias. They classify photo multiplier effects, laser power, turbulence intensity and presence or absence of frequency shift as contributors to amplitude bias. The reason for the term ‘amplitude’ bias is that signal amplitudes of high velocity seeding particles in some cases are smaller than amplitudes for low velocity particles. This will bias the measurements in favour of lower velocities.

Erdmann and Tropea (1982) found the magnitude of bias errors to be less than 0.2% of the true mean velocity for a flow with 5% turbulent intensity. In a flow with 40% turbulence, errors up to 10% were detected. Durão et.al (1982) estimated the errors of statistical bias to never exceed 6% in the mean velocity or 10% in the corresponding rms-values for a range of flows with 5-25% turbulence intensity. However, these quantifications should not automatically be transferred to all systems.

CHAPTER 5:
GAMMA DENSITOMETRY

5.1 INTRODUCTION

Gamma densitometry, sometimes referred to as the gamma-ray attenuation technique, can be used to determine void fractions as in the work of Bøe (1997) and Åbro (1999). The method is also useful for determination of local phase fractions in liquid-liquid flows. In this work, a traversing gamma densitometer is used to determine the local water fraction (and oil fraction) in oil / water flow. Flow pattern identification is carried out using the results in combination with visual observations.

Gamma densitometers are also employed for field measurements of phase fractions in offshore pipelines. Among other things, information of phase fractions is important in multiphase mass flow metering.

The gamma-ray attenuation technique basically makes use of the observation that a stationary homogeneous material will absorb a monochromatic beam of constant intensity and short wavelength radiation. The absorption occurs exponentially with increasing absorption length at constant linear absorption coefficient. Thus, the exponential law can be defined by:

$$\frac{I(x)}{I_0} = \exp\left(-\gamma x\right) \tag{5.1}$$

where I(x) is the local intensity of the beam photons [counts/sec], I_0 is the incident intensity of the beam photons [counts/sec], x is the absorber thickness [m] and γ is the linear absorption coefficient [m^{-1}]. Equation (5.1) is valid only for the ideal case of a thin collimated beam.

In principle this technique is very simple. A suitable source of radiation is collimated to produce an incident unidirectional photon flux normal to the test section (see flow

charts described in Chapter 3). The beam is then attenuated through the pipe wall, the two-phase mixture and the opposite pipe wall before it is received by the detector collimator and finally the detector itself.

5.2 BASIC PRINCIPLES

Imagine a narrow beam of single energy γ–rays of intensity, I_0, passing through a homogeneous material of density, ρ, as illustrated in Figure 5.1.

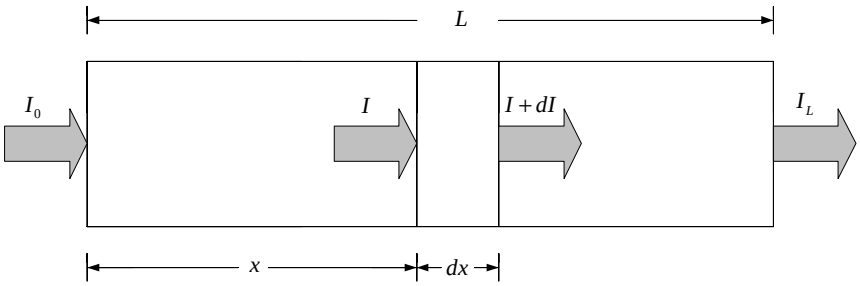

Figure 5.1 Attenuation of a gamma beam.

The rate of attenuation of such a beam is proportional to the beam intensity I and to the density of the medium:

$$\frac{dI}{dx} \propto \rho I \tag{5.2}$$

or

$$\frac{dI}{dx} = -\mu \rho I \tag{5.3}$$

where the constant of proportionality μ is called the mass absorption coefficient, and is a function of both the material and the energy of the gamma photon.

Furthermore the linear absorption coefficient included in Equation 5.1 γ is defined, which depends upon the composition of the absorber and is a function of the photon energy. It is related to the total atomic absorption cross section by the following equation:

$$\gamma = \mu\ \rho = \frac{N_A \rho}{A}\sigma \tag{5.4}$$

where N_A is the Avogadro Number [$6.022 \cdot 10^{23}$], A is the atomic mass number [kg/kmol], ρ is the absorber density [kg/m^3] and σ is the atomic absorption cross section [m^2/mol].

Since $I=I_0$ at $x=0$, integration yields:

$$\ln\left(\frac{I_0}{I}\right) = \mu \rho x \tag{5.5}$$

or

$$I = I_0 \exp(-\mu \rho x) = I_0 \exp(-\gamma x) \tag{5.6}$$

which is identical to Equation 5.1. Therefore, for a known material and a given gamma energy, the thickness x can be determined from knowledge of the intensity of the gamma beam. Similarly, for a system made of two materials of a known overall geometry, it is possible to determine the different thickness of each material using a gamma beam of a particular energy. In this case:

$$I = I_0 \exp(-\gamma_1 x_1 - \gamma_2 x_2) \tag{5.7}$$

where I_0 is the incident gamma-ray intensity not absorbed by the wall. Subscripts 1 and 2 denote the two different materials.

For a known geometry (i.e. when $x_1 + x_2$ is known), the amount of each material can be calculated. A more detailed analysis of how this can be adapted to multiphase systems can be found in Petrick and Swanson (1958) and in the thesis of Pan (1996).

If water (subscript w) and oil (subscript o) are used as absorbing materials, Equation 5.7 can, in terms of water hold-up ε_w, be expressed by:

$$I = I_0 \exp\left[x(-\gamma_w \varepsilon_w - \gamma_o(1-\varepsilon_w))\right] \tag{5.8}$$

or

$$\varepsilon_w = \frac{\ln\left(\frac{I_0}{I}\right)/x - \gamma_o}{\gamma_w - \gamma_o} \tag{5.9}$$

The absorption coefficients γ_o and γ_w can be obtained by calibration of the system with scans of single-phase oil and water. The attenuation equation for both single-phase scans when substituted into Equation 5.9 becomes:

$$\varepsilon_w = \frac{\ln\left(I/I_o\right)}{\ln\left(I_w/I_o\right)} \tag{5.10}$$

where I is the measured intensity for a given oil/water mixture, I_o the calibrated intensity for oil and I_w the calibrated intensity for water.

Note that I_0, the incident gamma-ray intensity that is not absorbed by the wall, defined in Equation 5.5 has cancelled out, and thus no knowledge about the wall is required for measurements of water hold-up.

The particular instrument used for these measurements as a tool for obtaining phase distribution profiles, is a traversing single-energy gamma densitometer as shown in Figure 5.2. The source collimator is a 3 mm circular slot, while the detector collimator is a 3 x 10 mm rectangular slot (3 mm height and 10 mm width), which enable increased accuracy of the readings in the horizontal plane. The instrument uses step motors, one linear and one angular, which enables rotation of the beam as well as vertical (linear) movement across the pipe to obtain an average density profile or grid inside the test section in consideration. The operation of the instrument is carried out using an in house LabVIEW™ programme.

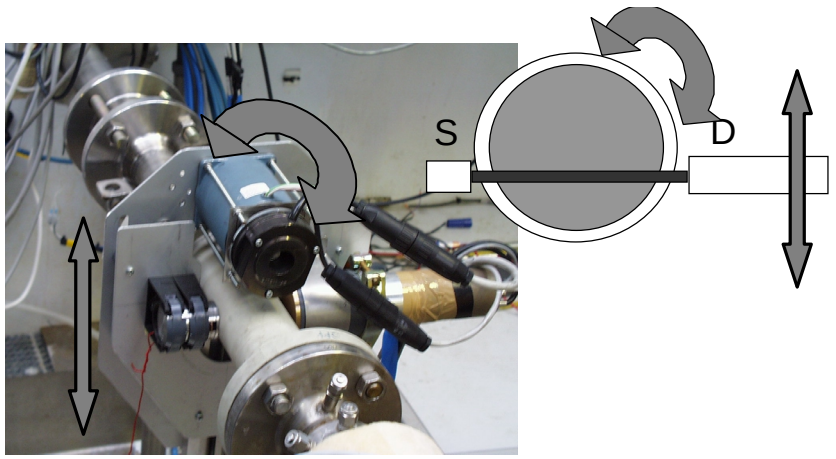

Figure 5.2 The traversing gamma densitometer.

Figure 5.3 shows typical raw data from the gamma instrument. Here, the beam starts just outside the bottom of the pipe (position = - 45 mm) and works its way to the top (position = + 37 mm). The solid lines represent the single-phase calibration scans (obtained by running single-phase oil and water through the test section) while the markers represents two-phase oil/water flows. The number of counts (or intensity) received is plotted in the y-axis of the graph and the linear (vertical) position of the pipe is plotted in the x-axis.

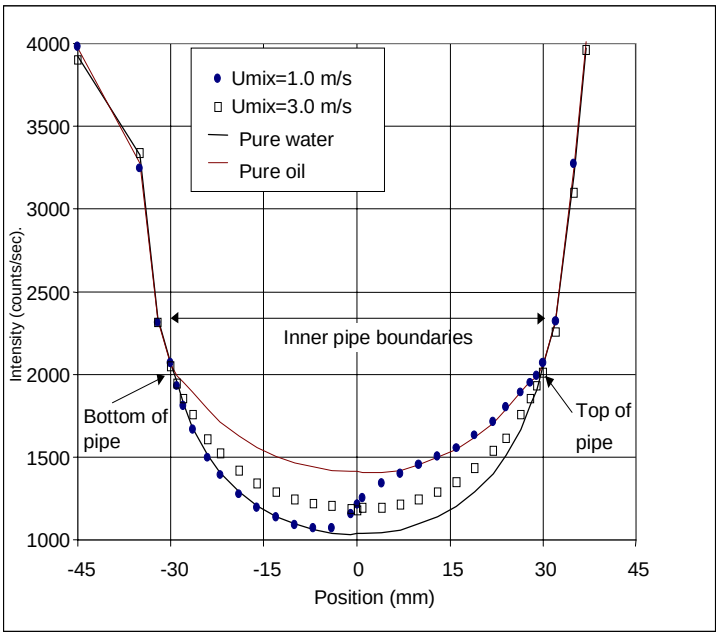

Figure 5.3. Calibration gamma scans for oil and water.

Since the densities before entering the inside of the pipe are equal at the bottom and at the top of the pipe section (provided there is a constant thickness pipe wall), the intensity should be equal before the marked position "Bottom of pipe" and after the marked position "Top of pipe". These marked positions on either side of the graph defines the boundaries of inner pipe wall. Thus, at this position, the whole beam is in the pipe wall, which means that the beam centre position is 1.5 mm outside the inner pipe wall. From this, it was found that the inner pipe wall extends from position -28.5 mm to 28.5 mm. As seen from Figure 5.3, different flow configurations can be observed. The two cases shown here represent two extremes: pure stratified and fully dispersed. From the stratified case it is evident that up to a position of -7 mm, the measured intensity equals pure water and from +7 mm it equals pure oil, hence, a

typical stratified flow. For the dispersed case the measured intensity is somewhere in-between pure water and pure oil throughout the entire cross section.

By converting the data given in Figure 5.3 using Equation 5.10 we obtain data as shown in Figure 5.4. Here, the non-dimensional position is given on the y-axis and water fraction is given on the x-axis, as if the pipe is seen from the side.

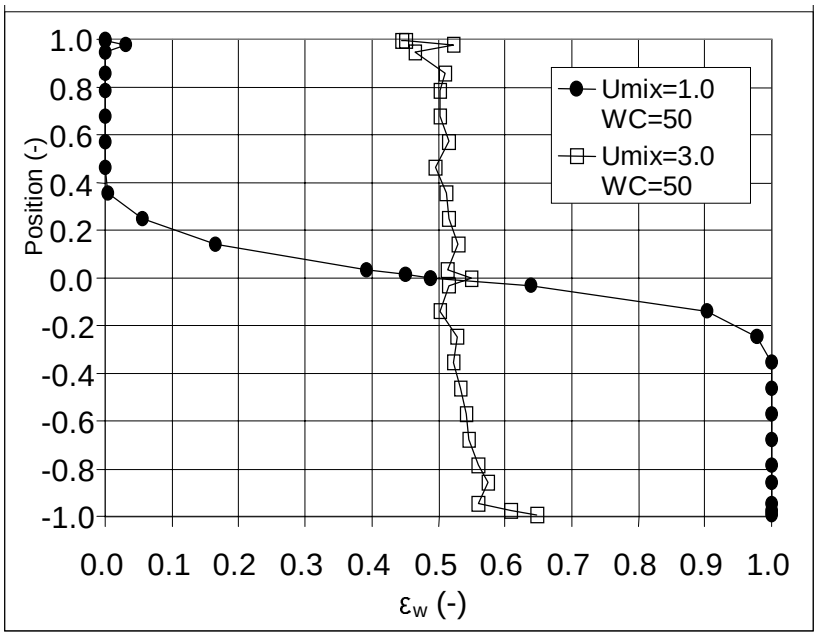

Figure 5.4 Gamma densitometer scans of stratified and dispersed flow.

For the stratified case, the interface (where the water fraction rise from zero to unity) covers about 30% of the pipe diameter almost symmetrically about the pipe centre (which is expected due to 50% water cut). For the dispersed case, a larger concentration of water is located at the bottom of the pipe than at the top (due to gravity).

When observing these curves to determine the flow pattern, one must keep in mind that these are taken by a 3 mm wide beam. Thus, close to the wall a major part of the

beam will still penetrate it and measurements will be very inaccurate in this region. This means that if there is a thin water or oil layer present at the inner pipe wall, it will be difficult to detect it from the gamma scans.

5.3 INSTRUMENTAL SETUP AND SIGNAL PROCESSING

The instrument contains the following main elements:

- A collimated radioactive source (Am^{241}, 45 mCi)
- A photo multiplier tube (PMT) with bias supply and preamplifier
- A signal amplifier and delay line amplifier (DLA)
- A single channel analyser (SCA)
- A multi-channel analyser (MCA)
- A counting system (PC with a specific data acquisition card)

The overall setup is given in Figure 5.5. Figure 5.6 displays a sketch of the typical signal outputs at each stage in the form that can be seen if an oscilloscope is used.

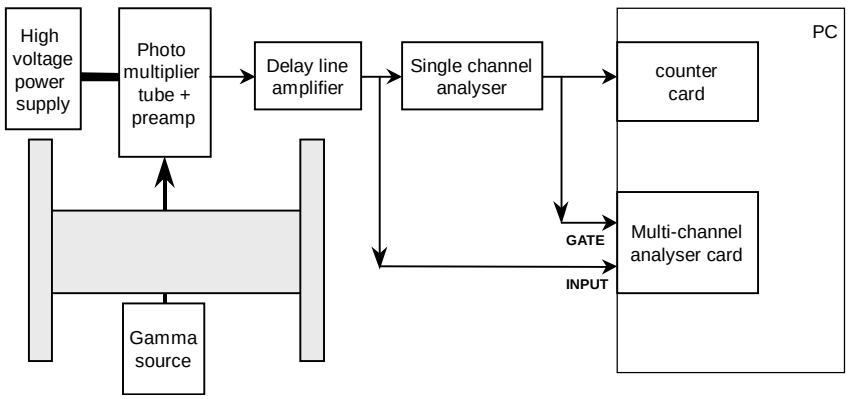

Figure 5.5 Overall setup of the instrument.

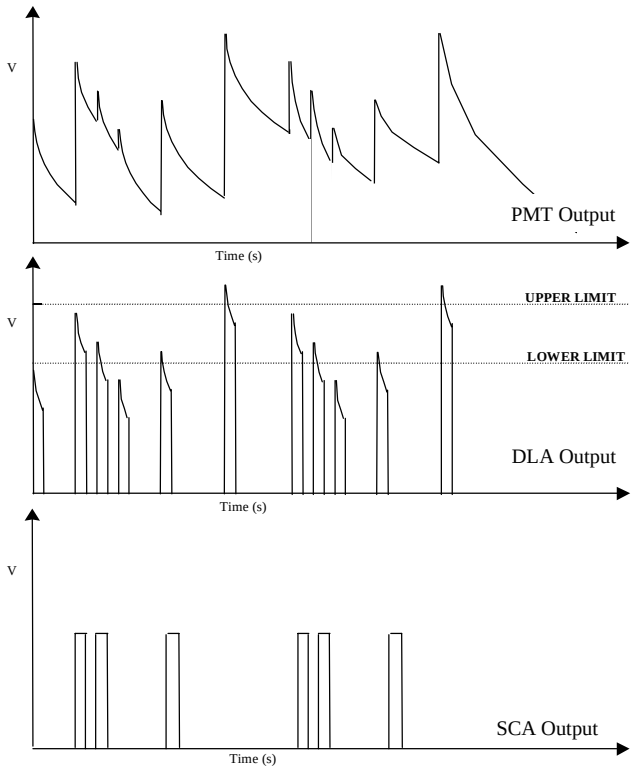

Figure 5.6 Signal outputs for the different electronic components.

Photo multiplying tube with bias supply and preamplifier

Each photon that enters the photo multiplier tube (PMT) creates a step peak in the output voltage, directly related to the energy of the photon. This voltage decreases, exponentially to zero unless another photon creates another peak. Since this signal is very small a preamplifier is used to enlarge it enough to be transmitted through the connecting cables. Care must be taken in setting the level for the bias supply. If this is set too high, the PMT reaches what is known as saturation, and the output voltage reaches a maximum, see Figure 5.7. If the bias supply is set above this region there is no longer a relationship between the voltage of the peak and the gamma energy, making single energy analysis impossible.

Delay line amplifier

A delay line amplifier (DLA) is used to amplify the signal further and to remove the tails from each of the photon detection signals, turning them into discrete electronic pulses of the type that could be easily counted electronically. The peaks at this stage are still related to the energy of the gamma photon pulse.

The amplification gain for the DLA needs to be set carefully. The gain has a similar effect to the bias supply on the shape of the voltage spectrum leaving the DLA, namely the higher the gain is set, the more the spectrum is stretched along the x-axis, see Figure 5.8. Regular checks are needed to make sure the value of the gain is set correctly, since the PMT always is subject to drift.

Single channel analyser

For the use of single energy gamma densitometry the signal from just one gamma energy is required in order to use Equation 5.10 to calculate the water cut. This filtering is done in the Single Channel Analyser (SCA), which removes all peaks outside of a particular range. Figure 5.6 shows, on the DLA output where the upper and lower limits have been set for the SCA. As can be seen, only signals that peak inside those limits are turned into digital pulses at the SCA output.

Multi-channel analyser

A Multi-channel analyser (MCA) is an important tool for viewing the emission energies from a radioactive material. In general, the MCA reads the electronic pulses leaving a DLA and counts the number of peaks in particular energy bands. It then plots a histogram of number of counts versus energy. This is called the spectrum of the source. This spectrum is constantly updated until a maximum number of counts have been reached. Figure 5.9 shows a sketch of the spectrum of Americium 241, which has a strong peak at 59.5keV and a smaller one in the x-ray range. Also shown in the figure are the typical settings for the upper and lower limits of an SCA in order to count only the single energy of interest.

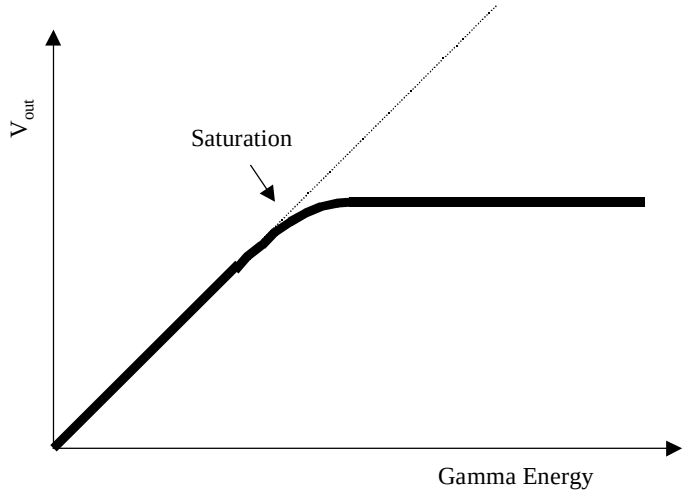

Figure 5.7 Saturation of PMT.

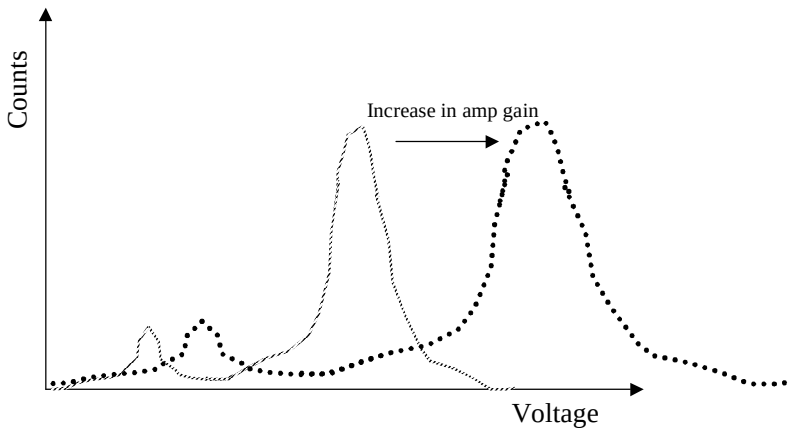

Figure 5.8 Effect of DLA gain on the gamma source spectrum.

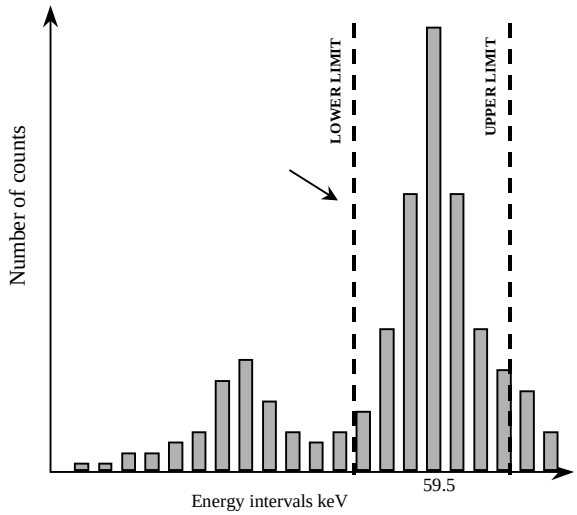

Figure 5.9 Multi-channel analyser - Am^{241} spectrum.

5.4 ERROR ANALYSIS

Errors in phase fraction measurements occur from two main sources. The first one is the fundamental statistical uncertainty that exists due to the random nature of photon emission by radioactive sources. This error is called the random photoemission error. The fractional standard deviation σ_{sd} is given by:

$$\sigma_{sd} = \sqrt{1/N} \tag{5.11}$$

where N is the total number of counts. The fractional standard deviation decreases with increasing source strength and/or counting time. This gives a fundamental restriction on the speed at which data can be acquired.

The second source of error arises if the void fraction is fluctuating with time. Then the exponential nature of the absorption relationship gives a bias in the averaging [Hewitt (1982)]. Equation 5.10 shows that the water hold-up is a linear function of the *natural*

logarithm of the count rate. The average water hold-up is therefore a function of the *average* natural logarithm of the count rate (not the logarithm of the average count rate, something that is mathematically different). Having many short count times for one position, taking the natural logarithm of each count, then averaging, reduces this error. However, such short count times will increase the error from random emissions and hence a compromise has to be reached when calculating time-averaged phase fractions in transient flow patterns such as slug flows.

For quasi-steady flow systems such as stratified or annular flow, where time fluctuations of phase fraction due to events such as waves or droplet transport are small, only the random photoemission error dominates. Pan (1996) has calculated this error to be:

$$\delta\alpha_1 = \frac{\pm 1}{(\mu_w\rho_w - \mu_o\rho_o)H\left\{\, tI_0 \exp\left[-\mu_{wall}\rho_{wall}x_{wall} - (\mu_w\rho_w\varepsilon_w + \mu_o\rho_o(1-\varepsilon_w))H\right]\right\}} \quad (5.12)$$

where γ is the linear absorption coefficient, μ the mass absorption coefficient, ρ the density, ε the fraction, x the fractional thickness, H the total height (wall + oil + water) and I_0 the initial intensity (or count rate per unit time). Subscript *w* denotes water and *o* denotes oil.

As seen from Equation 5.12 a total number of eleven parameters determine the actual error. However, the mass absorption coefficients are dependent on the gamma energy, so for a fixed system (fluids and gamma source) the error is determined by nine independent parameters.

Below, the effects of some of the parameters on this error are outlined. All error sources are shown relative to a test case that has an error of 1%.

Choice of radioactive source

The mass absorption coefficient changes not only with material but also with energy of the incident gamma ray. Pan (1996) correlated the mass absorption coefficient as a

function of gamma energies for oil and water, from the data given by Grodstein (1957). These are given by:

$$\mu_{oil} = 0.1\exp(-14.794762 + 89.049017\ln\ln E - 164.299552(\ln\ln E)^2 + 131.5987(\ln\ln E)^3 - 48.73664(\ln\ln E)^4 + 6.813107(\ln\ln E)^5) \quad (5.13)$$

$$\mu_{water} = 0.1\exp(-60.439566 + 261.844766\ln\ln E - 408.63705(\ln\ln E)^2 + 296.81687(\ln\ln E)^3 - 102.856866(\ln\ln E)^4 + 13.736626(\ln\ln E)^5) \quad (5.14)$$

where E is the gamma energy with unit [keV].

From these mass absorption coefficients a linear absorption coefficient γ as a function of energy from the gamma source can be calculated. Figure 5.10 displays this relation. The effect of gamma energy on the error is displayed in Figure 5.11.

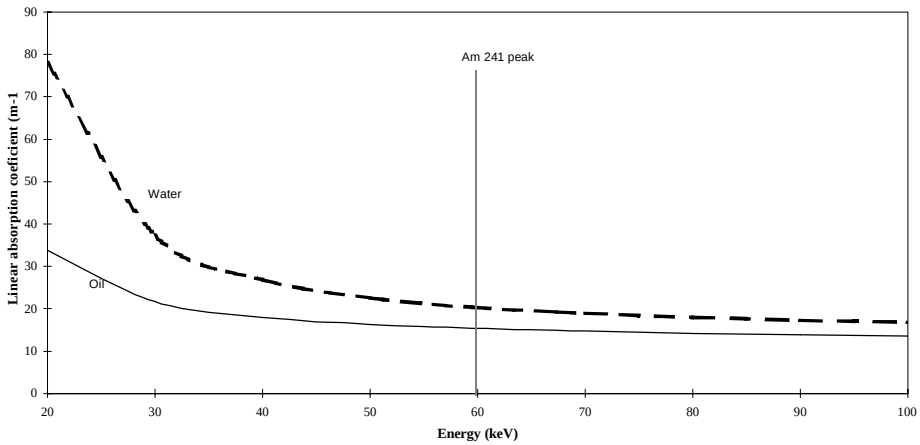

Figure 5.10 Linear absorption coefficients of oil and water.

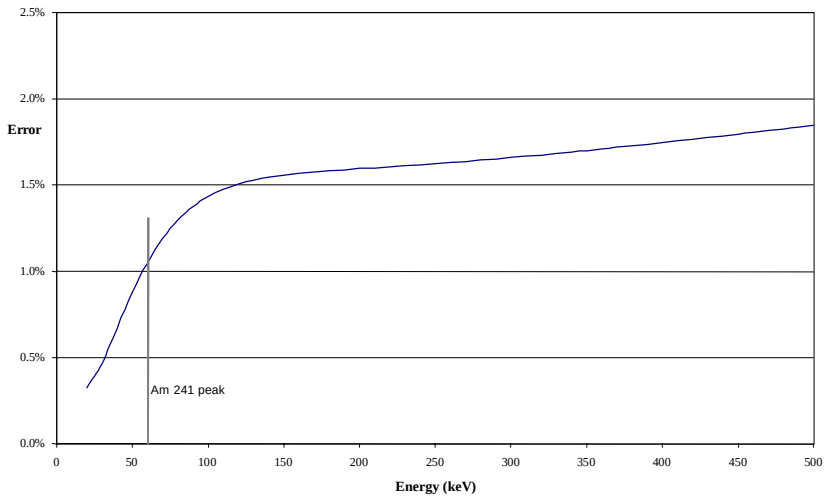

Figure 5.11 Effect of gamma energy on error.

As can be seen, the main peak for Americium (59.5keV) shown in the plot appears half way up a sharp increase in the error to energy slope. This shows that sources with lower energy would be unsuitable for oil-water studies.

Counting time

As with all random nuclear emissions, the number of counts taken over a certain period of time will have a standard deviation equal to the square root of the average number of counts as given by Equation 5.11. For obtaining measurements with low error, a large number of counts are required. This is shown in Figure 5.12.

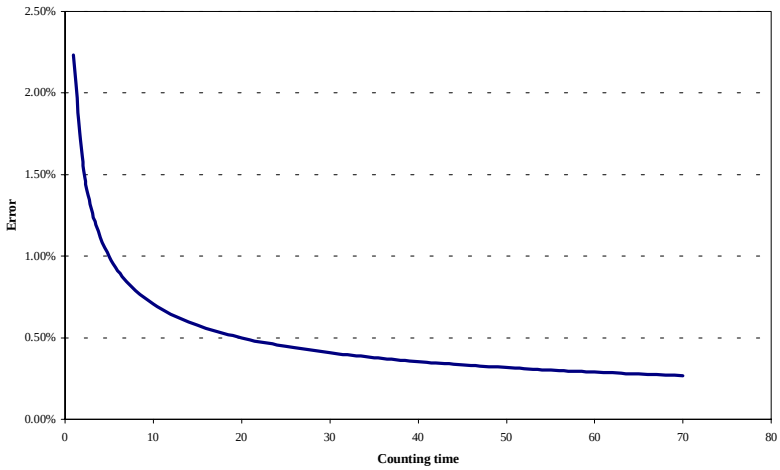

Figure 5.12 Effect of counting time on error.

Beam position

The present system transmits a 3 mm wide, parallel beam from a collimated source to a collimated detector. This system is then traversed span-wise across the pipe cross section. As can be seen in Figure 5.13, two different beam positions will indicate different thickness for the wall and the liquid. Therefore, the error for these two positions in the same counting time will be different.

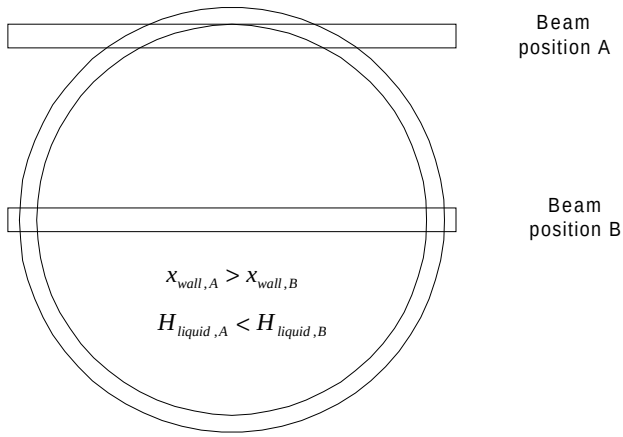

Figure 5.13 Comparison of two different beam positions.

In order to study this effect, it is necessary to calculate a beam average wall and liquid "thickness" that the beam passes through. Consider a beam of thickness b passing through a circle of radius r_{int} at a distance x' from the centre position as illustrated in Figure 5.14.

An average liquid thickness across the thickness of the beam can be calculated by dividing this area by the beam thickness b (Watson (1989)). In the equations below θ is in radians and is indicated in Figure 5.14:

$$\overline{H_{LIQ}} = \frac{r_{\text{int}}^2}{2b}\left[\sin(2\theta) + 2\theta\right]_{\arcsin\left(\frac{x'}{r_{\text{int}}}\right)}^{\arcsin\left(\frac{x'+b}{r_{\text{int}}}\right)} \tag{5.15}$$

Similarly for the wall:

$$\overline{H_{WALL}} = \frac{r_{ext}^2}{2b}\left[\sin(2\theta) + 2\theta\right]_{\arcsin\left(\frac{x'}{r_{ext}}\right)}^{\arcsin\left(\frac{x'+b}{r_{ext}}\right)} - \frac{r_{\text{int}}^2}{2b}\left[\sin(2\theta) + 2\theta\right]_{\arcsin\left(\frac{x'}{r_{\text{int}}}\right)}^{\arcsin\left(\frac{x'+b}{r_{\text{int}}}\right)} \tag{5.16}$$

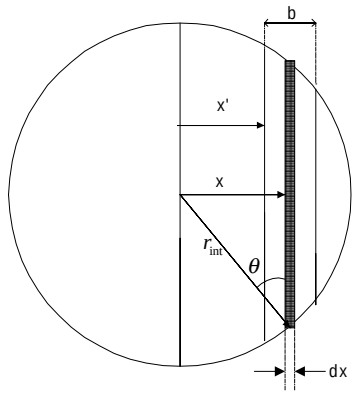

Figure 5.14 Calculation of average liquid thickness.

From these equations an estimate of the error for a 3 mm beam as a function of distance from the pipe wall can be calculated. This is shown in Figure 5.15. The largest error (for a constant counting time) is when the 3 mm beam is only exposed to 1 mm of the internal pipe (the rest of the beam passes through the wall).

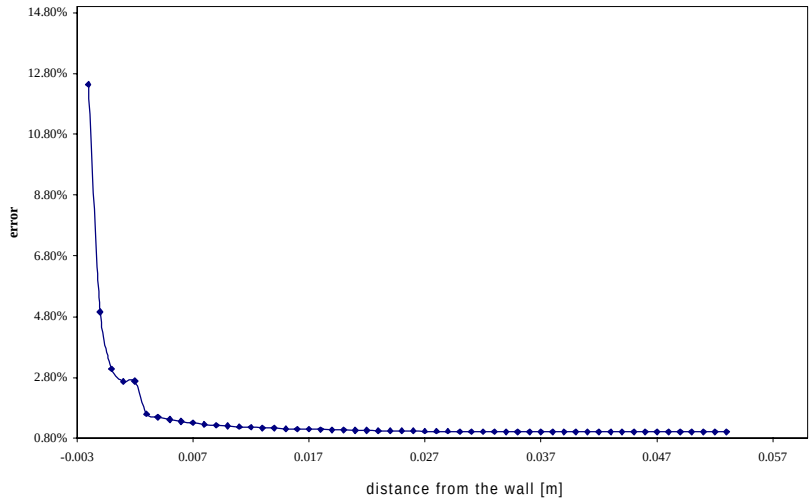

Figure 5.15. Effect of position on error.

CHAPTER 6:
FLOW PATTERN EXPERIMENTS

6.1 FLOW PATTERN DEFENITIONS

In the following sections flow pattern (or flow regime) experiments carried out in the Model Oil Facility (MOF), see Chapter 3.1, are outlined and discussed. A model oil, Exxsol D-60, and water are introduced into the horizontal test section by the mixture unit described in Figure 3.3. For observation of flow patterns a 0.8 m long plexiglass section with 2" inner diameter is located 10.5 m downstream the mixing unit. The measurements of flow patterns are carried out by a traversing gamma densitometer placed 1.5 m further downstream.

As discussed in Chapter 2.1 a number of parameters such as physical fluid properties (density, viscosity, surface tension), flow geometry (pipe diameter, mixing unit), wetting properties (pipe material) and operating temperature and pressure can influence the formation of flow patterns. In this study all of the above parameters are fixed (only small variations in temperature and pressure exists). Only mixture velocity and input water cut are varied. These variables are defined by:

$$U_m = \frac{Q_o + Q_w}{A} \tag{6.1}$$

$$C_w = \frac{Q_w}{Q_o + Q_w} \tag{6.2}$$

The experiments are carried out at constant mixture velocities with variations of input water cut from 10 to 90%. The different flow patterns that appear are classified by use of visual observations, video camera recordings and gamma densitometry. Visual observations and video camera recordings are done in the transparent part of the pipe while gamma densitometer scans are conducted further downstream as mentioned above. The flow experiments are recorded for about one minute.

The flow patterns observed can be categorized in two main classes. Stratified flows (Figures 6.1-6.3) and dispersed flows (Figures 6.4-6.9).

Stratified flow

Stratified flows are flows where the oil and water are completely separated. Some dispersion (droplets of one phase in the other) may occur at the interface but in general the phases flow separately.

Stratified smooth (SS) flow shown in Figure 6.1, appears at low mixture velocities and intermediate water cuts, and is characterized by a smooth interface with no droplets and only small waves. By increasing the mixture velocity or by introducing low or high water cuts, larger amplitude waves will start to appear at the interface and droplets of oil in water and water in oil may occur near the interface. This flow pattern is defined as *stratified wavy* (SW) and is shown in Figure 6.2.

At higher flow rates the interface becomes even wavier and a large number of droplets exists. The droplets are formed by break-up of the interfacial waves but are still kept close to the interface since neither of the phases contains sufficient energy to distribute the droplets across the pipe. Such a flow pattern is defined as *stratified mixed* (SM). Mixed, because the phases being mixed with droplets near the interface. Stratified mixed flow has three appearances shown in Figure 6.3a to c. The droplets can appear as water dispersed in oil (a), oil dispersed in water (b) or both (c). From now on it will not be distinguished between these three cases.

Dispersed flow

Dispersed flows are flows in which one phase is either fully or partially dispersed in the other. In other words, when one of the phases is no longer continuous, but rather exists as droplets flowing in the continuous phase, the flow is in the dispersed flow category. Depending on flow conditions several forms can appear.

Under certain conditions (i.e. at low water cut and intermediate mixture velocity), a dense packed layer of water droplets may appear near the pipe wall. This is shown in

Figure 6.4. The dispersed water droplets are so closely packed that it looks like a layer. Because the mixture velocity is relatively low, the droplets avoid being distributed across the pipe cross section. This pattern is called an *oil continuous dispersion with a dense packed layer of water droplets* (Do-DP). This pattern occurs only at low water cuts and sufficiently high mixture velocity for formation of water droplets. The thickness of the DP layer varies with time and has a wavy character. It is believed that effects due to gravity forces and surface tension overcome the distribution properties of the turbulence in the continuous phase. At the same mixture velocity one may go from a SM pattern to a Do-DP pattern by lowering the water cut sufficiently. In other words, transformation from a stratified flow pattern to a dispersed flow pattern occurs by lowering the water cut alone.

At high water cuts a similar dense packed layer of oil droplets may occur. This pattern is defined as a *water continuous dispersion with a dense packed layer of oil droplets* (Dw-DP) and is presented in Figure 6.5. For such a pattern to appear, the mixture velocity must be high enough to disperse the oil yet low enough to avoid distribution. For SM flow with a proper mixture velocity the Dw-DP pattern is obtained by increasing the water cut sufficiently. Trallero et al. (1997) also identified such a pattern and called it a dispersion of oil in water and water (Do/w & w). Nädler and Mewes (1997) named it an oil-in-water dispersion above a water layer. Arirachakaran et al. (1989) classifies it as mixed layers (a mix of stratified and dispersed) of a dispersion and a “free” phase.

By further increasing the mixture velocity the DP layer will break up and droplets are distributed across the pipe as a consequence of the turbulent motion of the continuous flow. The flow now becomes fully dispersed. An *oil continuous dispersion with an inhomogeneous distribution of water droplets* (Do-I) will eventually appear if mixture velocity is increased in a Do-DP flow. This pattern is shown in Figure 6.6. Similarly a *water continuous dispersion with an inhomogeneous distribution of oil droplets* (Dw-I) shown in Figure 6.7 appears if the mixture velocity is increased in a Dw-DP flow. At very high mixture velocities the distribution of droplets becomes homogeneous across the pipe. A *homogeneous oil continuous dispersion* (Do-H) and a *homogeneous water continuous dispersion* (Dw-H) are shown in Figure 6.8 and 6.9, respectively.

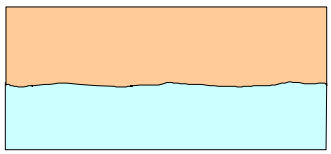

Figure 6.1 Stratified Smooth (SS).

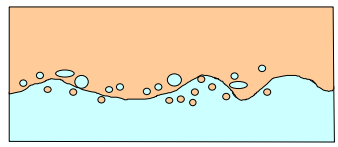

Figure 6.2 Stratified Wavy (SW).

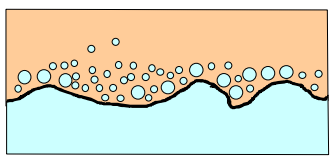

Figure 6.3a Stratified Mixed (SM) with water droplets in oil.

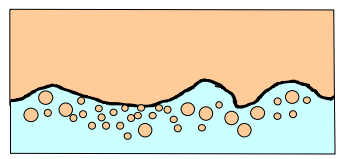

Figure 6.3b Stratified Mixed (SM) with oil droplets in water.

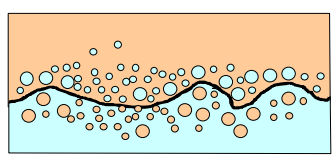

Figure 6.3c Stratified Mixed (SM) with droplets of both water in oil and oil in water.

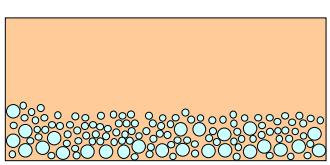

Figure 6.4 Oil continuous dispersion with dense packed layer of water droplets(Do-DP).

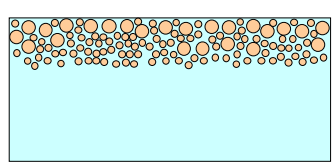

Figure 6.5 Water continuous dispersion with dense packed layer of oil droplets (Dw-DP).

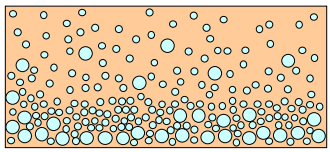

Figure 6.6 Oil continuous dispersion - inhomogeneous (Do-I)

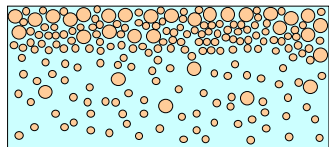

Figure 6.7 Water continuous dispersion – inhomogeneous (Dw-I)

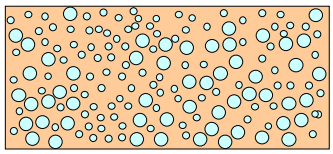

Figure 6.8 Oil continuous dispersion - homogeneous (Do-H)

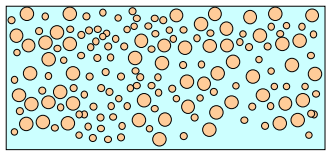

Figure 6.9 Water continuous dispersion - homogeneous (Dw-H)

6.2 MEASUREMENTS OF LOCAL PHASE FRACTION

Local phase fractions of oil and water in the pipe are measured with a traversing gamma densitometer according to the principles outlined in Chapter 5. This technique does not require transparent fluids as the LDA technique employed for velocity studies does. The gamma densitometer gives an average value over a certain time period, which in most cases is 10-15 seconds in each position, except during calibration, when the time period is 30 seconds. The raw gamma scans are calculated into water concentration profiles (x-axis) by Equation 6.3 and plotted versus the normalised pipe diameter (y-axis).

$$\varepsilon_w = \frac{\ln\left(I/I_o\right)}{\ln\left(I_w/I_o\right)} \tag{6.3}$$

6.2.1 Characteristic gamma densitometer scans for the various flow patterns

Measurements of local phase fractions or hold-ups are superimposed on still pictures from video camera recordings. The y-axis is scaled to fit the inner pipe diameter on the pictures. Keep in mind that these pictures are an instantaneous representation of the flow, while the video recordings show a highly dynamic behaviour. The gamma densitometer produces time-averaged values.

Most of the flow patterns defined in the previous section are well presentable as a picture. Homogeneous dispersions though, do not exhibit enough contrasts, and thus the picture of this flow pattern is of lower quality.

Figure 6.10 shows a typical stratified smooth (SS) flow pattern. As seen in the picture, oil and water is separated by a sharp interface. The top of the pipe consists of pure oil, and a 0% water concentration profile is obtained from the gamma scan. As the gamma instrument traverses down through the pipe diameter the water fraction suddenly rises to 100% when the oil/water interface is crossed, because pure water exists below this interface. The SS flow pattern is determined by the almost horizontal gradient of the curve at the interface of water and oil. Since the phase fraction curve displays a sharp increase from zero to unity (the nearly horizontal part) and the concentration of water at the bottom of the pipe reaches 100%, we can conclude that this flow pattern is stratified flow with little or no waves/droplets at the interface, even without using the picture. From the figure it is seen that the 0.5 water fraction (the core of the interface) lies slightly above the interface as it appears on the picture. In general for all the pictures the reason for these deviations may be explained by the dynamics of the interface. For Figure 6.10 this means that the interface has a certain wavy nature.

As the mixture velocity increases (an increase in energy input), the stratified wavy (SW) flow pattern displayed in Figure 6.11 appears. This gamma scan is very similar to the scan obtained in the Figure 6.10, but the interface region is broader than in the stratified smooth flow case. In other word, steeper gradients (i.e. steeper than the horizontal gradient) in the local phase fraction are seen in SW flows compared to that of SS flows. This is due to the waves and the entrained droplets around the interface.

When the interface is even more chaotic, that is when there are more droplets dispersed in both phases near the interface region and also larger amplitude waves, as shown in Figure 6.12, the pattern is defined as stratified mixed (SM). The gamma scan profile has an even steeper gradient at the interface than the SW flow. The interface region of such a flow can cover the major part of the pipe leaving only small continuous zones at the top and at bottom of the pipe. As seen from the concentration profile in Figure 6.12 about half the pipe is influenced by the interface.

Figure 6.13 shows a typical flow pattern of an oil continuous dispersion with a dense packed layer of water droplets (Do-DP). As expected, the gamma scan displays pure oil in the top part of the pipe. The dense packed layer consists of dispersed water droplets driven by the continuous oil phase. Thus, we do not observe pure water in the bottom of the pipe. The water concentration in this region is up to 80%. Furthermore, the concentration profile gradient at the interface is much steeper than for the stratified flow patterns described earlier. The height of the dense packed layer varies during the time period of each gamma measurement. The height seen on the picture is an average value (positions –0.10 to –1.0).

The gamma scan of the opposite flow pattern, the water continuous dispersion with a dense packed layer of oil droplets (Dw-DP), is shown in Figure 6.14. Water concentration equals unity in the lower half of the pipe, but falls to about 0.05 near the upper wall when the dense packed layer is passed. Pure oil is not observed in the top of the pipe. Similarly as for Do-DP flows the concentration gradient is determined by the height of the dense packed layer. With the naked eye, the dense packed layer looks like a layer of even concentration. However, the gamma scan shows that the concentration of oil falls through the whole layer from the wall towards the pure water layer.

The gamma scans of the inhomogeneous dispersions Do-I and Dw-I are shown in Figure 6.15 and 6.16. For this particular oil continuous case (Do-I), the concentration profile is zero from position 1.0 to 0.7. In the rest of the pipe the profile has a steep gradient and reaches 80% concentration at the bottom wall. The characteristic dense packed layer is not seen. The concentration profile for the water continuous (Dw-I)

case shows higher water concentration in the bottom (90%) compared to the oil continuous (Do-I). The curvature is also different, as can be seen from Figures 6.15 and 6.16. For water continuous dispersions the gradient of the concentration curve is reduced from bottom to top in the pipe. For oil continuous dispersions though, the gradient of the curve increases from bottom to top. The curvature difference in the gamma scans is helpful since it can be difficult to distinguish between Do-I and Dw-I with visual observations alone. The change of curvature in a water continuous dispersion compared to an oil continuous dispersion may perhaps be used to detect the phase inversion, that is, when the dispersion changes from being oil continuous to being water continuous. However, this is not a reliable method for predicting the phase inversion point.

Homogeneous dispersions appear only at high mixture velocities. The Do-H pattern is not seen in any of the experiments carried out in the model oil facility. The reason is the limitations in the delivery from the oil-pump. In this work, dispersions are classified as homogeneous when the concentration curve looks something like the one presented in Figure 6.17 for a Dw-H flow. Here, the water concentration is between 85 and 95% in all positions. Constant liquid fractions are not seen in any of the experiments. The water continuous dispersion shown in the figure is not well displayed as a picture. The reason is that droplet concentration is too high and the droplet sizes too low for any contrasts to appear in a picture. To distinguish between inhomogeneous and homogeneous dispersions without the use of the gamma densitometer would have been difficult.

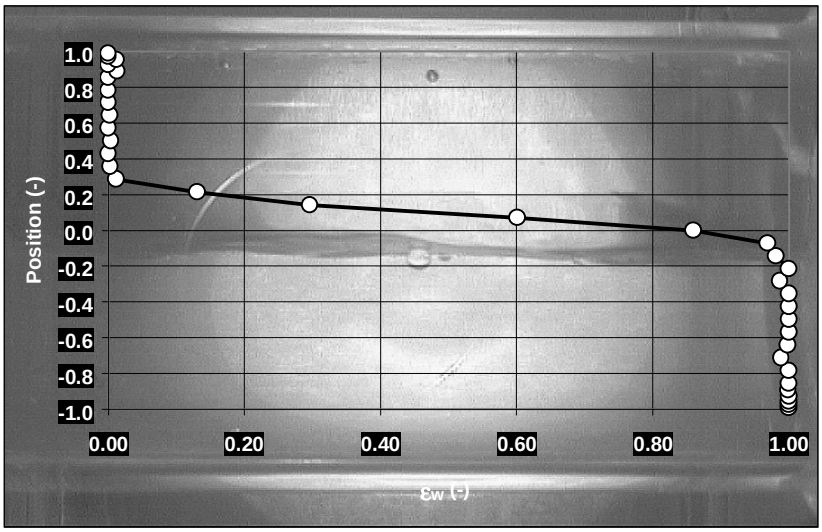

Figure 6.10 Stratified smooth (SS) flow at a mixture velocity of 0.67 m/s and input water cut of 50%.

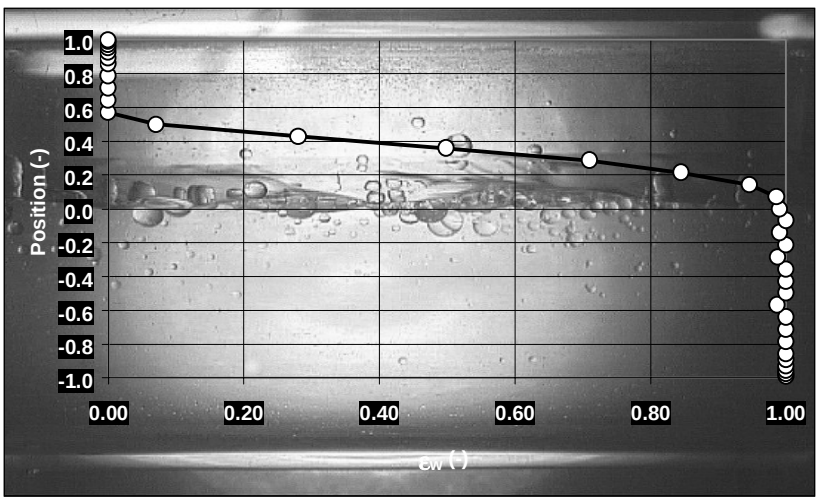

Figure 6.11 Stratified wavy (SW) flow at a mixture velocity of 1.0 m/s and input water cut of 70%.

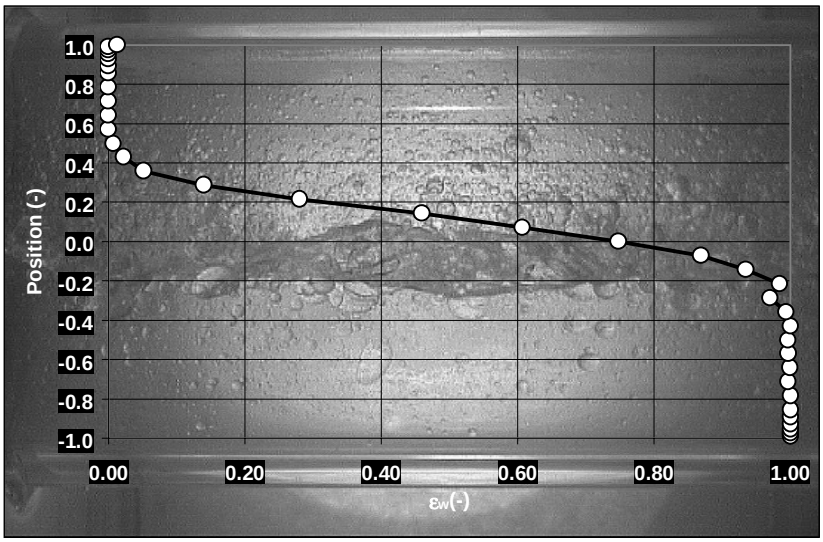

Figure 6.12 Stratified mixed (SM) flow at a mixture velocity of 2.0 m/s and input water cut of 50%.

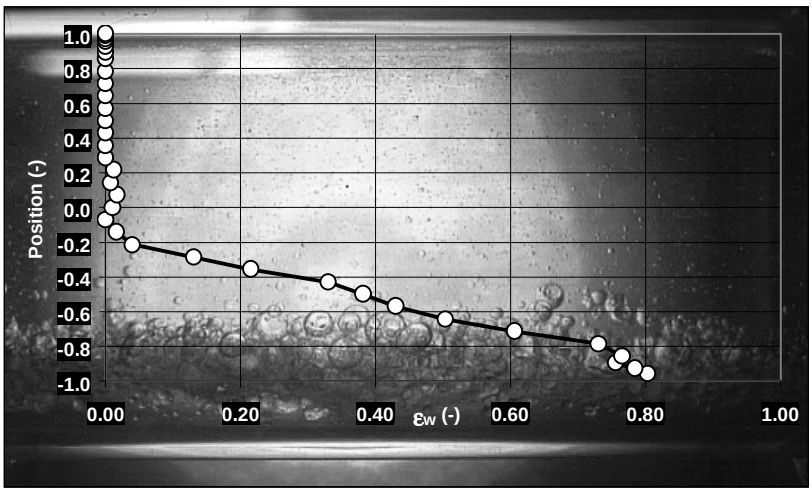

Figure 6.13 Oil continuous dispersion with a dense packed layer (Do-DP) at a mixture velocity of 1.0 m/s and input water cut of 10%.

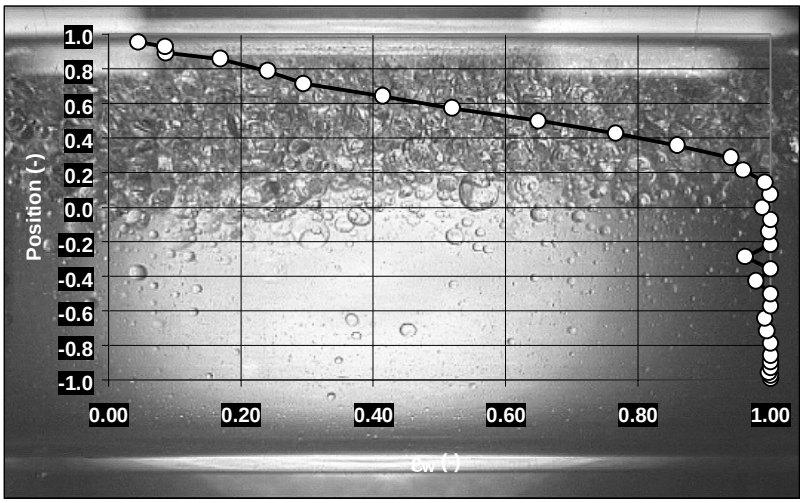

Figure 6.14 Water continuous dispersion with dense packed layer (Dw-DP) at a mixture velocity of 1.0 m/s and input water cut of 90%.

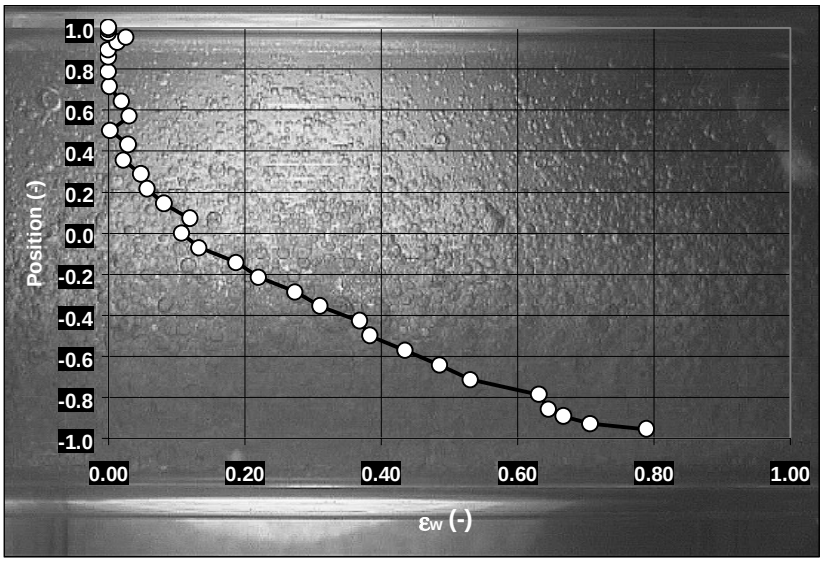

Figure 6.15 Oil continuous dispersion, inhomogeneous (Do-I), at a mixture velocity of 1.67 m/s and input water cut of 15%.

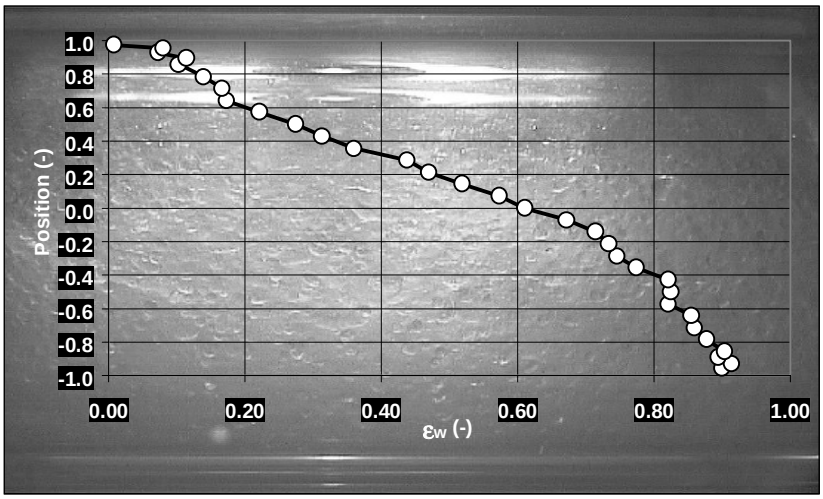

Figure 6.16 Water continuous dispersion, inhomogeneous (Dw-I), at a mixture velocity of 3.0 m/s and input water cut of 50%.

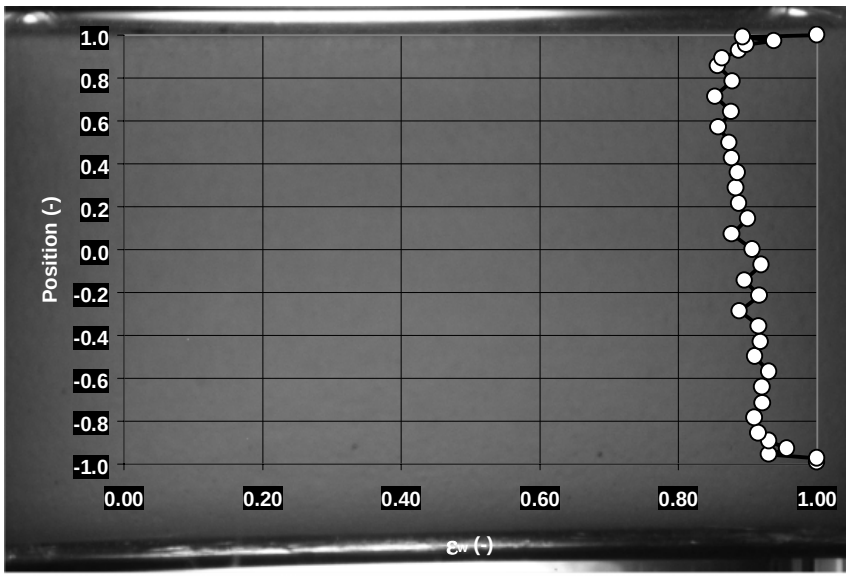

Figure 6.17 Water continuous dispersion, homogeneous (Dw-H), at a mixture velocity of 2.5 m/s and input water cut of 90%.

6.2.2 Measurements of local phase fractions at constant mixture velocity

Now that the concentration profiles of each flow pattern have been described, the results from all the experiments are presented. Figures 6.18 to 6.26 present measurements of local phase fractions often referred to as hold-ups, for variations of input water cut at constant mixture velocity. Bear in mind that pump/flow meter limitations regarding very low and very high volumetric flows reduce the number of possible water cuts at some mixture velocities.

For the mixture velocity of 0.4 m/s presented in Figure 6.18 all three water cuts are stratified smooth. The gradient of the curves are almost alike and the interface is located in the centre for 50% water cut and equally off-centre for 25% and 75% water cuts. When the mixture velocity is increased to 0.67 m/s as presented in Figure 6.19 the concentration gradients are steeper. By studying video recordings together with gamma densitometer results all water cuts with the exception of 90% are classified as stratified. The flow of the 90% water cut does not show zero water concentration in the top of the pipe, but rather varies from 5% to 12%. The flow pattern is classified as Dw-DP.

A further increase in mixture velocity to 1.0 m/s and 1.34 m/s is shown in Figures 6.20 and 6.21, respectively. Here, dispersed flows are located both at high and low water cuts. The transition water cut from stratified flow to dispersed flow also decreases for higher water cuts. The transition is between 80% and 90% water cut for 1.0 m/s and between 60% and 75% water cut for 1.34 m/s. For the case of 1.0 m/s, the concentration profiles of 85% and 90% water cuts show dispersed character. The 10% water cut is dispersed while the 15% water cut is a borderline case, but classified as stratified. For 1.34 m/s, dispersed flows are seen for water cuts of 75% and 85%. In the low water cut region at this mixture velocity, the first inhomogeneous dispersion occur. This flow of 15% water cut is classified as oil continuous (Do-I). The stratified flows are either SW or SM for both mixture velocities.

If we look at the mixture velocities of 1.5m/s and 1.67 m/s presented in Figures 6.22 and 6.23, the tendency continues. Transition from stratified to dispersed flows are close to 70% water cut for 1.5 m/s and close to 60% for 1.67 m/s. This is seen from

the change is the concentration profiles. Stratified flows now only appear as SM patterns. The interface region in each of the stratified flows becomes broader as the mixture velocities increase, as can be seen from the concentration profiles.

At a mixture velocity of 2.0 m/s shown in Figure 6.24 the first inhomogeneous dispersions that are water continuous occur. All water cuts from 75% to 90% have Dw-I pattern. Likewise all water cuts from 30% to 10 % are Do-I flows. At 2.5 m/s presented in Figure 6.25 the gradient of the 90% water cut concentration profile is almost vertical. This flow is classified as a homogeneous water continuous dispersion (Dw-H). Hardly any of the curves at this mixture velocity show stratified character, but small layers where the concentration is zero or one, can be seen for 45% to 60% water cut. The interface in these SM flows covers the major part of the pipe. At the highest mixture velocity of 3.0 m/s presented in Figure 6.26 no stratified flows are seen. The 80% water cut is Dw-H. For water cuts between 70% and 40% the flow appears as Dw-I. For the case of 35% water cut it is hard to decide whether the dispersion is oil continuous or water continuous, but in the end it is classified as Do-I. It is assumed that phase inversion occurs somewhere between the 35% and 40% water cut cases.

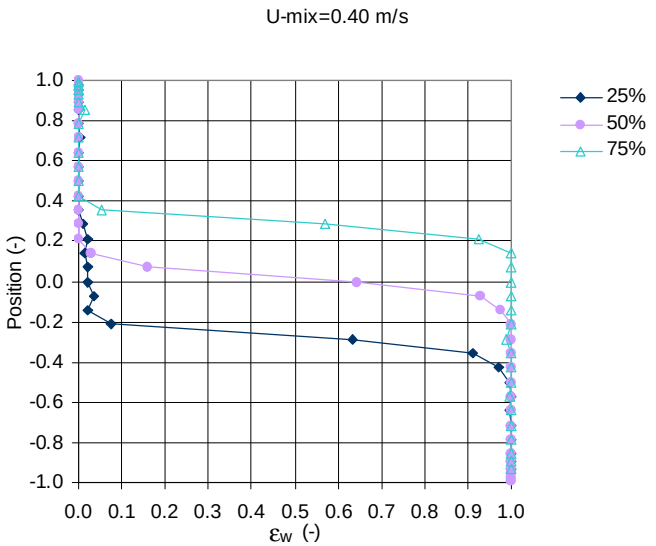

Figure 6.18 Local phase fractions at U_m=0.40 m/s at varying input water cuts.

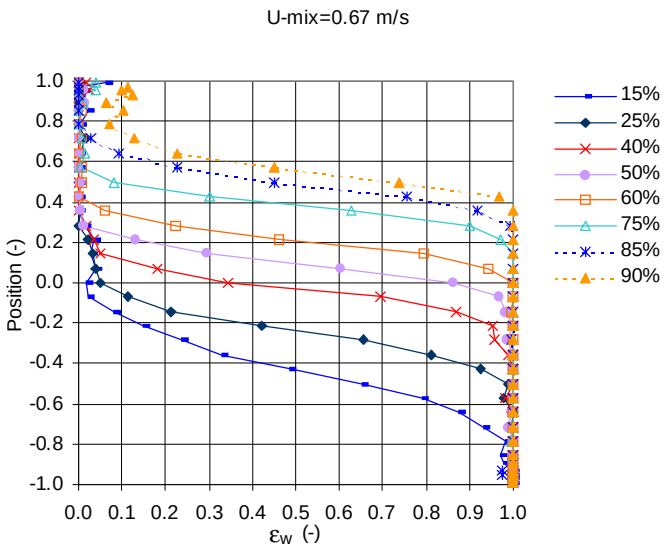

Figure 6.19 Local phase fractions at U_m=0.67 m/s at varying input water cuts.

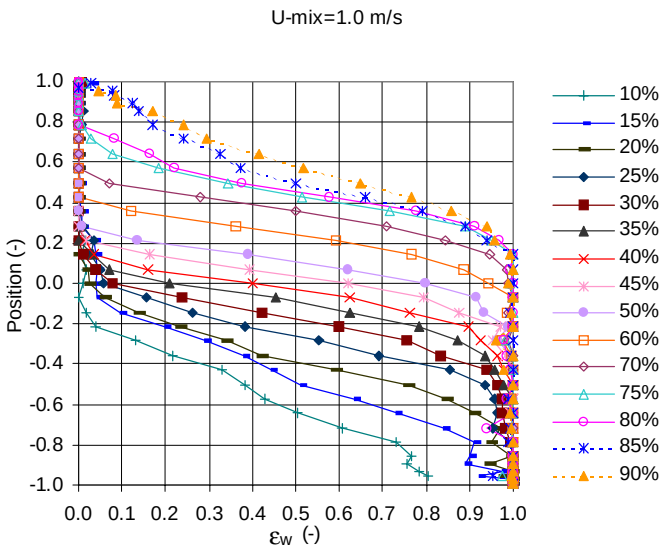

Figure 6.20 Local phase fractions at U_m=1.0 m/s at varying input water cuts.

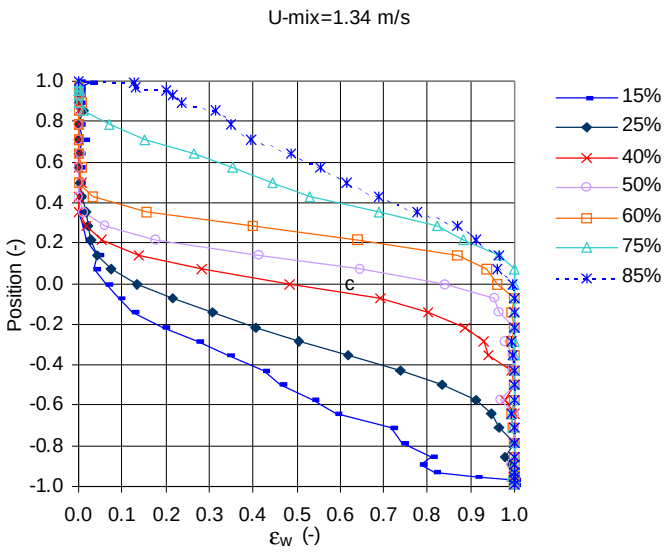

Figure 6.21 Local phase fractions at U_m=1.34 m/s at varying input water cuts.

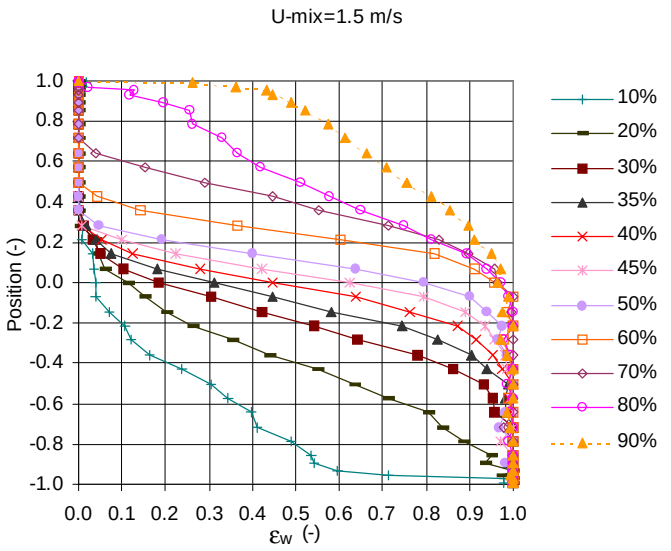

Figure 6.22 Local phase fractions at U_m=1.5 m/s at varying input water cuts.

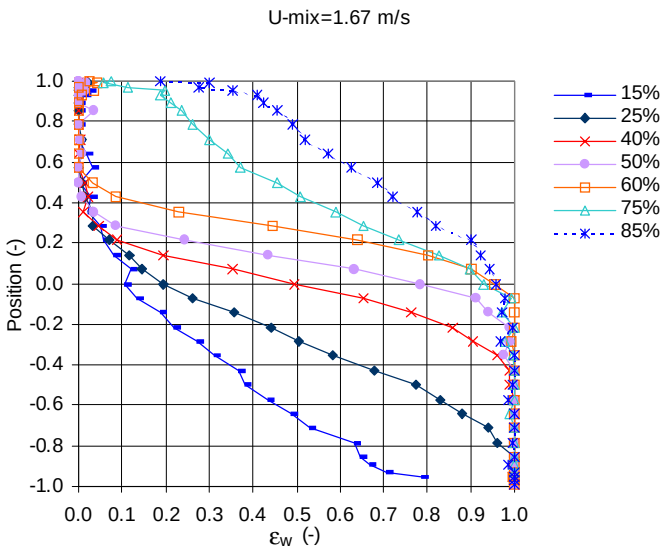

Figure 6.23 Local phase fractions at U_m=1.67 m/s at varying input water cuts.

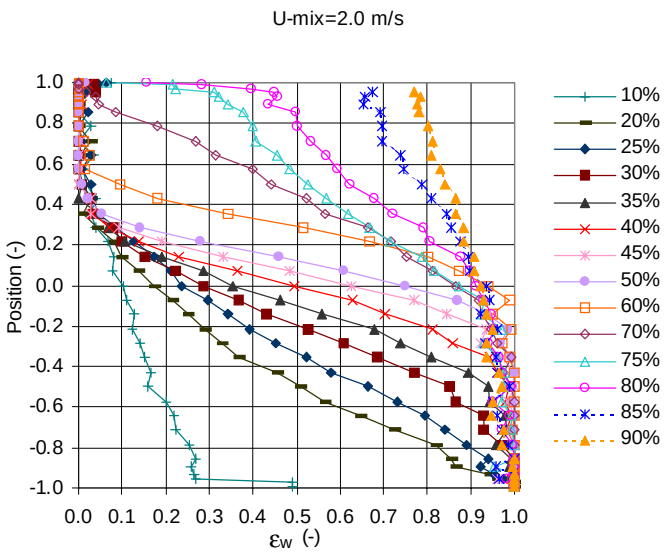

Figure 6.24 Local phase fractions at U_m=2.0 m/s at varying input water cuts.

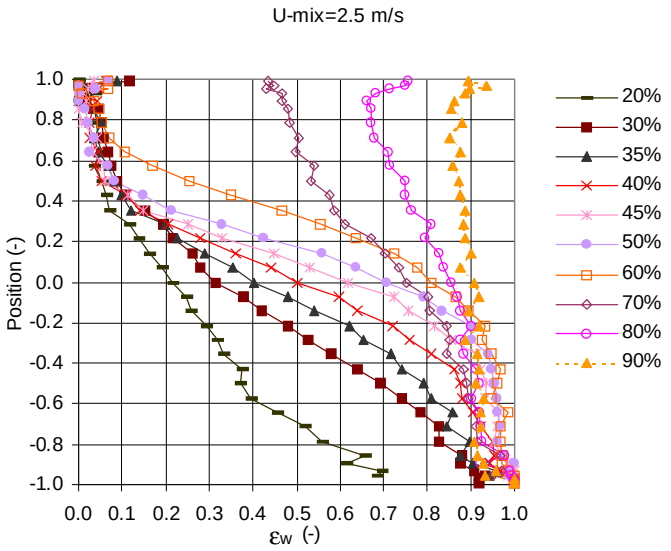

Figure 6.25 Local phase fractions at U_m=2.5 m/s at varying input water cuts.

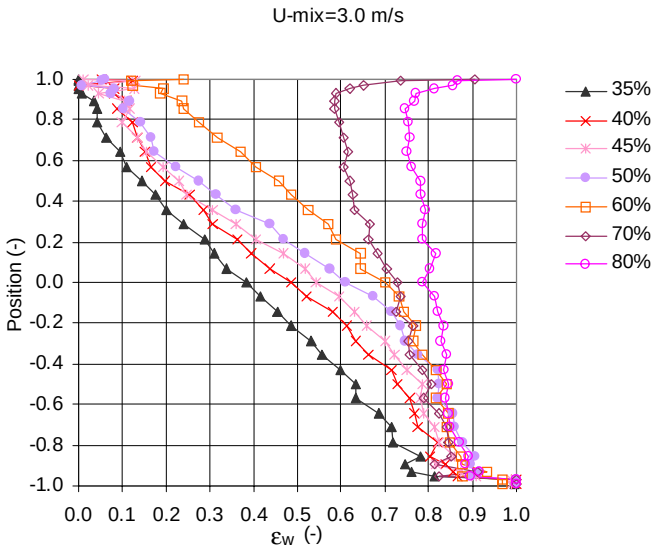

Figure 6.26 Local phase fractions at U_m=3.0 m/s at varying input water cuts.

6.3 FLOW PATTERN MAPS

For comparison with the work of other investigators, such as those presented in Chapter 2, flow pattern maps for the whole range of stratified and dispersed flows are constructed. Figure 6.27 presents the flow patterns as functions of mixture velocity and input water cut. A similar map for variations in superficial velocities of the phases is given in Figure 6.28. The earlier defined superficial velocities are given by:

$$U_{so} = \frac{Q_o}{A} \qquad U_{sw} = \frac{Q_w}{A} \tag{6.4}$$

As seen from both maps the distribution between stratified flows and dispersed flows are almost equal. At low mixture velocities the dispersed flows are located outside the intermediate water cuts, but becomes more and more pronounced as the mixture velocity increases. Compared to Trallero et al. (1997) and Nädler and Mewes (1997) the same trends can be seen (i.e. stratified flows appear at low mixture velocities and intermediate water cuts and dispersed flows appear at high mixture velocities and/or either low or high water cuts.

This study of flow patterns in the model oil facility system is the basis for the pressure drop- and slip measurements discussed in the following chapter. It also displays valuable information for the laser Doppler measurements that are presented later in the thesis. Since LDA measurements require transparency of the fluids, something that is inhibited by waves and droplets, it is the stratified flow patterns that are given most attention in the following chapters.

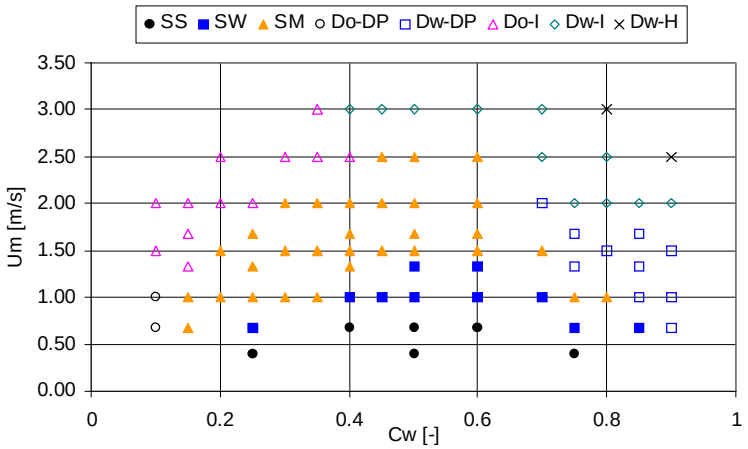

Figure 6.27 Flow patterns as functions of mixture velocity and input water cut for Exxsol D-60 and water in the model oil facility.

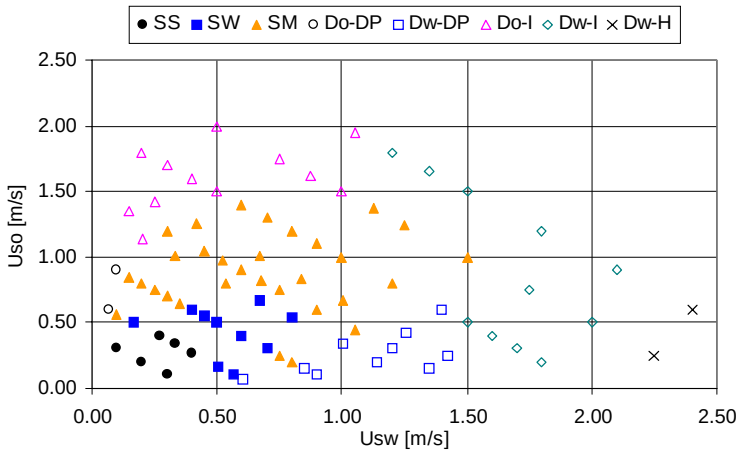

Figure 6.28 Flow patterns as functions of superficial velocities for Exxsol D-60 and water in the model oil facility.

CHAPTER 7:
PRESSURE DROP EXPERIMENTS

7.1 PRESSURE GRADIENTS IN SINGLE-PHASE FLOW

In Section 3.1.8, verification experiments of pressure drop in single-phase flow in the model oil facility were presented. Experimental friction coefficients were calculated from the measured pressure gradients for the lowest possible to the highest possible volumetric flow. Experimental coefficients as functions of Reynolds number follow empirical correlations quite well for both water and oil, which was shown in Figures 3.6 and 3.7. The conclusion from these experiments is that the pressure drop measurement system in the model oil facility operates satisfactorily. The single-phase pressure gradient experiments act as a basis for the following experiments in two-phase flow.

The maximum loadings that are used for the pumps are 18 m^3/h (pumps are designed to have 30 m^3/h each). Thus, it is possible to obtain a single-phase flow of 36 m^3/h using both pumps. However, when producing two-phase flows the flow limits means that only a few input water cuts can be produced at high mixture velocities. For instance, at a mixture velocity of 3.0 m/s input water cut is limited to between 0.33 and 0.67. At very low mixture velocities similar limits in water cuts exist.

7.2 PRESSURE GRADIENTS IN TWO-PHASE OIL / WATER FLOW

Pressure gradients in stratified and dispersed flows of oil and water are presented in Figures 7.1 and 7.2. For each mixture velocity the input water cut is varied from 10% to 90% or as much as allowed within the restrictions given by the pumps. Single-phase flow measurements were conducted at random flow rates and two-phase flow measurements at fixed mixture velocities. The single-phase values plotted in the figures (at Cw = 0 and Cw =1) are found from trend line regression of the single-phase data presented in Figure 7.3. Here, the data are curve-fitted by the least squares method with 2^{nd} order polynomial regression for prediction of future values. The R-squared value shown in the figure is known as the coefficient of determination, and is

an indicator that ranges in value from 0 to 1. It reveals how closely the estimated trend line corresponds to the actual data. A trend line is most reliable when its R-squared value is at or near 1. For n samples of a pair of values (x,y), the definition of R-squared given by Miller et al. (1990) is:

$$R^2 = \frac{S_{xy}^2}{S_{xx} S_{yy}} \tag{7.1}$$

where:

$$S_{xx} = \sum_{i=1}^{n} (x_i - \bar{x})^2, \quad S_{yy} = \sum_{i=1}^{n} (y_i - \bar{y})^2, \quad S_{xy} = \sum_{i=1}^{n} (x_i - \bar{x})(y_i - \bar{y}) \tag{7.2}$$

For mixture velocities from 1.0 m/s and higher, a fall in pressure gradient is observed at low water cuts compared to that of pure oil (Cw = 0). The tendency becomes more pronounced as the mixture velocity is increased. For the two highest mixture velocities there exist no measurements between that of zero water cut and 35% water cut. What happens to the pressure gradient in this region is not resolved by the curves presented.

Water cuts around 35% are probably close to the point where the dispersion changes from being oil continuous to being water continuous as discussed in the previous chapter. A peak in pressure drop around the point of inversion as observed by several investigators, as for instance Guzhov (1973), Valle and Utvik (1997) and Soleimani et al. (1997), is not seen in any of the experiments. Most likely the mixture velocity is too low for the expected peak to appear. Also, the mixing unit at the entrance of the test section described in Chapter 3 is made in a way that reduces dispersion.

Soleimani et al. (1997) and Soleimani (1999) also report a similar fall in the pressure gradient at low water cuts. The phenomenon is probably attributed to the formation of oil continuous dispersions. The previous study of flow patterns reveals that the flow is either Do-DP or Do-I in the region where the initial fall in pressure gradient is found. For 0.40 m/s and 0.67 m/s the flow is for the most part stratified even at these low

water cuts, and no initial fall in the pressure gradient is observed. According to Soleimani (1999), presence of drops will repress turbulence and because of that also exhibit drag reduction. The opposite effect is observed with water continuous dispersions that are formed at higher water cuts. Especially for the lower mixture velocities presented in Figure 7.2 a peak in the pressure gradient is observed. It is located at about 95% water cut for 0.67 m/s, and shifts to lower water cuts as the mixture velocity increases. At 1.67 m/s the peak is observed already at 70% water cut. If we look at the flow pattern map presented in Figure 6.27 the flow patterns that exist in the peak region are classified as Dw-DP. The flow changes from stratified with two continuous phases to dispersed oil droplets in a continuous water phase. If we look at the stratified oil layer alone, it undergoes an inversion-like transition in the way that it changes character from continuous to droplet flow. Thus, the process may have a similar effect on viscosity and pressure drop as ordinary inversion has in fully dispersed flows. However, the mechanism of inversion is not completely understood. Therefore at this point we can only ascertain this increase in the pressure gradient for this particular two-phase system of Exxsol D-60 and water.

The summary of this discussion is that pressure drop in oil/water flow is dependent on flow pattern conditions. Also the effect of phase inversion in fully dispersed flows does not appear on the pressure gradient at the employed mixture velocities and water cuts. The “inversion like” transition from SM to Dw-DP that leads to increased pressure drops is a phenomenon that is seen in the experiments where the mixture velocity is below 2.0 m/s.

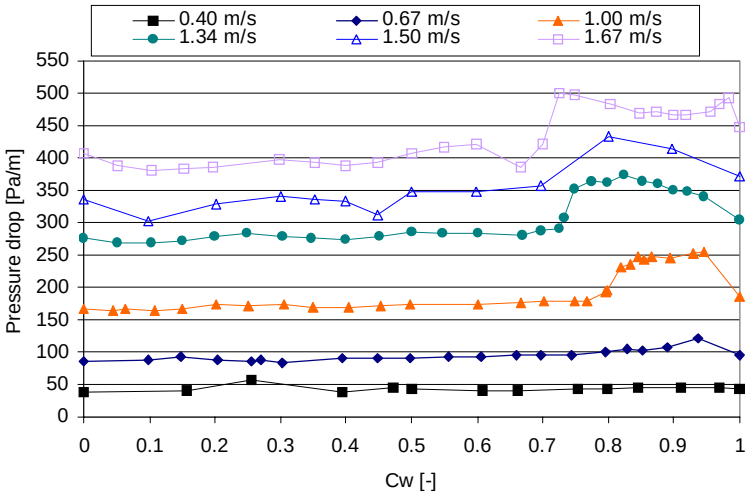

Figure 7.1 Pressure gradients in oil/water flow – low mixture velocities.

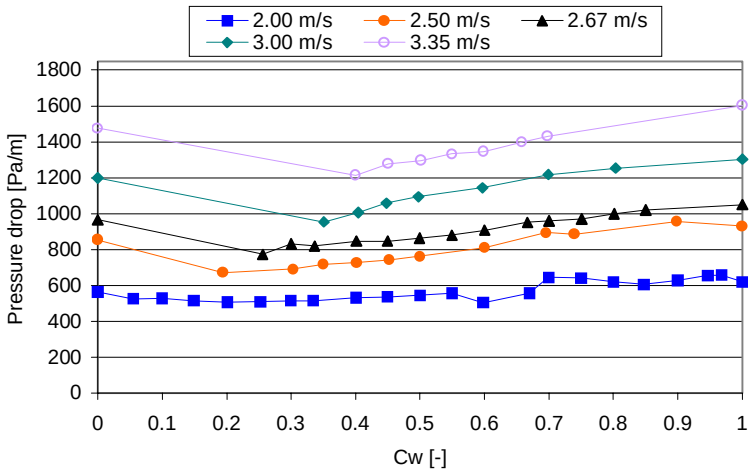

Figure 7.2 Pressure gradients in oil/water flow – high mixture velocities.

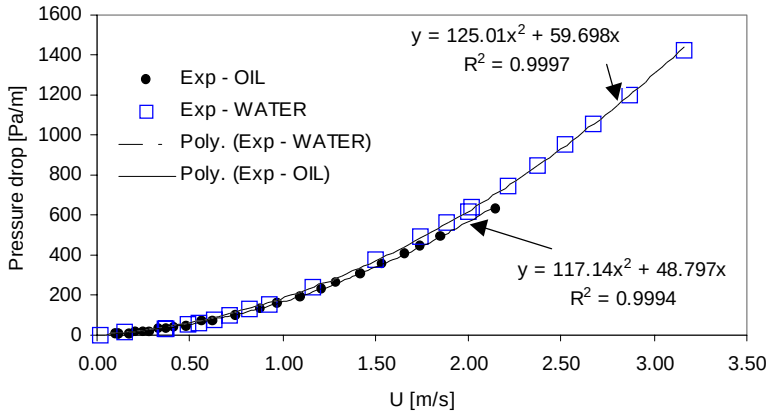

Figure 7.3 Polynomial regression of pressure drop experiments for single-phase oil and water.

7.3 EXPERIMENTAL PRESSURE GRADIENTS COMPARED TO COMPUTER SIMULATIONS

7.3.1 The two-fluid model for stratified flow

The two-fluid model is based on a momentum balance for each phase. Gravity and shear forces balance the pressure gradient of each phase according to Equations 7.3 and 7.4. The model is outlined in detail in Section 2.2.1.

$$A_o\left(\frac{dp}{dx}\right)-\tau_o S_o-\tau_{ow} S_{ow}-\rho_o A_o g\sin\theta=0 \tag{7.3}$$

$$A_w\left(\frac{dp}{dx}\right)-\tau_w S_w+\tau_{ow} S_{ow}-\rho_w A_w g\sin\theta=0 \tag{7.4}$$

For horizontal pipes ($\theta = 0$) and elimination of the pressure gradient, leads to a non-linear algebraic equation, which has to be solved iteratively with respect to the in-situ water fraction:

$$\varepsilon_w \tau_o S_o + \varepsilon_w \tau_{ow} S_{ow} - (1-\varepsilon_w)\tau_w S_w + (1-\varepsilon_w)\tau_{ow} S_{ow} = 0 \tag{7.5}$$

The pressure gradient is then found by insertion into either Equation 7.3 or 7.4.

In stratified flow it is common to speak about slip between the phases. The slip ratio, sometimes referred to only as slip, is given by:

$$S = \frac{A_w}{A_o}\,\frac{U_{so}}{U_{sw}} = \frac{\varepsilon_w}{(1-\varepsilon_w)}\,\frac{U_{so}}{U_{sw}} \tag{7.6}$$

From gamma densitometer experiments, as discussed in the previous chapter, local phase fractions are found in each of the selected positions in the pipe. The total holdup or in-situ volume fraction is estimated and the slip ratio then calculated.

Experimental pressure gradients together with slips obtained from gamma densitometry are compared with simulation results using the two-fluid model. Mixture velocities ranging from 0.40 m/s to 1.67 m/s are presented in Figures 7.4 to 7.9. Flow pattern studies show that the flow is mainly stratified or dispersed with a dense packed layer (Do-DP, Dw-DP) at these mixture velocities. Exceptions are the lowest water cut in the mixture velocities ranging from 1.34 m/s to 1.67 m/s where the flow is fully dispersed (Do-I). Nevertheless, the two-fluid model is employed for both the semi-dispersed, Do-DP and Dw-DP water cuts, as well as for the fully dispersed.

From Figure 7.4 it is evident that the pressure gradient is under-predicted in the whole region of two-phase flow. The single-phase measurements are satisfactory predicted by the model. The measured slip ratio is close to the simulated at 50% water cut, but the slopes of the curves are different, resulting in under-prediction at the low water cuts and over-prediction at the high water cuts. The comparisons at the next mixture velocity, presented in Figure 7.5, show a similar under-prediction of the two-phase pressure gradient and the pressure gradient in pure oil. The slope of the measured slip ratio is close to the simulated. At high water cuts the experimental and the simulated slip curves approach each other.

At 1.00 m/s and 1.34 m/s displayed in Figures 7.6 and 7.7, the pressure gradient is well predicted by the model for intermediate water cuts. When the flow is dispersed Dw-DP the pressure drop is highly under-predicted by the two-fluid model. The under-prediction is also present for Do-DP flows at low water cuts. The single-phase pressure drops are well predicted except for that of pure oil at 1.34 m/s. The slip ratios are well predicted at water cuts above 25% for both mixture velocities.

A further increase in mixture velocity to 1.50 m/s as shown in Figure 7.8, displays the same tendency for the pressure gradient. Between 10% and 70% water cut, with the exception of the measurement at 45%, the pressure gradient is well predicted. Outside this stratified region the same under-prediction as before is seen. The single-phase pressure gradients are under-predicted. The measured slip ratio is higher than the simulated for water cuts above 30%.

At the highest mixture velocity of 1.67 m/s presented in Figure 7.9 the flow is stratified between 25% and 60% water cut and dispersed elsewhere in the two-phase region. The two-fluid model over-predicts the gradient in the stratified region and under-predicts it in the dispersed region, especially at water cuts above 70% and for single-phase oil the under-prediction is seen. The slip ratio however, is well predicted up to 60% water cut.

The overall conclusion is that the two-fluid model predicts the pressure gradient well for intermediate water cuts, except for the lowest mixture velocities. In general, the model under-predicts in the regions where the flow is dispersed Do-DP and Dw-DP. For the water continuous dispersions the disagreement is largest. The measured slip ratios follow the same falling trend from low to high water cut as predicted by the model. Except at 0.67 m/s and 1.50 m/s the slip ratios are well predicted.

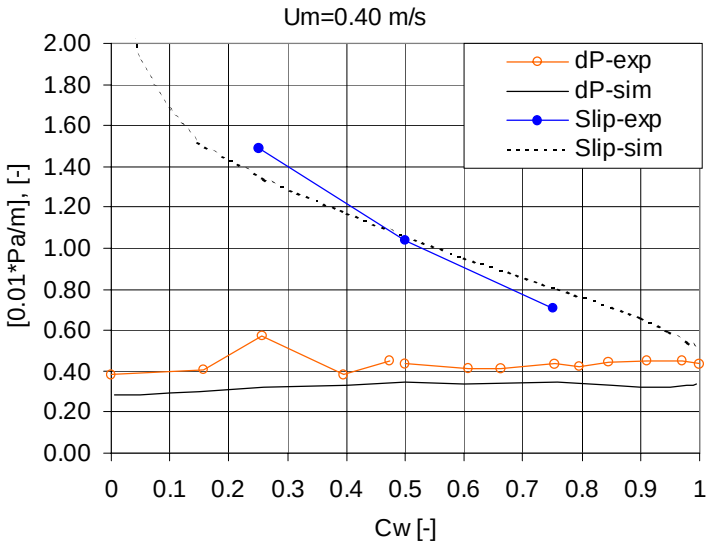

Figure 7.4 Experimental data compared to simulations with the two-fluid model for a mixture velocity of 0.40 m/s.

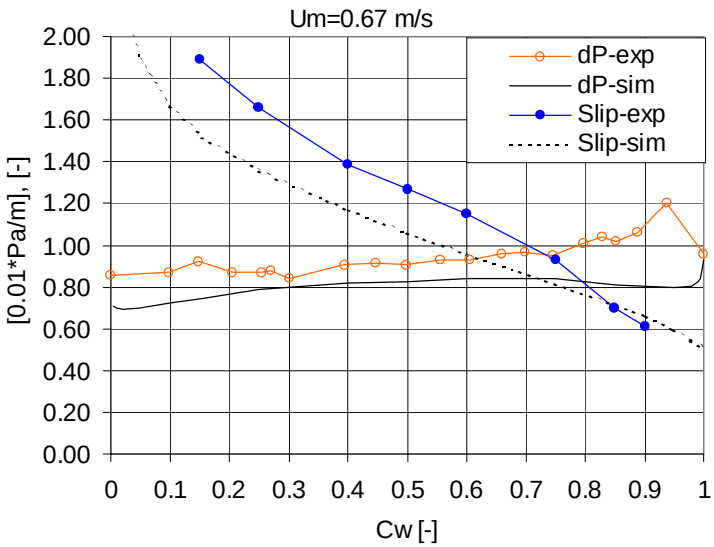

Figure 7.5 Experimental data compared to simulations with the two-fluid model for a mixture velocity of 0.67 m/s.

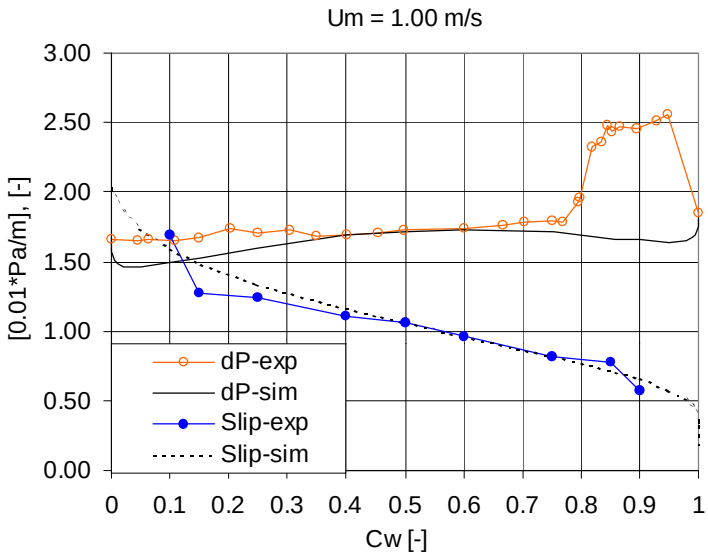

Figure 7.6 Experimental data compared to simulations with the two-fluid model for a mixture velocity of 1.00 m/s.

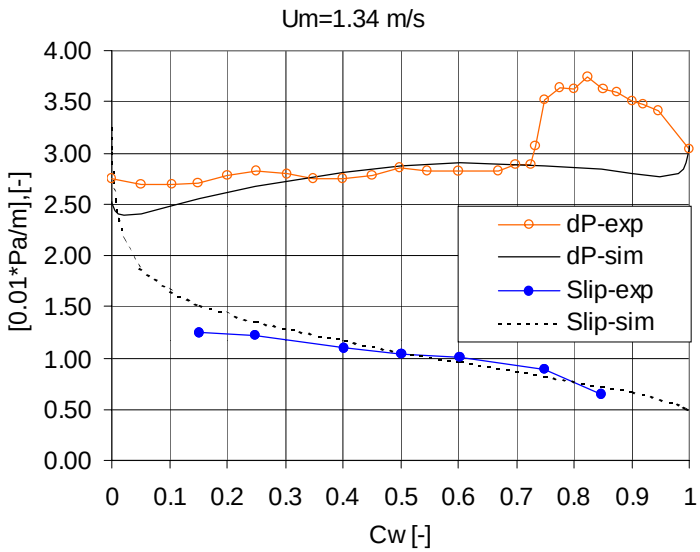

Figure 7.7 Experimental data compared to simulations with the two-fluid model for a mixture velocity of 1.34 m/s.

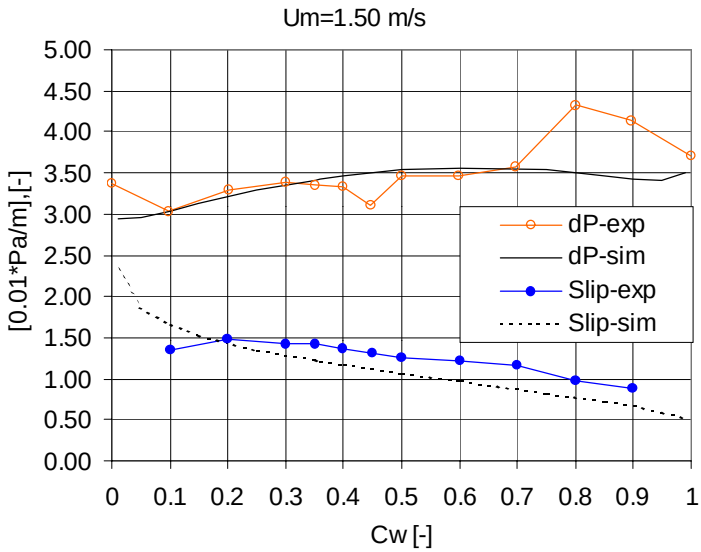

Figure 7.8 Experimental data compared to simulations with the two-fluid model for a mixture velocity of 1.50 m/s.

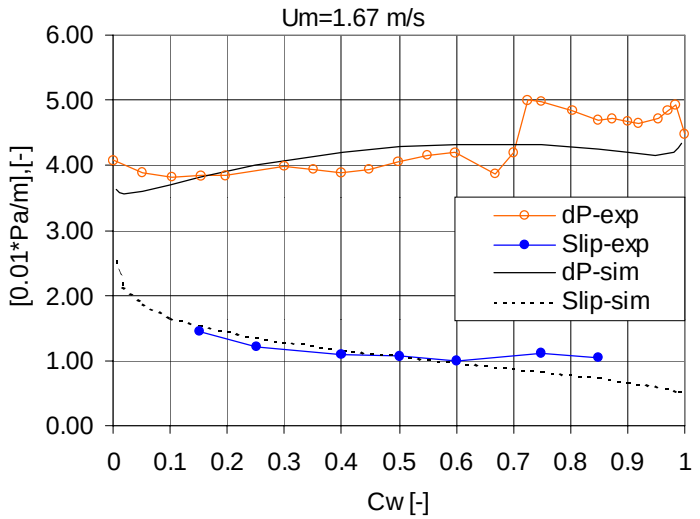

Figure 7.9 Experimental data compared to simulations with the two-fluid model for a mixture velocity of 1.67 m/s.

7.3.2 Analysis of the interfacial friction coefficient

One way to model the interfacial friction coefficient is to set it equal to the friction coefficient of the faster flowing phase. Another procedure is to ignore the interfacial friction when the phases travel with approximately equal velocity. This is due to the interface being seen as a free surface with respect to each of the phases. In the simulations done in this thesis, the interfacial friction coefficient is calculated in a similar manner to the friction coefficient for oil, but the roughness in the equation of Haaland (1983) is set to zero:

$$f_{ow} = \left[-3.6 \log_{10} \left(\frac{6.9}{\mathrm{Re}_o} + \left(\frac{e}{3.7 D_{ho}} \right)^{1.1} \right) \right]^{-2} \tag{7.7}$$

where e is equal to zero.

This calculation is generally used for all water cuts. In Figures 7.10-7.12 the output from iterations on Equation 7.5, for a mixture velocity of 1.0 m/s, is compared when the interfacial friction coefficient is calculated based on oil (I-o) or based on water (I-w). The water-based calculation implies that the Reynolds number for oil is exchanged with that of water in Equation 7.7.

As seen from Figure 7.10 and Figure 7.11 there are insignificant changes in the perimeters (defined in Figure 2.17) and holdups, respectively. There are some differences in the shear stresses as shown in Figure 7.12. This is especially evident for the oil shear at high water cuts, the water shear at low water cuts and the interfacial shear at both high and low water cuts. The overall pressure gradients displayed in Figure 7.13 show small deviations at water cuts below 10% and above 90%. Simulations of other mixture velocities show similar trends.

From these simulation results it is concluded that calculation of the interfacial friction coefficient with either the oil-based or the water-based method for all water cuts show only small deviations in the pressure gradient. If the oil-based method were used whenever the actual oil velocity, U_o, is higher than the actual water velocity, U_w, and

otherwise the water-based method were used when $U_w > U_o$, the simulated pressure gradient will follow the full line at low water cuts and the dashed line at high water cuts. All experimental data are taken between 10% and 90% water cut, and thus the comparisons in Figures 7.4 to 7.9 are more or less unaffected by the above discussion.

7.3.3 The homogeneous model for dispersed flow

The homogeneous model for estimation of pressure gradients in dispersed flow is given by:

$$\frac{dp}{dx} = -\frac{f_m \rho_m U_m^2}{2 d_i} - \rho_m g \sin(\theta) \tag{7.8}$$

For horizontal pipes ($\theta = 0$) the gravity term is neglected. The friction coefficient of the mixture is calculated by the Blasius equation:

$$f_m = 0.312 \mathrm{Re}_m^{-0.25} \tag{7.9}$$

where the Reynolds number of the dispersed mixture can be calculated using a single-phase analogy if the dispersion is homogeneous (or close to):

$$\mathrm{Re}_m = \frac{\rho_m U_m d_i}{\mu_m} \tag{7.10}$$

The mixture density is modeled by:

$$\rho_m = \varepsilon_w \rho_w + \varepsilon_o \rho_o \tag{7.11}$$

For the mixture viscosity several models exist as described in Chapter 2.2.2. One of them is the empirical model by Pal and Rhodes (1989):

$$\mu_r = \frac{\mu_m}{\mu_c} = \mu_r\left(\frac{\varphi}{\varphi_{\mu=100}}\right) = \left[1 + \frac{0.8415\dfrac{\varphi}{\varphi_{\mu=100}}}{1 - 0.8415\dfrac{\varphi}{\varphi_{\mu=100}}}\right]^{2.5} \tag{7.12}$$

Søntvedt and Valle (1994) suggested $\varphi_{\mu=100}$=0.765. Another model is the more simple equation developed by Guth and Simha (1936):

$$\mu_m = \mu_c\,(1 + 2.5\,\varphi + 14.1\,\varphi^2) \tag{7.13}$$

Both models imply knowledge of the phase inversion concentration. This is because the dispersed mixture viscosity, μ_m, and the dispersed phase concentration, φ, is related to oil in oil continuous dispersions and to water in water continuous dispersions. The models predict a peak in the viscosity and the pressure gradient at the inversion water cut. In practice the use of these two models are as follows:

1. The inversion concentration must be known.
2. In the case of oil continuous dispersions the mixture viscosity is a function of the oil viscosity. Simulations are made from low water cuts and up to the inversion water cut.
3. In the case of water continuous dispersions the mixture viscosity is a function of the water viscosity. Simulations are made from high water cuts and down to the inversion water cut.

When we have no knowledge of the inversion concentration, the mixture viscosity can be estimated in a similar way to the density. In general, the inversion concentration is not known for the system of Exxsol D-60 and water, but indications from the gamma densitometer experiments are close to 35%. By weighting the water viscosity by the in-situ water fraction and the oil viscosity by the in-situ oil fraction, the resulting mixture viscosity becomes:

$$\mu_m = \varepsilon_w \mu_w + \varepsilon_o \mu_o \tag{7.14}$$

The experimental pressure gradients at mixture velocities from 2.0 m/s to 3.35 m/s are compared to simulations with the homogeneous model in Figures 7.14 to 7.16.

For the mixture velocity of 2.0 m/s presented in Figure 7.14 the intermediate water cuts from 30% to 60% results in stratified mixed flow (SM). The experiments are thus compared to both the two-fluid model and the homogeneous model. The homogeneous model highly over-predicts the pressure gradient if the viscosity models of Pal and Rhodes (1989) or Guth and Simha (1936) are used to calculate the mixture viscosity. If the concentration-weighted viscosity model is used, the homogeneous model fits better, but still over-predicts at intermediate water cuts. In the dispersed regions an under-prediction is observed. The two-fluid model also over-predicts at the stratified intermediate water cuts, and produces similar results as for the concentration-weighted viscosity homogeneous model. When approaching either single-phase flow, the concentration-weighted viscosity homogeneous model fits the experiments better except at very high water cuts where the experiments show a peak that is closer to Pal and Rhodes (1989) and Guth and Simha (1936). With single-phase flows all models predict the same result and thus they all fit the experiments equally well.

At the mixture velocity of 2.5 m/s shown in Figure 7.15 the comparison with Pal and Rhodes (1989) is dropped. The two-fluid model is also left out since the flow is dispersed for all water cuts except between 45% and 60%. Still the homogeneous model with the concentration-weighted viscosity calculation fits the experiments best. Both models over-predict at intermediate water cuts.

For the mixture velocities of 2.67 m/s to 3.35 m/s presented in Figure 7.16 only comparisons with the homogeneous model with concentration-weighted viscosity are made. The model over-predicts the pressure-gradient at intermediate water cuts and under-predicts it at low and high water cuts.

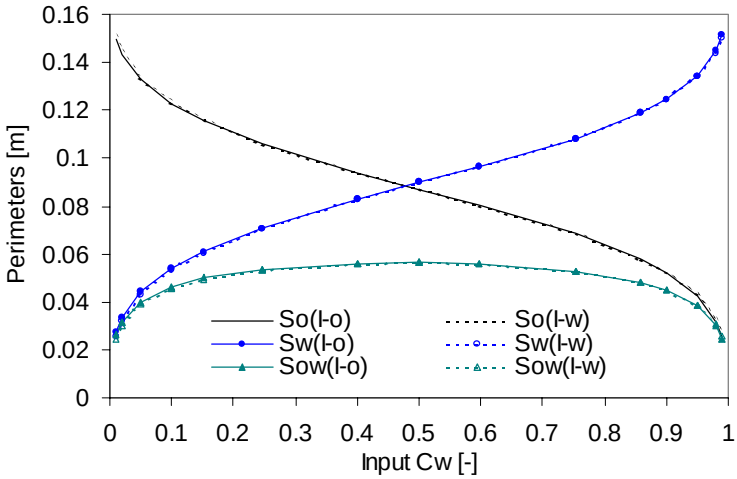

Figure 7.10 Perimeters calculated with oil-based (I-o) interfacial friction coefficient compared to those calculated with water-based (I-w), U_m=1.0 m/s.

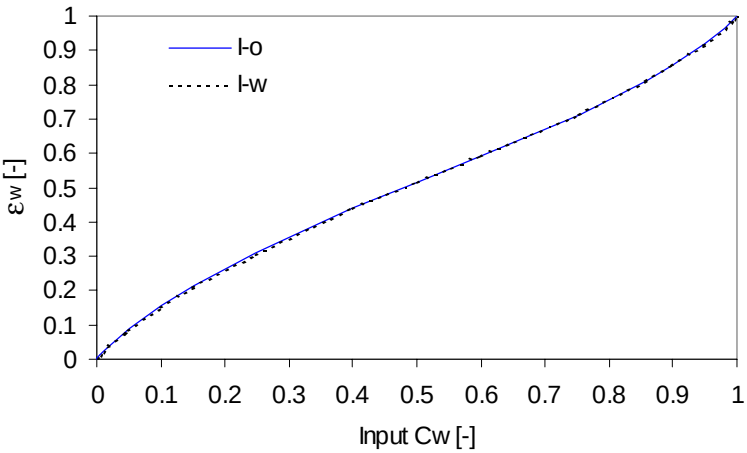

Figure 7.11 Holdups calculated with oil-based (I-o) interfacial friction coefficient compared to those calculated with water-based (I-w), U_m=1.0 m/s.

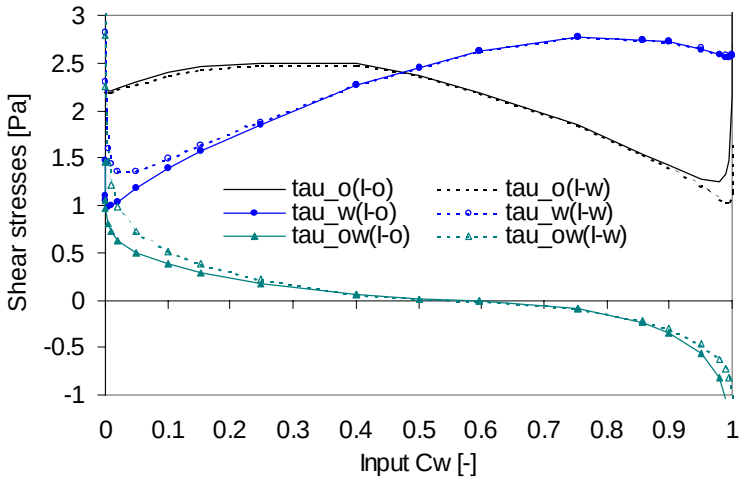

Figure 7.12 Shear stresses calculated with oil-based (I-o) interfacial friction coefficient compared to those calculated with water-based (I-w), U_m=1.0 m/s.

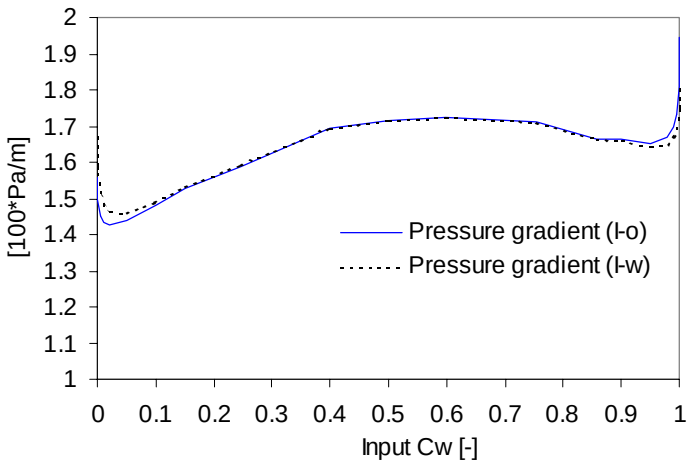

Figure 7.13 Pressure gradients calculated with oil-based (I-o) interfacial friction coefficient compared to those calculated with water-based (I-w), U_m=1.0 m/s.

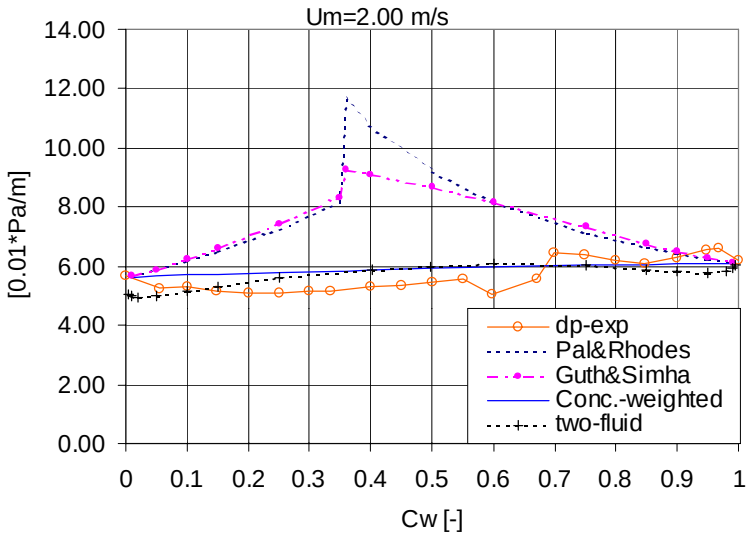

Figure 7.14 Comparison of experimental pressure gradients at a mixture velocity of 2.00 m/s with the two-fluid model and the homogeneous model.

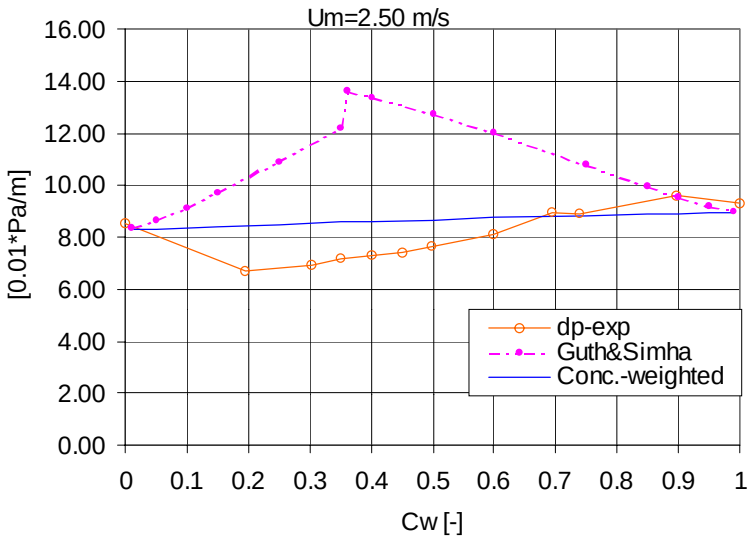

Figure 7.15 Comparison of experimental pressure gradients at a mixture velocity of 2.50 m/s with the homogeneous model.

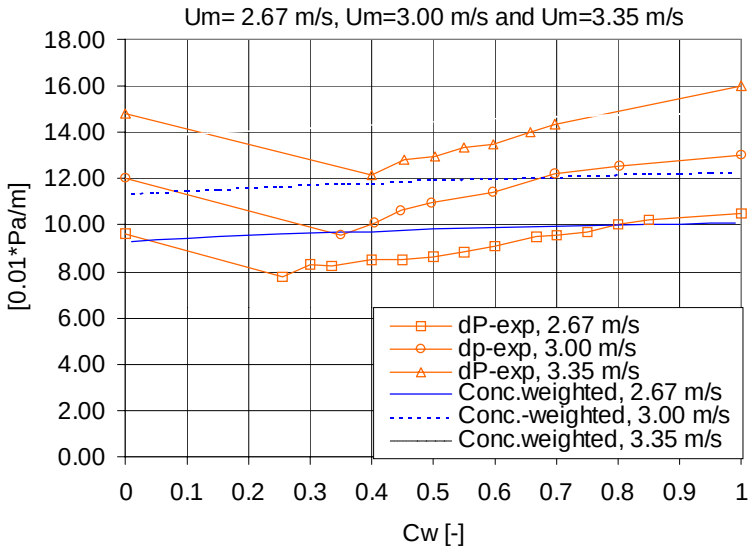

Figure 7.16 Comparison of experimental pressure gradients at a mixture velocity of 2.67 m/s to 3.35 m/s with the homogeneous model.

In general, the homogeneous model with no consideration of inversion fits the experiments best. Since both Pal and Rhodes (1989) and Guth and Simha (1936) predict a peak in the pressure gradient at the inversion fraction, these models will inevitably differ more from the experiments. At higher mixture velocities than presented in this work, phase inversion will induce a peak in the pressure gradient, and these models will most probably fit better. Experiments done by Soleimani et al. (1997) on Exxsol D-80 (which is a slightly different oil than Exxsol D-60) and water in horizontal pipes confirm the peak in the pressure gradient.

CHAPTER 8:
MEASUREMENTS OF VELOCITY AND TURBULENCE IN STRATIFIED OIL/WATER FLOW

8.1 INTRODUCTION

In this chapter, which completes the experiments carried out in the model oil facility, laser Doppler anemometry is used to study velocities and turbulence in two-phase pipe flow.

The model oil facility was described in detail in Section 3.1. The fluids are Exxsol D-60 and water, and they flow simultaneously in a horizontal pipe. Depending on the mixture velocity and the input water cut different flow patterns will occur. They are described in Section 6.1. Laser Doppler anemometry requires transparent pipes and fluids. Also, to improve optical conditions a partial refractive index matching (RIM) procedure is needed. The specially designed measurement section along with the partial RIM procedure was outlined in Section 4.4. Basically the procedure is to use water in the rectangular box around the pipe when measurements are carried out in the water phase, and oil when measurements are carried out in the oil phase. In that way, the optical conditions are improved (although the pipe material, which has a different refractive index than water and oil still produces difficulties). Even if the partial RIM procedure is carried out, the LDA are limited to measurements mainly in the continuous phase. This means that in stratified flows (SS, SW and SM), both phases can be studied. It is also possible to do measurements in the continuous phase in the semi-dispersed flow patterns (Dw-DP and Do-DP). LDA measurements in fully dispersed flows (Dw-I, Dw-H, Do-I and Do-H) are not possible without a full RIM procedure (something that requires exactly the same refractive indices for oil, water and pipe material). Measurements of axial and vertical velocities are conducted along the vertical pipe diameter (i.e. from the top wall, through the centre, to the bottom wall). With one exception, only cases where it was possible to obtain a full velocity profile are presented. The exception is measurements in both phases in a Dw-DP flow, to demonstrate the difficulties that arise when it is attempted to measure in

dispersed flow. All measurements in two-phase flow are compared to measurements in single-phase flow.

Before we continue with the results from the experiments the basic equations for axisymmetric pipe flow are presented (the axisymmetry refers to single-phase flow only). The x-momentum equation for laminar axisymmetric flow in a circular pipe, when using a boundary layer approach is given by:

$$\rho u \frac{\partial u}{\partial x} + \rho v \frac{\partial u}{\partial r} + \frac{dP}{dx} = \frac{1}{r}\frac{\partial}{\partial r}\left(r \mu \frac{\partial u}{\partial r} \right) \tag{8.1}$$

One of the characteristics of turbulent flow is time dependence. The time dependence follows from small-scale vortices in the flow. According to what is known as the Reynolds decomposition theory, the velocity in turbulent flow can be described as the sum of a steady component and a fluctuating component. The fluctuating component varies with time, but becomes zero when averaged over time. The instantaneous velocity components u and v together with the static pressure, P, can be decomposed as follows:

$$u = \bar{u} + u' \qquad v = \bar{v} + v' \qquad P = \bar{P} + P' \tag{8.2}$$

By substituting the Reynolds decompositions into Equation 8.1 followed by time-averaging the momentum equation for turbulent pipe flow appears when using the boundary layer approach and constant density, the following equation can be obtained:

$$\bar{u}\frac{\partial \bar{u}}{\partial x} + \bar{v}\frac{\partial \bar{u}}{\partial r} + \frac{1}{\rho}\frac{d\bar{P}}{dx} = \frac{1}{r}\frac{\partial}{\partial r}\left[\nu r \frac{\partial \bar{u}}{\partial r} - \overline{u'v'} \right] \tag{8.3}$$

The details about the Reynolds decomposition and the time-averaging technique are fond in for instance, Kays and Crawford (1993). The evaluation of the cross-moment term $\overline{u'v'}$ is referred to as the “closure” problem. When the cross-moment is

multiplied by density the product is called Reynolds stress. One way to model it is to assume that it is proportional to the axial velocity gradient in the radial direction:

$$\overline{u'v'} = -\varepsilon_M \frac{\partial u}{\partial r} \tag{8.4}$$

The proportionality constant is called the eddy diffusivity and has the same dimensions as the kinematic viscosity ν. The momentum equation then becomes:

$$\bar{u}\frac{\partial \bar{u}}{\partial x} + \bar{v}\frac{\partial \bar{u}}{\partial r} + \frac{1}{\rho}\frac{d\bar{P}}{dx} = \frac{1}{r}\frac{\partial}{\partial r}\left[(\nu + \varepsilon_M)\frac{\partial \bar{u}}{\partial r}\right] \tag{8.5}$$

For comparison with laminar quantities, an eddy viscosity or turbulent viscosity may be defined as:

$$\mu_t = \rho\varepsilon_M \tag{8.6}$$

The boundary layer models

We start with the simplest model called the *two-layer model*. From experiments in turbulent pipe flow at least two different regions are observed. The first region is located close to the wall and viscous shear is the predominant mechanism in momentum transfer. This region is referred to as the *viscous sublayer* or sometimes only the *sublayer*. The Reynolds number determines the "thickness" of the sublayer. Consider a given fluid flowing in a constant diameter pipe. Then, by increasing the bulk velocity the thickness of the sublayer will decrease. For the pipe flow of water and oil presented here, the thickness varies from about 0.1 mm to about 1.0 mm. These values are based on theoretical calculations and are also confirmed in the LDA experiments.

The other region, the *fully turbulent*, is assumed to cover the rest of the pipe. In this region turbulent eddies are produced and momentum is transferred by turbulent diffusion.

In the *viscous sublayer* close to the wall $\nu >> \varepsilon_M$ and in the *fully turbulent region* of the flow $\nu << \varepsilon_M$. The total shear stress is the sum of the molecular or laminar part and the turbulent part:

$$\frac{\tau}{\rho} = \frac{\tau_L + \tau_T}{\rho} = (\nu + \varepsilon_M)\frac{\partial \bar{u}}{\partial r} \tag{8.7}$$

Substituting this into Equation 8.5 yields:

$$\bar{u}\frac{\partial \bar{u}}{\partial x} + \bar{v}\frac{\partial \bar{u}}{\partial r} + \frac{1}{\rho}\frac{d\bar{P}}{dx} = \frac{1}{\rho r}\frac{\partial (r\tau)}{\partial r} \tag{8.8}$$

For fully developed flow, $\bar{v}$ is zero and $\bar{u}$ is only a function of r, and Equation 8.8 becomes:

$$\frac{1}{r}\frac{d(r\tau)}{dr} = \frac{d\bar{P}}{dx} \tag{8.9}$$

It is often convenient to use *wall coordinates* for non-dimensional presentation of velocity data. The shear velocity or the friction velocity of the flow is defined by:

$$u_\tau = \sqrt{\tau_0 / \rho} \tag{8.10}$$

where the wall shear is given by:

$$\tau_0 = \frac{f}{8}\rho u_b^2 \tag{8.11}$$

and f is the Moody friction factor. Alternatively, the wall shear may be calculated by:

$$\tau_0 = \frac{d_i}{4}\left|\frac{d\overline{P}}{dx}\right| \tag{8.12}$$

The latter is recommended since it requires no information on velocity. The wall coordinates for velocity and position are then defined by:

$$u^+ = \frac{\overline{u}}{u_\tau} \tag{8.13}$$

$$z^+ = \frac{z\,\rho\,u_\tau}{\mu} = \frac{z\,u_\tau}{\nu} \tag{8.14}$$

As for the mean velocities, the rms velocities are scaled with the friction velocity. Cross-moments are scaled with the second power of the friction velocity.

The viscous sublayer can be modelled:

$$u^+ = z^+ \tag{8.15}$$

From experiments it is shown that the sublayer extends from $z^+=0$ to just above $z^+=11$. The fully turbulent region is generally described by the logarithmic equation called the *law of the wall*, which is valid for flow between flat plates:

$$u^+ = 2.44\ln(z^+) + 5.0 \tag{8.16}$$

For pipe flow a slight modification of this equation produces the *Nikuradse equation*, which is known to fit experimental data better:

$$u^+ = 2.5\ln(z^+) + 5.5 \tag{8.17}$$

It is common to use the term “law of the wall” for all three equations above.

Another possibility is to divide the pipe flow into four regions (as opposed to two in the *two-layer model*) as was done by Tennekes and Lumley (1974). Figure 8.1 shows a sketch of the four regions forming what we can call the *four-layer model*. The *viscous sublayer* is located close to the wall and extends from $z^+=0$ to $z^+=5$. The $u^+=z^+$ model fits experimental data well in this region as for the two-layer model presented above. The *fully turbulent region* is located from $z^+=30$ towards the centre of the pipe. However, when the centre is approached experiments often deviate from the Nikuradse equation that is valid in this region as illustrated in the figure. The region where this deviation occurs is called the *wake* region. As the Reynolds number is increased the wake moves to higher z^+ (i.e. the wake is shifted to the right). The region between the viscous sublayer and the fully turbulent region from $z^+=5$ to $z^+=30$ is called the *buffer layer*. Measurements are often seen to deviate from the correlations given by Equations 8.15 and 8.17 in this region.

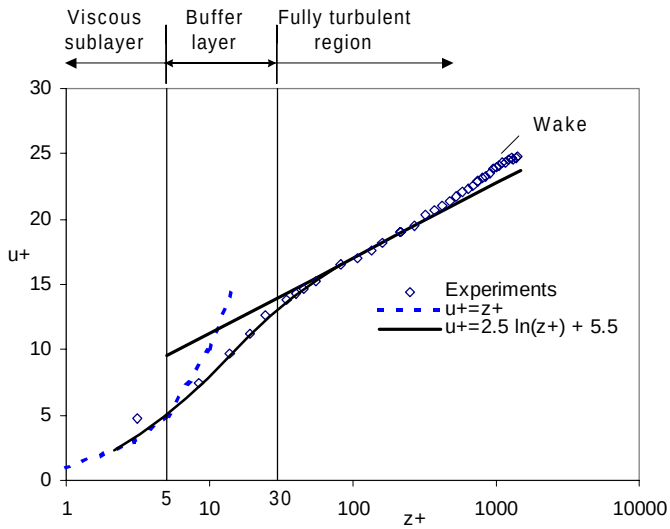

Figure 8.1 The four-layer model. Such a model is presented by for instance, Tennekes and Lumley (1974). The experiments are conducted at 1.02 m/s of water in a 55.7 mm pipe.

8.2 LDA-MEASUREMENTS IN SINGLE-PHASE FLOW

8.2.1 Experimental matrix and measurement variables

Measurements of local phase fractions and pressure drops were described in Chapters 6 and 7, respectively. These measurements were carried out at several mixture velocities with variations in the water cut. The laser Doppler anemometry measurements described in this chapter are carried out at similar mixture velocities as in the previous experiments. LDA measurements in single-phase flow are done prior to the two-phase measurements at the same bulk velocity as the mixture velocities for two-phase flows. This is done to produce a foundation for comparison. Table 8.1 shows the experiment matrix for the single-phase LDA experiments.

Table 8.1 Single-phase experimental conditions.

Flow rate [litre/min]	Bulk velocity [m/s]	Reynolds numbers [-]		Friction velocities [m/s]		Friction Reynolds numbers [-]	
		Re_w	Re_o	$u_{\tau,w}$	$u_{\tau,o}$	$Re_{\tau,w}$	$Re_{\tau,o}$
60	0.41	22832	11439	0.0248	0.0258	1381	721
100	0.68	37868	18972	0.0366	0.0386	2038	1076
150	1.02	56802	28458	0.0508	0.0539	2829	1501
200	1.37	79293	38223	0.0650	0.0694	3620	1936
250	1.71	95227	47709	0.0791	0.0843	4405	2353
300	2.04	113604	56916	0.0929	0.0993	5173	2772

The friction velocities are calculated from single-phase pressure drop measurements according to Equations 8.10 and 8.12. The friction Reynolds number is defined by:

$$\mathrm{Re}_\tau = \frac{u_\tau \, d_i}{\nu} \tag{8.18}$$

Velocity disagreement:

When velocity profiles of single-phase water or oil were integrated to produce the volume flow, a small deviation compared to the flow meter reading was discovered.

Control measurements of the inner plexiglass section revealed that the diameter was 55.8 mm in the position where measurements where conducted instead of 56.3 mm as in the rest of the test section pipe. However, the flanging of the stainless steel section and the entrance of the plexiglass section is specially designed to be as smooth as possible to ensure fully developed flow for the LDA measurements. Thus, the plexiglass section has the same inner diameter as the rest of the measurement section at the entrance, but narrows down to 55.3 mm at the exit. The LDA measurements are carried out in the middle of the section and hence if the narrowing is linear the diameter here is 55.8 mm. These diameter ratios are confirmed by vertical traversing of the laser control volume inside the pipe close to the entrance, the middle and the exit (it is easy to "find" the wall when the signals from LDA are studied). The result of the narrowing of the diameter is slightly higher mixture velocities for the LDA measurements as they were carried out at the same flow rates as measurements of local phase fraction and pressure drop. It is assumed that the errors in the LDA measurements from the narrowing of the plexiglass section are small.

From the raw velocity measurements (u_i, v_i) several statistical quantities referred to as moments can be calculated. These are listed in Table 8.2.

Table 8.2 Statistical moments.

Quantity	Axial component	Vertical component	Equation
Mean	$\bar{u} = \sum_{i=1}^{N} \eta_i u_i$	$\bar{v} = \sum_{i=1}^{N} \eta_i v_i$	(8.19)
Root mean square (RMS)	$u_{rms} = \sqrt{\sum_{i=1}^{N} \eta_i (u_i - \bar{u})^2}$	$v_{rms} = \sqrt{\sum_{i=1}^{N} \eta_i (v_i - \bar{v})^2}$	(8.20)
Turbulence intensity	$T(u) = \frac{u_{rms}}{\bar{u}} \cdot 100\%$	$T(v) = \frac{v_{rms}}{\bar{v}} \cdot 100\%$	(8.21)
Cross-moments	$\overline{u'v'} = \overline{uv} - \bar{u}\bar{v} = \sum_{i=1}^{N} \eta_i (u_i - \bar{u})(v_i - \bar{v})$		(8.22)

In Equations 8.19 to 8.22 the weighting factor, provided that the samples are independent, is given by:

$$\eta_i = \frac{1}{N} \tag{8.23}$$

If one cannot make the assumption that the measurements are statistically independent, then strictly speaking, Equation 8.23 should not be used. An alternative method of providing statistically reliable data is the use of transit-time weighting. Here, the raw data are weighted by the transit time, which is the time it takes a tracer particle to travel through the measurement volume. The transit time weighting is done after the raw data are collected (i.e. with the signal processor operated in the burst mode):

$$\eta_i = \frac{t_i}{\sum_{j=1}^{N} t_i} \tag{8.24}$$

The weighting factor is described in detail in Chapter 4. The procedure for obtaining reliable data is to obtain samples with the signal processor operated in the dead-time mode (if this is featured). This means that a certain time is allowed to elapse between each validated sample. However, this increases the total sampling time, something that is not desired in our case. Thus, the transit time weighting method is used.

8.2.2 Measurements

Axial velocity

Figure 8.2a presents axial velocity profiles for bulk velocities ranging from 0.41 m/s to 2.04 m/s of single-phase water flow (which is used in all the single-phase experiments). Each profile shows the turbulent character of high gradients close to the wall (in the viscous sublayer and the first part of the turbulent region) and lower gradients as the pipe centre is approached. All profiles show symmetry around the pipe centre (z/R = 0). The velocity reaches a maximum in the centre and drops down to zero at the wall. The density of measurement points is highest in the near wall area.

The velocity profiles are scaled by the friction velocities and plotted in wall coordinates in Figure 8.2b. A similar study of LDA in single-phase pipe flow was carried out by den Toonder (1995). Due to symmetry, only measurements in the top half of the pipe are presented. The measurements are compared to the *law of the wall* as well as DNS data by Moser et al. (1999) for flow in a horizontal rectangular channel and DNS data by Eggels et al. (1994) for flow in a horizontal pipe. The measurements show satisfactory agreement compared to the *law of the wall* and the DNS data for z^+ above 11 (i.e. in the turbulent region). Although it is worth noticing that the DNS data for channel flow fit the experiments better than the data for pipe flow. Still, for the rest of the LDA measurements only the work by Eggels et al. (1994) will be used as a basis for comparison. Eggels et al. (1994) compared their DNS data with PIV and LDA experiments and concluded that measurements of axial mean velocity displayed similar deviations from the *law of the wall* as can be seen from Figure 8.2b. As mentioned above the LDA measurements presented in this thesis follow the law of the wall, and thus it does not support the conclusions by Eggels et al. (1994).

Close to the wall, in the viscous sublayer, the measurements show some scattering. By employing the two-layer model the "thickness" of the viscous sublayer can be calculated from Equation 8.14 by substituting z^+ with 11.3. Single-phase flow of water at the velocities presented has a sublayer thickness that varies from 0.44 mm at 0.41 m/s to 0.12 mm at 2.04 m/s. As discussed in Section 4.4.2 it is difficult to get reliable 2-D measurements close to the wall due to partial and sometimes total separation of the individual control volumes. This is probably the reason for the scattering of the measured velocities in the sublayer. In all experiments the laser was operated in 2-D mode.

Velocity fluctuations – u-rms and v-rms

The root mean square (rms) velocities u-rms and v-rms describe velocity fluctuations in the horizontal (axial) and vertical directions. They are presented in Figures 8.3 and 8.4. The same velocity profiles in wall-coordinates (i.e. both rms velocity and position are scaled by the friction velocity) are displayed in Figures 8.5 and 8.7. Eggels et al. (1994) use a pipe with ID=95.4 mm at Re=5450, whereas these LDA measurements

are conducted in a two-inch pipe. Furthermore Eggels et al. (1994) do not reveal the fluid they used. The comparison is demonstrated in Figures 8.6 and 8.8. Looking at the non-scaled velocity profiles presented in Figures 8.3 and 8.4 it is evident that the same symmetry as for the mean velocity is present. The rms-velocities are zero at the wall and reach a maximum value close to the wall before they drop down to minima in the pipe centre. For u-rms presented in Figure 8.3 it is difficult to identify the peak very close to the wall. However, for v-rms presented in Figure 8.4, it is easier to observe the peak. In fact, this is an important observation. LDA measurements presented by den Toonder (1995) confirm that the peak in u-rms is located closer to the wall than that of v-rms. This becomes more evident when the rms-velocities are plotted in wall-coordinates. The peak seems to be at $z^+ \approx 11$ for u-rms (Fig.8.5) and z^+ between 60 and 300 for v-rms depending on the Reynolds number. In the work of den Toonder (1995) it was found that the v-rms peak was shifted to higher z^+ as the Reynolds number was increased. In the present work, this could not be confirmed. For u-rms it is difficult to observe if the position of the peak shows Reynolds number dependence. den Toonder (1995) states that this is not the case. Compared to the DNS data by Eggels et al. (1994) the measured profiles of u-rms$^+$ in Figure 8.6 are slightly higher from r/D ≈ 0.33 toward the pipe centre at r/D = 0. Eggels et al. (1994) have a peak value of u-rms$^+$ = 2.73 located at r/D ≈ 0.46 whereas the LDA measurements have a peak of u-rms$^+$ ranging from 3 to 4 located at r/D ≈ 0.49 (i.e. closer to the wall). The LDA peak is also much steeper. A part of the reason for the disagreement may again be attributed to the poor measurement conditions close to the pipe wall, but probably the difference in Reynolds number compared to the DNS data also have an effect.

The same comparison for v-rms is presented in Figure 8.8. Here, the DNS data is lower everywhere except for some of the centre measurements. The maximum value is v-rms$^+$ = 0.83 at r/D ≈ 0.33 for the DNS data. For the LDA experiments maximum values for v-rms$^+$ range from 0.92 to 0.99 and are located from r/D = 0.42 to r/D = 0.45. Thus, the magnitude of the maximum values for LDA measurements is higher than the maximum value for DNS.

Turbulence intensity

The turbulence intensity in the axial direction, T(u), is calculated according to Equation 8.21. This parameter is often used as input in CFD simulations. Figure 8.9 shows that the profiles for all bulk velocities are quite similar. The intensity in the pipe centre varies from 3.5 to 5% and increases monotonically to about 10% at z/R = +/-0.9. Beyond this point a sharp increase is observed when the wall is approached (followed by a decrease to zero at the wall). Again, the errors in the LDA measurements as a consequence of poor optical conditions in this region may cause abnormal intensities (e.g. measured u-rms is probably to high).

Cross-moments and Reynolds stresses

Figures 8.10 and 8.11 present the cross-moments for the three lowest and the three highest bulk velocities, respectively. Each curve has the characteristic linear profile in the major part of the pipe. The cross-moments are zero in the centre and reach an absolute maximum close to the wall before it drops to zero again at the wall. A straight line that intersects the centre is added so it fits the measurements as closely as possible in the region where they are linear. For fully developed pipe flow the shear stress varies linearly with the pipe radius as given by Equation 8.9. The idea of the straight line is to extrapolate the curves to the pipe wall to obtain the wall shear by multiplying with the density. Table 8.3 includes the wall shears obtained from the LDA experiments compared to wall shear calculated from the measured pressure drops using Equation 8.12. As seen from Table 8.3, the wall shear calculated from pressure drops are from 8 to 20% higher. Both values for wall shear are plotted against the bulk velocity in Figure 8.12. The shear distribution determined by LDA is calculated along the vertical pipe diameter and extrapolated to the wall. Some of the deviation may be attributed to this extrapolation.

Figures 8.13 and 8.14 show the scaled cross-moments displayed in the same way as for the velocity fluctuations. To obtain the Reynolds stresses the cross-moments have to be multiplied by the density of the fluid. Since the curves of Reynolds stresses are equal in shape compared to those of cross-moments, they are not presented for single-

phase flow. From Figure 8.13 it can be seen that the peak in the cross-moments distribution shows Reynolds number dependence. It is shifted towards higher z^+ as the Reynolds number is increased. For the bulk velocity of 0.41 m/s the peak is located at $z^+ = 160$ and for 2.04 m/s it is located at $z^+ = 282$. This observation is confirmed by the work of den Toonder (1995). Comparison with the DNS-data of Eggels et al. (1994) in Figure 8.14 shows good agreement with respect to the shape of the distribution. Although the measurements indicate lower Reynolds stresses from r/D =0.1 to r/D =0.45.

Table 8.3 Calculation of wall shear from LDA-experiments compared to pressure drop experiments in single-phase water.

Q [m^3/h]	U_b [m/s]	$\tau_{w,dP/dx}$ [Pa][1]	$\tau_{w,LDA}$ [Pa]	Deviation [%]
3.6	0.41	0.50	0.40	20
6	0.68	1.2	1.1	8
9	1.02	2.5	2.1	16
12	1.37	4.2	3.6	14
15	1.71	6.2	5.3	15
18	2.04	8.6	7.4	14

[1] Measurements of pressure drop are calculated during the LDA experiments, and may vary some from the pressure drop experiments presented in Chapter 7.

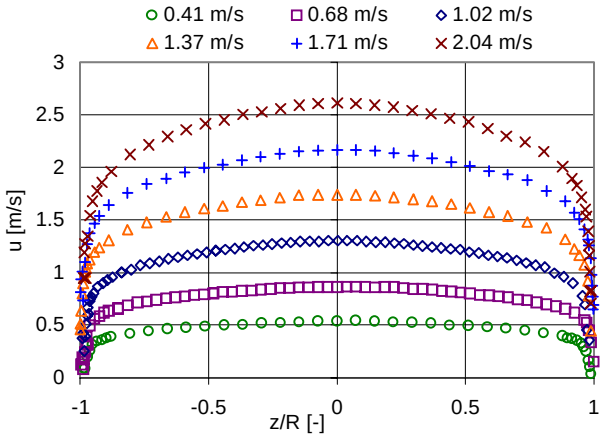

Figure 8.2a Axial mean velocity profiles.

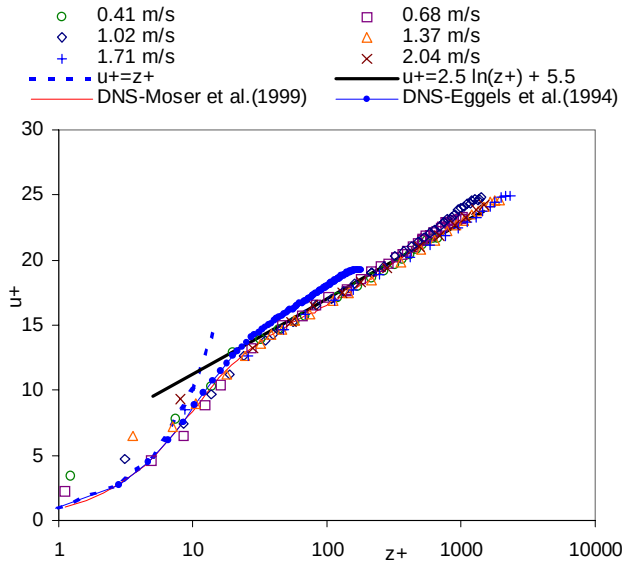

Figure 8.2b Axial mean velocity profiles normalized with the friction velocity.

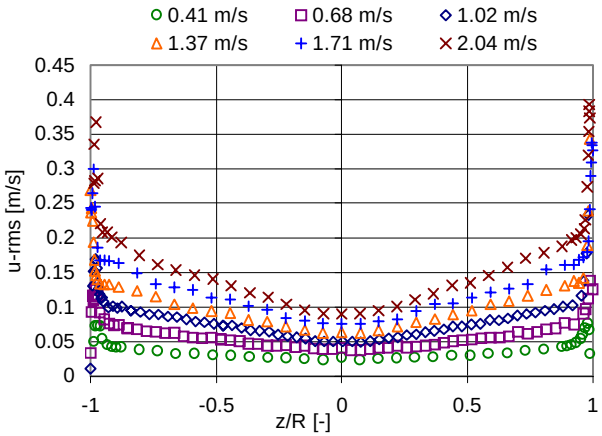

Figure 8.3 Axial rms profiles.

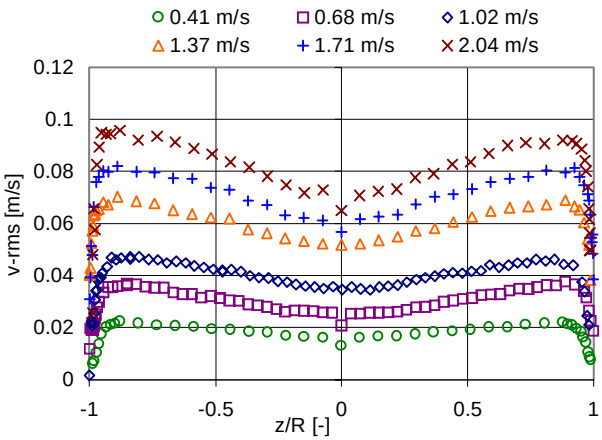

Figure 8.4 Vertical rms profiles.

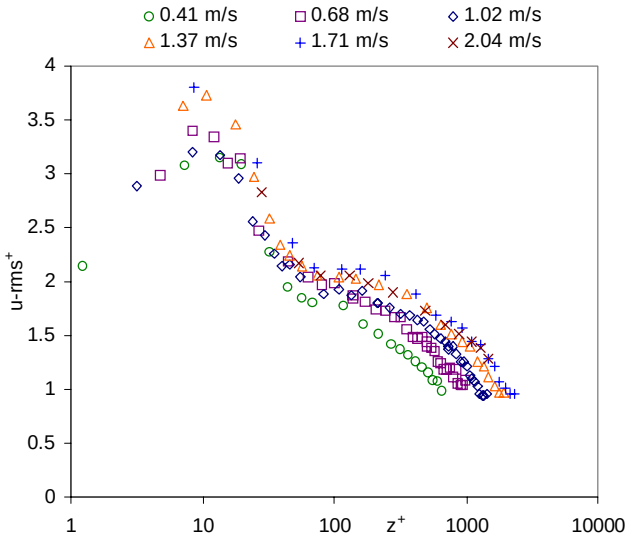

Figure 8.5 Axial rms profiles normalized with the friction velocity in a semi-logarithmic plot.

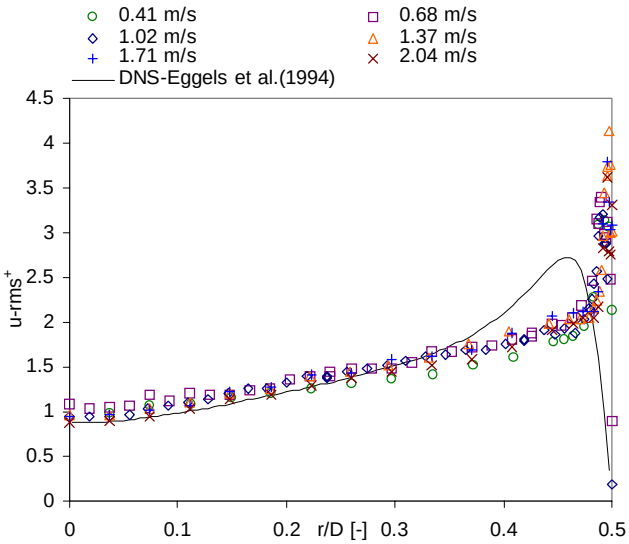

Figure 8.6 Axial rms profiles normalized with the friction velocity.

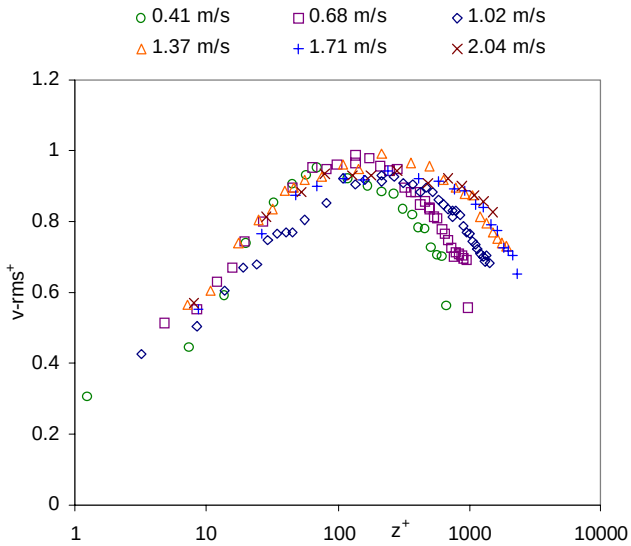

Figure 8.7 Vertical rms profiles normalized with the friction velocity in a semi-logarithmic plot.

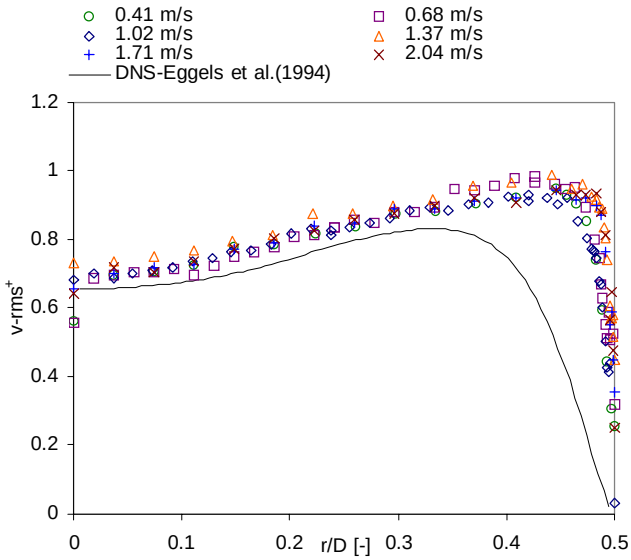

Figure 8.8 Vertical rms profiles normalized with the friction velocity.

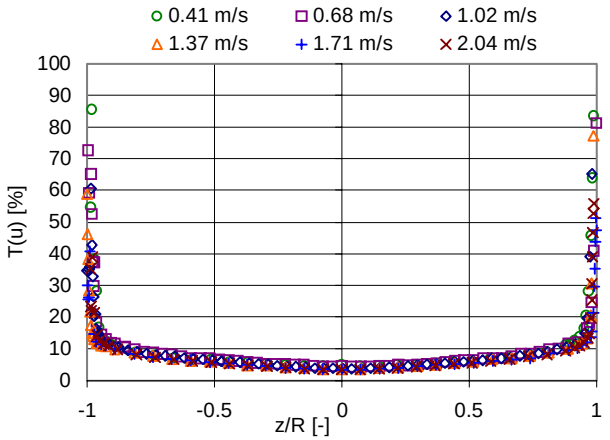

Figure 8.9 Axial turbulence profiles.

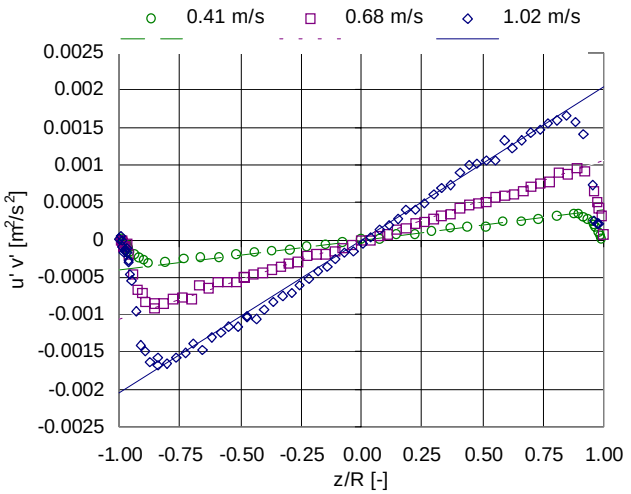

Figure 8.10 Cross-moments $\overline{(u'v')}$ for bulk velocities of 0.41 m/s, 0.68 m/s and 1.02 m/s.

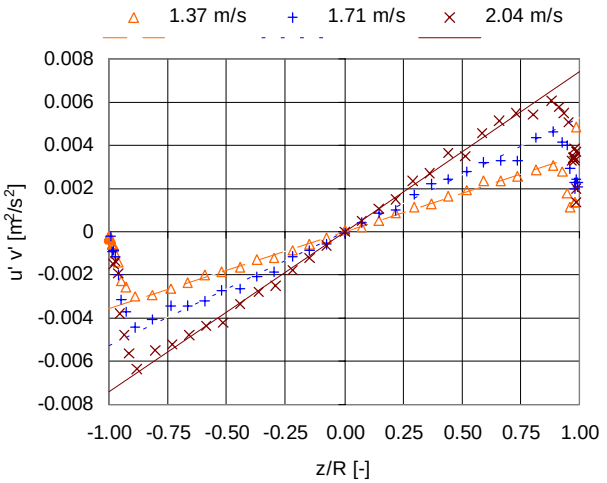

Figure 8.11 Cross-moments $\overline{(u'v')}$ for bulk velocities of 1.37 m/s, 1.71 m/s and 2.04 m/s.

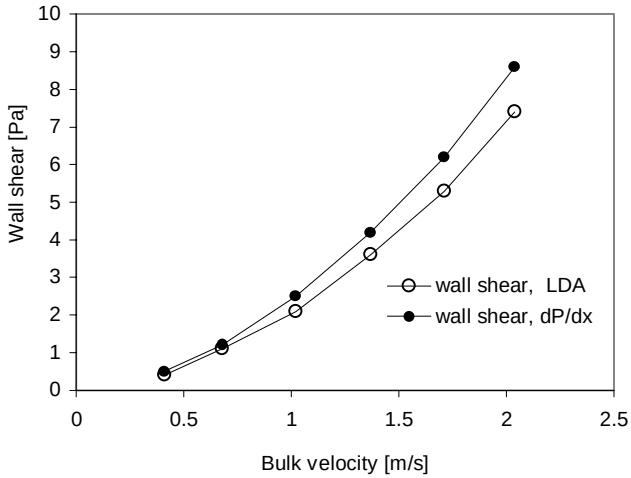

Figure 8.12 Wall shear as a function of bulk velocity.

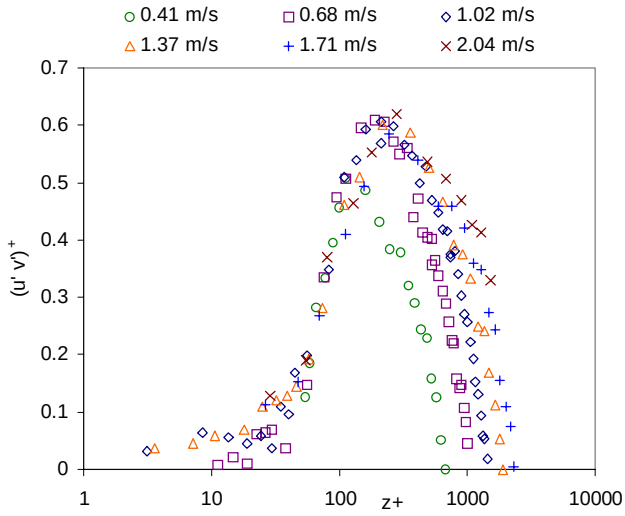

Figure 8.13 Cross-moments $\overline{(u'v')}^{+}$ normalized with the friction velocity in a semi-logarithmic plot.

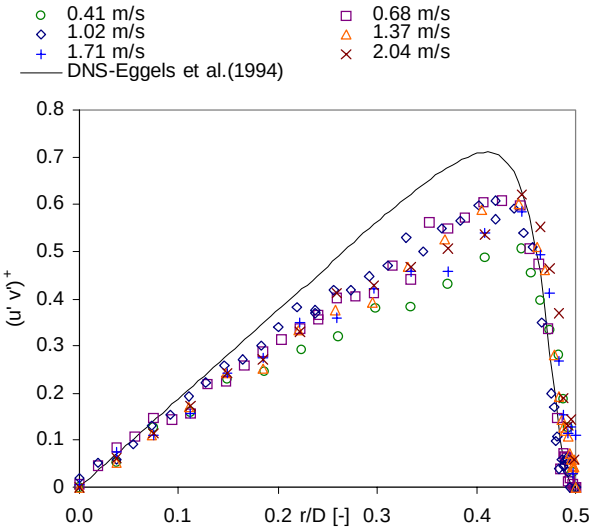

Figure 8.14 Cross-moments $\overline{(u'v')}^{+}$ normalized with the friction velocity.

8.3 LDA MEASUREMENTS IN STRATIFIED OIL/WATER FLOW

In this section, measurements of the distribution of axial mean velocity, axial and vertical rms-velocities, axial turbulence intensity, cross-moments and finally Reynolds stresses are presented. Gamma measurements are included to show the local phase distribution. The experiments are carried out at mixture velocities that correspond to the bulk velocities for single-phase flow. All measurements in two-phase flow are compared to similar measurements in single-phase flow. Input water cuts are varied between 15 and 85% in accordance with Table 8.4. It is mainly water cuts producing stratified flow that are analysed. A minor part of the work presented in the next sections is also presented in Elseth et al. (2000). Further details of the measurement procedure are described in Chapter 4. Keep in mind that the oil phase is less dense than water and hence it floats above the water layer in the pipe. All figures that present LDA measurements of two-phase distributions are flipped ninety degrees compared to the plots in the previous section. This is done to better illustrate the effect of the horizontal two-phase flow.

Table 8.4 Experimental matrix.

Flow rate [m^3/h]	Mixture velocity [m/s]	Input water cut [%]
3.6	0.41	25
6	0.68	25,50
9	1.02	15,25,40,50,60,75,85
12	1.37	15,25,40,50,60
15	1.71	25,40,50,60
18	2.04	25,40,50,60

All experiments are carried out at temperatures between 19 and 21°C.

8.3.1 Axial mean velocity distribution for varying water cuts at constant mixture velocity

Figures 8.15 to 8.20 present distributions of axial mean velocity for mixture velocities ranging from 0.41 m/s to 2.04 m/s. In every plot the local water fraction or holdup is presented to indicate the position of the interface. However, this is done only for axial

velocity. When other quantities are studied the plots of axial velocity have to be consulted to see where the interface is.

At the mixture velocity of 0.41 m/s presented in Figure 8.15, only measurements of 25% water cut are presented. The flow pattern is stratified smooth (SS) as can be seen from the local phase distribution, ε (25%). The flow pattern maps presented in Figures 6.27 and 6.28 show the flow pattern for each of the experiments to be discussed. In general, interfacial waves and droplets create poor measurement conditions. For the case of 25% water cut no droplets or waves are present, and it is possible to obtain measurements very close to the interface. From the figure it can be seen that the maximum velocity is positioned in the oil phase at z/R=0.37. The position of the interface is located at z/R= -0.30. This is where the local water fraction is equal to 0.5, which holds for a sharp interface without waves and droplets. This means that the maximum velocity is located almost in the middle of the oil phase, slightly closer to the wall than the interface. In the case of modelling such a system, the water layer could be looked upon as a moving wall under the oil layer, with extinction of turbulence towards the interface. Compared to single-phase flow, sometimes referred to as 100% water cut, the 25% water cut has a slightly higher maximum velocity, and the distribution shows the expected higher velocities in the oil phase and lower velocities in the water phase.

In Figure 8.16 the mixture velocity is increased to 0.68 m/s and distributions at 25% and 50% water cut are presented along with 100% water cut. Flow patterns are stratified mixed (25%) and stratified smooth (50%). Again the oil phase moves faster than the water phase at 25% water cut. What is more surprising is that this is also the case with the 50% water cut. One would think that oil, which has higher viscosity (1.6 cP) than water would flow slower than water. However, the density ratio counteracts the viscosity effect. An analysis of the effect of the physical properties for the oil/water system and their effect on friction and wall shear is given in the section where measurements of Reynolds stresses are presented. The case of 50% water cut has one velocity maximum in each phase (a smaller maximum in the water phase), whereas the case of 25% has only one. The maximum velocities are located closer to the interface than the wall for the case of 50% water cut while the maximum is more

like halfway between the interface and the wall for the case of 25% water cut. The highest velocity is measured at 25%. Compared to 100% water cut the velocity distribution at 25% water cut shows lower velocities in the water phase and higher ones in the oil-phase. The velocity distribution of 50 % water cut has lower velocity than 100% water cut in the middle of the pipe and a higher one in the oil phase. Even parts of the water phase seem to have higher velocities than for 100% water cut. The flow rates are equal for single-phase and two-phase flows. If velocity profiles are integrated across the pipe, the volume flows should be equal. Thus, if the velocity of a two-phase distribution is higher than for the single-phase distribution in some regions of the pipe, it has to be lower in other regions to preserve mass. This discussion refers to axisymmetry about the pipe axis. In two-phase flow this is not the case. Deviations may be different in other planes and 3D effects are not included in these measurements.

By increasing the mixture velocity to 1.02 m/s as presented in Figure 8.17 several flow patterns may appear. Experiments at this particular mixture velocity is also presented as transparent graphs of LDA data together with local phase distribution on top of pictures of the flow patterns in Section 8.3.5. At 15%, 25% and 75% water cuts the flow is stratified mixed (SM), at 40%, 50% and 60% the flow is stratified wavy (SW) and at 85% water cut, a water continuous dispersion with a dense packed layer of oil (Dw-DP) is present. All of the water cuts presented in Figure 8.17a, 15%, 25% and 40%, have higher velocities in the oil phase and lower ones in the water phase compared to 100% water cut. The highest velocity is measured at 15% water cut, the second highest at 25% water cut and the third highest at 40% water cut (i.e. all two-phase flows have higher maximum velocities than that of single-phase flow).

Again it is seen that the oil phase travels faster at 50% water cut (Figure 8.17b). Even at 60% water cut, which corresponds to flow rates of 3.6 and 5.4 m^3/h for oil and water, respectively, this is the case. At 75% water cut the maximum velocity is found in the water phase. As for the mixture velocity of 0.68 m/s the intermediate water cuts (40% - 60%) at 1.02 m/s have one velocity maximum in each phase. When the water cut is 85% the flow pattern is Dw-DP. It is possible to obtain reliable measurements in the water phase, but the layer of oil droplets creates problems. The reason is that the

refractive index difference between water and oil is quite large (1.33 versus 1.43) and the beams will refract differently. When measurements are conducted in the continuous water phase the rectangular box around the pipe is, as mentioned earlier, filled with water. Oil droplets that pass the intersection or control volume thus represent disturbances in the measurements. If we try to measure the oil droplet layer, oil has to be filled in the rectangular box, but then the continuous water may create disturbances since the droplets are dispersed, the control volume will be subjected to both oil droplets and continuous water in the measurement interval. Hence, the dispersed dense packed oil droplet layer was measured with water in the box, which means that it is probably the continuous water that is measured in the dense packed region as well. The number of samples in each measurement position in this region is very low (between 50-200) compared to the continuous region (between 10000-25000). The only reason for presenting this distribution is that it shows that dispersed flows are difficult to measure with LDA without proper refractive index matching. The 85% water cut is left out when the other quantities (rms and cross-moments) are discussed in relation to varying water cuts at constant mixture velocity. It is worth noticing that the maximum velocity is 1.41 m/s at this water cut compared to 1.29 m/s at 100% water cut. The position of the maximum velocity is just below the centre of the pipe at z/R=-0.1.

A further increase of mixture velocity to 1.34 m/s is presented in Figure 8.18. The flow of 15 % water cut is categorised as an inhomogeneous oil continuous dispersion (Do-I). However, it is possible to obtain measurements in the water phase close to the lower wall. For the rest of the water phase though, velocities cannot be measured. This is seen as the section without markers in the velocity distribution curve. Even at 25% water cut (SM) a part of the pipe is without measurements. The velocity distributions at 15% to 40% water cut have one velocity maximum located in the oil phase. Compared to 100% water cut, lower velocities are again found in the water phase and higher ones in the oil phase. At 50% (SW) and 60% (SW) water cut one velocity maximum in each phase is found (the highest in the oil phase). The distribution in these experiments follows that of 100% water cut in the lower region of the pipe, but deviates from it in the middle and in the top of the pipe. Compared to the

distributions presented at 1.02 m/s one difference at 1.34 m/s is that 75% water cut is inaccessible to LDA in the oil phase and thus, it is not presented.

At even higher mixture velocities the flow becomes more and more dispersed at the various water cuts tested. Only water cuts between 25 and 60 % are presented. At 1.71 m/s as seen in Figure 8.19 all water cuts are stratified mixed, although the interface at 25% water cut covers almost the whole part of the water phase. Compared to the previous mixture velocities, the interface in each experiment is wider with more waves and droplets. Otherwise the same comments can be made.

At 2.04 m/s presented in Figure 8.20, the interface effects are intensified. The intermediate water cuts of 40% (SM) and 50% (SM) no longer have two maxima on the velocity distribution curve. The reason is probably that the oil and water are no longer separated by a sharp interface because of a wavy interface and movement of droplets from oil to water and vice versa. At 25% water cut (Do-I) and 60% water cut (Dw-I) about half of the pipe is inaccessible to LDA.

To sum up the comparison of axial velocity distribution in two-phase flows compared to single-phase flows the following general remarks can be made:

- The maximum velocity located somewhere on the distribution curve is in general higher for two-phase flow compared to single-phase flow.

- Intermediate water cuts of mainly 50% and 60% have one velocity maximum in each phase except for the highest mixture velocity of 2.04 m/s.

- The oil phase flows faster than the water phase for water cuts up to 60%.

- Regarding continuity, all two-phase velocity distributions at a certain mixture velocity that have higher velocity than single-phase flow in some regions must have lower velocities than single-phase flow in other regions. However, measurements are conducted along the vertical pipe diameter only, and not in other positions. This means that 3-D effects in the flow will be missed. Thus,

when the presented distributions are compared to the axisymmetric single-phase distributions this must be kept in mind.

- As the mixture velocity is increased the number of water cuts that are accessible to LDA becomes lower. By accessible it is meant that the entire velocity profile can be obtained.

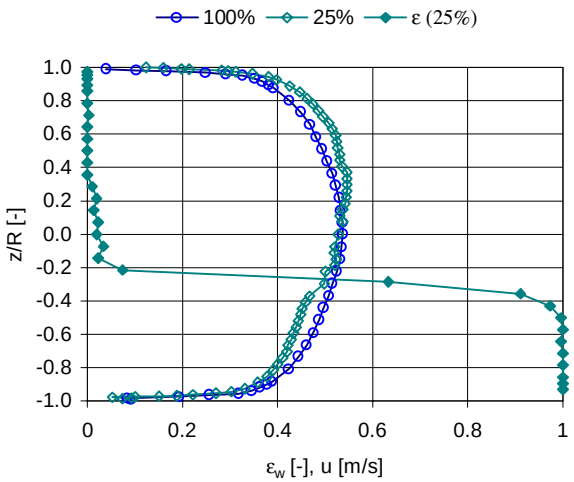

Figure 8.15 Axial velocity, 0.41 m/s.

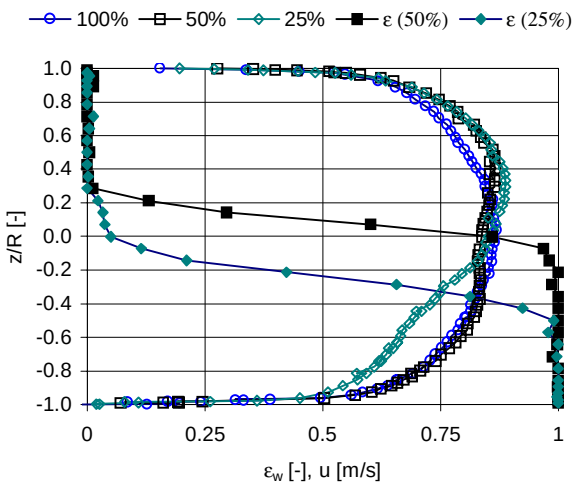

Figure 8.16 Axial velocity, 0.68 m/s.

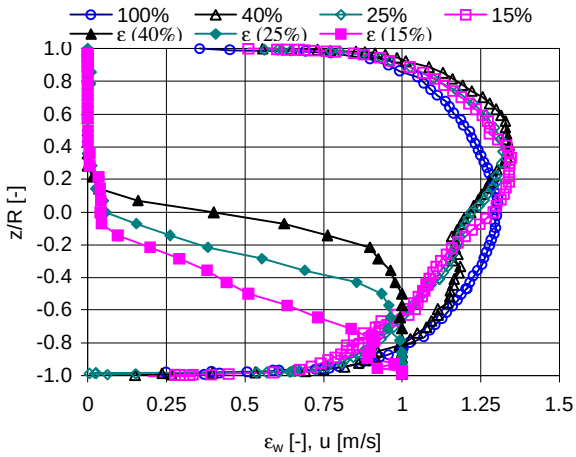

Figure 8.17a Axial velocity, 1.02 m/s.

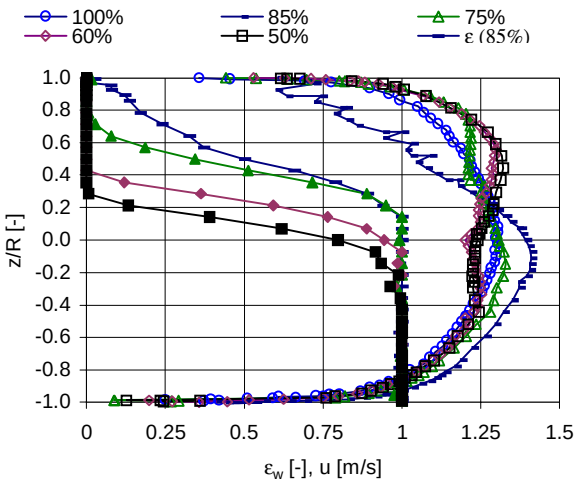

Figure 8.17b Axial velocity, 1.02 m/s.

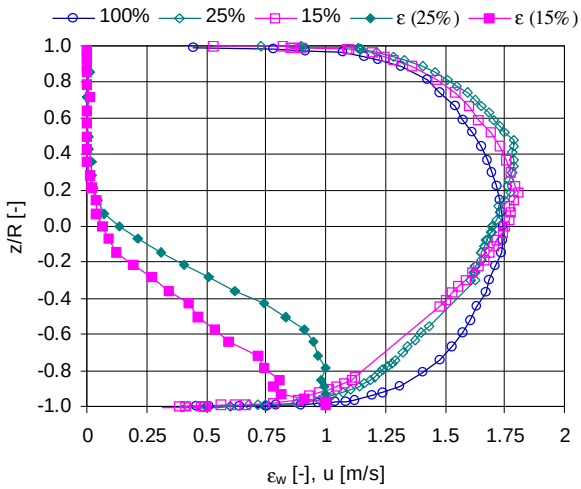

Figure 8.18a Axial velocity, 1.34 m/s.

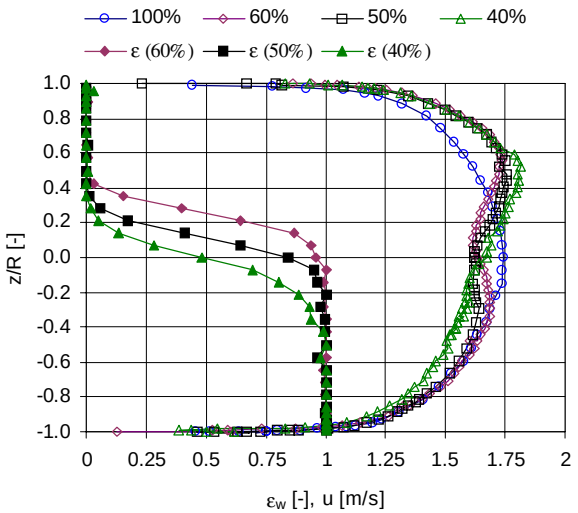

Figure 8.18b Axial velocity, 1.34 m/s.

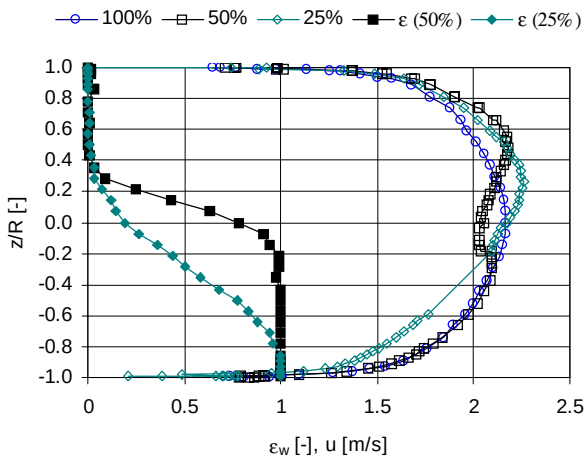

Figure 8.19a Axial velocity 1.71 m/s.

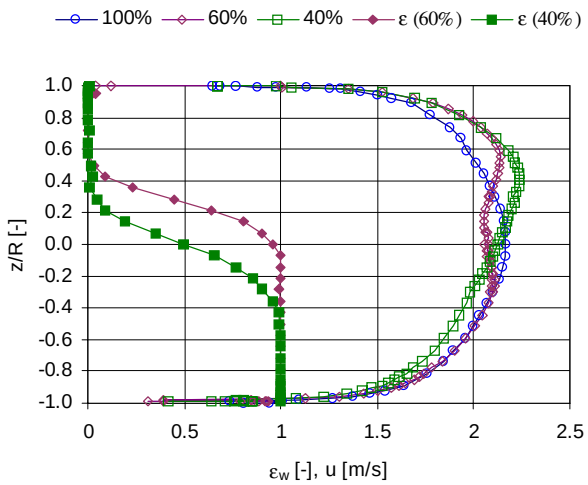

Figure 8.19b Axial velocity 1.71 m/s.

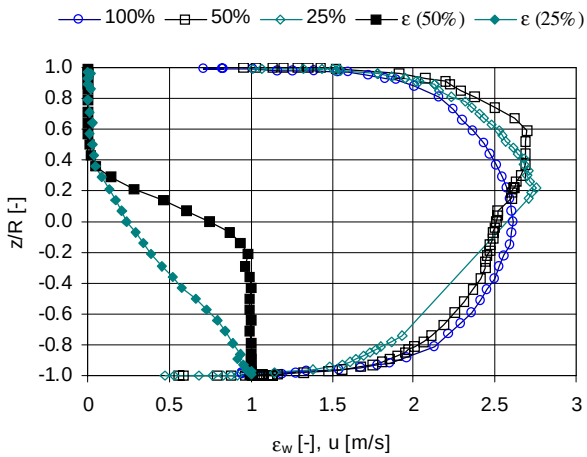

Figure 8.20a Axial velocity 2.04 m/s.

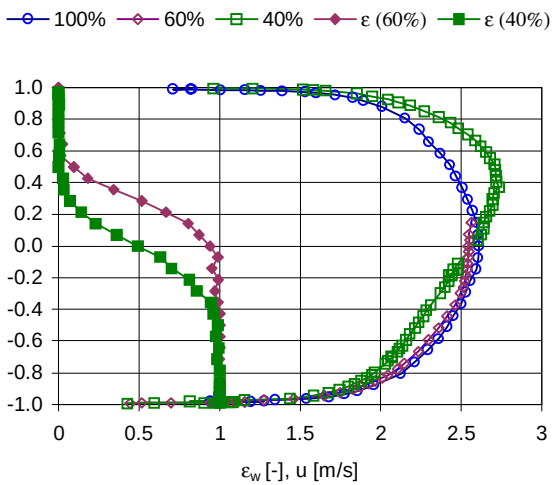

Figure 8.20b Axial velocity 2.04 m/s.

8.3.2 Rms velocity distributions

As for the axial mean velocity the distributions of rms velocities are presented at varying water cuts at constant mixture velocity. Distributions for single-phase flow of oil (sometimes referred to as 0% water cut) are presented along with those of single-phase water for comparison. Each mixture velocity will be discussed individually and in the end general remarks are summed up. The axial rms velocities are discussed first and the vertical rms velocities next.

Axial rms distributions

Figures 8.21 to 8.26 present the distributions of axial rms velocities at increasing mixture velocities. At 0.41 m/s, as observed in Figure 8.21, it is found that the distribution at 25% water cut has higher rms velocities than both 0% and 100% water cut in both the oil phase and the water phase. In general this does not apply for other mixture velocities. Another observation is that the rms velocity distributions for 0% and 100% are not equal. However this is not that strange since oil and water have different physical properties, and hence different Reynolds numbers. Measurements of u-rms at 0% water cut are done in one half of the pipe and mirrored about z/R=0. The deviation is greatest in the centre and the peaks near the wall are sharper for 100% water cut. By comparing the peak values it is seen that they are in the same order of magnitude in all three experiments (≈ 0.075 m/s).

At 0.68 m/s presented in Figure 8.22 it is observed two minimum values are observed (apart from the measurements on the wall) on the distribution curve at 50% water cut. The minimum values, one in each phase, is significantly lower than what is observed in single-phase (0.029 m/s versus 0.036 m/s). The peak values and the centre values are quite similar for 50% water cut compared to single-phase. The same applies for 25% water cut. Another observation at 25% water cut is that the rms velocities are lower in the water phase compared to 0% and 100% water cut. Even parts of the oil phase have lower rms than the single-phase distributions, and the lowest value appears in the oil phase. The flow pattern is stratified mixed (SM), and by examining Figure 8.16 once again, it is seen that the interface for 25% water cut stretches from $z/R \approx 0.2$ to $z/R \approx -0.5$. In this region, the rms velocities for 25% water cut do not differ much from single-phase. Above this region, in the oil phase, the minimum value is

found (0.032 m/s). As for 0.41 m/s, it is observed that rms velocities in pure oil are a little lower than in pure water.

In Figure 8.23, the mixture velocity is increased to 1.02 m/s. The flow patterns are either stratified wavy or stratified mixed. Here, deviations between single-phase and two-phase flows become more evident. This is seen at 15% water cut where the flow is stratified mixed with a broad interface. The u-rms measurements fluctuate in the interface region and it is believed that the great extent of waves and droplets cause the fluctuations. For the other two-phase flows the distribution curves are smoother (i.e. the interface is less disturbing). In general, rms values are lower in two-phase than in single-phase flows outside the near wall region, but occasionally peak values outside the wall region may exceed the single-phase measurements. These peaks are not identified exactly at the interface positions (as read from the hold-up distributions), but they move higher and higher in the pipe as the water cut is increased. In other words, they are probably caused by the interface. For single-phase flow the u-rms velocity is lowest in the pipe centre (except for the values at the wall). This is a consequence of lowest gradients in the mean velocity distribution in the centre. For two-phase flow the u-rms values are clearly not lowest in the centre. The reason is that the lowest mean velocity gradients for two-phase flow are located off-centre (depending on the water cut). At 50% and 60% water cut the axial mean velocities had one maximum in each phase and thus it is expected that two corresponding minimum values for u-rms exist. This seems to be the case. However, distributions of u-rms for other water cuts have more than one minimum as well. Compared to distributions of axial mean velocity the distributions of u-rms are more complex. As for the lower mixture velocities (0.41 m/s and 0.68 m/s) the measured peak values close to the wall are of similar magnitude. However, measurements conducted in this region are subjected to errors caused by refraction.

When the mixture velocity is increased to 1.34 m/s as presented in Figure 8.24 the same observations as for 1.02 m/s are made. Again lower u-rms velocities are measured in two-phase flows compared to single-phase flows except for occasional peak values. At 15% water cut the flow pattern is Do-I, and as described earlier measurements could not be obtained in the part of the pipe where droplet

concentration is highest. Above this region, the u-rms distribution almost coincides with that of 0% water cut. Even for the SM flow of 25% water cut, droplets at the interface exclude measurements in a significant part of the pipe. For all two-phase flows one minimum is found in each phase. In the oil-phase this minimum is shifted towards the upper wall as water cut is increased.

When the mixture velocity is increases further to 1.71 m/s and 2.04 m/s as presented in Figures 8.25 and 8.26 respectively, tendencies are almost the same as before. At 1.71 m/s and 25% water cut the flow is SM, but the extent of dispersion increases. For the previous mixture velocity it was seen that the 15% water cut experiment had a similar distribution as single-phase oil in the top of the pipe. Now the same is observed for 25% water cut at 1.71 m/s. At 2.04 m/s the typical minima observed in the water phase at the lower mixture velocities have disappeared. This is because the oil and the water phases no longer are separated by a distinct interface. All water cuts presented at this mixture velocity have a distribution of u-rms that is more similar to single-phase distributions than the lower mixture velocities.

For the distributions of u-rms the general remarks are as follows:

- Single-phase oil and water produce approximately equal u-rms velocity profiles.

- Two minimum values, one in each phase, are observed for several of the two-phase distributions. This is more pronounced at lower mixture velocities. The minima, which are significantly lower than for the single-phase measurements, are located at positions where the mean velocity gradients are low (see distribution curves for axial mean velocity).

- The order of magnitude for the peaks close to the wall is similar for both single-phase and two-phase. However, due to refraction, measurement errors are largest in this region of the pipe. For the same reasons it has not been attempted to locate the exact position of the peaks.

- Waves and droplets create fluctuations in the u-rms profiles if they are present to a great extent. These fluctuations are more pronounced than what was seen in the distributions of axial mean velocities.

- The u-rms velocities increase as the mixture velocity is increased (i.e as observed for single-phase flow).

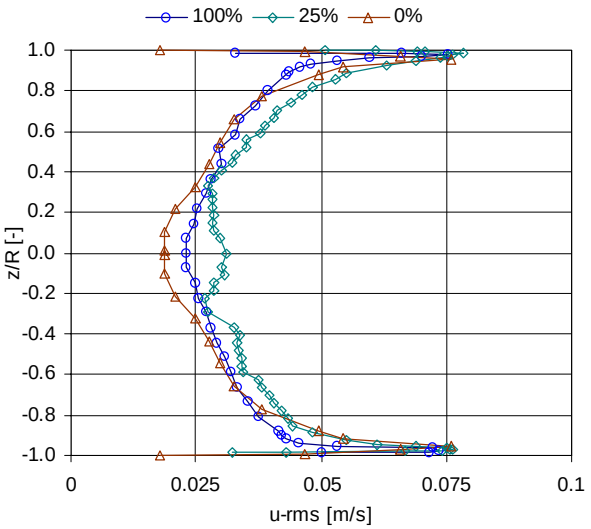

Figure 8.21 Axial rms-profiles, 0.41 m/s.

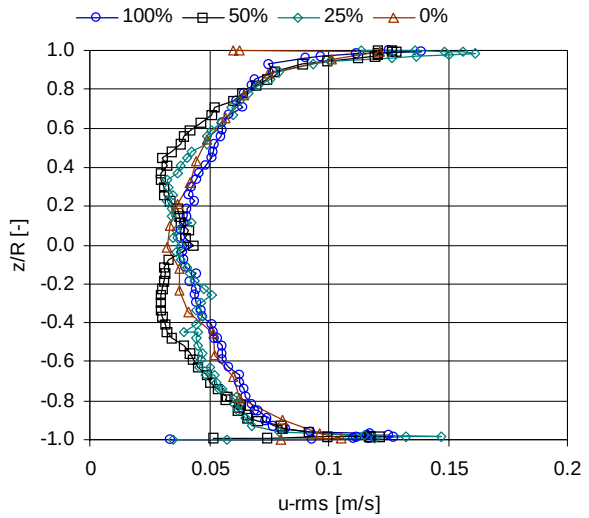

Figure 8.22 Axial rms-profiles, 0.68 m/s.

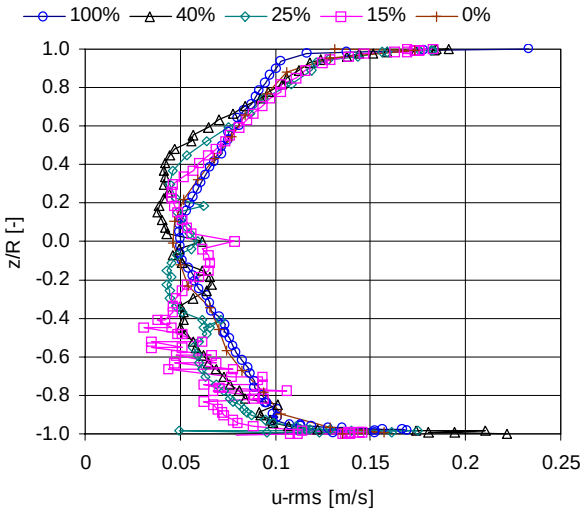

Figure 8.23a Axial rms-profiles, 1.02 m/s.

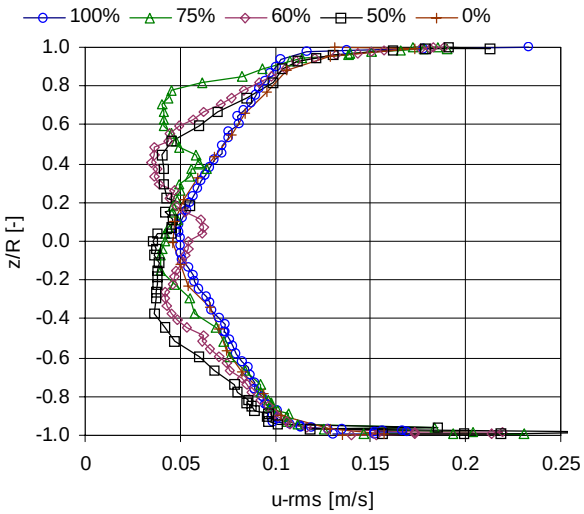

Figure 8.23b Axial rms-profiles, 1.02 m/s.

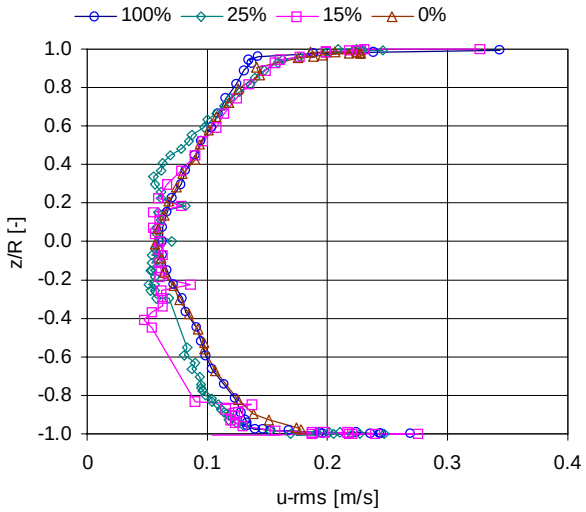

Figure 8.24a Axial rms-profiles, 1.34 m/s.

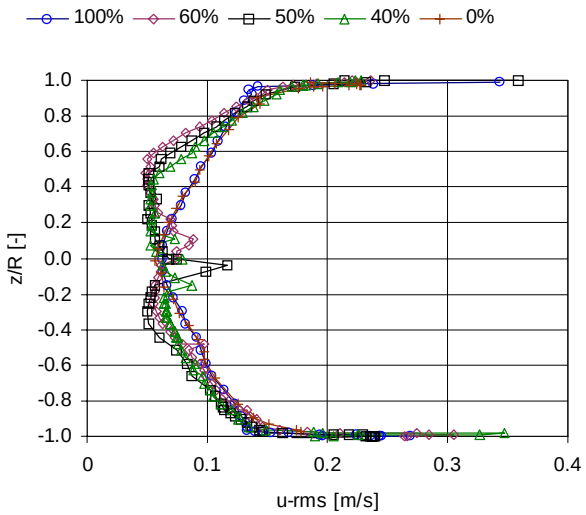

Figure 8.24b Axial rms-profiles, 1.34 m/s.

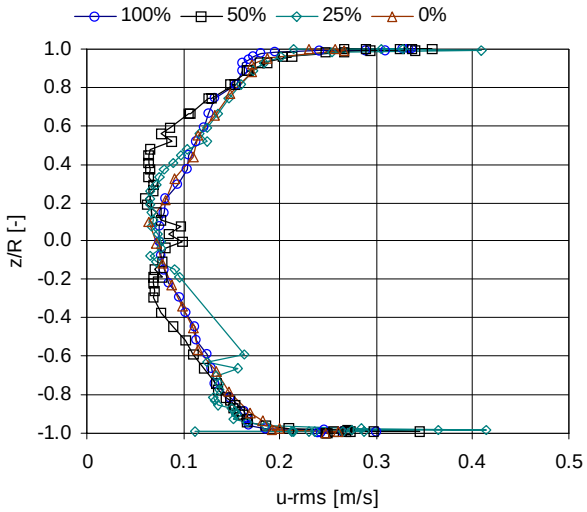

Figure 8.25a Axial rms-profiles 1.71 m/s.

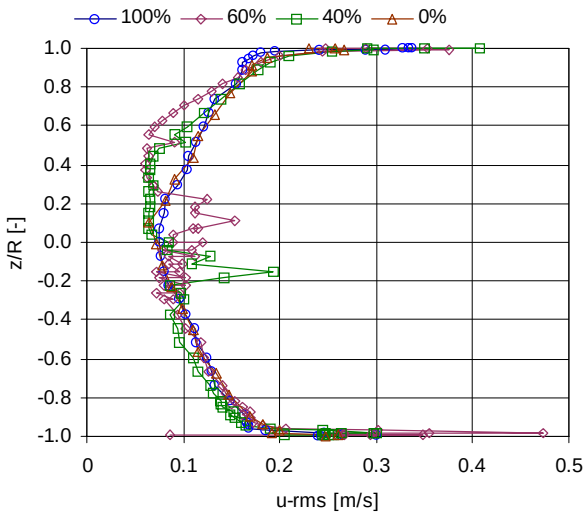

Figure 8.25b Axial rms-profiles 1.71 m/s.

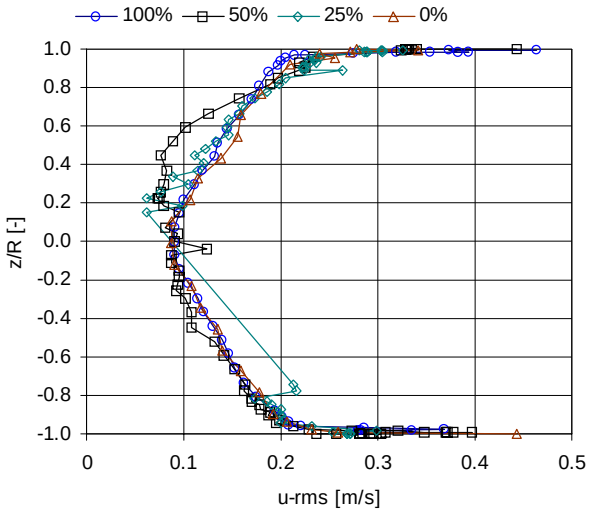

Figure 8.26a Axial rms-profiles 2.04 m/s.

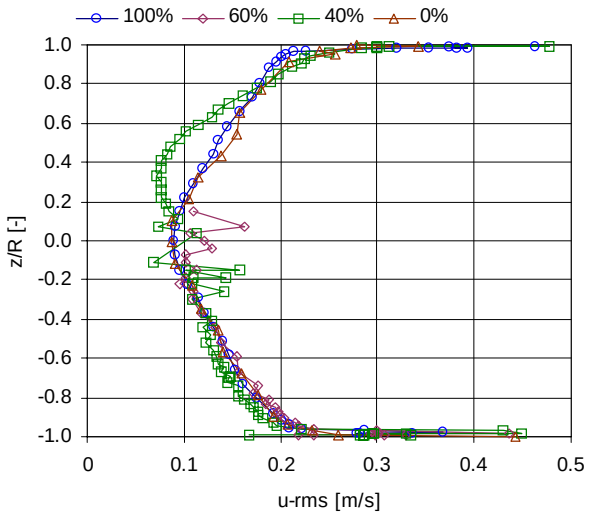

Figure 8.26b Axial rms-profiles 2.04 m/s.

Vertical rms

Figures 8.27 to 8.32 present the distributions of vertical rms velocities at increasing mixture velocities.

Figure 8.27 presents v-rms distributions at a mixture velocity of 0.41 m/s. The distribution for single-phase flow of oil (0%) and single-phase flow of water (100%) are almost identical, except for slightly lower values in the centre region for 0% water cut. Measurements of v-rms at 0% water cut are done in one half of the pipe and mirrored about z/R=0. At 25% water cut the v-rms distribution is significantly lower in the water phase and in the interface region compared to single-phase (see Figure 8.15 for position of the interface). The minimum value is 0.012 m/s at z/R=-0.37. Close to the wall the maximum v-rms in each phase is found. In the water-phase the peak is lower at 25% water cut compared to single-phase, and in the oil phase the peak is higher. The positions of the peaks are easier to identify for v-rms than for u-rms since the u-rms peaks are located closer to the wall. Comparing 25% water cut with 0% or 100% the peak positions are found at equal z/R, but the peak in the oil phase is more steep for the two-phase experiment.

At 0.68 m/s as shown in Figure 8.28, the values at 0% is clearly higher than those at 100%. Again the measurements of two-phase flow display lower values in the region between the “wall-peaks”, (i.e. in the centre part of the pipe). Both at 25% and 50% water cut the interface creates a peak. The distribution at 25% water cut has lower v-rms in the water-phase than observed at 50% water cut. The opposite is seen in the oil phase except for the peak values close to the wall. For 50% water cut the lower peak close to the wall is almost as high as that for 100%. Compared to 0% water cut the upper peaks at 25% and 50% water cut are slightly higher and located closer to the wall.

At 1.02 m/s presented in Figure 8.29, water cuts from 15% to 75% are examined. The peaks at the lower wall become higher as the water cut is increased. At 15% and 25% water cut the peak is lower than for 100% water cut. At the other water cuts the peak is higher than for 100%. The peak at the upper wall is of the same order of magnitude for all two-phase experiments and also similar to 0% water cut. As for the lower

mixture velocities the interface creates a peak in the v-rms distribution. From the figure it is also seen that at 15% water cut the interface is disturbing the measurements over a larger part of the pipe than at the other water cuts. This is because the high content of droplets and waves at the interface. The flow pattern is classified as stratified mixed, but as seen from the distribution of the water fraction in Figure 8.17 the interface is quite wide.

The same observations that are made for 1.02 m/s also holds for 1.34 m/s to 2.04 m/s as can be seen in Figures 8.30 to 8.32. As the mixture velocity is increased, the flow becomes more and more dispersed. Especially the interfaces become wider, and thus some parts of the distribution curves are without markers (e.g. 25% water cut at 1.71 m/s and 2.04 m/s). As mentioned before the 60% water cut experiment at 2.04 m/s contains only measurements in the water phase.

The general remarks that sum up the v-rms measurements are as follows:

- The distributions of v-rms displays higher values for single-phase oil compared to single-phase water especially outside the center region of the pipe. The exception is the distribution at 0.41 m/s. The differences between 0% and 100% water cut are greater for v-rms than for u-rms. One reason may be due to optical disturbances, which is greater for the beams measuring the vertical velocity than the ones measuring horizontal velocity.

- The interface creates a peak similar to that observed for u-rms. Sometimes this result in two minima, one in each phase, at intermediate water cuts with a sharp interface.

- For all mixture velocities the v-rms values are lower for two-phase flow compared to single-phase flow in the region between the “wall peaks” (i.e. from the center of the pipe towards each of the peaks located close to the walls). The exception is the peak that is induced by the interface. This peak has generally higher v-rms values than both 0% and 100% at the same position in the pipe.

- The peak in the water phase at the lower wall increases often with increasing water cuts for each mixture velocity. In general, the peaks are lower for two-phase flows than for single phase flows. However, at 1.02 m/s it is higher for water cuts above 50%.

- The peak in the oil phase at the upper wall is similar in magnitude for two-phase flow and flow of single-phase oil.

- As for u-rms, the magnitude of v-rms increases with mixture velocity for both single-phase and two-phase flows.

- Since the wall-peaks are located further away from the wall for v-rms compared to u-rms, it is easier to compare single-phase and two-phase measurements.

- Comparison of u-rms and v-rms distributions at the same mixture velocity reveals that the peaks close to the wall in general are more than three times larger in magnitude in u-rms distributions than in v-rms distributions. Also the peaks are located closer to the wall in u-rms distributions than in v-rms distributions. The minimum values located closer to the center of the pipe are more similar in magnitude, but in general a little higher in the u-rms distributions.

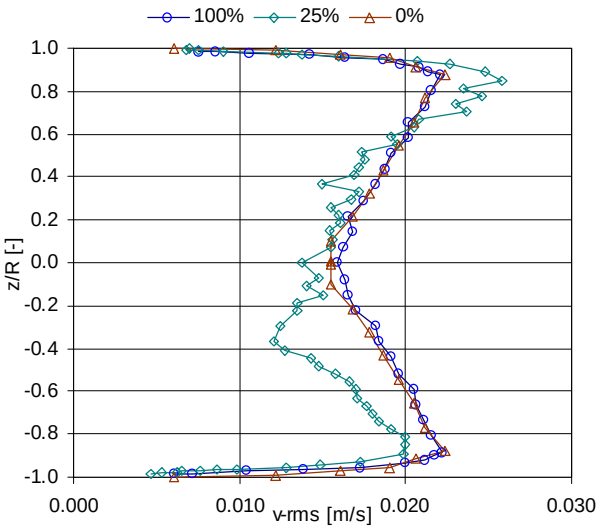

Figure 8.27 Vertical rms-profiles, 0.41 m/s.

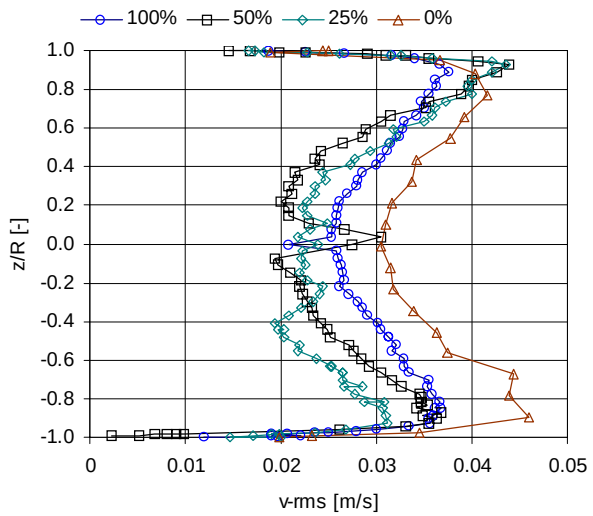

Figure 8.28 Vertical rms-profiles, 0.68 m/s.

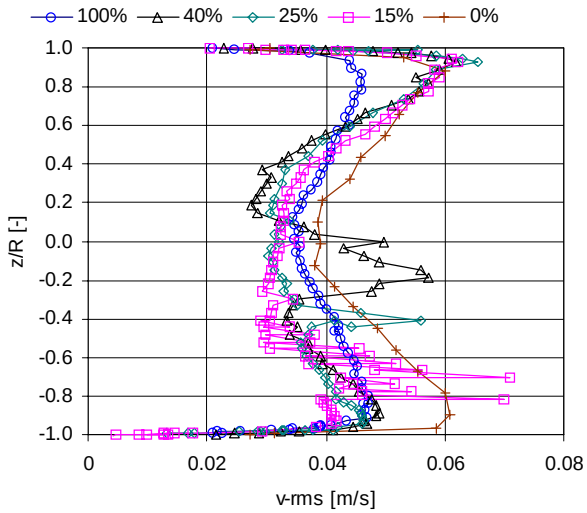

Figure 8.29a Vertical rms-profiles, 1.02 m/s.

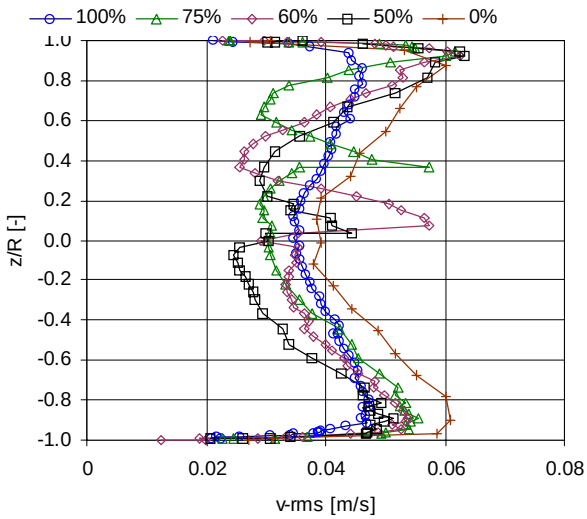

Figure 8.29b Vertical rms-profiles, 1.02 m/s.

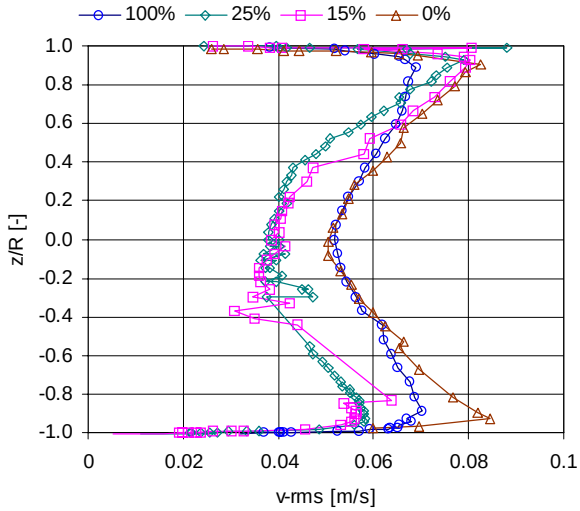

Figure 8.30a Vertical rms-profiles, 1.34 m/s.

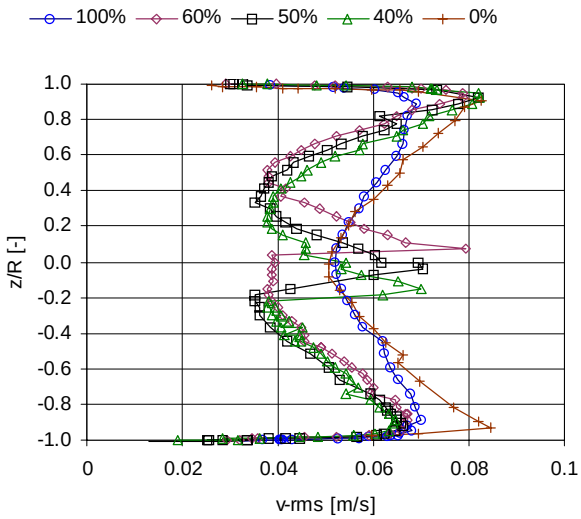

Figure 8.30b Vertical rms-profiles, 1.34 m/s.

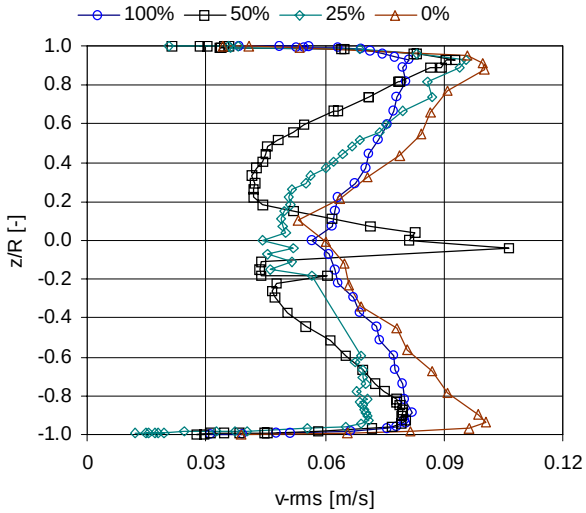

Figure 8.31a Vertical rms-profiles 1.71 m/s.

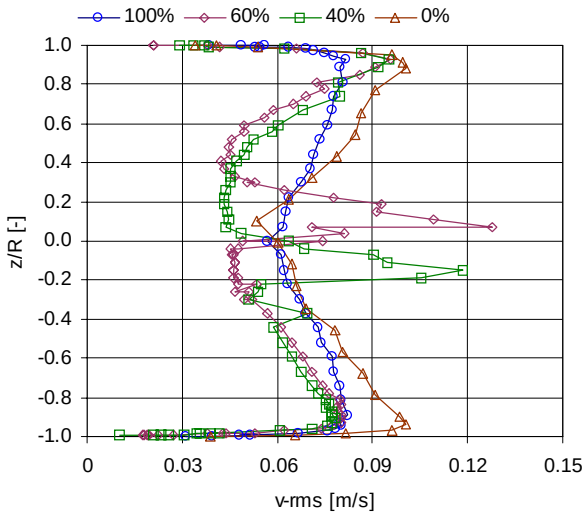

Figure 8.31b Vertical rms-profiles 1.71 m/s.

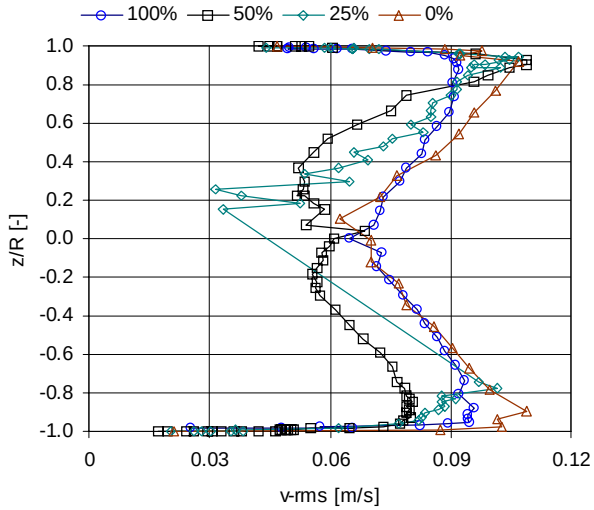

Figure 8.32a Vertical rms-profiles 2.04 m/s.

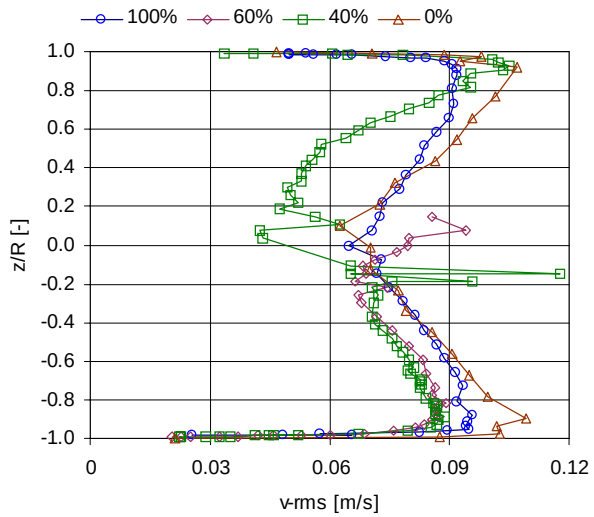

Figure 8.32b Vertical rms-profiles 2.04 m/s.

8.3.3 Axial turbulence intensity distributions

The turbulence intensity, that is the ratio of u-rms to u-mean multiplied by 100%, is calculated for the same experiments discussed in the previous sections. The resulting distributions across the pipe diameter for the various mixture velocities are presented in Figures 8.33 to 8.38. All distribution curves are cut off at 30%. This is because measurements very close to the wall have low mean velocity and high rms velocity, resulting in high turbulence intensity. The near wall measurements are also subjected to optical disturbances. Thus, focus is set on the interface regions of the pipe (i.e. the graphs are scaled in a manner that differences in the interface regions are revealed). The distribution of axial turbulence intensity has a similar shape as the distribution of axial rms velocity.

The distribution of turbulence intensity for the case of 25% water cut at 0.41 m/s is compared to that of single-phase water in Figure 8.33. The largest difference is found in the water phase, where the intensity is higher than in single-phase. Above the interface the two-phase distribution approaches the single-phase distribution, but apart from a small area around z/R=0.35, it never becomes lower. The minimum turbulence intensity at 25% water cut is 5% at that position, whereas the minimum at 100% is 4.3% in the centre. The highest intensity is found close to the wall. As seen from the single-phase intensities presented in Section 8.2 the intensity was above 80% for some cases. The same is observed for the two-phase water cuts, but to focus on the interface regions this is not shown in the graphs.

At 0.68 m/s it can be seen from Figure 8.34 that the minimum turbulence intensity at 50% water cut (3.5% in both phases) is lower than for 100% water cut (4.2%). Closer to the wall the distributions approach each other and become almost identical. Similarities are higher between 25% and 100% water cut. Here, the minimum is located in the oil phase (3.6%).

Apart from the interface regions for each of the two-phase experiments, the intensities at 1.02 m/s presented in Figure 8.35 are below the distribution at 100% water cut. The minimum is between 2.8% and 3.2% for the two-phase distributions and 3.8% at 100% water cut.

At 1.34 m/s shown in Figure 8.36, the minimum varies between 2.9% and 3.1% for the two-phase flows and 3.5% for single-phase flow. Deviations from 100% increase with water cut. For the case of 1.71 m/s presented in Figure 8.37 the minimum turbulence intensity of all two-phase flows are 2.8% compared to 3.5% at 100 % water cut. Finally, at 2.04 m/s displayed in Figure 8.38, the minimum intensity varies between 2.3% and 2.8% for the two-phase flows whereas it is 3.4% at 100% water cut.

The general remarks are as follows:

- For most mixture velocities the turbulence intensities for two-phase flow are lower than for single-phase flow

- The minimum turbulence intensity for single-phase flow decreases from 4.5% to 3.4% as the mixture (bulk) velocity increases from 0.41 to 2.04 m/s. For the two-phase flows the minimum intensities are lower with the exception of 25% water cut at 0.41 m/s.

- In some experiments the interface creates a peak with intensities from 5% to 10% (e.g. 50% water cut at 1.34 m/s and both 40% and 60% water cut at 1.71 m/s).

- At the walls the intensities rise to values that range from 30% to 90%. No significant differences between single-phase and two-phase flows are observed here, and thus to focus on the interface regions the distributions are cut off at 30 %.

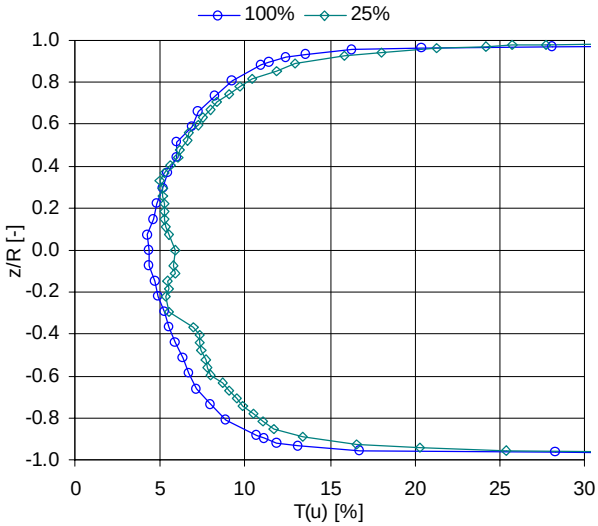

Figure 8.33 Axial turbulence intensity, 0.41 m/s.

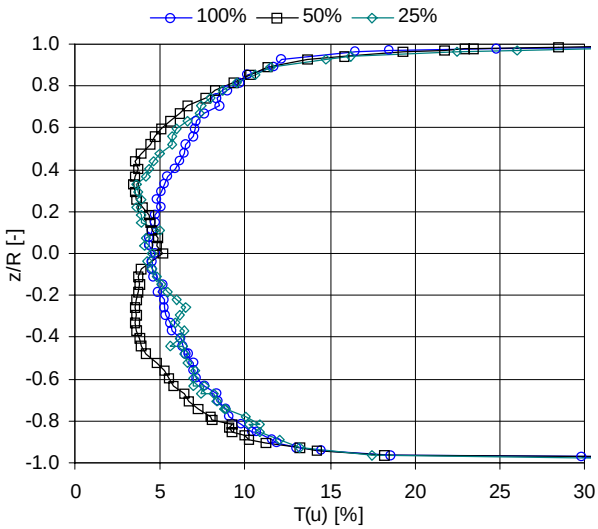

Figure 8.34 Axial turbulence intensity, 0.68 m/s.

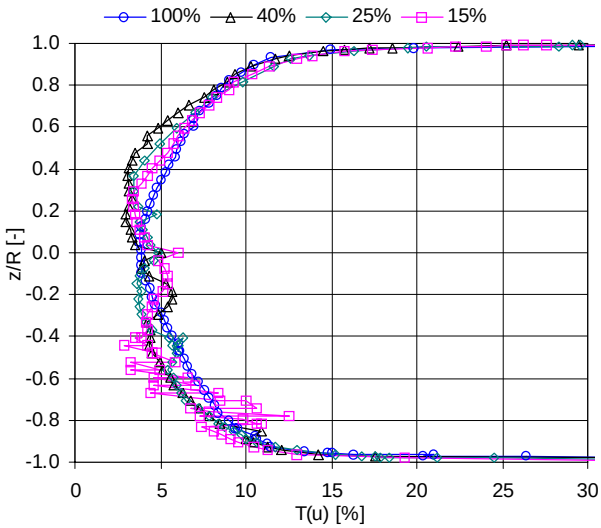

Figure 8.35a Axial turbulence intensity, 1.02 m/s.

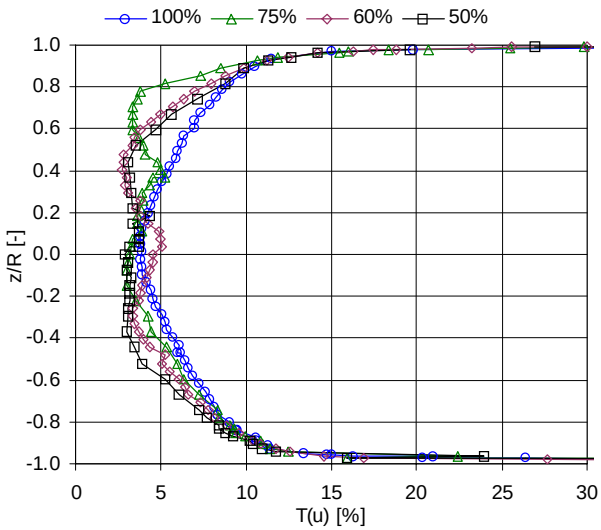

Figure 8.35b Axial turbulence intensity, 1.02 m/s.

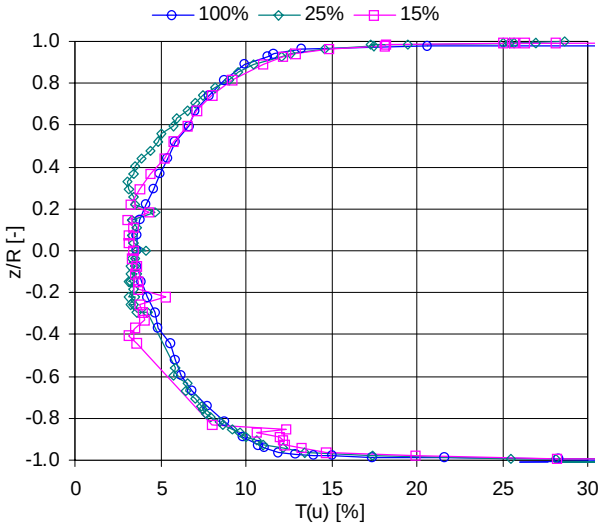

Figure 8.36a Axial turbulence intensity, 1.34 m/s.

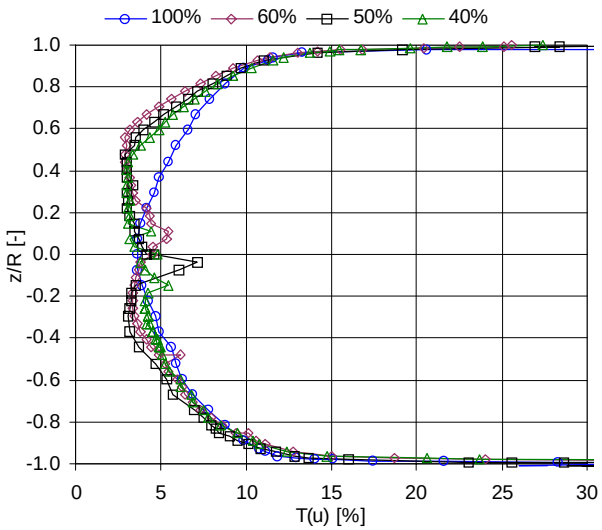

Figure 8.36b Axial turbulence intensity, 1.34 m/s.

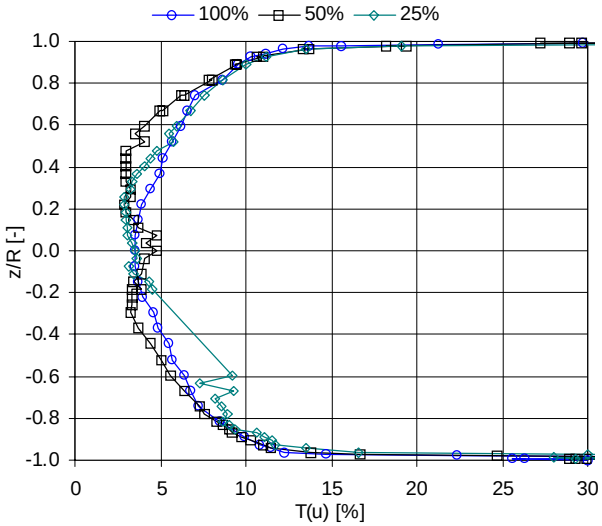

Figure 8.37a Axial turbulence intensity, 1.71 m/s.

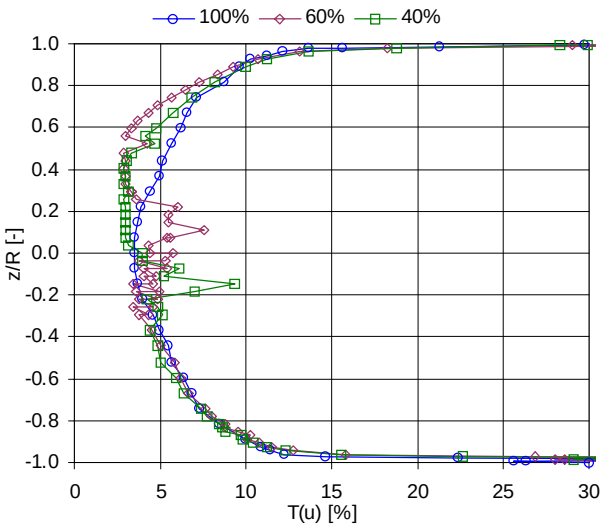

Figure 8.37b Axial turbulence intensity, 1.71 m/s.

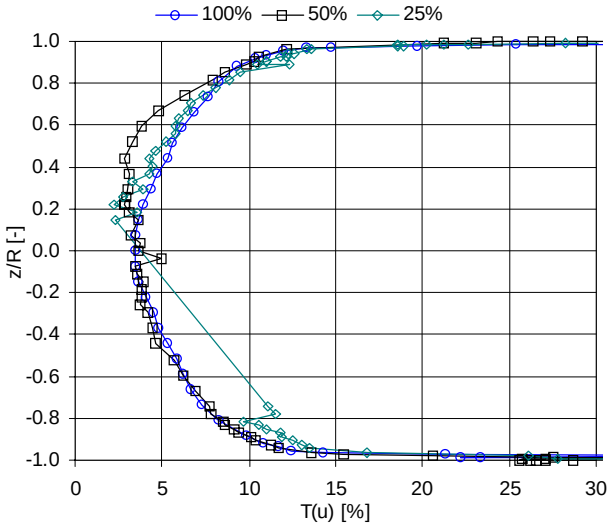

Figure 8.38a Axial turbulence intensity, 2.04 m/s.

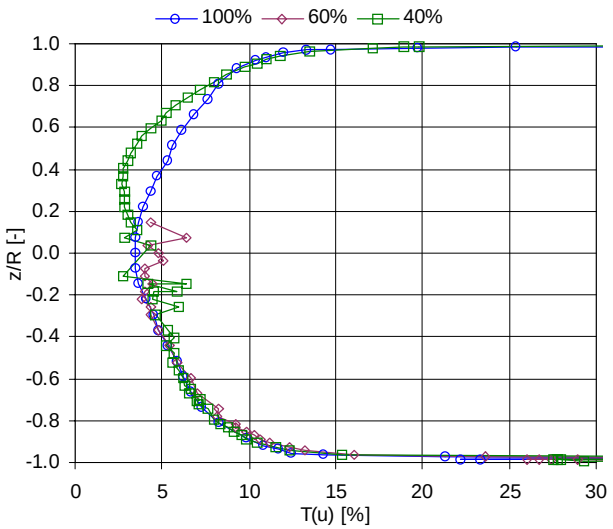

Figure 8.38b Axial turbulence intensity, 2.04 m/s.

8.3.4 Cross-moments and Reynolds stress distributions

In this section, cross moments for two-phase flow are calculated and presented along with cross-moments for single-phase flow. In Section 8.2 the Reynolds stresses were not presented since the distributions across the pipe diameter were identical to the distributions of cross-moments. For two-phase flow of oil and water this is no longer the case. The reason is the difference in density. Thus, both cross-moment and Reynolds stress distributions are presented for each mixture velocity.

At 0.41 m/s the distributions of cross-moments and Reynolds stresses are presented in Figures 8.39a and 8.39b, respectively. When the distributions of u-rms and v-rms were presented it was seen that single-phase oil and single-phase water had slightly different shapes. The differences become more evident when the cross-moments are studied. In general, the observed peaks close to the wall are higher in pure oil (0%) than in pure water (100%). This applies for all mixture velocities. However, when cross-moments in each phase are transformed into Reynolds stresses by multiplication by the density for each phase, the height of the peaks become almost identical. And by this observation it is time to analyze the effects that this has on the mean velocity distributions that were presented in Section 8.3.1. Here, it was observed that the maximum velocity in the oil phase was higher than in the water phase for 50% and 60% water cut.

Consider the comparison between flow of single-phase oil and single-phase water. The density and viscosity data of the liquids are 790 kg/m^3 and 0.0016 Pas for oil and 995 kg/m^3 and 0.001 Pas for water. Hence, kinematic viscosities are ν_o=2.025 10^{-6} m^2/s and ν_w= 1.005 10^{-6} m^2/s. The Reynolds number is given by:

$$\mathrm{Re} = \frac{u_b\, d_i}{\nu} \tag{8.25}$$

If we look at the Reynolds number ratio, it is inversely proportional to the ratio of kinematic viscosities:

$$\frac{\mathrm{Re}_o}{\mathrm{Re}_w} = \frac{\nu_w}{\nu_o} = 0.4962 \tag{8.26}$$

where it is assumed equal velocity and pipe diameter.

The wall friction is a function of the Reynolds number, and by the use of the Blasius equation $f=0.312\ \mathrm{Re}^{-0.25}$ in Equation 8.11 we obtain:

$$\frac{\tau_{wall,o}}{\tau_{wall,w}} = \frac{\mathrm{Re}_o^{-0.25}}{\mathrm{Re}_w^{-0.25}} \frac{\rho_o}{\rho_w} = 0.4962^{-0.25} \frac{790}{995} = 0.946 \tag{8.27}$$

Since this means that the wall shear stress in oil flow is lower than in water flow at equal velocities, it is fair to assume that the oil phase in a two-phase flow at 50% water cut should flow faster. So, based on this analytical approach the observations made in Section 8.3.1 are explained. The distributions of Reynolds stresses that are discussed in this section should also verify this.

Bird et al. (1960) conducted a similar analysis of equal amounts of two immiscible fluids flowing between two flat parallel plates. The difference between their analysis and the one presented above is that they used a less dense, less viscous (dynamic) fluid over a denser, more viscous fluid. Their analysis applied to laminar flows. They concluded that the maximum mean velocity in the direction of flow was well inside the less dense phase (i.e. above the interface, which is in the centre of the channel). They also stated that the distribution of shear stress was zero at the position of the maximum mean velocity. This was called the “plane of zero shear”. The wall shear was lower in the less dense, less viscous phase.

In the system presented here, the oil is less dense, but more viscous than water. However, the density ratio outweighs the viscosity ratio and the wall shear is, as

shown above, lower in the oil phase than in the water phase. The difference in wall shear as shown in Equation 8.27 is rather small, and may be counterbalanced by other effects such as the ability to wet the wall. Examination of the Reynolds stress profiles presented in the figures in the end of this section will confirm that the wall shear ratios deviate from the theoretical predictions using in Equation 8.27.

Back at 0.41 m/s in Figure 8.39a it can be seen that the distribution of cross-moments at 25% water cut is different from the single-phase distributions. This is especially seen in the middle of the pipe. Here, the cross-moments are close to zero, not only in the exact centre, but also a distance away from the centre. In fact, the distribution shows that the cross-moments sometimes are lower than zero in the upper half of the pipe and higher than zero in the lower half of the pipe. This is in great contrast to single-phase flow. When the wall is approached, the distribution shows that the gradient is steeper. In the oil phase the peak is higher than in single-phase oil, whereas it is a little lower in the water phase compared to single-phase water.

When the Reynolds stress distribution at 25% water cut presented in Figure 8.39b is viewed, it is seen that the differences between the phases becomes smaller compared to the similar distribution of cross-moments. This is due to the density ratio, which is 0.8. The ratio of the peaks is 1.93 in the cross-moments distribution and 1.54 in the Reynolds stress distribution.

The distributions at 0.68 m/s are presented in Figure 8.40. In general the same observations are made. Deviations from the single-phase distributions are significant for both 25% and 50% water cut. At 50% water cut the cross-moments are close to zero from z/R=-0.4 to z/R=0.4. This means that the Reynolds stresses are damped by the nature of the interface. The peak in the oil-phase is higher in two-phase flow than in single-phase flow, especially for the cross-moment distributions. For the peak in the water phase the differences are less evident. The lower peak at 50% water cut is almost equal to the peak in single-phase water. At 25% water cut the peaks are less than for 50% water cut.

When the mixture velocity is increased to 1.02 m/s as presented in Figure 8.41 a-d, all two-phase flow experiments show the same dampening that is observed at the lower velocities. Depending on the position of the interface, the dampening covers different parts of the diameter. What is worth noticing is that the extension of the dampening is much wider than the interface itself. For the case of 15% water cut it even looks as though the dampening occurs above the interface. In addition to the deviations surrounding the centre of the pipe, the same deviations as before are found by comparison of the peaks in the oil phase. Comparing the peaks in the water phase with respect to single-phase and two-phase flow reveals that differences are present for high water cuts. This is seen from Figure 8.41b or d.

Measurements at the mixture velocity of 1.34 m/s are presented in Figure 8.42a-d. Apparently the observations are as before. However, it appears that the peaks in the oil phase are almost equal in single-phase oil and in the two-phase experiments, particularly at low water cuts (Figure 8.42a or c). At low water cuts the peaks in the water phase are lower than in single-phase water.

Measurements at the two highest mixture velocities, 1.71 m/s and 2.04 m/s are presented in Figures 8.43 and 8.44, respectively. The flow becomes more dispersed. By looking at the lower half of the pipe it can be seen that the two-phase flows are more similar to single-phase flow as that was seen for lower velocities (i.e. the dampening effect has diminished). In the upper half large differences are still present and the dampening is seen. However, it appears that the zero values no longer occur as high in the pipe, as seen for lower mixture velocities.

To sum up the observations above, the following applies:

- *Cross-moments versus Reynolds stresses.* In general the distributions of Reynolds stresses are more similar with respect to differences between the water phase and the oil phase. This is because the lower density of oil reduces the peak in the oil phase when cross-moments are turned into Reynolds stresses.

- *Single-phase oil versus single-phase water.* It is not always seen that the extrapolated wall shear is lower in the single-phase oil (0%) than in the single-phase water (100%). The reason may be that the extrapolation is inaccurate. Another aspect that should be kept in mind is that the measurements are conducted along the vertical pipe diameter only. This means that the wall shear is calculated only in two points on the wall. Thus, from these measured distributions of Reynolds stresses a conclusion of the connection between wall shear stress and fluid velocity cannot be given. (i.e. it is not that evident that the oil phase should flow faster than water at 50% water cut as predicted in the analysis presented above). A larger part of the pipe wall must be investigated before a final conclusion can be made.

- *Interfacial dampening of stresses.* The cross-moments and hence the Reynolds stresses are damped in the regions surrounding the interfaces. Compared to single-phase, which has zero values only at the walls and in the centre, the two-phase distributions have zero or almost zero values over a large part of the diameter. It seems like the interface acts like an oscillating wall, preventing turbulent diffusion across it. This is seen particularly at mixture velocities lower than 1.71 m/s. The dampening effect seems to be reduced at the two highest mixture velocities. This is probably because the interface is less distinct and that eddies are allowed to cross it. The dampening zone is wider than the interfacial zone. This is seen for instance at 0.68 m/s and 50% water cut. Here the flow pattern is stratified smooth (i.e. sharp without waves and droplets) and the interfacial zone is only a few mm wide. Nevertheless the distribution of Reynolds stresses show that the zone, in which the values are zero, is almost 20 mm wide.

- *u-rms and v-rms versus cross-moments and Reynolds stresses.* As peaks were observed at the interface for u-rms and v-rms the distributions of cross-moments and Reynolds stresses are smooth. The reason is probably that the peaks in the velocity fluctuations cancel each other out.

- *Wall peaks*. In the upper half of the pipe, in the oil phase, it is observed that the peaks are equal to or higher than in two-phase flows compared to single-phase oil. In the lower half of the pipe both higher and lower peaks are found in two-phase flow compared to single-phase water.

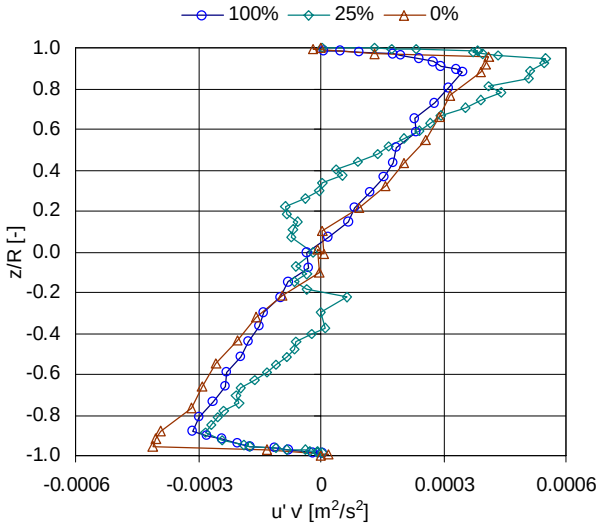

Figure 8.39a Cross moments ($\overline{u'v'}$), 0.41 m/s.

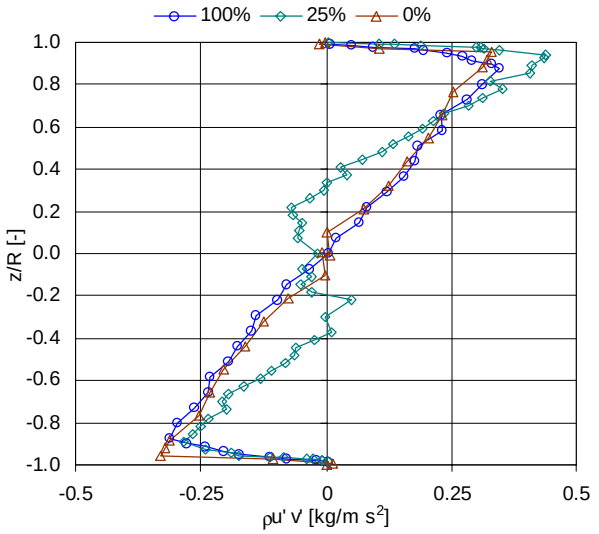

Figure 8.39b Reynolds stresses ($\overline{\rho u'v'}$), 0.41 m/s.

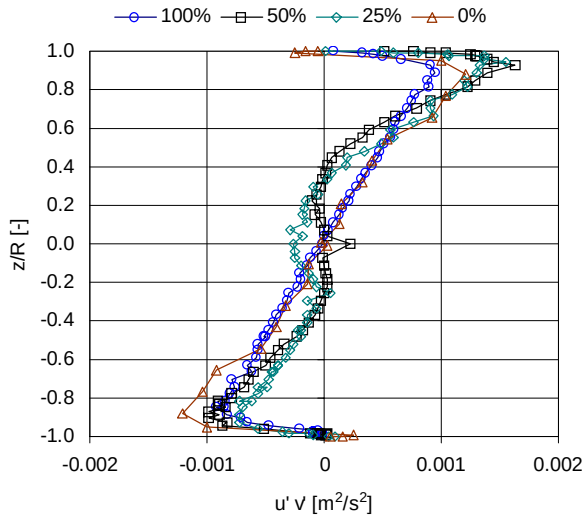

Figure 8.40a Cross moments ($\overline{u'v'}$), 0.68 m/s.

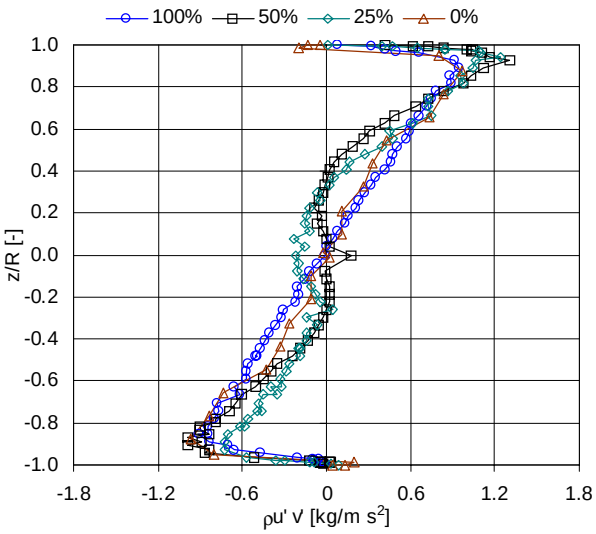

Figure 8.40b Reynolds stresses ($\overline{\rho u'v'}$), 0.68 m/s.

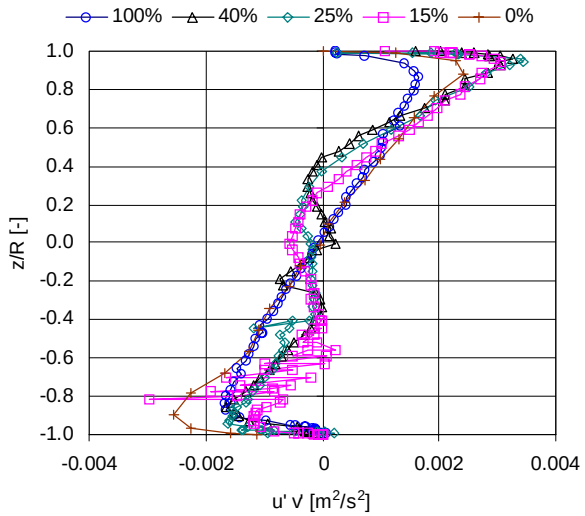

Figure 8.41a Cross moments ($\overline{u'v'}$), 1.02 m/s.

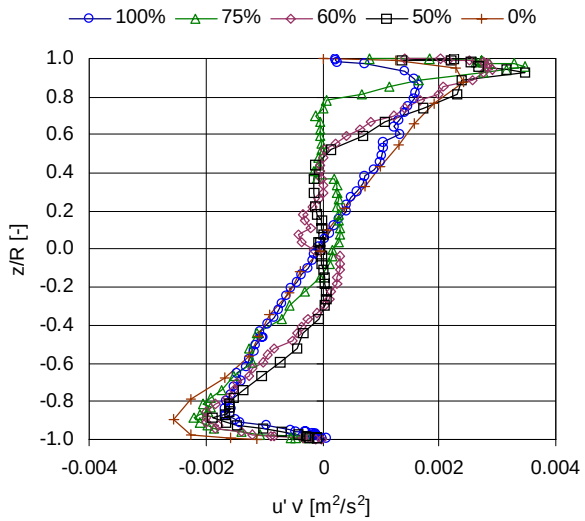

Figure 8.41b Cross moments ($\overline{u'v'}$), 1.02 m/s.

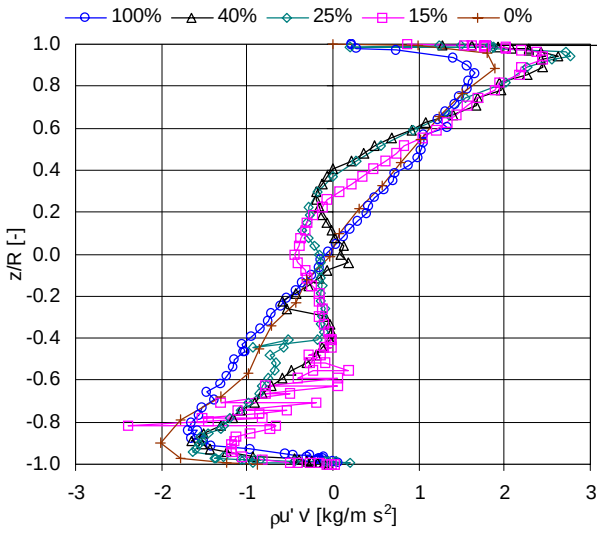

Figure 8.41c Reynolds stresses ($\overline{\rho u'v'}$), 1.02 m/s.

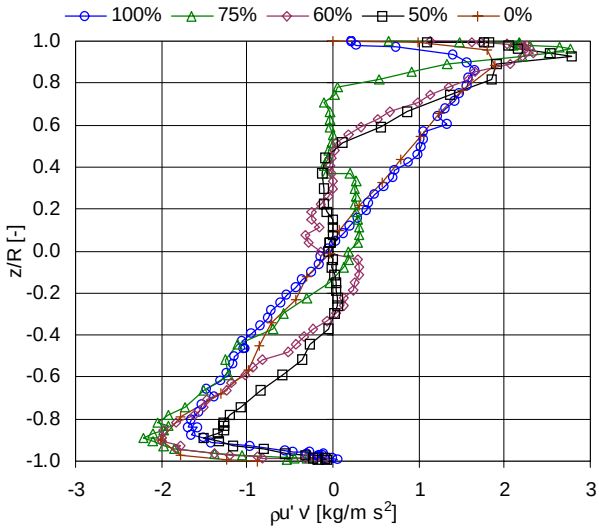

Figure 8.41d Reynolds stresses ($\overline{\rho u'v'}$), 1.02 m/s.

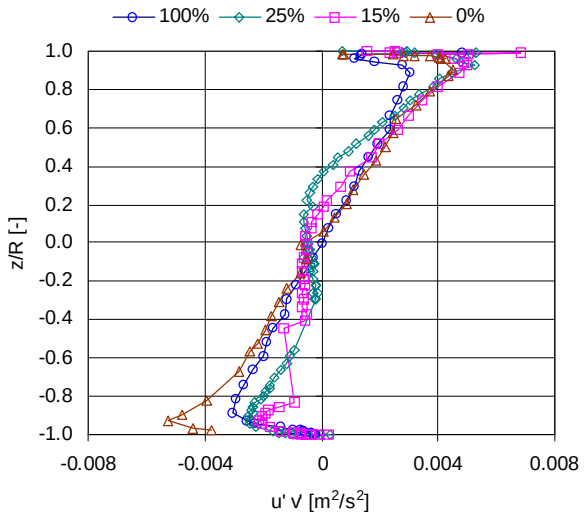

Figure 8.42a Cross moments ($\overline{u'v'}$), 1.34 m/s.

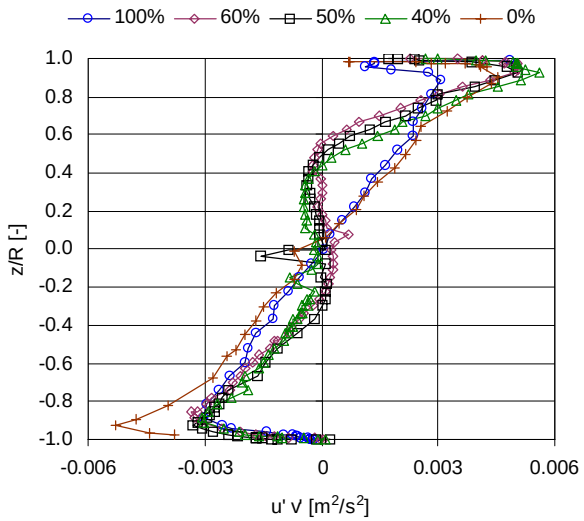

Figure 8.42b Cross moments ($\overline{u'v'}$), 1.34 m/s.

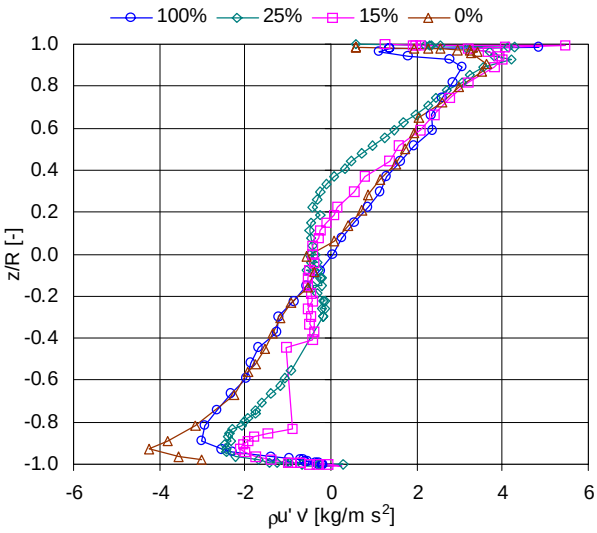

Figure 8.42c Reynolds stresses ($\overline{\rho u'v'}$), 1.34 m/s.

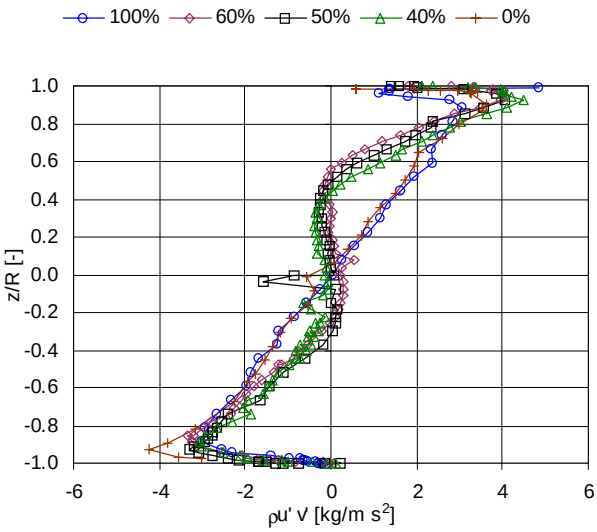

Figure 8.42d Reynolds stresses ($\overline{\rho u'v'}$), 1.34 m/s.

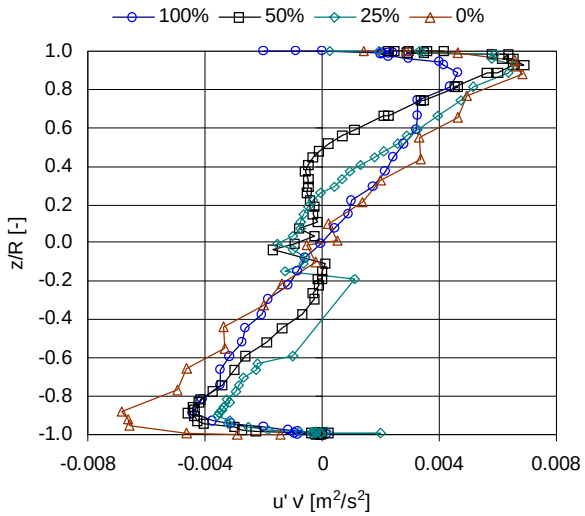

Figure 8.43a Cross moments ($\overline{u'v'}$), 1.71 m/s.

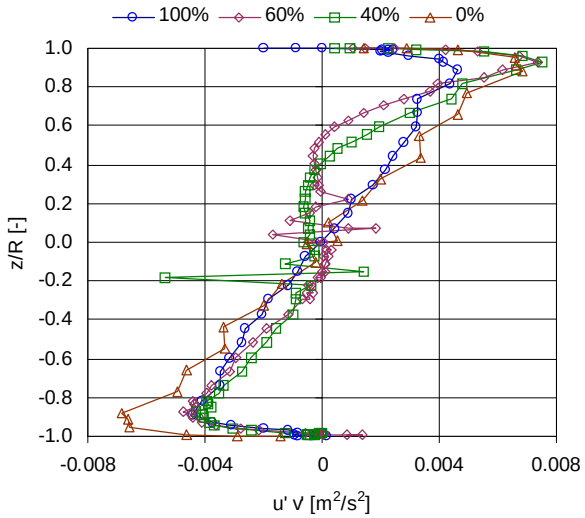

Figure 8.43b Cross moments ($\overline{u'v'}$), 1.71 m/s.

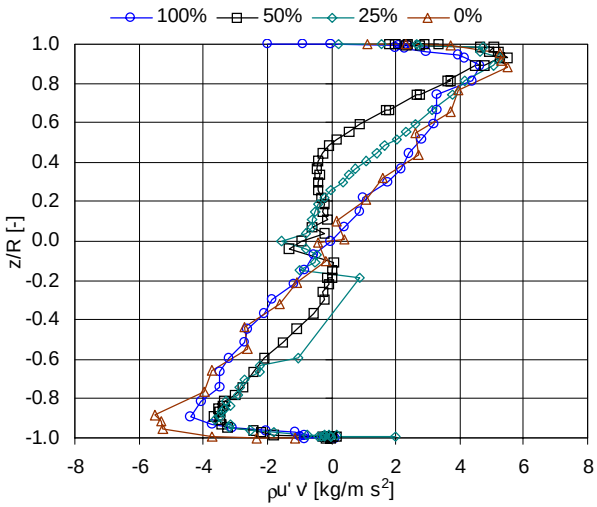

Figure 8.43c Reynolds stresses ($\overline{\rho u'v'}$), 1.71 m/s.

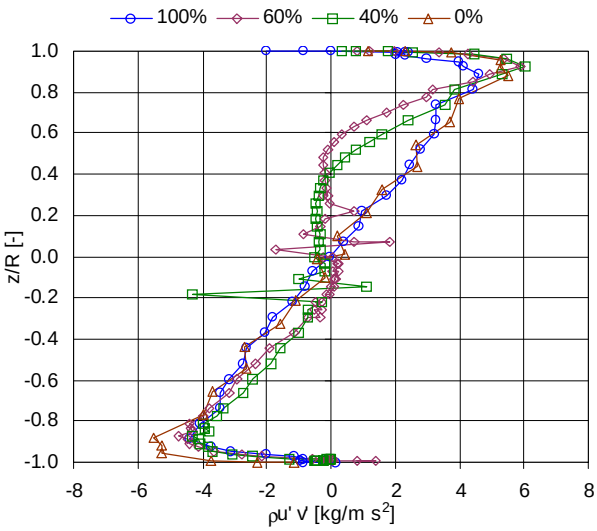

Figure 8.43d Reynolds stresses ($\overline{\rho u'v'}$), 1.71 m/s.

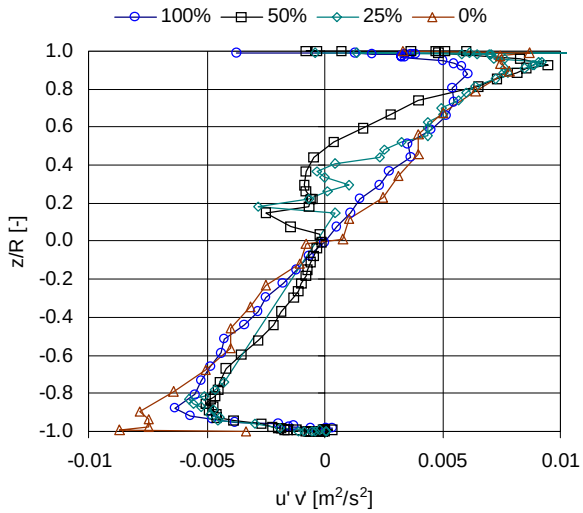

Figure 8.44a Cross moments ($\overline{u'v'}$), 2.04 m/s.

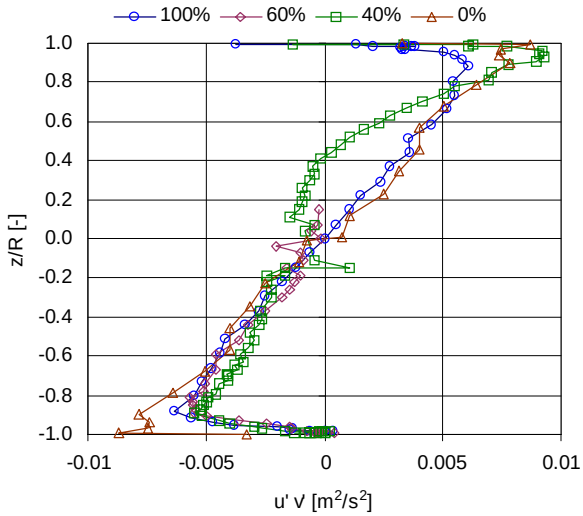

Figure 8.44b Cross moments ($\overline{u'v'}$), 2.04 m/s.

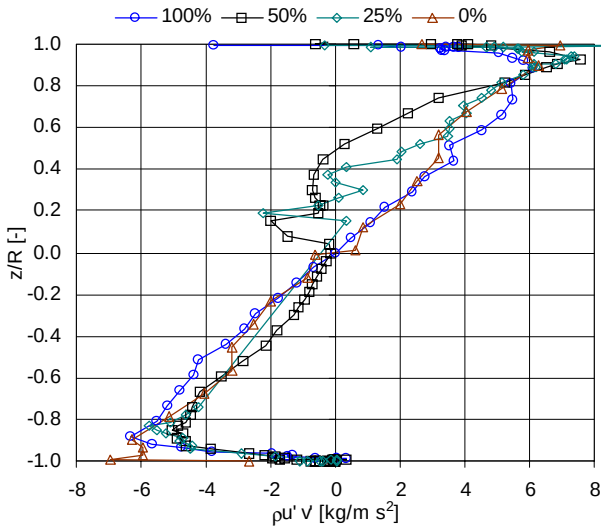

Figure 8.44c Reynolds stresses ($\overline{\rho u'v'}$), 2.04 m/s.

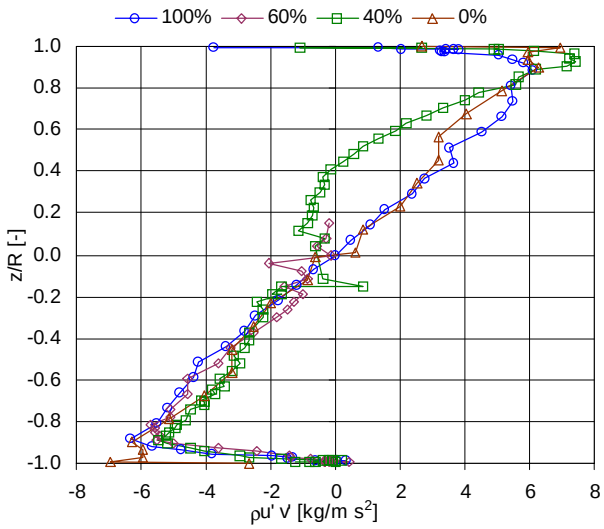

Figure 8.44d Reynolds stresses ($\overline{\rho u'v'}$), 2.04 m/s.

8.3.5 Influence on the LDA measurements by the nature of the interface

The previous sections have shown that the interface that separates oil and water may create problems when it comes to LDA measurements. In this section the focus is set on the mixture velocity of 1.02 m/s. Here, several water cuts were measured. Depending on the input water cut, the interface will vary from being smooth with only a few small droplets to being quite wavy with a high concentration of large droplets.

In the figures below, u-mean, u-rms, v-rms and the cross-moments are presented along with the water hold-up or local water fraction. To be able to show all quantities in the same figure the rms velocities are multiplied by a factor of 5 and the cross-moments by a factor of 100. Also keep in mind that the pictures are instantaneous and that the interface for this reason may affect a wider region of the pipe.

In Figure 8.45 the water cut is 15% and the flow pattern is stratified mixed. The interface extends approximately from z/R=-0.8 to z/R=0. This is seen from either the picture or the hold-up. The concentration of droplets is high. The droplets vary in size from about 5 mm and less (diameter). Because of the wavy nature of the interface, the available region for the LDA measurements is larger than indicated above. The reason is that the LDA measurements are taken over a certain time interval in each position. Thus, the flow needs only to be continuous in parts of this time interval. As seen from the figure the mean velocity profile is quite smooth. The main influence of the interface is on the rms velocities and on the cross-moments. This is seen as the jagged part of the distribution curves. Clearly, the maximum velocity in the axial direction is located in the oil phase. This is also expected, since the flow rate of oil is much larger than the flow rate of water.

When the water cut is increased to 25% as shown in Figure 8.46, the interface shrinks significantly. The flow pattern is still stratified mixed, but the concentration of droplets is less. The droplets are now a little larger, with diameters up to 8 mm. The distribution of mean velocity is smooth through the entire interface. Even the other distributions are quite smooth except from a small peak, which is positive for rms and negative for cross-moments, at the core of the interface. This peak is induced by the interface but most likely as a consequence of difficult measurement conditions. It has

probably little to do with physics. Again it is seen that the axial mean velocities are highest in the oil phase.

Figure 8.47 displays the case of 40% water cut. Here, the flow pattern is stratified wavy. The concentration of droplets is small compared to the above cases. The diameter is seen to be about 3 mm for the largest droplets. Again, distributions are smooth with the exception of a peak induced by the interface for rms velocity and cross-moment curves. The highest axial mean velocity is located well inside the oil phase.

Little is changed when the water cut is increased to 50% as shown in Figure 8.48. The flow pattern is stratified wavy with slightly less droplets at the interface. Also the largest droplet diameter seems to be less than 3 mm. Regarding the LDA measurements it can be seen that they are disturbed only across the interface region for the rms velocities. At equal flow rates the oil phase still has higher maximum velocity than that of water.

When the water cut is increased to 60% the interface is broader. From Figure 8.49 it can be seen that droplets are slightly larger than at 50% water cut. The flow pattern is still stratified wavy. The peaks in the rms velocity and cross-moment distributions are seemingly below the actual interface, but probably this is only because of the waves. This particular water cut implies that the input flow rates of oil and water are 3.6 m^3/h and 5.4 m^3/h, respectively. Nevertheless, the maximum velocity is located in the oil phase. An explanation based on differences in physical fluid properties was given in the previous section.

At 75% water cut, which is presented in Figure 8.50, the flow pattern has changed to stratified mixed. The interface is wider, wavier and contains more droplets. The sizes of the largest droplets are 7-8 mm. The dispersed regions of this water cut are close to the limit of what is possible to measure with LDA under the prevailing optical conditions. All distributions are smooth with the exception of the well-known peaks at the interface region.

The highest water cut which is subjected to LDA is 85%. From Figure 8.51 it is seen that the flow pattern is a water continuous dispersion with a dense packed layer of oil droplets (Dw-DP). The concentration of droplets is high, and the size is 5 mm and less. The thickness of the dense packed layer is almost equal to the pipe radius. However, droplets are seen to appear also almost at the bottom of the pipe. The dispersed layer is "attached" to the upper wall and prevents continuous flow above it. Thus, the LDA measurements are poor in almost the entire region of dense packed droplets. The full distributions are shown, but in the dense packed region the number of samples obtained is very low. Thus, the measurements cannot be trusted statistically in this region.

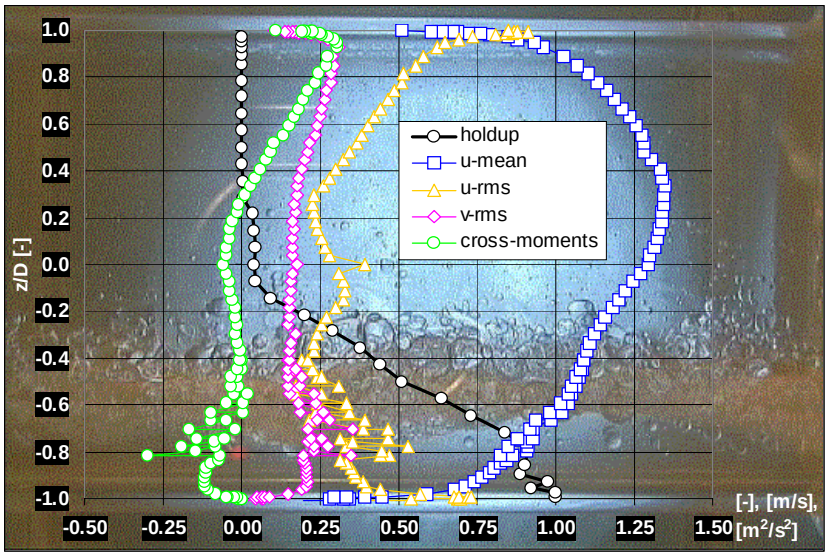

Figure 8.45 LDA measurements at 1.02 m/s and 15% water cut. Rms profiles are multiplied by a factor of 5 and cross-moments by a factor of 100.

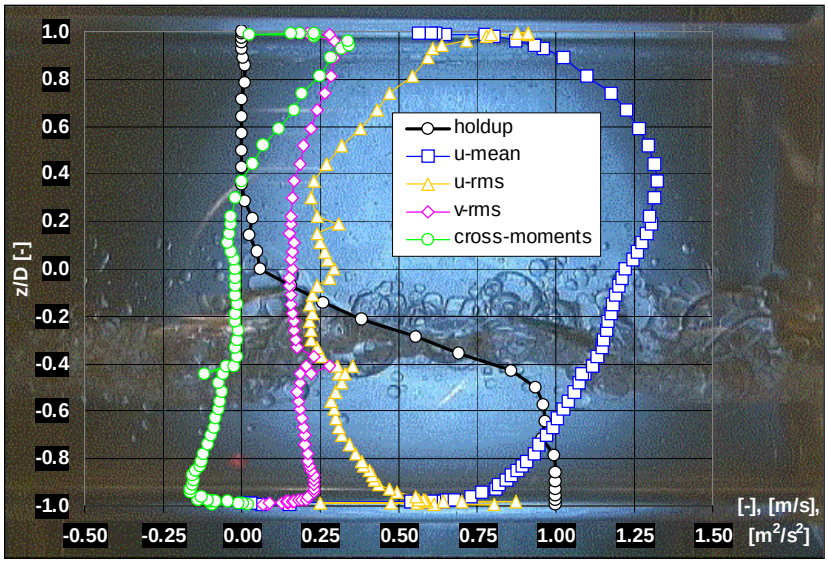

Figure 8.46 LDA measurements at 1.02 m/s and 25% water cut. Rms profiles are multiplied by a factor of 5 and cross-moments by a factor of 100.

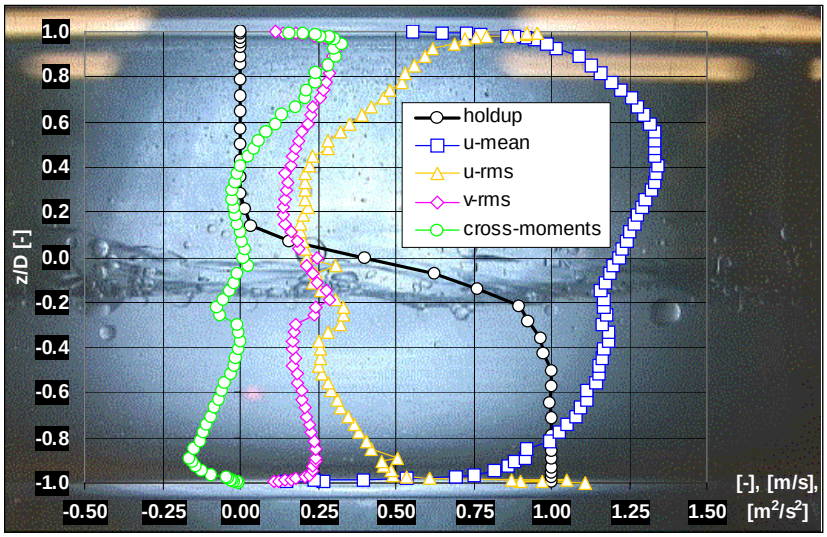

Figure 8.47 LDA measurements at 1.02 m/s and 40% water cut. Rms profiles are multiplied by a factor of 5 and cross-moments by a factor of 100.

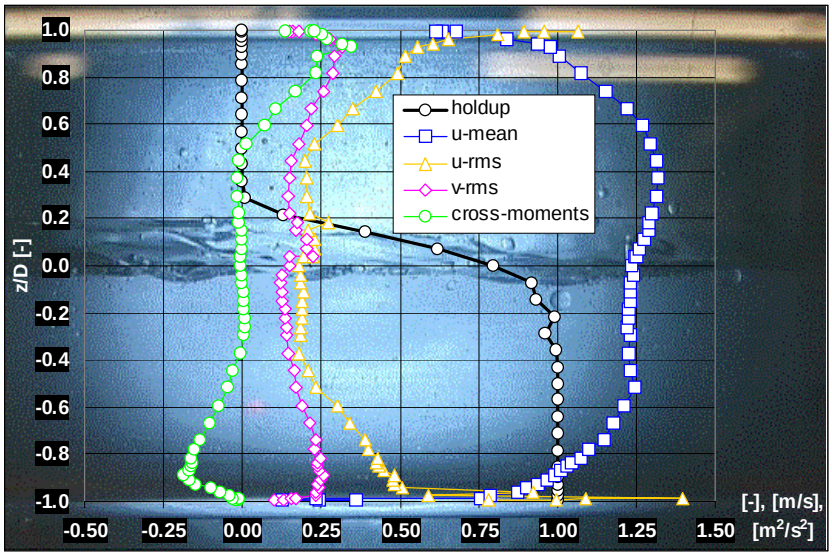

Figure 8.48 LDA measurements at 1.02 m/s and 50% water cut. Rms profiles are multiplied by a factor of 5 and cross-moments by a factor of 100.

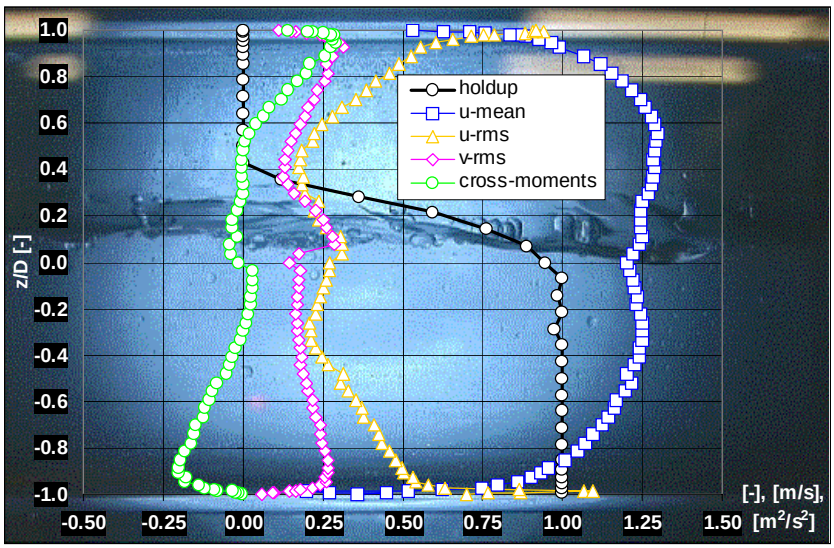

Figure 8.49 LDA measurements at 1.02 m/s and 60% water cut. Rms profiles are multiplied by a factor of 5 and cross-moments by a factor of 100.

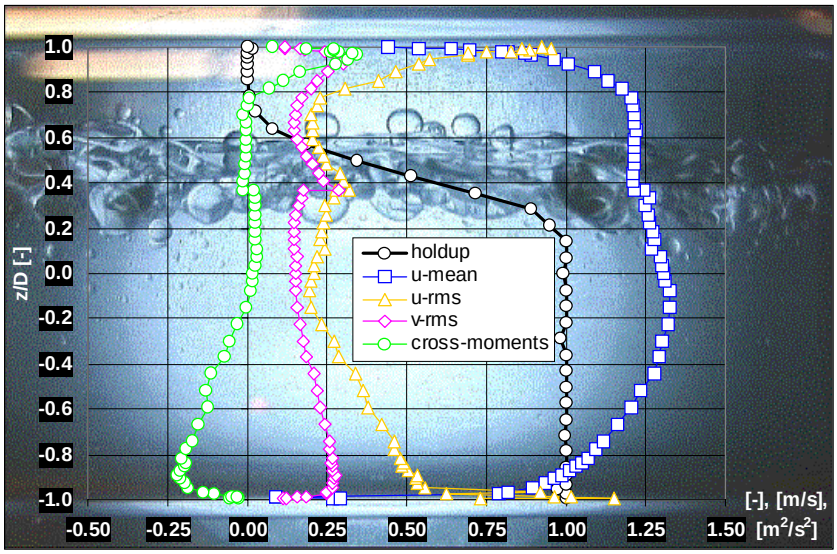

Figure 8.50 LDA measurements at 1.02 m/s and 75% water cut. Rms profiles are multiplied by a factor of 5 and cross-moments by a factor of 100.

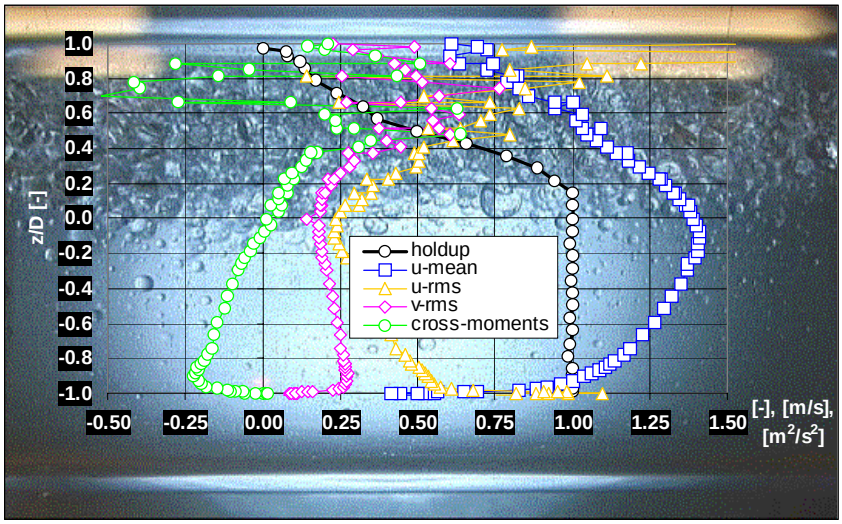

Figure 8.51 LDA measurements at 1.02 m/s and 85% water cut. Rms profiles are multiplied by a factor of 5 and cross-moments by a factor of 100.

CHAPTER 9:
MEASUREMENTS IN DISPERSED TWO-PHASE FLOW IN THE RIM FACILITY

9.1 INTRODUCTION

The previous chapter presented LDA measurements in stratified flow. These measurements were conducted in a flow facility using model oil together with water. In this chapter, measurements are conducted in the RIM flow facility using other fluids. This facility is described in Section 3.2. A full refractive index matching procedure is carried out to achieve optical accessibility to all parts of the pipe. This procedure is outlined in detail in Section 4.4.4. The flow patterns that appear are mainly dispersed. In addition to LDA, experiments conducted include pressure drop and local phase fraction (hold-up) measurements. The results from these experiments are reported in Kvandal et al. (2000).

9.2 PRESSURE DROPS AND FLOW PATTERNS

Prior to the LDA measurements a thorough investigation of pressure drops and flow patterns were conducted to identify the characteristics of the given fluid system. A number of experiments were performed within the full range of water cuts, with mixture velocities between 0.75-3.0 m/s. This screening phase was carried out to select the experimental conditions for the LDA measurements.

Analyses of the data from the traversing gamma instrument indicated that four typical trends of local phase distributions were observed for the fluid system. These are all shown in Figure 9.1, with the radial position on the y-axis and the water holdup on the x-axis. Based on these different trends, the flow patterns are classified as follows (also displayed in the legend of Figure 9.1):

SD	Stratified-dispersed flow
DIH-B	Dispersed flow with an *in-homogenous bulk* mixture
DIH-W	Dispersed flow with an *in-homogenous wall* mixture
DH	Dispersed homogenous flow

Based on this classification a full flow pattern map was produced for all data and this is presented in Figure 9.2.

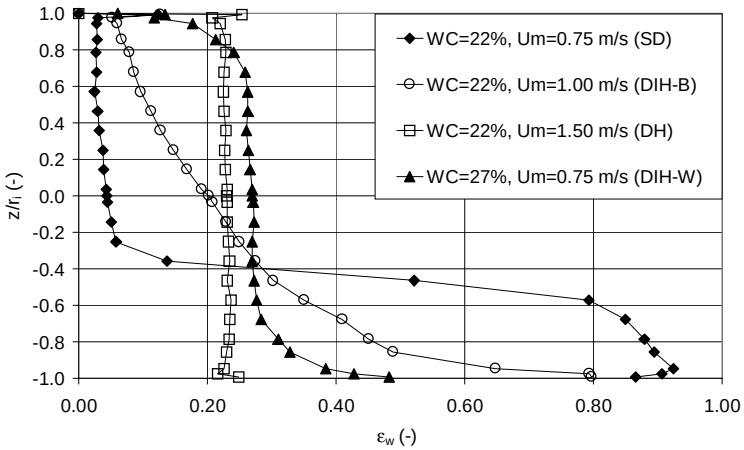

Figure 9.1. Phase distribution in the cross section of the pipe.

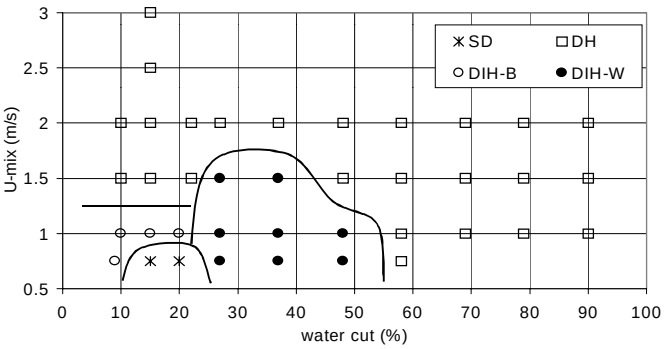

Figure 9.2. Flow pattern map.

Results from the pressure drop readings are presented as function of water cut in Figure 9.3. Here, the actual oil/water pressure drop is scaled with single-phase oil pressure drop in order to emphasise the effect of water at constant mixture velocity. From the figure it can be observed that the phase inversion point for the particular

fluid system is close to the water cut of 27%. This was confirmed with fluid sampling during the experimental runs. At water cuts lower than 27% the two fluids separated quickly (within seconds) while at higher water cuts the fluids separated slowly (within minutes).

By comparing Figures 9.2 and 9.3 it can clearly be seen that the pressure drop is directly related to the flow patterns. For water cuts lower than the phase inversion point, and velocities lower than 1.5 m/s, we observe that the trends are not uniform due to different degrees of in-homogeneity. On the other hand, velocities higher than 1.5 m/s show a uniform trend, which is explained by a completely homogenous flow. Between water cuts of 27 and 50%, the scatter in pressure drops between the different mixture velocities is large. This stands in great contrast to water cuts higher than 50%, where all measurements show the same trend. The explanation for the scatter in pressure drop is not clear, but it could be due to the specific DIH-W flow pattern that was observed for low velocities.

Based on this screening the goal was to investigate the fully dispersed oil continuous flow.

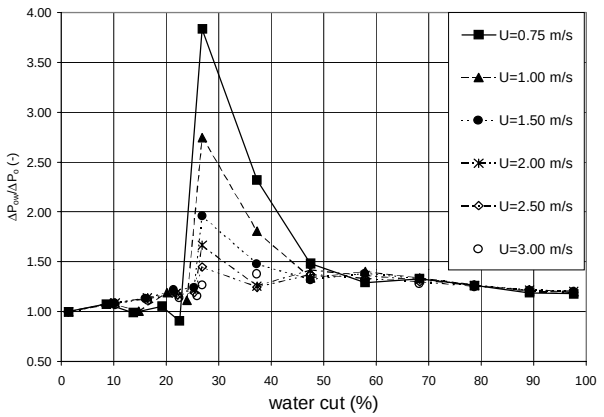

Figure 9.3. Pressure drop versus water cut.

9.3 VELOCITY AND TURBULENCE CHARACTERISTICS

The experiments with the LDA system were performed by traversing the measuring volume vertically through the pipe centre with a measuring grid of about 50 points. The density of measurement positions was highest near the pipe walls as velocities, rms-values and cross-moments have large gradients in these regions. Unfortunately, the number of velocity samples in these regions was rather low compared to that is recommended in order to satisfy the statistical basis for calculation of these values. The reason for this is the low velocity in the wall region, which means that the probability of receiving samples are considerably lower than in high velocity regions. For single-phase flow the addition of small (< 10 μm) tracer particles can enhance the data rate in all regions of the pipe, but in the case of a two-phase oil-water mixture such particles could affect the interfacial properties of the mixture.

The raw data from the LDA software, as used in Equations 8.19, 8.20 and 8.22, were further scaled to non-dimensional quantities for comparisons between different velocities and water cuts. For turbulent pipe flow it is common to scale the velocity and turbulence quantities with the maximum velocity, the bulk/mixture velocity or the friction velocity. To produce the wall coordinates the friction velocity defined in Equation 8.10 is used. Based on experiments described earlier this value was calculated for each set of experimental conditions as follows:

$$u_\tau = \sqrt{\frac{d_i \cdot \left(\Delta P / \Delta L\right)_{ow}}{4 \cdot \rho_{ow}}} \tag{9.1}$$

where d_i is the pipe inner diameter, $(\Delta P/\Delta L)_{ow}$ is the recorded pressure drop and ρ_{ow} is the recorded mixture density. Thus, the scaled parameters then become:

$$u^+ = \frac{\bar{u}}{u_\tau} \qquad v^+ = \frac{\bar{v}}{u_\tau} \qquad u_{rms}{}^+ = \frac{u_{rms}}{u_\tau} \qquad v_{rms}{}^+ = \frac{v_{rms}}{u_\tau} \qquad \overline{u'v'}^+ = \frac{\overline{u'v'}}{u_\tau^2} \tag{9.2}$$

The results from the measurements are shown in Figures 9.4 to 9.7. Data for all the experimental conditions are displayed in each of these figures for comparison

purposes. Figure 9.4 presents the axial mean velocity scaled with average mixture velocity u_m , versus the non-dimensional radius starting at the pipe wall. Radial (vertical) mean velocities are not presented in any figures, as they all were zero.

Figure 9.5 presents the local axial mean velocity in wall coordinates compared to the well-known law of the wall (or more precisely the Nikuradze equation). It can be seen from the figure that all measurements except for the 22% water cut at 1.50 m/s follow the law of the wall quite well. At z^+ lower than 5 some scatter is seen in all experiments. The deviation from the law of the wall regarding the 22% water cut at 1.5 m/s case is pronounced in the whole measurement region (except for the intersection). This particular velocity profile is more similar to a laminar profile than a turbulent one.

Figure 9.6 presents the scaled *rms*-values for both the axial and radial velocities, while Figure 9.7 presents the cross-moments, which is proportional to the Reynolds stresses. The abscissa in both cases is the non-dimensional radius. As seen from Figures 9.5-9.7 the data scatter is largest in the region close to the wall. As mentioned in the previous section this is probably due to a low sampling rate.

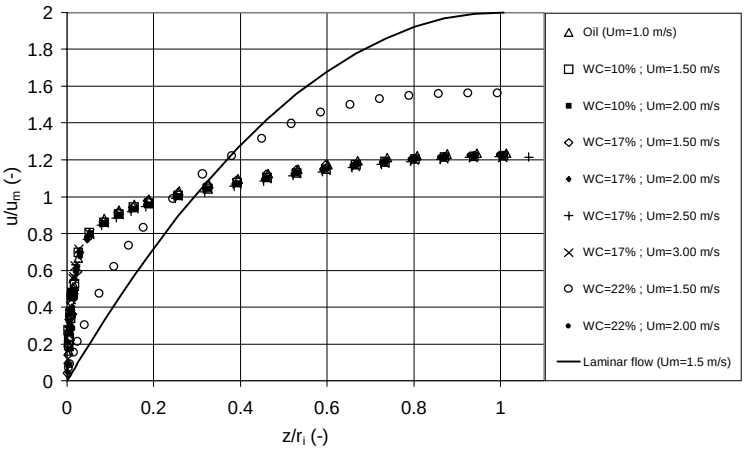

Figure 9.4. Mean velocities versus radial distance.

An important observation from Figures 9.4-9.7 is that all data sets, except for one, follow the same trend and become almost identical when scaled with either the mixture velocity or the friction velocity. In Figure 9.5 and 9.7 the data are compared with conventional theory for single-phase turbulent pipe flow and, as seen from the figures, they seem to follow the law of the wall and the theory presented by Hinze (1959) for cross-moments.

Only the data for 22 % water cut and a mixture velocity of 1.5 m/s do not follow the same trend for any of the presented parameters. From Figure 9.6 and 9.7 we see that the *rms* and *cross-moment* (Reynolds stress) values for this case are very close to zero, which indicate little or no turbulence activity at this flow condition. In Figure 9.4 we have indicated the analytical velocity profile for a laminar flow is shown and the reader will observe that the profile for 22% water cut is somewhere in-between a laminar and turbulent flow. The explanation for this is not obvious. There are no indications from the pressure drop readings that could explain this and by using conventional methods such as back-calculating the effective viscosity based on pressure drop one ends up with a Re number close to 20000, which is well into the turbulent flow regime. However, this particular condition is very close to the phase inversion point and the most likely explanation might therefore be connected to the phase distribution. From Figure 9.2 it was observed that the flow pattern changes from SD via DIH-B to DH at 22% water cut and is also close to the DIH-W region, which could mean that the DH flow pattern is not fully developed at a velocity of 1.5 m/s and that the droplets are in a phase of orientating themselves in the pipe. Another explanation could be that local phase inversion has occurred in the pipe and that some zones in the pipe are oil continuous while other zones are water continuous. Turbulence will most likely not be transported between the continuous phase and the droplets, and will therefore be damped out in a system with local phase inversion.

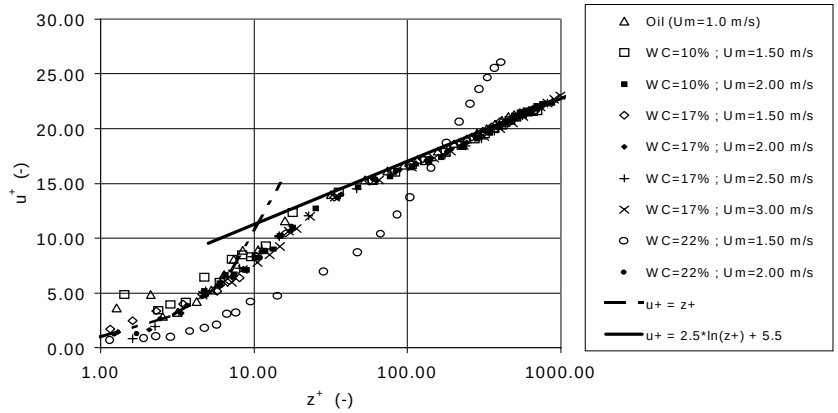

Figure 9.5. Scaled axial mean velocity plotted in wall coordinates.

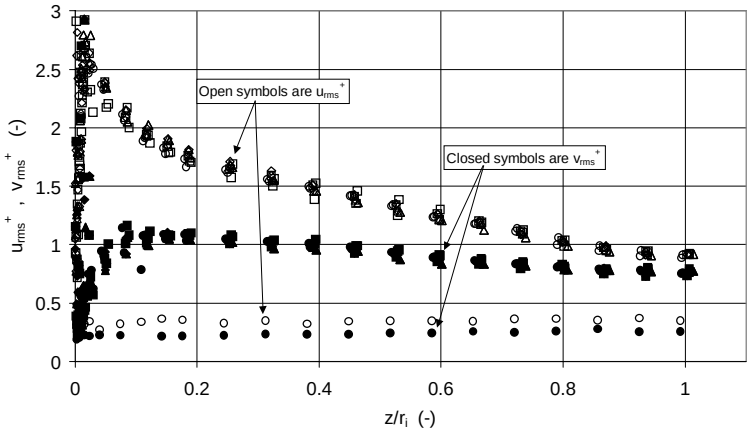

Figure 9.6. u_{rms}^{+} and v_{rms}^{+} versus radial distance.

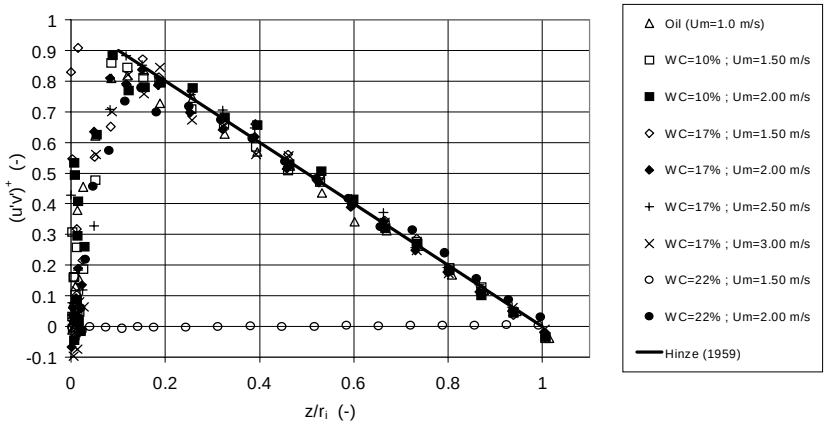

Figure 9.7. Cross-moments ($\overline{u'v'}^{+}$) versus radial distance.

CHAPTER 10:
CONCLUSIONS AND SUGGESTIONS FOR FURTHER WORK

The main part of this thesis has involved experimental work in two flow facilities, which act as models for horizontal pipes and wells for oil production. Measurements of local phase fractions, pressure drops, slip ratios and velocity and turbulence distributions were conducted.

Flow patterns and local phase fractions

A digital video camera combined with a traversible gamma densitometer was used to study the flow patterns and the distribution of water hold-ups over the pipe cross-section for mixture velocities ranging from 0.4 to 3 m/s and water cuts ranging from 0 to 100%.

Nine different flow patterns were identified. The flow pattern classifications are subjective and thus, might differ some from classifications of other investigators. In general the observed patterns fall into two classes; *stratified flows* (SS, SW, SM) and *dispersed flows* (Do-DP, Dw-DP, Do-I, Dw-I, Dw-H). The identified flow patterns have different distribution curves, some quite characteristic, and thus the gamma densitometer scans prove to be a reliable method for identification of flow patterns.

The local phase fraction of water is measured along the vertical diameter of the pipe. The distributions or profiles clearly show the position and the width of the interface between oil and water. This is vital information when velocity and turbulence distributions are measured. In the work presented in this thesis, the information of flow patterns provided by the gamma scans and the video recordings was used to select the experiments that were suitable for LDA measurements.

Pressure drops and slip ratios

The pressure drop in the horizontal test pipe is measured for single-phase flow at bulk velocities ranging from 0.4 to 3 m/s, which correspond to Reynolds numbers ranging from 22500 to 168900 for water (11000 – 82300 for oil). When the friction factor is calculated from experimental pressure drop data and plotted against the Reynolds

number it fits the empirical correlations of Haaland (includes roughness parameter) and Blasius (smooth pipes) well. Measurements in single-phase are used as comparison to two-phase measurements.

The pressure drop in two-phase flows at the same mixture velocities as the bulk velocities for single-phase flows was measured. The water cuts varied from 0 to 100%. When pressure drop is plotted as a function of water cut for the various mixture velocities a peak is observed at mixture velocities higher than 1 m/s. As the mixture velocity increases the peak is observed for successively lower water cuts. To explain the peak one has to use the information from the flow pattern. It turns out that a dense packed layer of oil droplets is formed at high water cuts. The droplets increase the mixture viscosity and thus create an increased pressure gradient, similar to what is common to observe in phase inversion.

Effects on the pressure drops from phase inversion are not observed in any of the experiments. Probably the mixture velocity is too low.

The pressure drops as function of water cut for the various mixture velocities were compared to model predictions. The two-fluid model was used for stratified flows. Empirical models by Pal and Rhodes (1989) and Guth and Simha (1936) for homogeneous flow are included for comparison with pressure drop data at some mixture velocities. In addition to pressure drop, the slip ratios calculated from gamma densitometer scans are compared with the model predictions. In general the pressure drop data fit the two-fluid model best for intermediate water cuts. For high water cuts the model under predicts the pressure drop. The slip ratio is fairly well predicted by the model for all water cuts. Both empirical models require input of the phase inversion water cut and predict a peak in the pressure drop at this particular water cut. These models highly over-predict the pressure drop data here.

For dispersed flows the homogeneous model was employed. In general the model over-predicts at low water cuts and under-predicts the pressure drop data at high water cuts. The model based on concentration weighting proved to fit the experimental data best.

Velocity and turbulence distributions

Laser Doppler anemometry experiments are conducted on stratified flow in a model oil facility and on dispersed flow in a refractive index matched facility. Axial mean velocities, axial (horizontal) and radial (vertical) rms-velocities, axial turbulence intensities and cross-moments (Reynolds stresses) are the parameters that were measured for selected bulk velocities for single-phase flow and selected mixture velocities and water cuts for two-phase flows. The velocity ranged from 0.41 m/s to 2.04 m/s and the water cut ranged from 15% to 85% in the model oil facility.

The measurements on single-phase flows were conducted prior to the two-phase flow experiments. Compared with classical theory and with the recent direct numerical simulations by Moser et al. (1999) and Eggels et al. (1994) these results showed good agreement. The axial mean velocities fit the *law of the wall* well except for regions very close to the wall, where some scattering is present in the experiments. The deviation from the DNS data is also most evident close to the wall.

The measurement in stratified oil/water flow showed that the velocity and turbulence profiles are highly asymmetrical (i.e. in contrast to single-phase flow) about the centre axis of the pipe. One of the findings was that the oil phase moved faster than the water phase at 50% and 60% water cut. The reason is attributed to the differences in physical properties (viscosity and density) between the two fluids. Another observation is that the interface seems to dampen the turbulence in the flow. This is pronounced in the distribution curves for cross-moments and Reynolds stresses. Some of the results are also presented in Elseth et al. (2000).

The measurements in dispersed flow are presented in Kvandal et al. (2000). A matched refractive index system has been developed with physical properties that can simulate a real oil and water mixture in flow behaviour. This system has a distinct phase inversion point and allows flow patterns from stratified to fully dispersed. The system has been used successfully in order to obtain velocity and turbulence distributions in a fully homogenous dispersed flow.

By scaling velocity and turbulence data from the dispersed flows by the friction velocity based on the measured pressure drop, all data merge to single-phase trends. Only one data set, which is close to the phase inversion point, does not follow the same trend. This particular data set has a more laminar flow regime.

Based on the presented experimental data for dispersed homogenous flow the velocity and turbulence characteristics follow a single-phase analogy with a modified viscosity and density for most cases. Thus, a homogenous model is applicable with an appropriate mixture viscosity model.

Overall conclusion

The measurement of velocity and turbulence in stratified and dispersed pipe flow has contributed to a better understanding on the topic. It can be concluded that LDA is applicable for obtaining velocity and turbulence distributions in both stratified and dispersed flows provided the optical conditions are good. However, it has to be pointed out that the measurements are conducted on model systems and that these systems are a simplification of real oil/water flow in horizontal pipes and wells.

The results may be used in the development of models and computer simulation programs for two-phase liquid-liquid flow. Such models exist, but in general the complexity of two-phase flows is difficult to resolve. Thus, experimental data is important in order to verify the model predictions.

Suggestions for further work

If any suggestions for further work should be made the following areas need more investigation:

- *Improvement of the optical conditions in the Model Oil Facility.* Although the optical conditions made velocity and turbulence distributions accessible for stratified flows, the optical conditions close to the pipe wall were far from perfect. By applying a full RIM technique to this flow facility, as done for the facility for dispersed flow, the near wall region can be investigated with a higher accuracy.

- *Off-centre measurements.* In order to obtain a better understanding of the asymmetric behaviour of two-phase flow, measurements should be conducted in off-centre positions in the pipe (i.e. vertical and horizontal traversing, but along other lines than the diameter). Among other things, such measurements will provide information about curved interfaces.

- *Inclined pipes.* Production of oil from sub sea reservoirs often takes place in wells that have inclination angles up to 10 degrees of the horizontal. The flow pattern transitions, the pressure drop and the velocity and turbulence distributions will most probably differ from the results presented in this thesis for horizontal flow.

- *Development of models* that are able to simulate oil/water flow in pipes for the various flow conditions.

NOMENCLATURE

Roman symbols

$\overline{P}$	average pressure	(Pa)
P'	fluctuating pressure	(Pa)
$\overrightarrow{V}$	velocity vector	m/s
$\vec{e}, \overrightarrow{e_1}, \overrightarrow{e_2}, \overrightarrow{e_3}$	unit vectors	(-)
$\vec{n}$	difference vector between unit vectors	(-)
$\overrightarrow{n_0}$	unit vector in a given direction	(-)
$\overline{u}, \overline{v}$	average velocities	(m/s)
u', v'	fluctuating velocities	(m/s)
$\overline{u'v'}$	cross-moments	(m^2/s^2)
A	cross sectional area of pipe	(m^2)
A	atomic mass in Eq. 5.4	(kg/kmol)
A_o, A_w	areas occupied by oil and water	(m^2)
b	gamma beam thickness	(m)
c	speed of light	m/s
C_o, C_w	volumetric fraction of oil and water (water cut)	(-)
D	inner pipe diameter	(-)
d_0	beam diameter	(m)
d_f	fringe spacing	(m)
D_{ho}, D_{hw}	hydraulic diameters in oil phase and water phase	(m)
d_i	inner pipe diameter	(m)
dp/dx	pressure gradient	(bar/m)
e	roughness parameter of pipe material	(m)
e	mathematical constant equal to 2.71828	(-)
E	maximum error of estimate, Eq. 4.37	(-)
E	gamma energy	(keV)
f	frequency	(s^{-1})

F(u), F(v)	flatness parameters	(-)
f_0	frequency shift in Fig. 4.13	(mHz)
f_D	Doppler frequency	(s^{-1})
f_I	incident laser beam frequency	(mHz)
f_m	mixture friction factor (dispersions)	(-)
f_{mr}	frequency from stationary source recorded by moving receiver, Eq. 4.10	(s^{-1})
f_{ms}	frequency from moving source recorded by stationary receiver, Eq. 4.13	(s^{-1})
f_o, f_w	friction factor in oil and water phase (Fanning's)	(-)
f_{ow}	interfacial friction factor (Fanning's)	(-)
g	gravity constant	(m/s^2)
h	height of interface above pipe centre	(m)
H	height	(m)
I	beam intensity of photons	(counts/s)
I(x)	local intensity of photons	(counts/s)
I_0	incident intensity of photons	(counts/s)
L	length, pipe length	(m)
n	refractive index	(-)
N	number of samples or number of counts	(-)
N_A	Avogadro number equal to 6.022E+23	(-)
N_f	number of fringes	(-)
P, p	pressure	(Pa)
Q	volumetric flow	(m^3/h)
R	pipe radius	(m)
R(z)	wave front radius	(m)
R^2	regression parameter in Eq. 7.1	(-)
Re	Reynolds number	(-)
Re_τ	friction Reynolds number	(-)
r_i	inner pipe radius	(m)
R_v	oil-water volume ratio	(-)
S(u), S(v)	skewness parameters	(-)
S_o, S_w	oil and water wetted perimeters	(m)

S_{ow}	interfacial perimeter	(m)
S_{xx},S_{yy},S_{zz}	parameters in trend line regression, Eq. 7.1	(-)
t	time	(s)
T(u), T(v)	turbulence intensities	(%)
t_i	transit time	(s)
u	axial (horizontal) velocity component	(m/s)
u^+, v^+	velocities scaled by the friction velocity	(-)
U_b, u_b	bulk velocity	(m/s)
U_m	mixture velocity	(m/s)
U_{mix}	mixture velocity	(m/s)
U_o, U_w	in-situ velocities or actual velocities	(m/s)
U_{so},U_{sw}	superficial oil velocity, superficial water velocity	(m/s)
u_τ	friction velocity	(m/s)
v	radial (vertical) velocity component	(m/s)
V_v	vertical projection of velocity vector	(m/s)
x	absorber thickness	(m)
x, y, z	axis directions	(m)
z	position	(m)
$Z_{\alpha/2}$	standardized mean	(-)

Greek symbols

$\overline{\rho u' v'}$	Reynolds stress tensor	(N/m^2)
α	angle in Figure 2.17, divergence angle Fig. 4.5	(rad)
γ	linear absorption coefficient	(m^{-1})
Δf_D	total frequency shift	(s^{-1})
Δf_r	frequency difference in Eq. 4.11	(s^{-1})
Δf_s	frequency difference in Eq. 4.8	(s^{-1})
Δp	pressure drop over a certain distance	(bar)
$\delta\alpha_1$	error calculated by Eq. 5.12	(%)
ε	in-situ area fraction	(-)
ε_M	eddy diffusivity	(m^2/s)

ε_w	water holdup	(-)
η_i	weighting factor	(-)
θ	inclination angle	(deg, rad)
θ_1, θ_2	angle of incidence and refraction angle	(deg, rad)
λ	wavelength	(m)
λ_{ms}	wavelength from moving source	(m)
μ	dynamic viscosity	(Pa s)
μ	mass absorption coefficient, Eq. 5.3	(m^2/kg)
μ_d	dispersed phase viscosity	(Pa s)
μ_m	mixture viscosity	(Pa s)
μ_r	relative viscosity	(Pa s)
μ_t	turbulent viscosity or eddy viscosity	(m^2/s)
ν	kinematic viscosity	(m^2/s)
π	pi	(-)
ρ	density	(kg/m^3)
σ	interfacial tension	(N/cm)
σ	microscopic absorption cross section	(m^3/mol)
σ, σ_{sd}	standard deviation	( )
σ^2	variance	( )
τ_0	wall shear	(N/m^2)
τ_i	integral time scale	(s)
τ_o, τ_w	wall shear in oil phase and water phase	(N/m^2)
τ_{ow}	interfacial shear	(N/m^2)
τ_w	wall shear	(N/m^2)
φ	dispersed phase fraction	(-)
φ_d	fraction of dispersed phase	(-)
$\varphi_{\mu=100}$	fraction in Eq. 2.23	(-)

Subscripts / superscripts

+	scaled by friction velocity
d	dispersed

ext	external
int	internal
L	laminar
mr	moving receiver
ms	moving source
o	oil
ow	oil-water interface
rms	root mean square
s	superficial
t	total
T	turbulent
w	water

REFERENCES

Angeli P., Hewitt G.H., *Flow Structure in Horizontal Oil-Water Flow,* International Journal of Multiphase Flow 26, pp 1117-1140, 2000

Angeli P., *Liquid-Liquid Dispersed Flows in Horizontal Pipes,* PhD Thesis. Imperial College, University of London, 1997

Arirachakaran S., Oglesby K.D., Malinowsky M.S., Shoham O., Brill J.P., *An Analysis of Oil/Water Flow Phenomena in Horizontal Pipes,* SPE Paper 18836, SPE Production Operations Symposium, pp. 155-167, Oklahoma, March 13-14, 1989

Barnea D., Taitel Y., *Kelvin-Helmholtz Stability Criteria for Stratified Flow: Viscous versus Non-viscous (Inviscid) Approaches,* Int. J. Multiphase Flow Vol. 19, No. 1, pp. 639-649, 1993

Bird R.B., Stewart W.E., Lightfoot E.N., *Transport Phenomena,* Second Edition, Wiley, 1960

Bøe R., *Void Fraction Measurements in Boiling Cryogenic Mixtures using Gamma Densitometer,* Int. J. Heat Mass Transfer. Vol. 41, No. 10, pp. 1176-1175, 1998

Brauner N., Moalem Maron D., *Flow Pattern Transitions in Two-Phase Liquid-Liquid Flow in Horizontal Tubes,* Int. J. Multiphase Flow Vol. 18, No. 1, pp. 123-140, 1992

Brauner N., Moalem Maron D., *Stability Analysis of Stratified Liquid-Liquid Flow,* Int. J. Multiphase Flow Vol. 18, No. 1, pp. 103-121, 1992

Brauner N., Moalem Maron D., *Two-Phase Stratified Flow,* PhysicoChemical Hydrodynamics Vol. 11, No. 4, pp.. 4487-506, 1989

Brayton D.B., Kalb H.T., Crosswy F.L., *Two Component Dual-Scatter Laser Doppler Velocimeter with Frequency Burst Signal Readout,* Applied Optics, Vol. 12, No. 6, June 1973

Charles M.E., Govier G.W., Hodgson G.W., *The Horizontal Pipeline Flow of Equal Density Oil-Water Mixtures,* The Canadian Journal of Chemical Engineering, February, 1961

Charles M.E., Redberger P.J., *The Reduction of Pressure Gradients in Oil Pipelines by the Addition of Water: Numerical Analysis of Stratified Flow,* The Canadian Journal of Chemical Engineering, April, 1962

Chervin P.A., Petrie H.L., Deutsch S., *Measurement of Spatial Correlations in the Near Wall Region of a Fully Developed Turbulent Pipe Flow by LDV,* Laser Anemometry-Proceedings of the 3rd International Conference, pp.379-389, 1990

Clark K.A., Shapiro A., U.S. Patent 2533878, May 31, 1949

Dantec Reference Guide, 2000 (Accompanies the LDA software)

Davis W.E.R., Unger J.I., *Velocity Measurements in Bubbly Two-Phase Flows using Laser Doppler Anemometry (Part 2),* Technical Note No. 185, Institute for Aerospace Studies, University of Toronto, 1973

Davis W.E.R., *Velocity Measurements in Bubbly Two-Phase Flows using Laser Doppler Anemometry (Part 1),* Technical Note No. 184 Institute for Aerospace Studies, University of Toronto, 1973

den Toonder J.M.J., *Drag Reduction by Polymer Additives in a Turbulent Pipe Flow: Laboratory and Numerical Experiments.* Thesis, Delft University of Technology, 1995.

den Toonder J.M.J., Nieuwstadt F.T.M., *Reynolds Number Effects in a Turbulent Pipe Flow for Low to Moderate Re*, Phys. Fluids 9 (11), November 1997

Durão D.F.G., Founti M.A., Laker J., Pita G., Vehlo A., Whitelaw J.H., *Some Consequences of Bias Effects in Laser Doppler Anemometry*, 1st International Symposium on LDA, Lisbon, 1982

Durão D.F.G., Laker J., Whitelaw J.H., *Bias Effects in Laser Doppler Anemometry*, J. Phys. E: Sci. Instrum., Vol.13, 1980

Durst F., Jovanović J., Sender J., *LDA Measurements in the Near-Wall Region of a Turbulent Pipe Flow*, J. Fluid Mech., vol. 295, pp. 305-335, 1995

Durst F., Melling A., Whitelaw J.H., *Principles and Practice of Laser Doppler Anemometry*, Second Edition 1981

Durst F., Zarè M., *Laser Doppler Measurements in Two-Phase Flows*, Proceedings of the LDA-Symposium Copenhagen 1975

Edmann J.C., Tropea C.D., *Statistical Bias of the Velocity Distribution Function in Laser Doppler Anemometry*, 1st International Symposium on LDA, Lisbon, 1982

Eggels J.G.M., Unger F., Weiss M.H., Westerweel J., Adrian R.J., Friedrich R., Nieuwstadt F.T.M., *Fully Developed Turbulent Pipe Flow: A Comparison Between Direct Numerical Simulation and Experiment.* J. Fluid Mech., No. 268. pp. 175-209, 1994.

Els H., Rouve G., *LDV-Measurements in Pipe Flow - Problems and Experiences*, International Symposium on Laser Anemometry, ASME, FED, Vol.33, p.293, 1985

Elseth G., Kvandal H.K. and Melaaen M.C., *Measurement of Velocity and Phase Fraction in Stratified Oil/Water Flow*, International Symposium On Multiphase Flow and Transport Phenomena, Antalya, Turkey 5-10 Nov. 2000

Fischer M., Jovanović J., *Feasibility Study on the Applicability of an LDA System to Two-Phase Liquid-Liquid Pipe Flows*, Internal Report from Industrial Project for Norsk Hydro Research Centre, Porsgrunn, Norway, 1998

George W.K., Lumley J.L., *The Laser Doppler Velocimeter and its Application to the Measurement of Turbulence*, Journal of Fluid Mechanics, Vol.60, part 2,pp. 321-362, 1973

Grodstein G.W., *X-Ray Attenuation Coefficients from 10 Kev to 100 Mev*, NBS circular 583, 1957

Guth E., Simha R., Kolloid Z., vol. 74 pp. 266, 1936

Guzhov A.I., Grishin A.D., Medvedev V.F., Medvedeva O.P., *Emulsion Formation During the Flow of Two Liquids in a Pipe*, Neft Khoz 8, pp.58-61, August 1973 (In Russian)

Haaland S.E., *Simple and Explicit Formulas for the Friction Factor in Turbulent Pipe Flow*, Journal of Fluids Engineering Vol.105, March 1983

Hewitt G.F., *Gas-Liquid Two-Phase Flow*, Handbook of Multiphase Systems, edited by G. Hetsroni, Hemisphere Publishing Corp., 1982

Hewitt G.F., Shires G.L., Polezhaev Y.V., *International Encyclopedia of Heat & Mass Transfer*, CRC Press LLC 1997

Hinze J.O., *Turbulence*, Second Edition, McGraw-Hill, 1959.

Kays W.M., Crawford M.E., *Convective Heat and Mass Transfer*, Third Edition, McGraw-Hill, Inc. 1993

Kehoe A.B., Desai P.V., *Compensation for Refractive-Index Variations in Laser Doppler Anemometry,* Applied Optics, Vol.26, No.13, 1987

Kusters K.A., van Strien C.J.G., Wijers J.G., Thoenes D., *Effect of Velocity Bias on Integral Time Scale,* Laser Anemometry-Proceedings of the 3rd International Conference, pp.557-566, 1990

Kvandal H.K., Elseth G., and Melaaen M.C., *Measurement of Velocity and Phase Fraction in Dispersed Two-Phase Flow,* International Symposium On Multiphase Flow and Transport Phenomena, Antalya, Turkey 5-10 Nov. 2000

Mazumder M.K., Wankum D.L., *SNR and Spectral Broadening in Turbulence Structure Measurement using a cw Laser,* Applied Optics 14, 894, 1970

McLaughlin D.K., Tiederman W.G., *Biasing Correction for Individual Realization of Laser Anemometer Measurements in Turbulent flows,* The Physics of Fluids, Vol.16, No.12, pp.2082-2088, December 1973

Miller I., Freund J.E., Johnson R.A., *Probability and Statistics for Engineers,* Fourth Edition, Prentice Hall, 1990

Moser R.D., Kim J., Mansour N.N., *Direct Numerical Simulation of Turbulent Channel Flow up to* $Re_\tau = 590$. Physics of Fluids, Vol.11, Issue 4, pp. 943-945, 1999

Mukherjee H., Brill J.P., Beggs H.D., *Experimental Study of Oil-Water Flow in Inclined Pipes,* Transactions of the ASME, Vol. 103, March, 1981

Fakta 2001 - Norsk Petroleumsvirksomhet, Published by the Norwegian Oil and Energy Dept., 2001

Nädler M., Mewes D., *Flow Induced Emulsification in the Flow of Two Immiscible Liquids in Horizontal Pipes,* Int. J. Multiphase Flow, Vol. 23, No.1, pp. 55-68, 1997

Nädler M., Mewes D., *The Effect of Gas Injection on the Flow of Immiscible Liquids in Horizontal Pipes,* Chem. Eng. Technol. 18 pp. 156-165, 1995

Pacek A.W., Nienow A.W., *A Problem for the Description of Turbulent Dispersed Liquid-Liquid Systems,* Int. J. Multiphase Flow Vol.21, No 2, pp. 323-328, 1995

Pal R., *Pipeline Flow of Unstable and Surfactant Stabilized Emulsions,* AlChE Journal Vol. 39, No. 11, pp. 1754-1764, November 1993

Pal R., Rhodes E., *Emulsion Flow in Pipelines,* Int. J. of Multiphase Flow Vol. 15, No. 6, pp. 1011-1017, 1989

Pan L., *High Pressure Three-Phase (gas/liquid/liquid) Flow,* PhD, Imperial College, London, 1996

Petrick M., Swanson B.S., *Radiation Attenuation Method of Measuring Density of a Two-Phase Fluid,* Review Scientific Instruments, Vol.29, No.12, 1958

Rashid Hasan A., Shah Kabir C., *A New Model for Two-Phase Oil/Water Flow: Production Log Interpretation and Tubular Calculations,* SPE Production Engineering, May 1990

Ruck B., *Distortion of LDA Fringe Pattern by Tracer Particles,* Experiments in Fluids 10, 349-354 (1991)

Rudd M.J., *A New Theoretical Model for the Laser Dopplermeter,* Journal of Scientific Instruments, (Journal of Physics E) Series 2, Volume 2, 1969

Russell T.W.F., Hodgson G.W., Govier G.W., *Horizontal Pipeline Flow of Mixtures of Oil and Water,* The Canadian Journal of Chemical Engineering, February, 1959

Saffmann M., Buchhave P., Tanger H., *Simultaneous Measurements of Size, Concentration and Velocity of Spherical Particles by a Laser Doppler Method,* 2nd

International Symposium on LDA, Lisbon, 1984

Shao S., *Study of the Flow Behavior of Multiphase Flow System Using Laser Doppler Anemometry (LDA),* Thesis, Chicago, Illinois 1996

Soleimani A., Lawrence C.J., Hewitt G.F., *Effect of Mixers on Flow Pattern and Pressure Drop in Horizontal Oil-Water Pipe Flow,* International Symposium on Liquid-Liquid Two-Phase Flow and Transport Phenomena, ICHMT, Antalya Turkey, 1997

Soleimani A., *Phase Distribution and Associated Phenomena in Oil-Water Flows in Horizontal Tubes,* PhD Thesis. Imperial College, University of London, 1999

Søntvedt T., Valle A., *Capacities of Troll Oil Flow Lines with High Water Cuts. Predictions based upon Recorded Pipe Flow Friction Factors for Stable Troll Oil Dispersions,* Report no. R-068557, Norsk Hydro ASA, Norway, 1994

Sööt P.M., Knudsen J.G., *Two-Phase Liquid-Liquid Flow in Pipes,* AlChE Symposium Series, Vol. 68, No.118, pp. 38-44, 1973

Sullivan J.P., Theofanous T.G., *The use of LDV in Two-Phase Bubbly Pipe Flow,* Laser Velocimetry and Particle Sizing, Ed.:H.D. Thompson and W.H. Stevenson, Hemisphere Publishing Corporation, Washington DC, 391-394, 1979

Tennekes H., Lumley J.L., *A First Course in Turbulence, MIT Press,* The Massachusetts Institute of Technology, 1974

Trallero J.L., Cem Sarica, Brill J.P., *A Study of Oil/Water Flow Patterns in Horizontal Pipes,* SPE Production & Facilities, August 1997

Trolinger J.D., *Laser Instrumentation for Flow Diagnostics,* AGARDograph No. 186, 1974

Valle A., Kvandal H.K., *Pressure Drop and Dispersion Characteristics of Separated Oil/Water Flow*, International Symposium on Two-Phase Flow, Modelling and Experimentation, Rome, 1995

Valle A., Utvik O. H., *Pressure Drop, Flow Pattern and Slip for Two-Phase Crude Oil/Water Flow: Experiments and Model Predictions*, International Symposium on Liquid-Liquid Two-Phase Flow and Transport Phenomena, ICHMT, Antalya Turkey, 1997

Vigneaux P., Chenais P., Hulin J.P., *Liquid-Liquid Flows in an Inclined Pipe*, AlChE J. 34, pp. 781-789, 1988

Vikram C.S., Billet M.L., *Modifying Tunnel Test Sections for Optical Applications*, Optical Engineering, Vol.25, No.12, December 1986

Watson M.J., *Report on the commissioning of the Norsk Hydro traversing gamma densitometer for Liquid-Liquid experiments* Internal Report, Norsk Hydro Research Centre, Porsgrunn, Norway, 1998

Yeh Y., Cummins H.Z., *Localized Fluid Flow Measurements with an He-Ne Laser Spectrometer*, Applied Physics Letters, Volume 4, Number 10, 1964

Zhang Zh., Eisele K., *On the Overestimation of the Flow Turbulence due to Fringe Distortion in LDA Measurement Volumes*, Experiments in Fluids, Vol. 25, pp.371-374, 1998

Zisselmar R., Molerus O., *Investigation of Solid-Liquid Pipe Flow with regard to Turbulence Modification*, The Chemical Engineering Journal, 18, pp. 233-239, 1979

Åbro E., *Measurements of Gas Fraction in Pipe Flows using Multi-beam Gamma-ray Attenuation*, Thesis, University of Bergen, Norway, 1999

APPENDIX A1

FULL FLOW SHEET – MODEL OIL FACILITY